Development and Characterization of Co-evaporated CZTSe solar cells

zur Erlangung des akademischen Grades eines

DOKTOR-INGENIEURS

von der KIT-Fakultät für Elektrotechnik und Informationstechnik des Karlsruher Instituts für Technologie (KIT)

genehmigte

Dissertation

von

Lwitiko Pholds Mwakyusa

geb. in Tansania

Tag der mündlichen Prüfung: 06.11.2019

Hauptreferent: Prof. Dr. B.S. Richards

Korreferent: Priv.-Doz. Dr. M. Hetterich

Kurzfassung

Chalkogenid-basierte Dünnschichtsolarzellen wie z.B. $Cu(In,Ga)Se_2$ (CIGS) und CdTe konnten bereits erfolgreich in kommerziellen Anwendungen eingesetzt werden, weisen eine vergleichsweise geringe Energierücklaufzeit auf und eignen sich für flexible Einsatzmöglichkeiten. Allerdings stellen sowohl die Toxizität des verwendeten Cadmiums (Cd) als auch die begrenzte Verfügbarkeit von Indium (In) und Tellur (Te) eine Hürde für ihr weiteres Wachstumspotential dar. Dünne Schichten der quaternären Verbindungen $Cu_2ZnSnSe_4$ (CZTSe) und Cu_2ZnSnS_4 (CZTS) sowie der daraus abgeleiteten Kompositionen $Cu_2ZnSn(S,Se)_4$ (CZTSSe) erlangten besondere Aufmerksamkeit innerhalb der Photovoltaik-Forschungsgemeinschaft aufgrund des reichhaltigen Vorkommens und der toxischen Unbedenklichkeit ihrer Bestandteile. Allerdings schränken das großes Defizit der offenen Klemmenspannung (V_{OC}) und teilweise der geringe Füllfaktor (*FF*) verglichen mit CIGS und CdTe die weitere Kommerzialisierung dieser Technologie ein. Die Verbesserung von V_{OC} und Füllfaktor hin zu konkurrenzfähigen Werten erfordert ein tieferes Verständnis sowohl der Wachstumsmechanismen des Absorbers als auch der Verteilung von Sekundärphasen und Defekten sowie der Art der Rekombinationsprozesse in den Solarzellen.

Dementsprechend wurden im Rahmen dieser Arbeit grundlegende Studien über das Wachstum des CZTSe-Absorbers sowie die Leistungscharakteristika der entsprechenden Solarzellen durchgeführt. Dabei wurden drei verschiedene Konfigurationen der Vorläuferschichten untersucht: i) homogene, Se-haltige, mittels Koverdampfung hergestellte (Cu-Zn-Sn-Se) Vorläuferschichten, ii) homogene, metallische, koverdampfte (Cu-Zn-Sn) Vorstufen und iii) mehrlagige, koverdampfte (Cu-Sn/Cu-Zn-Sn-Se/ZnSe/Cu-Zn-Sn-Se und Cu-Zn/Sn) Vorläuferschichten. Verschiedene Charakterisierungstechniken wurden sowohl auf die Vorläufer- und Absorberschichten sowie auf die vollständigen Solarzellen angewandt um deren Qualität beurteilen zu können.

Unter Verwendung von Se-haltigen, koverdampften Vorläuferschichten konnten Solarzellen mit Wirkungsgraden von bis zu 6,4% realisiert werden. Dennoch limitieren sowohl die Rekombination an der CdS/CZTSe-Grenzfläche als auch die Reproduzierbarkeit des Prozesses die Leistung der hergestellten Zellen. Es konnte gezeigt werden, dass die Bereitstellung von zusätzlichem Sn in der Se-Atmosphäre während des Rekristallisationsprozesses der Cu-Zn-Sn-Se-Vorstufen ein geeigneter Ansatz zur Unterdrückung von CdS/CZTSe-Grenzflächenrekombination sowie zur Stabilisierung des Herstellungsprozesses ist. Zusätzlich wurde der Einfluss des im Rahmen des Selenisierungsprozesses anfänglich eingestellten N_2-Hintergrunddrucks auf die strukturellen Eigenschaften der CZTSe-Absorberschicht und die entsprechenden Solarzellen-Charakteristika genauer untersucht und diskutiert.

Eine Untersuchung der Phasenübergänge, die während des Selenisierungsprozesses der bei niedrigen Temperaturen mittels Koverdampfung hergestellten Cu-Zn-Sn-Se-Vorläuferschichten stattfinden, wurde durchgeführt. Eine homogene Durchmischung der binären (Cu_2Se, $SnSe_2$ und ZnSe) und ternären (Cu_2SnSe_3) Phasen im Temperaturbereich von 300 °C bis 500 °C konnte mittels Röntgendiffraktometrie, Raman-Spektroskopie, Raster- und Transmissionselektronenmikroskopie nachgewiesen werden. Dies legt nahe, dass die Bildung des CZTSe-Absorbers über konkurrierende Reaktionen von binären ($CuSe_2$ + $SnSe_2$ + ZnSe → $Cu_2ZnSnSe_4$) und ternären (Cu_2SnSe_3 + ZnSe → $Cu_2ZnSnSe_4$) Phasen stattfindet.

Die Verwendung von mehrlagigen, koverdampften Cu-Zn/Cu-Zn-Sn-Se/ZnSe/Cu-Zn-Sn-Se-Vorstufen zeigte sich vorteilhaft gegenüber den zuvor verwendeten einlagigen Vorläuferschichten, da sie die Entstehung eines tiefenabhängigen Kompositionsgradienten begünstigt. Dies wiederum kann möglicherweise zu veränderten Reaktionspfaden bei der Bildung des CZTSe führen. CZTSe-Solarzellen mit Wirkungsgraden von bis zu 7,9 % bei einer V_{OC} von 428 mV und einem Füllfaktor von 62 % konnten unter Verwendung dieses Ansatzes erzielt werden. Allerdings begrenzt der verminderte Kurzschlussstrom (29 mA/cm^2) im Vergleich zum einlagigen Ansatz (37 mA/cm^2) ihre Leistung. Darüber hinaus konnte beobachtet werden, dass sich durch zusätzliches Tempern (*pre-annealing*) jeder einzelnen Lage der Mehrschichtsysteme einerseits die J_{SC} in einer Größenordnung von 2 mA/cm^2 verbesserte, aber andererseits V_{OC} und *FF* gleichzeitig verschlechterten. Zusätzlich führte das *in-situ* Tempern des gesamten Vorläufersystems zur Bildung einer dreilagigen Struktur bestehend aus feinkörnigen Kristalliten eingebettet zwischen größeren Körnern sowohl an der Oberfläche als auch der rückseitigen Mo-Grenzfläche. Mithilfe dieses Herstellungsverfahrens konnten Solarzellen mit einer V_{OC} von bis zu 433 mV sowie mit einem Solarzellen-Wirkungsgrad von 6,8 % und einem Füllfaktor von 48 % realisiert werden.

Weiterhin wurden CZTSe-Absorberschichten und daraus hergestellte Solarzellen auf der Basis von koverdampften, metallischen (Cu-Zn-Sn) Vorläuferschichten produziert und analysiert. Die Bildung metallischer Legierungen sowie der Einfluss der entsprechenden Temperatur auf die Absorber- und Solarzelleneigenschaften wurden untersucht. Aus den verschiedenen Vorläufern (legiert bei Temperaturen von 250 °C bis 350 °C) hergestellte CZTSe-Schichten wiesen verglichen mit den nicht legierten CZTSe-Absorbern größere Kristallite sowie eine $MoSe_2$-Schicht mit einer Dicke von 1200 nm auf. Im Hinblick auf die Solarzellen-Leistungsdaten zeigte sich bei Verwendung einer Temperatur von 300 °C während des Legierungsprozesses eine Verbesserung des Wirkungsgrades (von durchschnittlich 4,4 % für eine Temperatur von 250 °C hin zu 7,0% im Mittel bei 300 °C), die hauptsächlich auf eine Steigerung der V_{OC} und des Füllfaktors zurückzuführen ist. Bei Temperaturen oberhalb von 300 °C zeigten sich die erzielten Solarzellen-Wirkungsgrade sowie V_{OC} und Füllfaktor jedoch deutlich vermindert.

Darüber hinaus wurde eine temperaturabhängige Untersuchung des Entstehungsprozesses des CZTSe-Absorbers während der Selenisierung der koverdampften, legierten Cu-Zn-Sn-Vorläuferschichten durchgeführt. Dabei konnte nachgewiesen werden, dass die Bildung des CZTSe-Absorbers über konkurrierende Reaktionen von binären ($CuSe_2 + SnSe_2 + ZnSe \rightarrow Cu_2ZnSnSe_4$) und ternären ($Cu_2SnSe_3 + ZnSe \rightarrow Cu_2ZnSnSe_4$) Phasen vonstatten geht. Weiterhin wurde gezeigt, dass die Rate von Veränderungen in der Morphologie im Vergleich zu den Se-haltigen Vorläuferschichten vergleichsweise gering ausfällt. Allerdings induziert der Einbau von Ag an der Rückseite der Cu-Zn-Sn-Vorstufe eine beschleunigte Bildung (verglichen mit Ag-freien Vorläuferschichten) von großen Kristalliten in einem frühen Stadium. Dies ließ sich der Entstehung einer flüssigen Silberselenid (Ag–Se)-Phase zuschreiben.

Detaillierte Studien deuteten darauf hin, dass die Korngrößen innerhalb des Absorbers mit steigender Dicke der Ag-Schicht anwachsen. Mittels Flugzeit-Sekundärionen-Massenspektrometrie (ToF-SIMS) aufgenommene Tiefenprofile der Komposition zeigen eine verhältnismäßig homogene Verteilung von Cu, Zn, Sn, Se und Ag über die gesamte Dicke der Absorberschicht hinweg. Darüber hinaus verbesserte sich der Solarzellen-Wirkungsgrad von 6,9 % im Fall ohne zusätzliches Ag auf 7,6 % bei Verwendung einer

zusätzlichen 10 nm dicken Ag-Schicht an der Rückseite der Cu-Zn-Sn-Vorläuferschicht, was sich auf eine Verbesserung der V_{OC} sowie des Füllfaktors zurückführen ließ. Eine noch dickere Ag-Schicht verschlechterte hingegen den Solarzellen-Wirkungsgrad aufgrund eines erhöhten Serienwiderstands, was sowohl Füllfaktor als auch J_{SC} der Solarzellen signifikant beeinflusste. Temperaturabhängige elektrische Messungen legen nahe, dass der Einbau von Ag zu zusätzlichen Defekten führt, die die Rekombination an Grenzflächen begünstigen. Dementsprechend ergaben die hier durchgeführten Untersuchungen, dass sich eine geringe Menge von zusätzlich eingebautem Ag als vorteilhaft für die Entstehung von großen Kristalliten und eine Verbesserung des Wirkungsgrads der hergestellten Solarzellen erweist.

Die erzielten Ergebnisse und Analysen zeigen, dass der Wachstumsprozess des CZTSe-Absorbers sowie die Eigenschaften der entsprechenden Solarzellen stark von der Komposition und Konfiguration der Vorläuferschichten abhängen. Dennoch ist der Einsatz koverdampfter, mehrlagiger Vorstufen von großem Interesse, da sie im Vergleich zu homogenen Vorläufern insgesamt zu einer Verbesserung sowohl der V_{OC} als auch teilweise des Füllfaktors führten. Die weiterführende Optimierung der Selenisierungsparameter (z.B. die Se-Menge im Graphitbehälter, die Selenisierungstemperatur und–zeit) in Kombination mit einem Ag-Einbau kann möglicherweise zu einer weiteren Steigerung der Solarzellen-Wirkungsgrade führen.

Abstract

Chalcogenide-based thin-film solar cells such as $Cu(In,Ga)Se_2$ (CIGS) and CdTe have been successfully commercialized and have demonstrated a comparably low energy pay-back time as well as suitability for flexible applications. However, the toxicity of cadmium (Cd) and scarcity of indium (In) and tellurium (Te) jeopardize their growth potential. Thin-films based on the quaternary compounds $Cu_2ZnSnSe_4$ (CZTSe) and Cu_2ZnSnS_4 (CZTS) together with their derivatives $Cu_2ZnSn(S,Se)_4$ (CZTSSe) has generated tremendous attention in the photovoltaics community due to the abundance and non-toxicity of their constituents. However, the larger open-circuit voltage (V_{OC}) deficit and partially the lower fill factor (*FF*) compared to CIGS and CdTe limit the technology's future commercialization. Improving both V_{OC} and *FF* to a competitive level requires a better understanding of the absorber's growth mechanism and distribution of secondary phases and defects as well as of the nature of the recombination mechanisms in the solar cells.

Thus, in this work, an in-depth study of the CZTSe absorber's growth and the device performance of respective solar cells is conducted. Three precursor configurations were investigated, namely, i) homogenous Se-containing co-evaporated precursors (Cu-Zn-Sn-Se), ii) homogenous metallic co-evaporated (Cu-Zn-Sn) precursors and iii) co-evaporated multilayer stacks (Cu-Sn/Cu-Zn-Sn-Se/ZnSe/Cu-Zn-Sn-Se and Cu-Zn/Sn). Several characterization techniques were performed on the precursors, absorber layers, and complete solar cells in order to analyze their quality.

Utilizing homogenous Se-containing co-evaporated precursors, solar cells with power-conversion efficiencies of up to 6.4 % could be demonstrated. However, the performance was limited by CdS/CZTSe interface recombination and process reproducibility. Providing additional Sn in the Se atmosphere during the recrystallization process of Cu-Zn-Sn-Se precursors was demonstrated to be a suitable approach to suppress CdS/CZTSe interface recombination and to stabilize the fabrication process. In addition, the impact of the initial N_2 background pressure used for the selenization process on the structural properties of the CZTSe absorber and respective solar-cell properties was studied and discussed.

An investigation of the phase transitions during the selenization of the low-temperature co-evaporated Cu-Zn-Sn-Se precursors was performed. The intimate mixing of binary ($CuSe_2$, $SnSe_2$, ZnSe) and ternary (Cu_2SnSe_3) phases in the temperature range from 300 °C to 500 °C was confirmed by X-ray diffractometry, Raman spectroscopy, scanning electron microscopy, and transmission electron microscopy. This suggested that the CZTSe formation pathway proceeds via a competition reaction of binaries ($CuSe_2$ + $SnSe_2$ + ZnSe → $Cu_2ZnSnSe_4$) and ternary phases (Cu_2SnSe_3 + ZnSe → $Cu_2ZnSnSe_4$).

The utilization of co-evaporated multilayer Cu-Zn/Cu-Zn-Sn-Se/ZnSe/Cu-Zn-Sn-Se precursor stacks is more advantageous than the previously used single-layer precursors as it promotes a compositional depth gradient. This could potentially alter the CZTSe formation pathways. CZTSe solar cells with maximum power-conversion efficiencies up to 7.9 % with V_{OC} and *FF* of 428 mV and 62 %, respectively, could be achieved utilizing this approach. However, a lower short-circuit current (29 mA/cm^2) compared to the homogenous co-evaporated approach (37 mA/cm^2) limits the performance. Moreover, it was observed that an *in-situ* pre-annealing of each layer of the multilayer stacks improved the J_{SC} in the order of 2 mA/cm^2, however, led to poorer V_{OC} and *FF*. In addition, *in-situ* pre-annealing of the whole precursors led to the formation of a triple-layered structure associated with fine grains in between larger grains at the surface and Mo back interface. Utilizing this approach, a solar cell with V_{OC} up to 433 mV associated with a maximum power conversion efficiency of 6.8 % and *FF* of 48 % could be demonstrated.

CZTSe absorber layers and solar cells prepared from co-evaporated metallic (Cu-Zn-Sn) precursors were investigated. The effect of alloying and the influence of respective temperatures on absorber and solar-cell properties were studied. CZTSe absorbers prepared from different precursor types (alloyed at temperatures from 250 °C to 350 °C) exhibited larger grains compared to their unalloyed counterparts and a 1200-nm-thick $MoSe_2$ layer. Comparing solar-cell performance, an improved power-conversion efficiency (from 4.4 % on average for an alloying temperature of 250 °C to 7.0 % on average for 300 °C) was achieved utilizing an alloying temperature of 300 °C — mainly, due to an increase in the V_{OC} and the *FF*.

On the other hand, alloying temperatures above 300 °C deteriorated the solar-cell parameters, mainly the V_{OC} and the *FF*. In addition, a temperature-dependent investigation of the formation mechanism of CZTSe layers during the selenization of co-evaporated alloyed Cu-Zn-Sn precursors was conducted. Thereby, it could be demonstrated that the CZTSe formation mechanism proceeds via competitive reactions of binary ($CuSe_2$ + $SnSe_2$ + ZnSe → $Cu_2ZnSnSe_4$) and ternary phases (Cu_2SnSe_3 + ZnSe → $Cu_2ZnSnSe_4$). It was further found that the rate of the morphology changes was relatively low compared to the Se-containing precursors. However, Ag incorporation at the back of Cu-Zn-Sn precursors induced a fast formation of larger grains in the early stages (compared to Ag-free precursors), which could be attributed to the formation of a silver–selenide (Ag–Se) liquid phase.

Detailed investigations indicated that the grain size in the absorber increased with increasing Ag-layer thickness. Time-of-flight secondary ion mass spectrometry depth profiles revealed a fairly homogenous distribution of Cu, Zn, Sn, Se, and Ag across the absorber thickness. Moreover, it was found that the power-conversion efficiency improved from 6.9 % for the Ag-free absorbers to 7.6 % when adding a 10 nm thick Ag layer at the back of Cu-Zn-Sn precursors due to an increase in the V_{OC} and *FF*. A thicker Ag layer deteriorates the solar-cell performance, mainly due to an increase in series resistance, which significantly impacts the *FF* and J_{SC} of the devices. Temperature-dependent electrical measurements suggested that the Ag incorporation induced defects promoting interface recombination. Therefore, the study sug-

gested that a small amount of incorporated Ag could be beneficial for the formation of large grains and the improvement of the solar-cell performance.

The obtained results and analysis show that the CZTSe growth and solar-cell properties strongly depend on the precursor composition and configuration. However, the utilization of co-evaporated multilayer-stack precursors is of high interest as it resulted in an overall improvement of the V_{OC} and partially of the *FF* compared to the homogenous co-evaporated precursors. The continuing optimization of the selenization parameters (e.g., the amount of Se in the graphite box, the selenization temperature and time) together with the incorporation of Ag in the precursors could potentially lead to a further increase of the overall solar cell efficiency.

Table of contents

Acknowledgments

This work is an outcome of the collective effort and love of several stakeholders in my home country, Tanzania, and Germany. At the top of my list of acknowledgment, I would like to thank my wife and my daughter Anna for their cherished time although they were away by WhatsApp and Skype App brought us close and together. I would say may God bless them.

I thank Prof Bryce Richards and Prof. Andrea Schäfer for the friendly welcome in Karlsruhe, Germany. Further, I would like to thank my supervisors Prof. Bryce Richards Priv-Doz. Dr. Michael Hetterich for giving me the opportunity to do my Ph.D. at Karlsruhe Institute of Technology (KIT), Germany. In connection to this, I can say thank you for your support in the development of research ideas, handling and planning experiments and how to organize and write a journal paper. Special thanks go to Prof. Dr. Heinz Kalt and Dr. Michael Hetterich for all the support, and allowing me to work in the Kalt group and Free INCA project. However, in a special way, I would like to faithfully thank Michael Hetterich for being a really good teacher to me. From you, I learned that most of the time things in research and publications are not always very perfect as we are expecting, a deeply courage and motivation could be the best option. Moreover, thank you for being there every time I needed your support in handling and repairing the MBE.

Special thanks go to Dr. Ulrich Paetzold for his heartful support and guidance on this work. Extended thanks go to Dr. Monika. Rinke of IAWP and Dr. Alexander Welle of IFG for their time, discussion and Raman spectroscopy and ToF-SIMS measurement, respectively. Big thanks go to Mr. Max Reimer for his training on how to operate the molecular beam epitaxy system. Further, special big thanks go to Dr. Markus Neuwirth for his training on the tube furnace, XRD, and solar simulator together with his time in the SEM laboratory. Other thanks go to Ms. Jasmie Seeger, Mr. Simon Woska, and Dr. Fabian Ruf for helping me with electroreflectance spectroscopy, *J-V-T*, and PL measurements, respectively. I would not forget my Bachelor students, Luis Kussi and Jakob for helping in this work, you guys, thanks very much.

Special appreciations go to Mr. Volker Zibat for his time and cherished discussion regarding SEM as well as performing SEM/EDXS measurements to my samples. Extended thanks go to Dr. Erich Müller Dr. Xiaowei Jin, Prof. Dr. Reinhard Schneider, and Prof. Dr. Dagmar Gerthsen for TEM/EDXS analysis.

Having a financial sponsor was a major challenge to me, thus, I would like to express my gratitude to DAAD, Germany and MoVET, Tanzania for the financial support in this study. Additional thanks go to KSOP for the financial support and give me a chance to extend my spectroscopy and management knowledge through KSOP modules.

An extended appreciation is for the Free INCA project team, ZSW (Dr. Erik Alswede, Dr. Thomas Schnabel, and Mr. Willi Kogler) and UOL (Dr. Levent Gütay and Teoman Taskesen) for your discussion during Telco and in project meeting as well as for depositing window layers to my samples and supplying SLG coated Mo substrates.

Big thanks go to the groups of Prof. Richards and Prof. Kalt for the great working atmosphere and much discussion regarding solar energy and European culture, politics, and traditions, it has been an honor to spend these years with all of you, and may God bless you all. I don't know the right way/words to express this, but I could only say thank Ngei Kitumo and Vu Li for helping me in proofreading my thesis. I do hope that this friendship and helping hand will last forever and wish you all the best in your carrier and social life.

Lastly, in a special way, I would like to express my gratitude to my parents and siblings for the love they have always shown to me, God be with you all.

Karlsruhe, im September 2019

Lwitiko Pholds Mwakyusa

List of journal Publications and Conference contributions

List of journal publications

Lwitiko P. Mwakyusa, Markus Neuwirth, Will Kogler, Thomas Schnabel, Erik Ahlswede, Ulrich W. Paetzold, Bryce S. Richards, Michael Hetterich, *CZTSe solar cells prepared by co-evaporation of multi-layer Cu-Sn/Cu,Zn,Sn,Se/ZnSe/Cu,Zn,Sn,Se stacks* Phys. Scr. 2019, 94 105007.

Lwitiko P. Mwakyusa, Lennart Leist, Monika Rinke, Alexander Welle, Ulrich W. Paetzold, Bryce S. Richards, and Michael Hetterich, *Impact of Silver Incorporation at the Back Contact of Kesterite Solar Cells on Structural and Device Properties* **Submitted.**

Contributions to workshops and conferences:

CZTSe solar cells prepared by co-evaporation of multilayer Cu-Sn/CZTSe/ZnSe/CZTSe stacks
Lwitiko P. Mwakyusa, Markus Neuwirth, Ulrich W. Paetzold, Bryce S. Richards, Heinz Kalt, Michael Hetterich, *7th European kesterite Workshop*, Barcelona, Spain (2017) (Oral presentation)

CZTSe solar cells prepared by co-evaporation of multilayer Cu-Sn/CZTSe/ZnSe/CZTSe stacks,
Lwitiko Mwakyusa, Markus Neuwirth, Ulrich Paetzold, Bryce Richards, Heinz Kalt, Michael Hetterich, *DPG Spring Meeting*, Berlin, Germany (2018) (Oral presentation)

Absorber surface treatment and alternative buffer layers for Cu2ZnSn(S,Se)4 solar cells
Markus Neuwirth, Elisabeth Seydel, Michael Wolf, Lwitiko Mwakyusa, Thomas Schnabel, Erik Ahlswede, Heinz Kalt, Michael Hetterich, *DPG spring meeting*, Dresden, Germany (2017) (Poster presentation)

Effects of selenium to sulphur ratio in $Cu_2ZnSn(S,Se)_4$ absorbers for thin-film solar cells,
Elisabeth Seydel, Markus Neuwirth, Michael Wolf, Lwitiko Mwakyusa, Thomas Schnabel, Erik AHlswede, Willi Kogler, Heinz Kalt, Michael Hetterich, *DPG Spring Meeting*, Dresden, Germany (2017) (Poster presentation)

Co-evaporated CZTSe solar cells: influence of Cu deposition rate during precursor processing on the growth and device performance,

Lwitiko Mwakyusa, Markus Neuwirth, Max Reimer, Simon Woska, Willi Kogler, Thomas Schnabel, Erik Ahlswede, Bryce Richards, Heinz Kalt, Michael Hetterich, *DPG Spring Meeting*, Dresden, Germany (2017) (Poster presentation)

Co-evaporation of alternative buffer layers in $Cu_2ZnSn(S,Se)_4$ solar cells, Max Reimer, Markus Neuwirth, Lwitiko Mwakyusa, Michael Wolfstädter, Erik Ahlswede, Michael Powalla, Heinz Kalt and Michael Hetterich, *DPG Spring Meeting*, Regensburg, Germany (2016) (Poster presentation)

Wet-Chemical Processing of CdS and Alternative Buffer Layers for $Cu_2ZnSn(S,Se)_4$ Solar Cells, Lwitiko Mwakyusa, Markus Neuwirth, Niklas Mathes, Mario Lang, Thomas Schnabel, Erik Ahlswede, Michael Powalla, Bryce Richards, Heinz Kalt and Michael Hetterich, *DPG Spring Meeting*, Regensburg, Germany (2016) (Poster presentation)

1. Introduction

1.1 General Introduction

Energy is essential for modern life. Thus, as a result of the new policies scenario, the energy demand increases by 60 % in 2040, due to the increment of incomes and the global population [1]. However, fossil fuel is providing more than 74 % of the global energy which corresponds to more than 35 gigatonnes CO_2 emission [1]. Following the latest United Nations Climate Summit in Paris, the major agreement has been set for countries to make some legal commitments to reduce CO_2 emission, which is the main contributor to global warming [2], [3]. Special interest was paid in the electricity sector which is responsible for a considerable share of greenhouse gas emissions. The access to energy for home lighting could be considered as a fundamental need for this modern humankind. As documented in Energy Outlook 2018, energy consumption in Africa as a whole increased by just under 60 %, however, surpasses that of the European Union, although it remains the lowest consumption of energy as per capita basis [1]. For instance, in Tanzania, the electrification rate reached 41 % in 2015 and is expected to increase to 90 % by 2035 [4]. Moreover, as documented in the Tanzanian national electrification program prospectus, for a grid connection it is economic feasible for the communities with the following conditions, i) they are close to the main grid, ii) they not too small population, and iii) the customer should not be scattered over the area but concentrated [4]. A similar situation could be expected across Africa. Therefore, the stabilization of greenhouse gas emission and electrification in the remote regions is of importance and it requires the use of renewable energy technologies such as wind and photovoltaic (PV).

As it is documented in ref. [5], PV technologies provide more than 1 % of the global energy, and around 7–8 % in some developed countries [5]. Besides that, PV installation can be readily scaled from a few watts to several megawatts (MW) lending itself to a wide range of applications. For instance, a PV-powered water purification system has been demonstrated to be useful in remote areas in northern Tanzania [6]. Thus, PV technology has the potential to bring human civilization greater long term economic and geopolitical sustainability than currently possible with fossil fuels [7]. In this consideration, the generation of electricity in remote areas, the prices, and the robustness of PV technologies are paramount.

Currently, Si-wafer based PV technology contributes more than 94 % to the PV market share, while the share from both thin-film based technologies is below 6 % [8]. Moreover, since its emergence thin-film photovoltaics (TFPV) take on two difficult challenges: (i) to compete with Si- wafer-based PV in terms of power conversion efficiency and manufacturing costs, (ii) to contain only earth-abundant and non-toxic materials without severe degradation in the long term. Chalcogenide-based thin-film solar cells such as $Cu(In,Ga)Se_2$ (CIGS) and CdTe have reached commercialized. However, not all constituting elements of

CIGS and CdTe are earth-abundant and innocuous—as the demand for In element in the electronic industries to fabricate the transparent electrode has been increasing drastically [9].

Due to the similarity of their properties to the well-established CIGS absorbers together with earth-abundance and non-toxicity of their constituents, thin-film solar cells based on kesterite Cu_2ZnSnS_4 (CZTS), $Cu_2ZnSnSe_4$ (CZTSe), and $Cu_2ZnSnSSe_4$ (CZTSSe) are considered a promising candidate which is able to challenge the dominance of the CIGS and CdTe thin-film photovoltaic technologies. The PV performance of CZTSSe based solar cells is relatively low compared to CIGS and CdTe—as the record efficiency is up to 12.6 % [10]. However, the Shockley Queisser (SQ) limit predicts that the efficiency of kesterite would be ~ 32.2 % [11], this huge difference can be traced back to a high V_{OC}-deficit and partially low *FF*. To narrow this hiatus requires a deep understanding of the absorber growth mechanism and distribution of defect and secondary phases as well as the nature of loss mechanism in the solar cells. Table 1.1 shows CZTSe and CZTSSe devices fabricated by using the vacuum-based approach, sputtering and co-evaporation. The latter is less investigated. However, co-evaporation has been proven to be the best approach to fabricating high efficient CIGS solar cells [12]. Thus, in this thesis, CZTSe absorbers are prepared by the selenization of low-temperature co-evaporated precursors. In this regard, this thesis is intended to be more explorative—and to identify auspicious prospects for future investigation on the co-evaporated approach.

Objective and scope of this thesis

In this thesis, different approaches to improving CZTSe solar cell's performance are investigated. The ultimate aim of this research work is to examine different precursor's configuration and composition on the CZTSe absorber growth and device properties. The details of the investigated topics are outlined as the following:

- Preparation of CZTSe absorber and solar cell by selenization of low-temperature co-evaporated Cu-Zn-Sn-Se precursors

The CZTSe absorber can be prepared via, i) a single-step process, where Cu, Zn, Sn, and Se are deposited on a substrate with a temperature above 500 °C [13], [14], and ii) a two-step process, where a precursor is co-evaporated at low temperature and following selenization in high-pressure chalcogen ambient to obtained CZTSe layer [12]. The latter has been proven to be the best approach to producing highly efficient CZTSSe and CZTSe solar cells [10], [15] as well as to suppress absorber decomposition [12]. In this consideration, in this thesis two-step approach was adopted with the aim to:

i. Investigate the impact of selenization parameters on the CZTSe absorber and solar cell properties.
ii. Study the formation pathways of CZTSe absorber prepared by selenization of low-temperature co-evaporated Cu-Zn-Sn-Se precursors.

Table 1.1: Selection of CZTSe and CZTSSe solar cells with power conversion efficiencies (η) over 8 % fabricated from a vacuum-based approach, where η and V_{OC} are power conversion efficiency and V_{OC} open-circuit voltage, respectively.

Method	Institute/Company	Absorber type	η (%)	V_{OC} (mV)	V_{OC}-deficit (mV)	Ref
Sputtering	DGIST	CZTSSe	12.3	521	576	[15]
Sputtering	Tsinghua University	CZTSe	11.95	432.22	637	[16]
Sputtering	CNU	CZTSSe	11.8	485	582	[17]
Co-evaporation	AIST	CZTSe	11.7	423	577	[18]
Co-evaporation	IBM (USA)	CZTSe	11.6	423	578	[19]
Sputtering	UOL	CZTSe	11.4	443	587	[20]
Sputtering	Solar Frontier	CZTSSe	11.0	516	N/A	[21]
Sputtering	UOL	CZTSe	10.7	433	N/A	[22]
Sputtering	IMEC	CZTSe	10.4	394	606	[23]
Sputtering	Nankai University	CZTSe	10.4	419	611	[24], [25]
Sputtering	Nankai University	CZTSSe	10.2	460	650	[26]
Sputtering	IMEC	CZTSe	9.7	408	592	[27]
Co-sputtering	EMPA	CZTSe	9.4	440	620	[28]
Sputtering	CNU		9.2	454.6	685	[29]
Co-evaporation (one-step)	IBM	CZTSe	9.2	377	N/A	[13], [14]
Sputtering	Ewha Woman's University	CZTSSe	9.1	420	N/A	[30]
Sputtering	IREC	CZTSe	8.2	392	628	[31]

AIST- National Institute of Advanced Industrial Science and Technology, Japan
UOL-University of Oldenburg, German
IMEC-Interuniversity Microelectronics Centre, Belgium
CNU- Chonnam National University

○ Fabrication of CZTSe absorber from multilayers stacks

Multilayer stack order has been proven to have a significant impact on the precursor film properties, including precursor alloy formation, composition, and elemental loss as well as absorber properties such as optoelectronic properties [32]. Thus, in this topic, we introduced two precursor multilayer stacks utilizing a configuration of i)Mo/Cu-Sn/Cu-Zn-Sn-Se/ZnSe/Cu-Zn-Sn-Se, and ii) Cu-Zn/Sn—with the motivation of altering the CZTSe formation pathways. Thus, the objectives of this topic are:

i. To investigate the effect of the proposed precursor configuration on the CZTSe structures and device properties.

ii. To explore the impact of the Cu-Sn pre-alloying temperature on the CZTSe and solar cell properties.
iii. To find out the impact of the pre-alloying of individual stacks on the CZTSe properties and device performance.

- Ag incorporation to the back contact of CZTSe solar cell and its impact on the structure and device properties

Formation of kesterite absorber with large grains with no secondary phases and unwanted phases has been paramount important from the beginning. Incorporation of silver (Ag) in CZTSe absorber can improve grain growth and band alignment at the CZTSe/CdS interface. Moreover, as reported previously, CZTSe formation pathways depend on the annealing conditions and precursor's composition. For instance, it has been reported that when metallic precursors are used, the formation of kesterite proceeds directly through the formation of binaries phases (Cu_2Se, ZnSe, and SnSe) [33]. This could somehow complicate the reaction process, with a numerous number of molecules involved, there is a high risk of secondary phases remaining after the end of the reaction process [33]—this could significantly deteriorate the device performance, especially the open-circuit voltage (V_{OC}). To circumvent this, pre-alloying before selenization or sulfurization is utilized with the motivation of enhancing the formation of metal alloys of (Cu-Sn and Cu-Zn)—thus the formation pathways could proceed via formation of ternaries (Cu-Sn-S(e)) which react with ZnS(e) at high temperature to form kesterite. Through this approach, CZTSe solar with efficiency up to 10.3 % could be demonstrated [22]. In this line argument, in this topic, CZTSe absorbers and solar cells are prepared from co-evaporated Cu-Zn-Sn metallic precursors. The objectives of this topic outline as:

i. To investigate the effect of pre-alloying temperature on the precursor's material phases, CZTSe absorber growth, and solar cells properties.
ii. To deduce reaction pathways during the selenization of alloyed precursors.
iii. To find out the influence of Ag incorporation at the back of Cu-Zn-Sn precursors on the phases and morphology transition during selenization
iv. To learn the impact of Ag incorporation at the Cu-Zn-Sn precursors on the absorber growth and solar cell performance.

Outline of the thesis

This thesis consists of seven chapters. Their contents are summarized as follows:

Chapter 1 gives an overview of the energy demand and the need for earth-abundant and non-toxic thin-film based solar cells. In this chapter, we also recapitulate a current status on the device's performance of vacuum processed CZTSe and CZTSSe solar cells.

Chapter 2 describes an overview of the physics of solar cells and thin-film solar cells. Moreover, the chapter gives a brief overview of kesterite properties. The relationship between precursor configurations

and composition on the formation of pathways for vacuum processed kesterite thin-film is presented in this chapter. Further, the role of Ge and Ag incorporation in kesterite solar cells on the defect and absorber formation is described in this chapter.

Chapter 3 explains the experimental techniques used to fabricate and characterize CZTSe solar cells in this thesis.

Chapter 4 focuses on the investigation of CZTSe absorber and solar cells prepared by selenization of low-temperature co-evaporated precursor—mainly concerns about establishing and optimizing a robust fabrication baseline process. Moreover, the chapter enlightens the recombination mechanism in the devices. Finally, the chapter proposed the CZTSe formation pathways during the selenization of low-temperature co-evaporated Cu-Zn-Sn-Se.

Chapter 5 is related to the development of CZTSe absorbers and solar cells using multilayer stacks of Mo/Cu-Sn/Cu-Zn-Sn-Se/ZnSe/Cu-Zn-Sn-Se and Mo/Cu-Zn/Sn and structure as: in the first section, fabrication of CZTSe solar cells using co-evaporated multilayer of Mo/Cu-Sn/Cu-Zn-Sn-Se/ZnSe/Cu-Zn-Sn-Se stacks is presented. The second section involves the elimination of fine grains at the back interface. Finally, the third section is concerned with the development of CZTSe absorber and solar cells using Cu-Zn/Sn stacks.

In chapter 6, the effect of pre-alloying temperature on the precursors properties, CZTSe absorbers growth, and device performance is presented. Moreover, the chapter extends by discussing the impact of Ag incorporation at the back of Cu-Zn-Sn on the CZTSe structures and device properties.

Chapter 7 presents the conclusion and recommendation for future research.

2. Principles of kesterite solar cells

2.1 Background

This chapter introduces an overview of the basics of solar cells, followed by a summary of the properties of kesterite absorber materials. We also pay great attention to the recent development of vacuum processed kesterite solar cells and the formation pathways occurring during the process because these studies have been relevant for the experimental work of this thesis.

2.1.1 Physics of Photovoltaics (PV)

A solar cell is, basically, a semiconductor device that converts sunlight directly to electricity. The working principle of a solar cell is based on the photovoltaic effect—where the electrical voltage is generated at the junction of the two dissimilar materials in responding to the energy of the incident photon. The generation of electrical voltage can be divided into three processes (i) generation of photocarriers due to the absorption of photon energy (it takes place at the absorber). This happens when a photon with energy higher than the absorber bandgap is absorbed. It also implies that an electron is promoted from the valance band (E_V) to the conduction band (E_C) and one hole is left behind ii) separation of photocarriers generated at the junction, and (iii) collection of photocarriers, it takes place at the terminals of the junctions. The solar cell can be made from a semiconductor in the form of a wafer (commonly Si wafer) or a thin-film. Thin-film based solar cells can be fabricated using organic or inorganic materials. An inorganic thin-film solar cell is also a *p*-*n* heterojunction device. The *p* and *n* are semiconductor materials that are either intrinsically or extrinsically doped to achieve required optoelectronic properties. A semiconductor with a deficit of electrons and the majority charge carriers are holes is called *p*-type semiconductor, while that with majority charge carriers are electrons is called *n*-type semiconductor (see Fig 2.1 (a)).

If *n*-type and *p*-type semiconductors come into contact, a *p*-*n* junction is formed. Excess electrons flow from a region of high concentration (*n*-type) to a region of low concentration (*p*-type), and similarly for holes. As electrons left the *n*-type side, ionized donors (positive charge) are leaving behind. Similarly, when holes left the *p*-type region, the ionized acceptors (negative charge) emerge. The natural diffusion of electrons and holes results in a diffusion current. The diffusion process also causes the formation of the depletion zone in the vicinity of the *n*- and *p*- side of the semiconductor. The depletion zone sets up the electric field that hampers the diffusion current and also enables a drift current of minority charges moving in the reverse direction of the diffusion current. Thus, equilibrium is eventually established and only one Fermi level is formed. This causes the energy band bending as illustrated in Figs 2.1 (b).

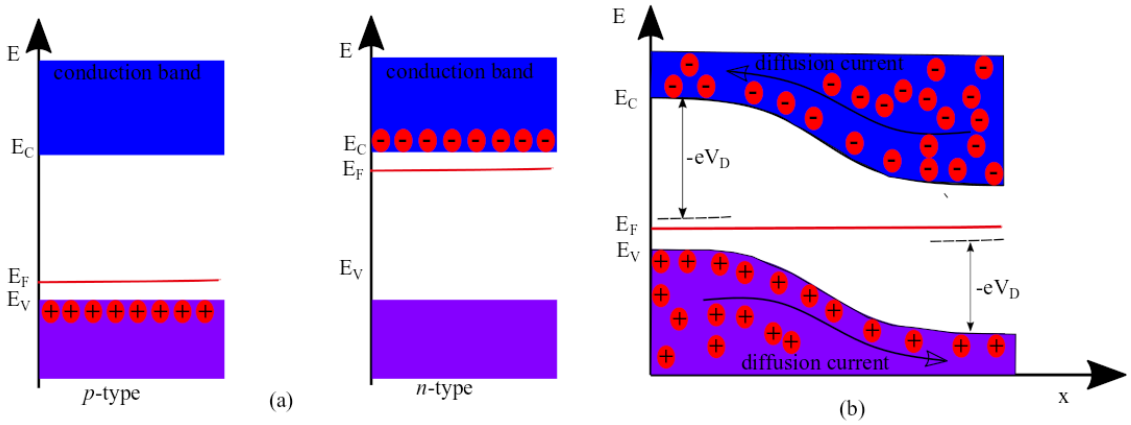

Figure 2.1: (a) the band model of the p- and n-type semiconductor. Each semiconductor type contains a different Fermi-energy. (b) corresponding to the band model when *p*- and *n*-type semiconductors are brought together. The Fermi-levels equalize each other, resulting in the band bending to about eV_D through the diffusion process adapted from [34].

At equilibrium, diffusion and drift currents balance each other. The potential difference generated in the depletion zone is called built-in potential V_{bi}. We have:

$$V_{bi} = \frac{k_B T}{q} . \ln \frac{n_A n_D}{n_i^{\,2}} \qquad 2.1$$

where n_A, n_D, n_i, k_B, and q are acceptor density, donor density, intrinsic density, Boltzmann constant, and electronic charge, respectively.

When an electrical voltage is applied to the *p*-*n* junction by connecting it with an external source, the direction and value of the total current will alter. Depending on the polarity of the applied voltage, the *p*-*n* junction is put into two distinct conditions called the reverse-biased condition and the forward biased condition. In the latter condition, the *n*-side is connected to the anode of the external source while the *p*-side is connected to the cathode. In this case, the depletion width is reduced and electrons flow from the *n*-side to the *p*-side. The forward biased current which flows in the *p*-*n* junction is defined based on the Shockley's equation:

$$I = I_0 (\exp^{\frac{qV}{nk_B T}} - 1) \qquad 2.2$$

where I_0, n, and V are reverse saturated current, diode ideality factor, and the voltage across the diode, respectively. When the junction is illuminated by the light, the photon energy gets absorbed by the solar cell. If the energy is sufficient, electron-hole pairs are generated in the vicinity of the *p*-*n* junction. The

electric field separates electrons to the *n*-side and hole to the *p*-side. The latter results in a change in the charge density and engenders bending of the energy bands. The resulting current under illumination is described as:

$$I = I_0(\exp^{\frac{qV}{nk_BT}} - 1) - I_{ph} \quad 2.3$$

where I_{ph} is a photoelectric current.

2.1.2 Overview of thin-film solar cells (TFSC)

PV modules based on thin-film solar cells such as CIGS and CdTe have been successfully commercialized at a similar or even lower cost than Si-wafer based modules [35]. However, both of these technologies contain elements (such as gallium (Ga), indium (In), tellurium (Te)) that have been considered as critical raw materials (CRM) for the energy sector by European Commission [2], [36]. Moreover, the presence of elements such as cadmium (Cd), lead (Pb) that are known as the hazardous substance will further limit the application of these technologies. Several absorber materials have been proposed in the literature as CRM-free materials. Table 2.1 summarizes CRM-free absorber material for inorganic PV technologies reported in the literature. Out of those mentioned CRM-free absorbers, CZTS, CZTSe, and CZTSSe (kesterite) absorbers are more promising as an alternative for well- established CIGS and CdTe technologies.

2.1.3 Crystal structure and defect chemistry of kesterite material

Quaternary CZTSSe materials are derived from the chalcopyrite (CIS) by replacing half of In atoms in with Zn, and the other half with Sn, resulting in I_2II-IV-VI_4 (I = Cu; II = Zn, or Fe; IV = Sn or Ge; and VI= Se or S) compounds. These compounds can be crystallized in the stannite (spacing group $I\bar{4}2m$) or kesterite (space group $I\bar{4}$) [37], [38] —see Fig 2.2. Both stannite and kesterite structures have a closed cubic-packed array of anions (S or Se) with cations occupying half of the tetrahedral sites [37], [39]. However, these two differ in the order of arrangement of Cu and Zn as described in [37]. From the ref. [37] it was stated that "kesterite structures involve alternating layers of CuSn and CuZn (at z = 0, ¼, ½, and ¾) separated by S or Se layer. One Cu occupies the 2a(0,0,0) position with Zn and the remaining Cu ordered at 2c(0,1/2,1/4) and 2d (0,1/2,3/4) . On the contrary, stannite is characterized by alternating layers of ZnSn with Cu_2. The divalent atoms, Zn is located at the origin (2a) and monovalent atom, Cu at the 4d position (0,1/2,1/4). However, Sn is located at the 2b site (0,0,1/2) in both structures. The anion, S or Se lies on the (110) mirror plane at 8i(x,x,z), for the stannite type and 8g(x,y,z) for the kesterite type."

Table 2.1: Summary of selected Critical Raw Material-free absorber for inorganic PV technologies reported in the literature. It should be noticed that organic and perovskite are excluded in this table [2].

CRM-free absorber	η (%)	V_{OC} (mV)	J_{SC} (mA/cm^2)	FF (%)	Main technological challenge
Se	6.5	969	10.6	63.4	Optimization of the buffer layer and increasing charge carrier lifetime
Cu_xS	10.2	599	18.5	74.8	Control of the different phases and instability due to the Cu diffusion
Cu_xO	8.1	1100	11.5	60	Control of the different phases, low current, and high processing temperature.
SnS	4.4	372	20.2	58	Control of the different phases and difficult *n*-type partner
FeS_2	2.8	187	42	50	Difficult to control the phase purity
Zn_3P_2	5.96	492	14.93	71	Low V_{OC}, difficult to find adequate buffer partner, uncontrolled diffusion of Mg used to doped *p*-type
Cu_2BiS_3	0.09	97	2.9	31.2	High doping level and poor charge transport properties.
Cu_2SnS_3	4.3	258	35.6	46.7	Difficult to control doping and phase purity.
$Cu_2ZnSnSe_4$	11.95	432.22	36.28	76.21	V_{OC} deficit
$Cu_2ZnSnSe_4$	11.0	731	21.7	69.3	V_{OC} deficit
$Cu_2ZnSn(S,Se)_4$	12.6	513	35.2	69.8	V_{OC} deficit
$Cu_2BaSn(S,Se)_4$	5.2	611	17.4	48.9	The buffer layer, carrier density, microstructure, and interface engineering

However, thermodynamically the kesterite structure is more stable than stannite. However, experimentally, partially disordered kesterite is typically formed. Moreover, the complexity of the kesterite material leads to the number of possible lattice defects, with particular interest for the cations disorder [39], [40]. Commonly, during kesterite growth antisite defects of Cu_{Zn}, Zn_{Cu}, Cu_{Sn}, Sn_{Cu}, Zn_{Sn}, and Sn_{Zn}, vacancies of V_{Cu}, V_{Zn}, V_{Sn}, and $V_{S\ or\ Se}$, intrinsic defects of Cu_i, Zn_i, and Sn_i, and charged−compensated defects of $[Cu_{Zn}^{-} + Zn_{Cu}^{+}]$, $[Zn_{Sn}^{2-} + Sn_{Zn}^{2+}]$, $[V_{Cu}- + Zn_{Cu}^{+}]$, $[2V_{Cu}- + Sn_{Zn}^{2+}]$, $[Zn_{Sn}^{2+} + 2\ Zn_{Cu}^{+}]$, and $[2Cu_{Zn}^{2-} + Sn_{Zn}^{2+}]$ are expected [39], [41], [42]. They can be classified to be electron acceptors or donors depending on the valance energy of the elements [42]. The acceptor defects are Cu_{Zn}, V_{Cu}, V_{Zn}, V_{Sn}, and $V_{s\ or\ Se}$ [40], [42]. However, the lowest formation energy acceptor in kesterite is Cu_{Zn} and expected to define the *p*-type semiconducting behavior of kesterite, these defects have an acceptor energy level of 0.12 eV above the valance band maximum (VBM) compared to the V_{Cu} defect (0.02 eV) [42]. In high concentrations, thus, the defects significantly impact solar cell performance [40]. The concentration of Cu_{Zn} antisite defects depends on the ratio of [Cu]/[Zn] + [Sn] and [Zn]/[Sn] [42]. For instance, a CZTSe with [Cu]/[Zn] + [Sn] = 0.8 and [Zn]/[Sn] = 1.2 (corresponding to Cu-poor and Zn-rich, used for high efficient kesterite solar cells), the formation energies of V_{Cu} and Zn_{Sn} are decreased, while those of Cu_{Zn} and Sn_{Zn} are increasing. Therefore, V_{Cu} becomes the dominate acceptor.

Concerning the charged—compensated defects, theoretical calculation shows that formation energies of these defects are lower relative to the sum of isolated ones [42]. As documented in [42], these defects have less impact on the electronic and optical properties of kesterite. However, high concentration might result in the partial disorder of Cu and Zn. It is further reported that Cu-poor and Zn-rich lead to either type A ($2Cu^{+} \rightarrow Zn_{Cu}^{2+} + V_{Cu}$) or type B ($2Cu^{+} + Sn^{4+} \rightarrow 2Zn_{Cu}^{2+} + Zn_{Sn}^{2+}$), while Cu-rich and Zn-poor result to either type C kesterite ($3Zn^{2+} \rightarrow 2Cu_{Zn}^{+} + Sn_{Zn}^{4+}$) or type D kesterite ($Zn^{2+} \rightarrow Cu_{Zn}^{+} + Cu_i^{+}$) [2], [43] . Fig 2.3 (b) illustrates these defect lines with respect to the [Cu]/[Zn] + [Sn] and [Zn]/[Sn] ratio. It should be noticed that the [Cu]/[Zn] + [Sn] and [Zn]/[Sn] ratios could further alter the formation of secondary phases. As reported in [39], a single-phase kesterite can be formed in a very narrow region in the equilibrium diagram of $Cu_2S(e)$-$ZnS(e)$-$SnS(e)_2$. In the other regions of the phase diagram, secondary phases such as ZnS(e), SnS(e), $SnS(e)_2$, $Cu_2SnS(e)_3$, $Cu_2S(e)$, $CuS(e)_2$, and $Sn_2S(e)_3$ co-exist with primary kesterite phase [39], [44]. The formation of these secondary phases not only depends on the cationic ratios but also on processing conditions such as chalcogen pressure during growth, temperature, and time.

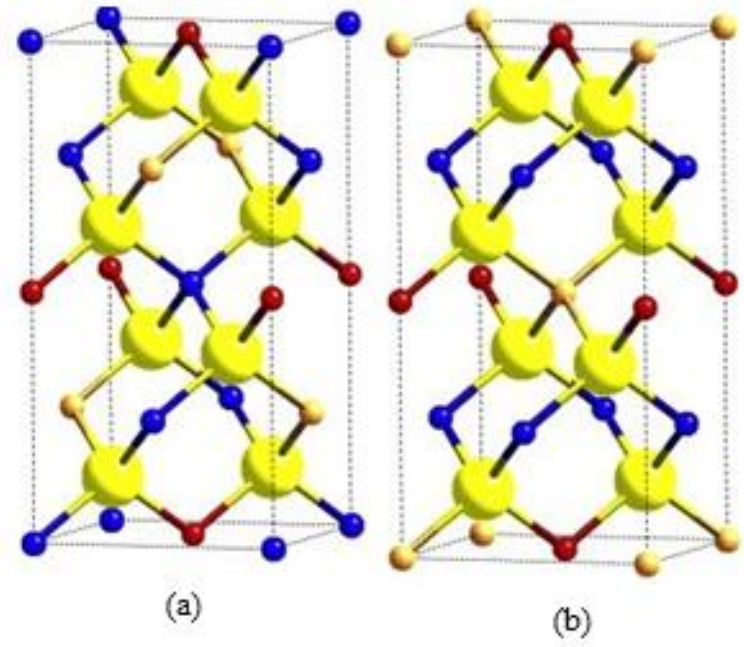

Figure 2.2: Unit cell representations for the (a) kesterite structure and (b) stannite structure. The Cu, Zn, Sn, and anions (S or Se) are represented by blue, orange, red, and yellow, respectively [40].

As reported previously in [45], kesterite is unstable at high processing temperatures. The reaction 2.1 describes the decomposition of CZTS(e) [39], [45], [46].

$$Cu_2ZnSnS(e)_4 \leftrightharpoons Cu_2S(e)_{(s)} + ZnS(e)_{(s)} + SnS(e)_{(g)} + S(e)_{(g)} \quad 2.1$$

Considering reaction 2.1, arguably, the decomposition process significantly depends on the chalcogen partial pressure during annealing. To suppress the decomposition, it is experimentally proved that a minimum chalcogen partial pressure of around 7×10^{-4} mbar and a minimum Sn-S(e) partial pressure of 1×10^{-3} mbar are necessary to stabilize the kesterite surface decomposition at high processing temperature [12]. Moreover, even if the material does not show obvious surface decomposition, it is still possible that unwanted defects could form due to the slight shift of the reaction equilibrium (see reaction 2.1) —thus,

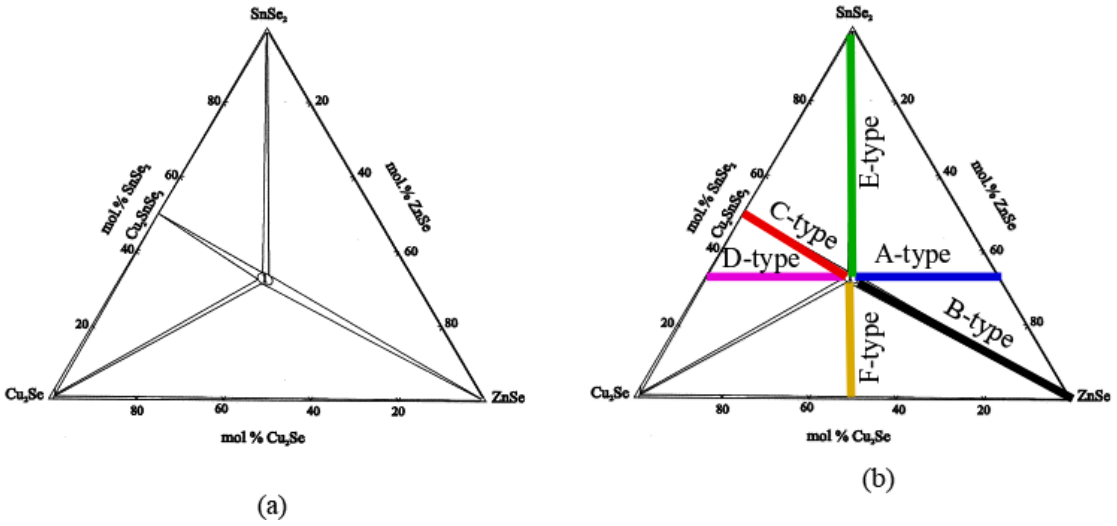

Figure 2.3: (a) Pseudo-ternary phase diagram of Cu2Se-ZnSe-SnSe2 at 670 K and (b) corresponding phase diagram indicating the compositional lines related to the charged compensated. These diagrams are adapted from [50], [51].

could significantly harm the device performance, especially the V_{OC} [12]. Commonly, kesterite absorber is prepared via a two-step process, where i) a precursor is deposited by either wet-chemical or a vacuum-based processed, followed by ii) a high-temperature (above 500 °C) re-crystallization in a high chalcogen partial pressure.

2.1.4 Kesterite material prepared from annealing of vacuum processed precursors: Recent development

Publication in kesterite based solar cells gained momentum since the first record of power conversion efficiency of 0.66 % was announced by Katagiri *et al*. [47], see Fig. 2.4. Despite the increase in the publication in recent year, the progress stalled to 12.6 % for CZTSSe [10], 11.95% for CZTSe [16], and 10 % CZTS [48]. The main limiting factor is a larger V_{OC}-deficit and partially *FF*. The world record CZTSSe devices demonstrate a V_{OC} deficit of 617 mV which is significantly larger than that of CIGS (379 mV) [49]. Several plausible causes for larger V_{OC} deficit have been proposed in the literature. For instance, Repins *et al*. [19] speculate that the existence of sub-bandgap states close to 0.02 eV to the band edge position significantly influences the V_{OC} of the devices. The high recombination rate attributed by band offset (CBO) at the front interface is also considered to be the main cause of the larger V_{OC} deficit [50], [51]. Gokmen *et al*. [52], associates this aspect with the electrostatic potential fluctuations, largely attributed to the Cu-Zn ordered/disordered and secondary phases in the absorbers and *p-n* junction [53]. However, it has been demonstrated that V_{OC} is not significantly altered by varying the degree of Cu-Zn disorder [54].

To understand the formation and position of secondary phases has been a paramount task in kesterite research. Thus, careful investigation of the kesterite formation pathways is expected to further enlighten this aspect.

There are several numbers of journal papers based on kesterite solar cells published to date. However, there have been few papers about the vacuum processed kesterite, this holds particularly to the pure-Se-kesterite which shows promising progress recently, see Fig. 2.4. Commonly, kesterite absorbers are prepared by selenization of the metallic [27], [55] or the chalcogen-containing precursors [56], [57]. Each of the precursors' composition leads to the kesterite absorber with some unique features including grain size, film adhesion, purity, and porosity. To our knowledge, no direct connection between a precursor configuration on the kesterite formation of pathways and solar cell properties of vacuum processed kesterite has yet been reviewed. To shed light on this aspect, a critical review of the vacuum processed kesterite absorbers is presented with the motivation of comparing different precursor's configuration with respect to the kesterite formation pathways. Moreover, the impact of Ag incorporation on the kesterite based absorber will be systematically discussed.

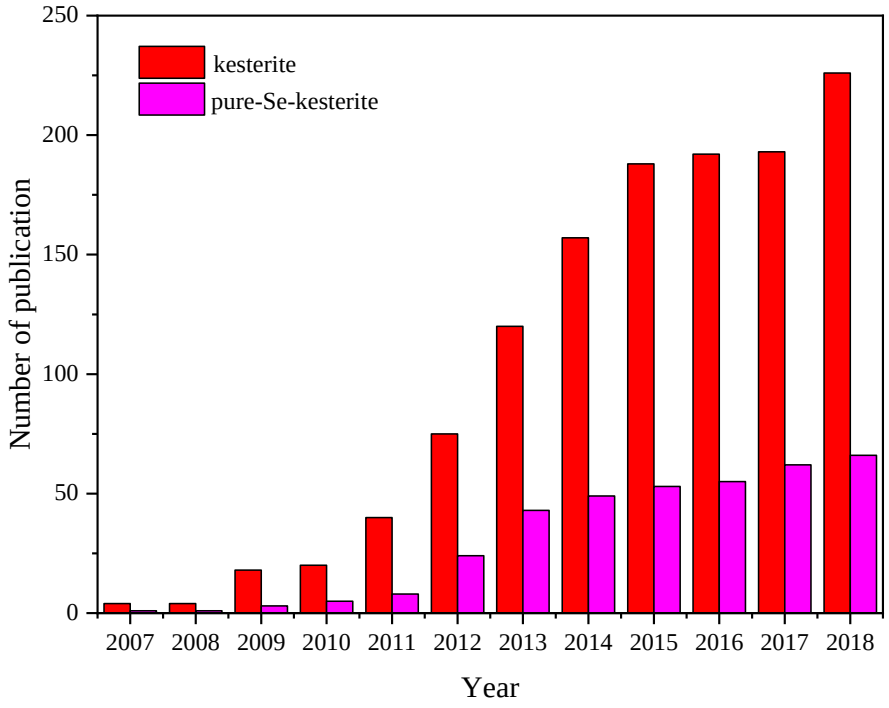

Figure 2.4: Number of the kesterite solar cells journal paper published versus publication year (source: web of science database).

2.1.4.1 Kesterite absorbers prepared from metallic precursors

Every year, a sparse research paper about the CZTSe absorber material is published and several metallic precursor configurations have been proposed. According to the results achieved in those papers, the metallic precursor configuration reveals to be a critical factor strongly impacting on the absorber morphology, back interface, porosity, and film adhesion as well as device performance. For instance, Fairbrother *et al*. [32], demonstrate that CZTSe composition, morphology, composition, and device performance strongly depend on the stacked configuration. It was also demonstrated that Mo/Sn/Zn/Cu stacks are expected to enhance absorber quality and device performance. Brammertz *et al*. [27] utilized a $Cu_{10}Sn_{90}$/Cu stacked configuration that could make a device with η up to 9.7 %. However, the CZTSe absorber was associated with a numerous number of voids at the Mo interface, caused by the low melting point of the $Cu_{10}Sn_{90}$ alloy phase (see Fig. 2.5). CZTSe solar cell with η up 11.4 % corresponding to the V_{OC} of 443 mV and *FF* 68 % could be achieved by utilizing a Mo/Zn/CuSn/Zn configuration [20]. Despite the remarkable value of V_{OC}, the devices suffer from strong cross-over between dark and illuminated *J-V* curves. It could be interpreted such that the presence of the blocking layer at the CZTSe/$MoSe_2$ interface significantly contributes to this aspect [16]. Looking to this configuration, one could argue such that the precursor's configuration does not enhance intermixing of layers, thus a great amount of ZnSe accumulates at the back of CZTSe absorber. The accumulation and segregation of ZnSe have been reported in the literature and linked with a Zn-rich absorber environment [58]. It should be noticed that the Zn-rich growth condition is favorable as it is expected to suppress the formation of the Cu-S(e) metallic-like phase at the back of the absorber, which could significantly deteriorate the device performance. To facilitate the intermixing of atoms of stacked metallic precursor, Li *et al*. [24] proposed that a splitting of Cu layer (Mo/Zn/Cu/Sn/Cu) could somewhat facilitate elemental diffusion in the short time during selenization, thus suppressing the formation of secondary phases at some local position in the CZTSe absorber.

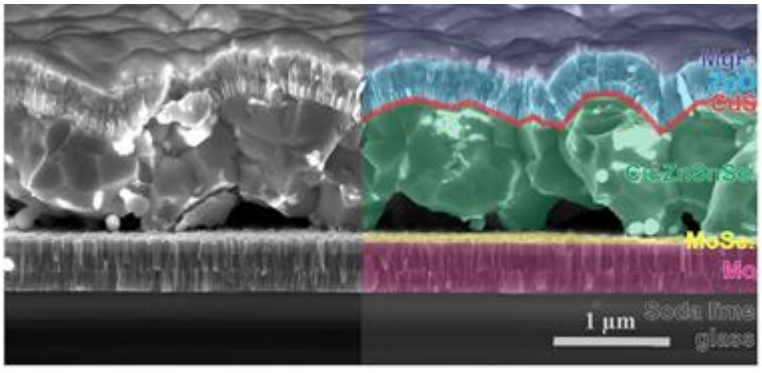

Figure 2.5: Cross-section SEM image of complete solar cells prepared from $Cu_{10}Sn_{90}$/Zn/Cu multilayers precursors [27].

However, the metallic stacking configuration could somewhat induce an in-depth composition gradient in the precursor, leading to the change in the formation pathways. It is often hypothesized that the formation

of CZTSe from metallic precursor proceeds either via the formation of the binary phases (Cu-S(e), ZnS(e), and Sn-S(e) phase) or the ternary phases (Cu-Sn-S(e) phases). As documented in [59], the formation pathway is pre-governed by the initial precursor composition. It is anticipated that pre-alloying of stacked precursors could promote the formation of metal alloys which are expected to alter the formation pathways. However, it has been demonstrated that co-existing elemental Sn with alloys of Cu-Sn and Cu-Zn in the precursors depends on the alloying temperature [60]–[62]. Giraldo *et al*. further postulate that the presence of elemental Sn in the precursors could somewhat promote to the Sn loss during the selenization process [63]. It was further showed that a pre-alloyed temperature of 300 °C could lead to better morphology and performance [29]. In connection to this, the alloying of the Mo/Zn/Cu/Sn/Cu metal precursor was investigated by Li *et al*. [64]. It was observed that alloying temperature (300 °C) leads to the formation of Mo/Zn, and Cu_5Zn_8/Cu_6Sn_5 which substantially suppress the formation of $MoSe_2$ (around 10 nm) during selenization [64]. Based on this finding, it could be interpreted such that the segregation of Zn and Cu_5Zn_8 lead to the formation of ZnSe and Cu-Se phases which might not only act as a temporary barrier but also trigger different formation pathways toward the formation of the CZTSe absorber. Moreover, it could be hypothesized that the CZTSe formation pathways proceed with the suppression of the formation of $SnSe_2$—which is prone to evaporation.

Jung *et al*. [65], performed the temperature-dependent study on phase evolution during annealing of sputtered Cu/Sn/Zn stacks. It was found that the CZTSe formation pathways proceed via reaction of Cu-Sn-S(e) and Zn at temperature > 300 °C. Giraldo *et al*.[63] reported that Cu out-diffuse rapidly to the surface and forms the Cu-Se phase on top of the Cu-Sn-Zn precursors. It was further showed that the reaction occurs via the formation of binaries. It was demonstrated in ref. [66] that the formation of the CZTSSe phase proceeds via reaction of binaries during the sulfo-selenization of Cu/Zn/Sn stacks. A detailed study on the phase transition during the sulfurization of sputtered Sn/Cu/Zn was carried out by Fairbrother *et al*.[67]. It was reported that the CZTS formation pathway proceeds via the formation of binaries at low temperature to ternaries at 480 °C, then Zn is incorporated at high temperature to form the CZTS phase.

Contrary to the stacked metallic precursor, CZTS(e) absorber can be fabricated from homogenous vacuum deposited metallic precursors. This approach allows uniform distribution of all four elements, resulting in less local inhomogeneity in the absorber. The precursor could be either co-evaporated or co-sputtered. However, the two processes are not fully investigated relative to the stacked precursors. The main reason could be a cost because the process involves four sputtering guns or evaporation sources. In this regard, a co-sputtering of the alloyed targets is commonly employed [68]–[70]. For instance, in ref. [69], [70] a pure-S-kesterite absorber was prepared from co-sputtered metallic precursors utilizing targets, Cu:Sn (60:40 at %) and elemental Zn target. Ericson *et al*. reported a very compact CZTS layer associated with local segregation of the ZnS phase at the surface, absorber bulk, and at the Mo interface [69].

In connection to this, the utilization of a single metallic target (Cu-Zn-Sn) to prepare a kesterite absorber has been reported [71]. It was observed that the utilization of the Cu-Zn-Sn sputtering target results in precursors with a smooth surface, however, the absorber quality depends on the selenization temperature and atmosphere. Kim and Amal [72], performed an investigation on phase transition during the selenization of Cu-Zn-Sn precursors, the study revealed that a uniform distribution of Cu, Zn, and Sn results into formation of selenide compounds at a relative lower temperature. However, based on this study it is convincing to argue that the utilization of Cu-Zn-Sn could promote CZTS(e) the formation pathways to proceed via the formation of the binaries as shown in reaction 2.2.

$$Cu_2S(e) + SnSe + ZnSe \leftrightharpoons Cu_2ZnSnS(e)_4 \qquad 2.2$$

However, the process following this pathway is difficult to be controlled due to the insufficient selenization/sulfurization time [58]. Subsequently, an incomplete reaction induces local inhomogeneity in the absorber potentially reduces the device performance [58], [73]–[75].

2.1.4.2 CZTSe absorber prepared from chalcogen-containing precursor

The formation of voids and cracks at the back interface is commonly observed and drastically deteriorates the device performance. When the CZTS(e) absorber prepared from the metallic precursor, numerous voids or cracks are observed in the back interface. It is often assumed that i) non-equilibrium condition is induced during the selenization process causing the vaporization of SnS(e), and thus the voids at the absorber layer [58], ii) a high diffusivity rate of Cu during annealing in the chalcogen atmosphere could lead to fast Cu out-diffusion which enables the formation of voids according to Kirkendall effect. These voids breakdown collectively resulting in the larger voids at the Mo/absorber interface [58], [76], and iii) volume expansion of the metals during annealing in chalcogen atmosphere could lead to the peeling off of the CZTS(e) layer or crack between the absorber and Mo back contact if the thermal stress is not effectively released [77]. To circumvent abovementioned potential issues, chalcogen is incorporated in the precursors, resulting in the chalcogen-rich (ratio of [S(e)]/[Cu]+[Zn]+[Sn] > 1) or chalcogen-poor precursors ([S(e)]/[Cu]+[Zn]+[Sn] < 1, allows the intimate mixing of selenide compounds, free metals, and alloys).

Incorporation of a thin ZnS layer between metallic precursor was proposed to released stress developed by metal layers underneath during the selenization of the Mo/Sn/Cu/ZnS/Sn/ZnS/Cu stacks [77]. The following configuration was adopted with the motivation that CZTSe formation should proceed via reaction of ternaries (Cu-Zn-S(e)) and binaries (ZnS(e)) and the growth should start from the bottom to the top [77], [78]. It was further observed that the grain growth at the bottom was limited due to less diffusion of Se vapor to the bottom of the precursor during selenization [77]. Son *et al*. [59], performed a temperature-dependence study on the phase and morphology evolution of CZTSSe absorber during the selenization of Mo/ZnS/SnS/Cu stacks. It was observed that at low-temperature binaries react to form ternaries, then CZTSSe absorber. Lai *et al*. [56], utilized a Zn_XSn_{1-X}/Cu_XSe precursor configuration could

demonstrate in-depth gradient of [Cu]/[Zn] + [Sn] ratio in the CZTSe absorber. It further suggests that it is possible to form a bandgap graded active layer. Moreover, it was postulated that at temperature < 500 °C binary phases react to form ternaries phases, which then react with ZnSe to form CZTSe at a temperature > 523 °C (see Fig. 2.6).

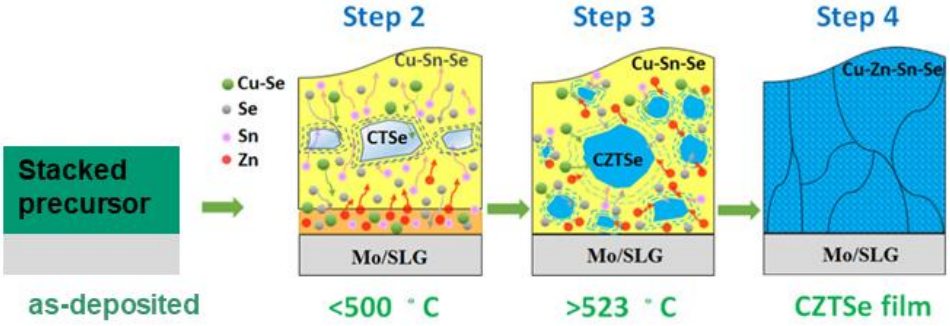

Figure 2.6: Schematic formation pathways of the CZTSe layer during the selenization of Zn_xSn_{1-x}/Cu-Sn-Se/Cu_xSe stacked precursors. This figure is adapted from [59].

Han *et al*. [79] performed both the temperature and time-dependent investigations on the phase evolution during annealing of co-sputtered Cu-ZnS-SnS_2 precursors. A temperature investigation showed a sequential formation of binaries which converted to CZTS at a high temperature. The time-dependent investigate displayed that disordered CZTS phase occurs at relatively low temperatures which improve with annealing time. Ren *et al*. [80], studied the evolution of CZTS phases and morphology during sulfurization of the co-sputtered CuS-ZnS-SnS precursors, where the evolution of grains from a columnar structure to a dense packing fine grains, then to dense packing large grains at 0 min, 1 min, and at 40 min were found, respectively. Moreover, a gradual change due to the sulfurization time of phases of Sn-S, ZnS, and CZTS at the surface and backside of the film was noticed. Phase evolution during the selenization of co-sputtered Cu-ZnS-SnS was reported by Temgoua *et al*. [81]. It was found that CZTSSe reaction pathways proceed via binaries reaction as shown in reaction 2.2.

Using a quaternary target, Sun *et al*. [82] conducted an investigation on the reaction pathways during the selenization of Cu-Zn-Sn-S precursor in the H_2Se atmosphere. It was noticed that the formation of the kesterite starts during precursor growth, then converts to high-quality CZTSSe phases at 560 °C. Wei *et al*. [53] showed that the formation of pathways for the CZTSe proceeds via reaction of Cu_2SnSe_3 and ZnSe at low temperatures during the selenization of sputtered Cu-Zn-Sn-Se in H_2Se atmosphere. Hernández-Martínez *et al*. [33] postulated that the formation pathways of CZTSe depend not only on the precursor configuration but also the chalcogen partial pressure.

It often assumed that the CZTSe absorber quality, the composition, and device performance of prepared from a stacked precursor could be enhanced by the optimization of selenization conditions. It is well known that the decomposition of the CZTSe absorber could be controlled by the accurate choice of Se partial pressure [12], [22], [83]. Teoman *et al*. [22] demonstrated the decrease in the ratio of [Cu]/[Zn]

with an increase in background pressure and the optimal ratio could be achieved at a pressure of around 10 mbar as shown in Fig. 2.7. This observation is somewhat different from most of the reports in the literature, where high chalcogen partial pressure (high N_2 background pressure) is utilized to suppress surface decomposition of CZTS(e) [33], [81], [83], [84]. Surprisingly, it was further demonstrated that using 10 mbar could results in CZTSe absorber with the photoluminescence (PL) emission peak at 1.00 eV which is only 30 meV below the bandgap of the material [20]. This further shows that it is possible to control the band tail in CZTSe which is sometimes assumed as the main culprit for the low V_{OC} in the devices. In connection to this, an intensive investigation on the dependence of the band tail to the background pressure during the selenization of sputtered stacked precursor (Cu/Sn/Zn) has been reported by Gang *et al*.[17]. They showed that the background pressure of 660 mbar led to the lowest band tail relative to the 540, 660, 800,940 mbar. This suggests that control the initial chamber pressure in a precise manner can effectively improve the quality of CZTS(e) absorber as well as the device performance [17], [22], [83]. It is should be noticed that it is not possible to completely suppress band tail in CZTS(e) absorber through controlling fabrication procedure. Hence, bandgap fluctuations would be inevitable [54]. To our knowledge, process reliability and reproducibility for CZTSe absorber and solar cells is less investigated. It is reported in ref. [22] that a low reactor pressure (10 mbar) leads to the very stable fabrication process—where the PL spectra of the reproduction sample showed a similar shape and position of the PL emission peak (see Fig. 2.7 (b)).

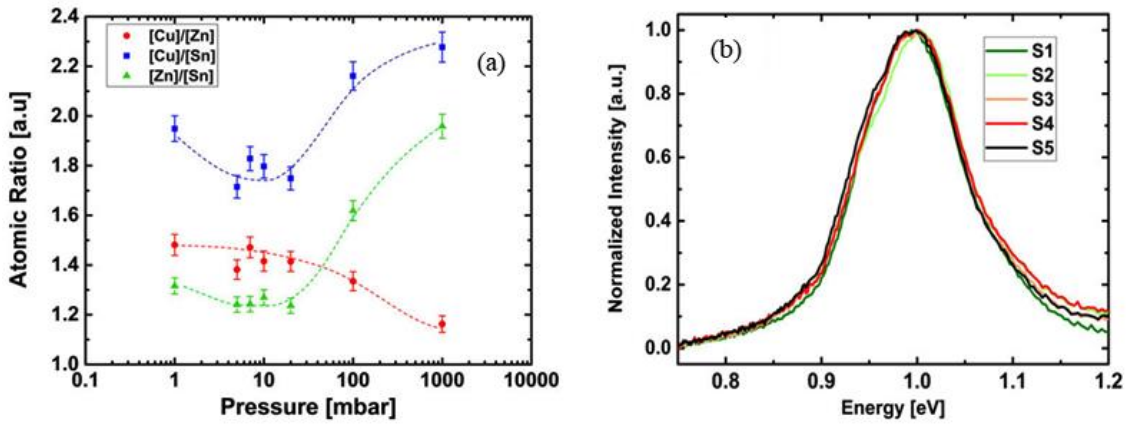

Figure 2.7:(a) cationic ratio of [Cu]/[Zn], [Cu]/[Sn], and [Zn]/[Sn] as a function of selenization pressure (b) PL spectra for five CZTSe samples prepared at the same conditions [22].

For the case of stacked metallic precursor, as high chalcogen partial pressure is achieved the formation pathways proceed via the formation of ternaries phases (Cu-Sn-Se). Consequently, the risk of secondary phase and local inhomogeneity in the absorber drastically reduces [33]. It was further reported in [24] that precise control of the $SnSe_2$ liquid phase can effectively improve the quality of CZTSe absorber and device performance. However, the formation of the $SnSe_2$ liquid phase depends on the Se partial pressure in the reactor chamber. Based on the evidence collected from previous studies, it can be interpreted that

the alloying process induces an in-depth composition gradient in the precursors which could potentially alter the formation pathways.

2.1.5 How to improve the efficiency of a kesterite solar cell?

To improve the optoelectronic properties of kesterite absorbers, several elements have been tested as dopants and alloying candidates. For instance, Li, Na, K, and Rb have been investigating as alkali dopants in the kesterite [2]. In other words, Ag, Cd, and Ge have been tested as alloying elements for Cu, Zn, and Sn, respectively. Each alloying element is selected with the motivation of altering the defects in the kesterite, enhancing grain growth as well as tuning the bandgap of the kesterite.

It was reported that it is possible to tune the kesterite bandgap from 1.5-1.9 eV for a pure-S-kesterite and from 1.07−1.4 eV for a pure-Se-kesterite through varying Ge concentration in the kesterite absorbers as shown in Fig 2.8 [85]. However, the modification of the bandgap of kesterite through Sn/Ge alloying leads to the tuning of the conduction band maximum (CBM), which could invoke a back-surface field, thus improves the device performance [86]. Additionally, incorporation of Ge into kesterite lattice could be expected to alter the number of deep-level traps associated with Sn, thus, it could lead to better absorber quality [86]–[88]. Theoretically, it has been proven that Cu-related defects (Cu_{Zn}, Zn_{Cu}, antisite, and V_{Cu} vacancies) significantly contribute to the optoelectronic properties of kesterite [5], [86], [88], [89]. Scragg *et al*. [88], postulate that Cu_{Zn} antisite leads to the local bandgap fluctuation and could cause a large V_{OC}-deficit in the kesterite solar cells. Nevertheless, theoretical studies further have shown that compensating defects that contribute to the semiconductor properties of kesterite involve Cu [86]. Thus, alloying Cu with Ag could be expected to alter the formation of these defects and the local location in the kesterite absorbers.

Due to Gershon *et al*. [90], Ag alloying leads to the modification of the bandgap and decrease a band tail in kesterite materials. Hages *et al*. [86], observed that the Ag alloying in the CZTSe improved the lifetime from 2.4 ns for Ag-free samples to 10 ns for the sample with 50 at.% of Ag. The difference between the bandgap and the PL maximum peak position for the pure-Se-kesterite and that from pure-Ag-kesterite (CZTSe) yields 110 meV for CZTSe and 0 meV for AZTSe. This strongly suggests that Ag alloying in kesterite could significantly reduce the band tail. This hypothesis is further supported by a detailed study of band tailing of pure-S-kesterite and Ag alloyed samples, which showed that the band tailing decreases with an increase in Ag content in the kesterite absorber [91]. Gershon *et al*. [90], further reported that the Fermi level pinning is significantly reduced to the highest Ag concentration CZTSe.

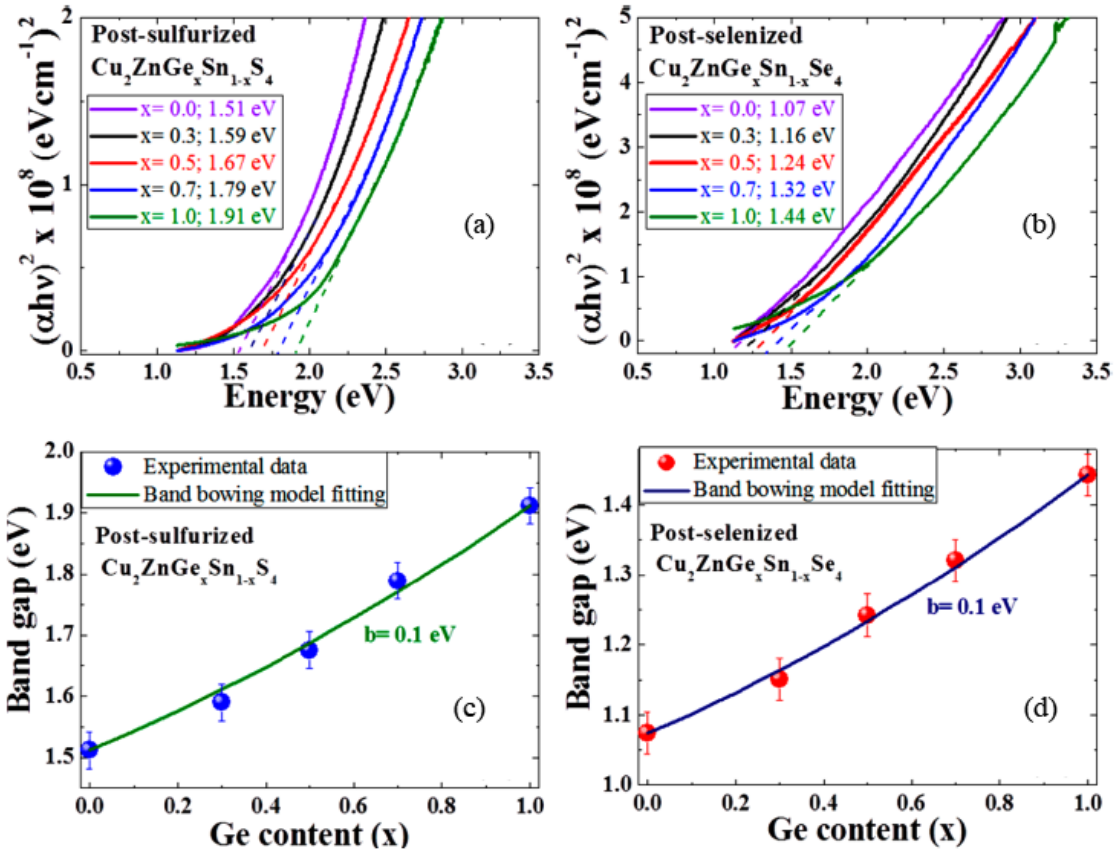

Figure 2.8: Extracted bandgap for (a) post-sulfurized CZTGS absorber and (b) post-selenized CZTGSe absorber. Corresponding bandgap together with bowing coefficient for (c) post-sulfurized CZTGS and (d) post-selenized CZTGSe absorbers [85].

Despite the suppression of the band tail with increased Ag alloying, it was further demonstrated that Ag alloying promotes grain growth and suppress structural defects such as twin boundaries [86], [89], [91], [92]. Kumar and Ingole [89], observed an increase in grain size from 0.13 to 2 µm with an increase in Ag content in the CZTS absorbers. This phenomenon was attributed to the liquid assisted growth mechanism due to the formation of a lower point (217 °C) eutectic of Sn-Ag-Cu [86], [89], [91]. However, it can be argued that during the annealing of kesterite precursor that a pseudobinary system of Ag_2S-SnS could be formed and had a positive impact on grain growth [89].

Qi *et al*. [93], demonstrated a V-shaped Ag graded structure with a higher Ag concentration on both the back and front surface layer (30 at.%/5 at.%/30 at.%). Through this approach, the highest η of 11.2 % which corresponds to the V_{OC} of 464 mV for Ag-alloying CZTSSe, has been reported. Interestingly, the device performance for Ag-alloying kesterite strongly depends on the Ag concentration in the absorber and one important loss mechanism to consider would be the interfaces [92].

Table 2.2: Efficiency of Ag alloyed kesterite absorber extracted from reference [94]

Material	Process and precursor configuration	Annealing	η
Chemical			
CZTS	Spray pyrolysis (chalcogen-containing precursor)	S @ 600 °C	7.1 %
CZTSSe	Slurries, spin coating (chalcogen-containing precursor)	Se @ 480 °C	11.2 %
CZTSe	Nanoparticle inks (chalcogen-containing precursor)	Se @ 500 °C	7.1 %
CZTS	Spin-coating (chalcogen-containing precursor)	S @ 530 °C	n/a
CZTSSe	Spray pyrolysis (chalcogen-containing precursor)	Se @ 470 °C	10 %
Physical			
CZTS	Sputtering (Ag- Zn/Cu/Sn)	S @ 570 °C	n/a
CZTSe	Thermal evaporation (Ag- Zn/Cu/Sn)	S @ 570 °C	4.4 %
CZTSe	Sputtering (Ag-Sn/Cu/Zn/Sn/Cu)	Se@ 550 °C	

2.1.6 Summary

In summary, we discussed the current development of vacuum processed kesterite—this holds in particularly on the relationship between precursor configuration and the formation pathways. It has been highlighted that despite significant progress in kesterite publication, the power conversion efficiency stagnates steady. Thus, substantial further improvements are necessary to reach industry competitive efficiency (> 18 %). The most dominant challenge that is heavily discussed is the V_{OC}-deficit—even reported in the high-efficiency kesterite solar cells. It was scientifically proved that kesterite contains a large number of defects at the surface and bulk of the absorber— and are mainly cause in the formation of band tail in the absorber and non-radiate recombination with the bandgap as well as band-edge potential fluctuation. This is more than likely due to the complexity of the quaternary structure of kesterite, thus, a lot of defects and secondary phases are expected to be formed. The formation and distribution of defects and secondary phases in the absorber depend on the precursor composition and configuration as well as annealing conditions. However, the latter is often assumed to significantly impact the defect and secondary phase formation and distribution. In particular, the decomposition of kesterite during processing can be quite harmful to the device performance. In regards to the discussion we made previously, we identified some research areas which are expected to further accelerate the progress in kesterite research. Firstly, and maybe very important, stabilize and optimize the baseline fabrication process. Moreover, based on the evidence collected under this review, it clearly that the kesterite formation pathway is pre-governed with precursor composition and annealing atmosphere. For instance, a chalcogen atmosphere in the reactor chamber could play a critical role in the formation of both Cu-Se and Sn-Se phases. However, on the

surface of CZTS(e), the formation of ZnS(e) could be also affected by chalcogen pressure. If the pressure is relatively low is anticipated that Cu will out-diffuse to the surface and Zn segregates to the bulk of the film and form the ZnS(e) phase. In this consideration, it could be hypothesized that kesterite formation pathways depend on the precursor's composition as well as annealing conditions. Therefore, this aspect will be later addressed in this thesis (see chapter 4 and chapter 6).

Recently, there is a tremendous effort was spend to seek for a feasible method to suppress the formation of Cu_{Zn} in the kesterite surface and bulk. The incorporation of Ag in the kesterite lattice is expected to significantly suppress the formation of these defects as well as grain growth. As it can be seen in Fig 2.9, Ag-alloying demonstrates a promising device performance, yet it is less investigated—this holds particularly to the vacuum-based approach. Moreover, the aspect of the reaction pathways during annealing of Ag-alloyed precursors is not yet reported. In this consideration, these aspects are addressed in chapter 6 of this thesis.

3. Experimental procedure

Fabrication of CZTSe solar cells involves the integration of several layers, thus, several instruments and advanced characterization techniques are needed. This chapter briefly explains the instruments and methodologies used for the preparation and characterization of CZTSe absorber and solar cells. At first, we describe how CZTSe and solar cells were fabricated—this includes a basic of ideas of molecular beam epitaxy (MBE), selenization process, and chemical bath deposition (CdS). The next section in this chapter is a short overview of the characterization techniques used to study the CZTSe absorber and solar cell properties.

3.1 CZTSe solar cells fabrication

Fabrication of CZTSe based solar cell was done in the two-step process, i) preparation of CZTSe precursors at low temperature by co-evaporation of homogenous or stacked layers and ii) re-crystallization of precursors at relatively high temperature in chalcogen ambient. In this section, detailed descriptions of the co-evaporation and re-crystallization processes are described.

3.1.1 Co-evaporation of CZTSe precursors

The precursors were deposited by a co-evaporation process using a custom-built molecular beam epitaxy (MBE) system. This technique belongs to the physical vapor deposition (PVD) family, particularly to the vacuum evaporation. However, MBE is more advanced relative to the conventional vacuum evaporation techniques—as it is possible to precisely control material purity, film composition and thickness, and doping concentrations. To achieve these qualities, an ultra-high vacuum (UHV) environment is required.

In this work, the MBE system equipped with eight water-cooled Knudsen effusion cells (Cu, Zn, Sn, Se, CdS, Mn, $ZnCl_2$, S) was used for deposition of either homogeneous or stacked precursors at relative low-temperature (~100 °C). For the case of co-evaporation of Cu-Zn-Sn-Se precursors, a low-temperature was utilized to avoid re-evaporation of Sn as $SnSe_2$ during precursor's growth. Each effusion cell is paired with a mechanical shutter that allows or prohibits the beam of molecules reaching the substrate. However, in this thesis, only four effusion cells were used (Cu, Zn, Sn, and Se) for fabricating the CZTSe precursors (see figure 3.1).

The system consists of two vacuum chambers, the transfer, and the single-walled with a liquid N_2 cryoshroud growth chamber. The transfer chamber is used for loading and unloading the sample. It is equipped with two vacuum pumps (rotary van-pump and turbo-molecular pump). Using these pumps it is possible to achieve a HV below 10^{-6} mbar. On the other hand, the growth chamber is equipped with an

ion-gauge pump, resulting in a UHV around 10^{-8} mbar. Moreover, thanks to the cryoshroud, see Fig 3.1, the chamber was able to be cooled down with liquid N_2, and thus the background pressure below 10^{-8} mbar could be achieved. Prior to the deposition, each individual Knudsen effusion cell was independently heated from standby temperature to working temperature (see Table 3.1). Utilizing the power supply, thermal-couple connected to the effusion cells, and PID controller the working temperature and the generated molecular beam flux from the effusion cell were stable and well-controlled. In this system, a beam flux could be calibrated using either quartz crystal monitor (QCM) or beam flux monitor (BFM) — which are attached in the sidewalls of the main chamber (see fig 3.1). However, in this thesis, QCM was the only tool used for calibration.

Table 3.1 shows the overview of all effusion cells with correspondence to the deposition rates used for the precursor's growth. Using these deposition rates, the precursors with an average bulk elemental composition of [Cu] / ([Zn] + [Sn]) ~ 0.71, [Zn] / [Sn] ~ 1.01, and [Se] / ([Cu] + [Zn] + [Sn]) ~ 0.50 were prepared. This precursor composition was deliberately chosen since it could be expected to lead to efficient devices as concluded in our previous studies [12], [95] as well as reported in the literature [7], [18], [19].

Prior to the deposition, 1.5 ×1.5 cm^2 Mo-coated soda-lime glass (Mo/SLG) coated with Mo back contact was ultrasonically cleaned by isopropanol, then bi-distilled at a temperature around 50 °C. The substrate was dried using N_2-pistol, then plasma etched for 5 min. The Mo/SLG coated substrate was loaded into the transfer chamber. Before loading the sample to the growth chamber, the transfer chamber was evacuated to attain pressure approximately to that of the growth chamber (below 10^{-6} mbar). Afterward, using a transfer rod, the sample is loaded or unloaded to the growth chamber. A detailed description of this system is found in the Ph.D. thesis of Hetterich [96]. It should be noticed that the system was not stable always—instability of the Cu-effusion cell (result in unstable Cu deposition rate) was the main limitation and had a huge impact on process optimization.

Table 3.1: The overview of the effusion cells standby temperature, working temperature, and corresponding deposition rate for Cu, Zn, Sn, and Se cells.

Effusion cell	Standby temp (°C)	Working temp$^{\Delta}$ (°C)	Deposition rate (nm/min)
Cu	880$^{\downarrow}$/1080$^{\downarrow}$	1111.0$^{\downarrow}$/1311.0$^{\downarrow}$	1.35
Zn	140	245.0	1.25
Sn	900$^{\downarrow}$/1100$^{\downarrow}$	1107.0$^{\downarrow}$/1252.0$^{\downarrow}$	2.15
Se	105	161.0	3.7

$^{\Delta}$Temperature is not fixed—it may change depending on the ambient conditions and effusion cell filling level.

$^{\downarrow}$Effusion cell bottom temperature

$^{\downarrow}$Effusion cell top temperature

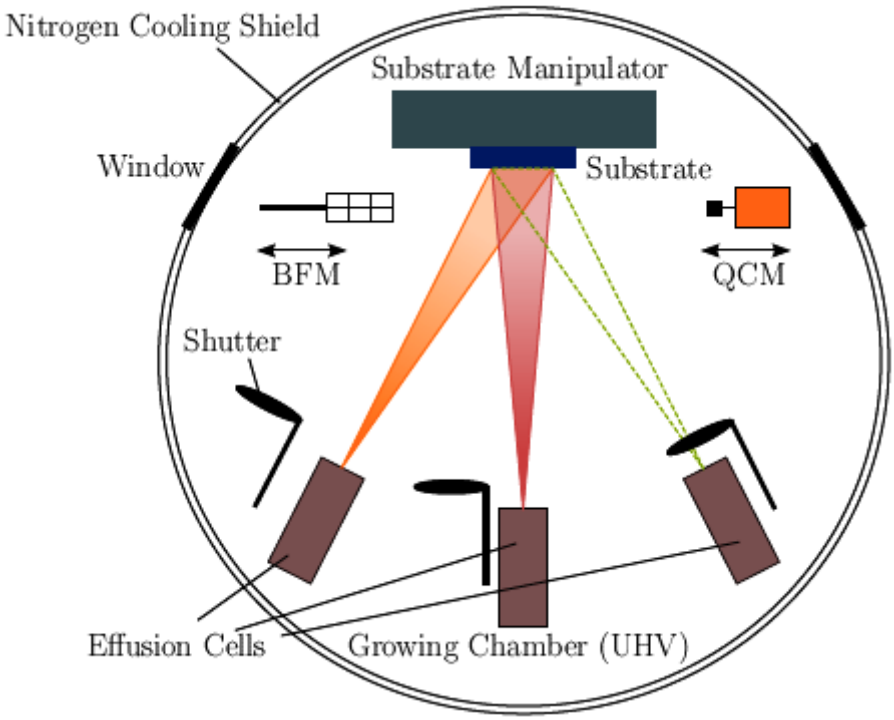

Figure 3.1: Illustration of the MBE growth chamber. The nitrogen cooling shield is commonly filled with liquid N_2 during calibration and growth. In effusion cells, the materials are evaporated and deposited onto the substrate. The beam of flux can be calibrated using a beam flux monitor (BFM) or quartz crystal monitor (QCM) [34], [97].

3.1.2 CZTSe absorber preparation

In order to obtain CZTSe absorbers, precursors were thermally annealed in an atmosphere containing Se vapor. To create this atmosphere, a semi-sealed graphite box which is a part of a custom-built rapid thermal annealing tube furnace (Fig. 3.2) was used for this purpose. Before inserting the sample to the semi-sealed graphite box, it was cleaned by an N_2-pistol and then placed in the middle of the box together with 180 mg of Se in the crucibles (for a certain time with Sn-wire), see Fig.3.3. Then, a graphite box was placed in the middle of the tube furnace. Prior to annealing, the furnace was evacuated to a base pressure of 10^{-6} mbar and subsequently re-filled with N_2 to the desired background pressure. Using a ramp rate of 40 °C/min, the furnace was heated to 540 °C, held for 10 min, then cooled down to room temperature. Before unloading the sample, the tube furnace was firstly evacuated to a pressure below 50 mbar. This step ensures that any residual gas generated during the previous selenization process is completely removed. Therefore, the loading and unloading processes are time-consuming, about 85 mins.

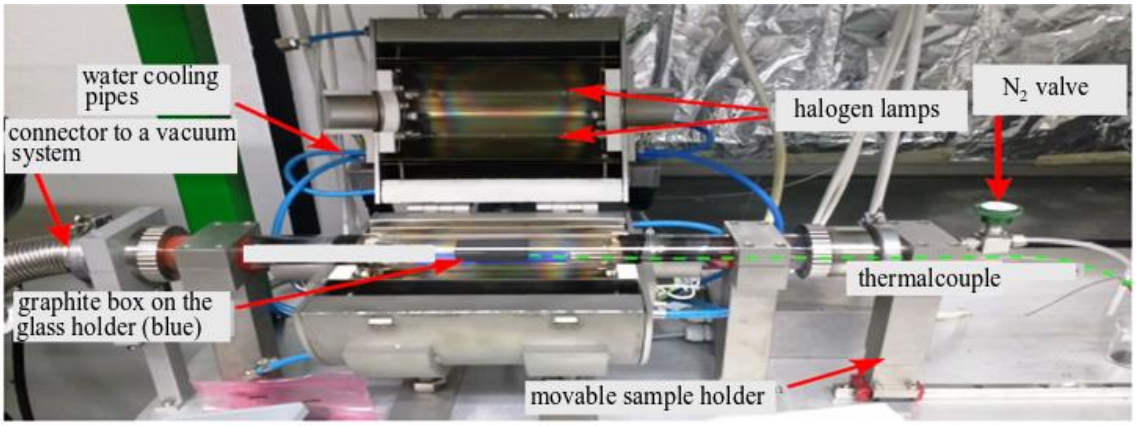

Figure 3.2: Custom-built made thermal annealing tube furnace. This figure was adapted from [34].

3.1.3 Deposition of the CdS buffer layer

As ascribed in section 2, the buffer layer was deposited onto the CZTSe absorber layer to form a *p-n* junction. As well established, CdS can be deposited by physical vapor [98], [99] or chemical deposition such as chemical bath deposition (CBD) [100]–[102]. Because of several reasons, the latter was selected as our method of choice to achieve high-efficiency devices. One of the plausible reasons is that the process involves soaking of the absorber in a bath solution containing Cd and S sources, resulting in surface etching, cleaning, and better CdS/CZTSe interface due to the isotropic coating. It is well known that CBD results in highly efficient devices. Traditionally, the bath solution composed of cadmium salt as a source of Cd, thiourea as a source of S, ammonia solution as a complexing agent, and ammonium salt as buffer solution (see Table 3.2). Formation of the CdS solution involves different steps as proposed in [102].

- The ammonia solution (NH_3OH) reacting with the Cd^{2+} to form a complex compound of tetraamine cadmium $[Cd(NH_3)_4]^{2+}$, then reversible adsorption of cadmium complex

$$CH_3COO)_2Cd.2H_2O + 4NH_3 \rightarrow [Cd(NH_3)_n]^{2+} + [(CH_3COO)_2.2H_2O]^- \quad 3.1$$

It should be noticed that the value of n takes a value between 1 and depending on the ammonium concentration.

$$[Cd(NH_3)_n]^{2+} + 2OH^- + Site \leftrightharpoons [Cd(OH), NH_3]_{ads} + nNH_3 \quad 3.2$$

- Formation of the metastable complex

$$[Cd(OH), NH_3]_{ads} + CN_2H_2 \rightarrow [Cd(OH)_2(NH)_2SC(NH_2)_2] \quad 3.3$$

- Decomposition of the metastable complex to form CdS and regeneration of the site

$$[Cd(OH)_2(NH)_2SC(NH_2)_2] \rightarrow CdS + CN_3H_5 + NH + 2O + site \quad 3.4$$

In this thesis, a computer-controlled custom-built CBD system was used for the deposition of CdS. Table 3.2. shows an overview of chemicals and their molar concentration used for the experiment. The bath solution was prepared by vigorously mixing 10 ml of bi-distilled water with 7.5 ml of

$(CH_3COO)_2Cd.2H_2O$ solution, 5 ml of a 25% ammonia solution, 10 ml of CH_3COONH_4 solution, and 18 ml of CH_4N_2S solution. Using an automated customer-built CBD system, CdS was deposited at around 58 °C. The system composed of a computer-controlled tower that moves in Y (up and down motions) and Z (steering motions) directions. Using a sample holder, the sample was attached to the motorized tower. Via a LabView program, dipping and steering functions were precisely controlled. We precisely control the deposition time by continuously monitoring the transmissivity of the bath solution. As soon as the transmission reached 40 %, the process will completely cease. The samples were washed with bi-distilled water and then dried using an N_2-pistol. Detailed information about this system can be found in the Master's thesis of Markus Neuwirth [103].

Table 3.2: Overview of the chemicals and concentrations used. Both chemicals were dissolved in the bi-distilled water.

Chemical	Chemical formula	Concentration (mol/L)
Cadmium acetate dihydrate	$Cd(CH_3COO)_2.2H_2O$	0.02
Ammonium acetate	CH_3COONH_4	0.02
Thiourea	CH_4N_2S	0.5
Ammonia solution	NH_3H_2O	13.4

3.1.4 Deposition of the window layer

To make a complete solar cell, a transparent bilayer of 50 nm i-ZnO and 400 nm ZnO:Al were DC-sputtered at a temperature around 180 °C. This process was done by our project collaborators at ZSW [1] or UOL[2]. To obtain a total active area of 0.16 cm^2, all the devices were mechanically scribed.

[1] Zentrum für Sonnenerergie-und Wasserstoff-Forschung Baden-Württemberg
[2] University of Oldenburg

3.2 Materials and device characterization techniques

Various characterization techniques were utilized to investigate the precursor properties, the absorbers, and the solar cell's properties. These techniques are described in this section. X-ray diffractometry (XRD) and Raman spectroscopy were used as tools to examine the precursor and absorber structural properties and secondary phases while the morphology of all samples was analyzed using scanning electron microscopy (SEM) and transmission electron microscopy (TEM). Furthermore, we elicit the information about elemental composition and distribution using EDXS attached in SEM and TEM, respectively. Conclusions on solar cell performance were basically drawn from the results of I-V measurements implemented by our solar cell simulator. Additionally, the temperature dependence of I-V curves was our basis to assess the loss mechanism. Finally, EQE was performed to investigate the photo-respond of a solar cell.

3.2.1 X-ray diffractometry (XRD)

X-ray diffractometry (XRD) is an analytical tool providing a considerable amount of useful information on the crystallinity, materials phases, lattice strain, and grain size and orientation of the bulk and thin-film samples. Moreover, this is one of the non-destructive analytical methods. It works under the principle of diffraction—whereby a monochromatic X-rays radiation interacts with the atomic planes of the crystalline sample, the X-rays can be scattered either elastically or inelastically. Elastic scattering is the scattering of a photon without energy loss and it is the bases of diffraction. The scattered X-rays are collected by the detector. The X-ray radiations scattered by the different lattice planes will interfere with each other constructively or destructively depending on the path difference of the radiations. If the path difference, $2d_{hkl}\sin\theta_{hkl}$, (where θ_{hkl} is the angle between the incident X-ray beam and d_{hkl} is related to lattice parameters) is equal to the integer m multiple of X-ray wavelength λ, the interference will be constructive, giving rise to the sharp diffraction peaks (Bragg peak). This phenomenon is described by Bragg's law and expressed as:

$$m\lambda = 2d_{hkl}\sin\theta_{hkl} \tag{3.1}$$

In this thesis, a Bruker D8 Discover XRD system was used. For safety reasons (protection against X-ray radiation), the XRD machine is located inside a box containing Pb-glass windows and doors.The system is equipped with a movable water-cooled Cu anode source with λ = 1.54184 Å, a movable sample holder, and a fixed detector. With such a configuration, the source and the sample holder can be moved alongside the angle θ of the reflection. Furthermore, because the sample holder can move in all 3-dimensions (x,y,z), a sample can be precisely fixed in the X-ray beam path. Additional to this, the system also offers options for different scan modes. However, in this thesis, Bragg–Brentano geometry ($2\theta-\omega-$scan) at a scan rate of 0.01°/s was used. In this geometry, both divergent and scattered beams are focused at a

fixed radius for the sample position—thus, Bragg peak intensities are excellently resolved. Fig 3.5 illustrates this scanning mode. As can be seen in Fig 3.3, this fulfills the condition such as $\omega = \theta$ that connects the angle of incoming radiation relative to the angle of the reflected radiation 2θ. In the diffractogram, the intensities of the Bragg peaks are plotted against the angle of detection 2θ. A detailed about this measurement can be found in ref. [34].

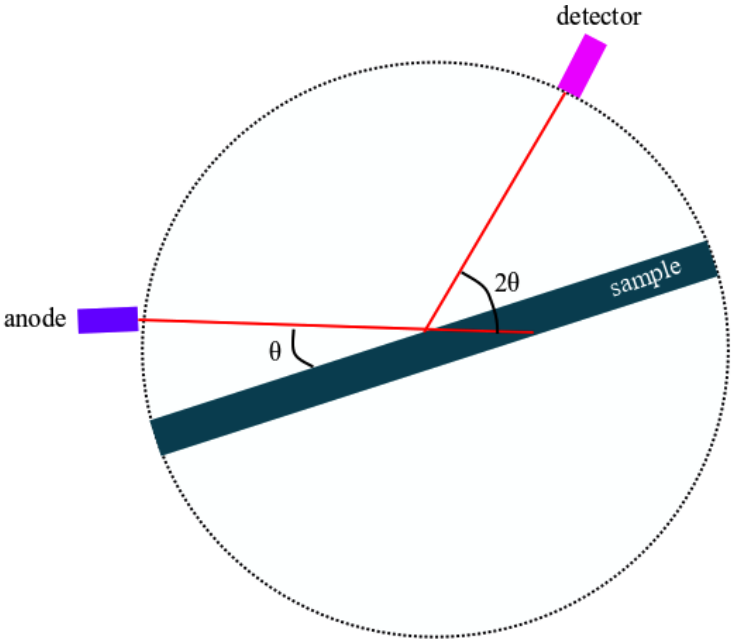

Figure 3.3 Schematic the Bragg-Brentano geometry, where to detect the whole range of the diffractogram, the X-ray source, and the detector are rotated. This figure is adapted from [34].

3.2.2 Raman spectroscopy

Raman spectroscopy is a technique that can offer various meaningful information about the material crystallinity, crystal phase, and chemical composition of the samples. Additionally, Raman spectroscopy also tells us about the stress distribution in the thin film sample. Basically, the Raman spectroscopy is a non-destructive technique—which based on a small portion of inelastically scattered light. When monochromatic light from a laser (near-ultraviolet, near-infrared, and visible range) illuminated in the material it could be elastically scattered (Rayleigh scattering) — the scattered light has the same energy with incident light. In contrary to this, there is a small portion of the light which is scattered inelastically—the scattered light has different energy with incoming light. The difference in energy of the incident photons relative to the inelastically scattered photons corresponded to the vibrational energy of the atoms in the material. For the case of solid material, this corresponds to the phonon vibrations.

Indeed, because we can find the fingerprint of material phases in a Raman spectrum, this analytical technique was exploited to further confirm the presence of minor secondary phases in CZTSe precursors and absorber. Due to the complexity of our sample structure, three different Raman spectroscopy systems were used for the analysis of CZTSe absorber and solar cells, i) the confocal-Raman microscope from spectroscopy and imaging (Warstein, Germany) with 488 nm, 457 nm, 442 nm, and 325 nm as excitation wavelength, (located in ZSW. All the micro-Raman measurements in ZSW was performed with the help of Dr. Thomas Schnabel), ii) the micro-Raman spectrometer (Renishaw 1000) equipped with an argon laser equipped with an argon-ion laser (Modu-Laser, Aries-163, 514.5 nm) (located in IAM-AWP[1], KIT. It should be noticed that the measurements at IAM-AWP were performed by the author and Dr. Monika Rinke), and iii) the micro-Raman spectrometer (BWS 415- *i*-Raman plus, from BWTEK with a red laser source of an excitation wavelength of 785 nm) located in IMT [2], KIT—all the measurements using this system was performed by the author

3.2.3 Scanning electron microscopy (SEM) and energy-dispersive X-ray spectroscopy (EDXS)

SEM and EDXS were used to investigate the morphology (of both surfaces and cross-sections) and composition, respectively. This technique was invented to overcome the diffraction limit of the traditional light microscope—as the electrons have a much shorter wavelength, it is possible to resolve smaller features. SEM produces images by probing the sample with a primary electron beam, which has been accelerated by an electrical field with a voltage of 1kV to several kV. The electron beam, produced by tungsten or LaB_6[3] electron gun, was focused on electromagnetic lenses before approaching the sample. When electrons in the primary beam collide with atoms on the sample surface, they lose energy through various mechanisms. After the collision, there are several beams of different kinds of particles (electron and photon) emerge from the sample. Those are low-energy secondary electrons (SE), high-energy backscattered electrons (BSE), light emission (cathodoluminescence), and X-ray emission. The SE is used to image the sample, while X-rays are used for elementary composition analysis.

In this thesis, the absorber morphology was analyzed using an SEM (Carl Zeiss SUPRA-55VP) with a 2 kV acceleration voltage. Note that Dr. Markus Neuwirth performed all the SEM measurements utilizing Carl Zeiss SUPRA-55VP. However, EDXS measurement was performed using Carl Zeiss LEO 15030 SEM in co-operation with the LEM [4], of the KIT. This measurement was done by Mr. Volker Zibat. Moreover, the acceleration voltage was set to 10 kV in all SEM/EDXS measurements. It is important to

[1] Institut für Angewandte Materialien
[2] Institute of microstructure Technology

[3] Lanthanum hexaboride
[4] Laboratorium für Elektronenmikroskopie

note that before taking the SEM image, all samples were cover with a very thin layer of either Pt or carbon film and properly earthed to suppress overcharging during the measurement.

3.2.4 Transmission electron microscopy (TEM)

Since it is important to us to gain deep knowledge about sample morphology, grain quality, properties of the interface between individual layers and elemental composition and distribution, TEM measurement was performed on either the CZTSe layer or to the complete solar cells. Although it is classified as a macroscopic analytical technique, TEM measurement enables us to analyze samples down to the angstrom range. In a TEM system, a primary electron beam is produced in an electron gun (cathode), accelerated by an anode, and focused by using electromagnetic lenses before approaching the sample. Typically, the magnitude of the acceleration voltage falls in a range from 80 to 1200 keV. When a primary beam of electrons impinges on the surface, parts of it are transmitted and others are scattered—this depends on the sample thickness and electron transparency property of the material constituting the sample. The emerging electron beam carries important information about the sample.

In this thesis, the FEI Technai Osiris microscope was our TEM system and the acceleration voltage was set at 200 kV in any measurement. Information about elemental distributions and composition were extracted from EDXS maps acquired in the scanning transmission electron microscope (STEM) mode. Elemental quantification was carried out by exploiting the Cliff-Lorimer method in the thin-foil approximation. The support calculation package for the method is embedded in the ESPRIT software (Bruker, version 1.9.4.3448) [104]. Quantification of the oxygen content was excluded due to the strong sample-thickness dependence of the quantification results. Prior to TEM measurement, cross-sectional TEM samples were prepared by focused-ion-beam (FIB) milling with a FEI Dual-beam Strata 400. The TEM lamellae were mounted on Mo lift-out grids. It should be noticed that all TEM measurements were performed in LEM with the help of Dr. Xiaowei Jin and Dr. Erich Müller.

3.2.5 Time-of-flight secondary ion mass spectroscopy (ToF-SIMS)

Scrutinizing the lateral and depth chemical composition of our samples is one of the necessary tasks in this research. Among different available techniques, ToF-SIMS is, in fact, the appropriate technique for this task due to its fantastic sensitivity. Conventionally, the ToF-SIMS system uses a focused beam of ion to sputter ions, atoms, or molecular compounds existing in the sample. The sputtered particles are accelerated through a flight path to the spectrometer. The time-of-flight of the particles is defined as the duration when the particles were sputtered and left the sample surface until the moment the particle reaches the spectrometer. On the basis of the time counted, it is easy to identify atoms or molecules distributing from the surface to the bulk of the sample. Therefore, with this technique, both depth-profile spectra together with the 3D image can be obtained.

In this thesis, the depth-dependent composition profile was measured using ToF-SIMS (TOF.SIMS5, ION-TOF GmbH). It should be noticed that this measurement technique was performed by Dr. Alexander Welle from IFG, KIT. This spectrometer is equipped with a Bi cluster primary ion source and a reflectron-type time-of-flight analyzer. The base pressure was < 1×10^{-8} mbar. For high mass resolution, the Bi source was operated in "high current bunched" mode providing short Bi^+ primary ion pulses at 25 keV energy, a target current of 1.2 pA, and a lateral resolution of approx. 4 µm. The short pulse length of 0.9 ns allowed for high mass resolution. For depth profiling, a dual-beam analysis was performed in interlaced mode: The primary ion source was scanned across an area of 200 × 200 μm^2 and a sputter gun (operated with O_2^+ ions, 2 keV, scanned over a concentric field of 450 × 450 μm^2, target current 450 nA) was applied to erode the sample. Thereby, the sputter ion dose density was >70000 times higher than the Bi ion dose density. Depth profiles in chapter 5 are plotted as secondary ion intensities (Σ ^{64}Zn, ^{66}Zn, ^{68}Zn; Σ ^{118}Sn, ^{120}Sn; Σ ^{63}Cu, ^{65}Cu; Σ ^{76}Se, ^{77}Se, ^{78}Se; Σ ^{92}Mo, ^{95}Mo, ^{96}Mo, ^{98}Mo; and Σ ^{107}Ag, ^{109}Ag) normalized to their maximum plotted over sputter ion fluence to obtain an arbitrary depth scale. Note that this scale is usually not linear due to the difference in the sputter yields of different layers.

3.2.6 *J-V* and *J-V-T* measurement

As described in section 2.1 that a solar cell is a *p-n* junction device. Thus, *J-V* measurement is utilized to determine its electronic properties. *J-V* measurement is usually carried out under two distinct conditions, one in dark and another one under the illumination of a light source. Two different kinds of *J-V* curves were combined and from which various solar cell parameters such as the short-circuit current (J_{SC}), the open-circuit voltage (V_{OC}), and fill-factor (*FF*) could be extracted as shown in Fig 3.4.

- The V_{OC} is the voltage measured at the illuminated when $J = 0$, is expressed as:

$$V_{OC} = \frac{k_B T}{q} \ln\left(1 - \frac{J_{SC}}{J_0}\right)$$

- The J_{SC} is the current measured at the illuminated if the $V = 0$ (no bias voltage is applied to the solar cell)
- The *FF* is the measure of the quality of the solar cell. The *J-V* curve describes the ratio of the two rectangles (see Fig. 3.6). Thus, it can be expressed as:

$$FF = \frac{P_{MPP}}{J_{SC}.V_{OC}} = \frac{J_{MPP}.V_{MPP}}{J_{SC}.V_{OC}}$$

It should be noticed that *FF* describes the squareness of the *J-V* curve. Thus, the ideal value of 1 of *FF* implies that the *J-V* curve has a rectangular shape. It is impossible to achieve this value in reality, so, the value of *FF* ranges from 25 % (the lowest theoretical value) to 90 %. Another important factor that should be taken into account is the voltage drops along the traveling path of photocarriers from the absorber to the external terminal. These voltage drops can be modeled by the series resistance (R_S) and parallel

resistance (R_P). The R_P originates from absorber defects which badly depreciate the V_{OC} of the solar cell. On the other hand, the R_S is due to the contact between layers in the solar cells—the high-value of this parameter adversely impacts the J_{SC}. In an ideal solar cell, the value of resistance is $R_P = \infty$ and $R_S = 0$, implies no an alternative path for the current to flow across the absorber and no voltage drop across the contact, respectively. However, practically this is not possible—thus, a high value of R_P and low value for R_S which could results in a flat with a steeply slope *J-V* curves is preferable.

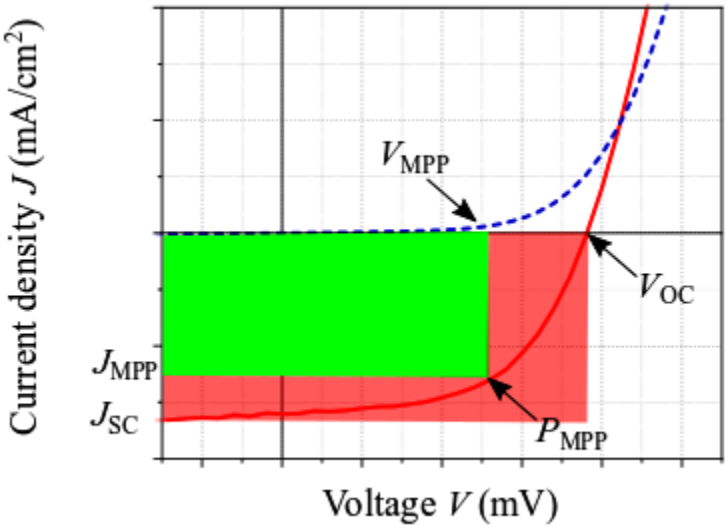

Figure 3.4: Sketch of the *J-V* curve of a CZTSe solar cell, blue and red curves represent dark and illuminated curves, respectively.

It is important to note that the power conversion efficiency (η) of a solar cell depends on all the parameters that have been discussed. However, it is defined as the ratio of the electrical power output (it can be considered as P_{MPP} of a solar cell) and the power of the incident radiation P_{in} (see Equation 3.9).

$$\eta = \frac{P_{MPP}}{P_{in}} = \frac{FF \times V_{OC} \times J_{SC}}{P_{in}} \qquad 3.9$$

One should be aware that P_{in} it is measured in W/m^2 (1000 W/m^2) and taken as the product of the irradiance of the light and the active area of the cells.

In the laboratory, a solar simulator is used to simulate the spectrum of the sun and to determine the above-mentioned parameters. Due to the presence of water vapor and gas molecules such as O_3 and CO_2 (causes

absorption and scattering) in the atmosphere, attenuation of the sun's radiation on the path to the earth's surface is unavoidable and has to be taken into account. The measure of the optical path of the atmosphere is called air mass (AM)—thus, it describes the level at which the atmosphere impacts the sun's radiation received at the earth's surface [105]. A solar simulator simulates a sun spectrum corresponding to AM 1.5 G—means solar radiation at 48°.

The *J-V* measurement of the solar cells of this thesis has been measured using a class AAA solar simulator (WACOM 1-lamp (Xe)) under 1000 W/m^2 AM 1.5 global with 2400 Keithley 2400 source meter. The measurements were performed at room temperature under a 4-point contacting mode. Prior to the measurement, the cells were mechanically scribed to obtain a total active area of 0.16 cm^2. Using a certified monocrystalline Si reference solar cell, a system was calibrated. The series resistance (R_S) was evaluated by a linear fit to the slope of the *J–V* curve around J_{SC} = 0 under illumination. Other diode parameters, such as the dark saturation current density (J_o) and diode ideality factor (n), were extracted from the dark *J–V* data as described [95], [106].

The existence of defects in the material provokes into recombination of photocarriers, thus, lower the solar cell performance. To elucidate the nature of the recombination pathway in CZTSe solar cell, temperature-dependent current density-voltage (*J–V–T*) measurements were performed in a cryostat (KONTI-IT-Cryostats, CryoVac) between T = 150 K and 300 K in 10 K intervals. A detailed about this measurement can be found in ref. [107].

3.2.7 External quantum efficiency (EQE)

EQE is an optical characterization technique that provides information on the current generated and recombination of a solar cell when it is illuminated by a particular wavelength of the light. Generally, defined as a ratio of the number of electron-hole pairs collected across the junction of the solar cells to the number of photos at a given wavelength of the incident on solar cells [108]. Mathematically, can be expressed as:

$$EQE = \frac{1}{q}\frac{dJ_{SC}(\lambda)}{d\phi(\lambda)} \tag{3.10}$$

where $d\phi(\lambda)$ is the incident photon flux in the wavelength interval $d\lambda$ leads to the dJ_{SC}. It implies that if EQE of a given solar cell is known, then the J_{SC} of a solar cell can be calculated for a given incident spectrum as:

$$J_{SC} = \int_{\lambda 0}^{\lambda 1} EQE(\lambda)\phi(\lambda)d\lambda \tag{3.11}$$

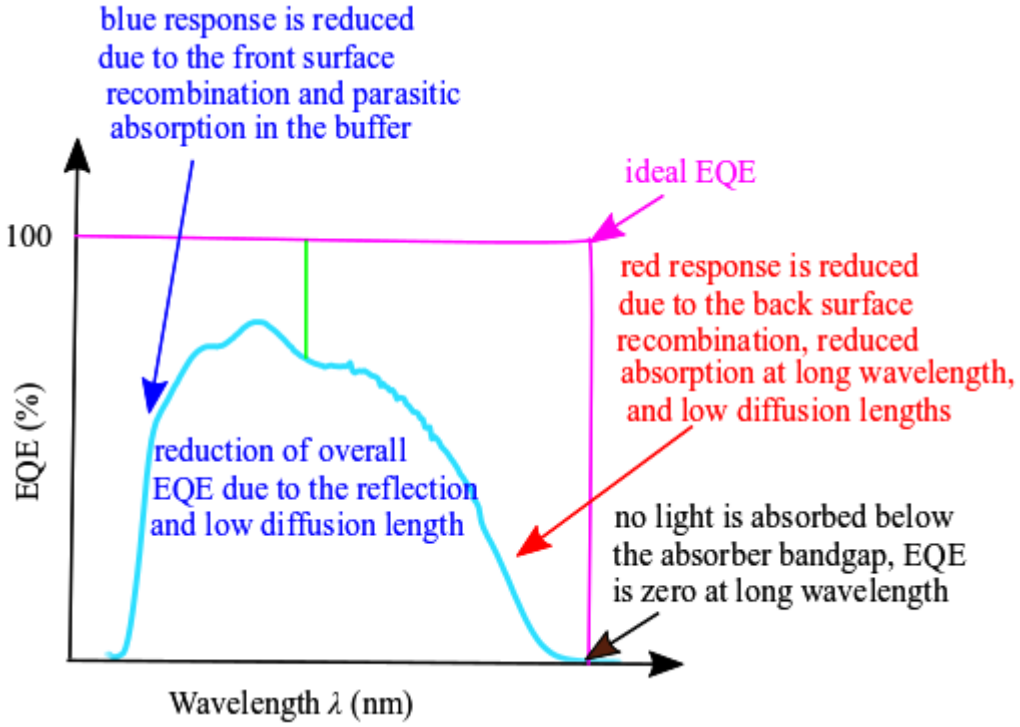

Figure 3.5: EQE spectra of the CZTSe solar cell with corresponding possible recombination mechanisms. The magenta and cyan represent an ideal and measured CZTSe EQE, respectively. Blue response reduction includes, i) front surface reflection from the air/ZnO/CdS/CZTSe interfaces, ii) absorption in the TCO layer and iii) absorption in the CdS layer [109].

It should be noticed that for a real solar cell the value of EQE is less than 1. Fig. 3.5 illustrates the EQE spectrum of CZTSe solar cell. Additional EQE measurements on solar cells are widely used to estimate the bandgap of the absorber layers. The approach was well established as documented [110], [111]. Thus, by assuming collection just in the space charge region (SCR), the EQE can be expressed as [20], [117]:

$$EQE \approx 1 - \exp(-\alpha W) \qquad 3.12$$

where, α and W are the absorption coefficient of the absorber material and the space charge region width, respectively. It is well documented that α is proportional to the bandgap of the absorber layer (see equation 3.13)

$$\alpha(h\upsilon) \propto \sqrt{h\upsilon - E_g} \qquad 3.13$$

Therefore, by plotting $[h\upsilon.\ln(1-EQE)]^2$ vs $h\upsilon$ and linear fitting of the long-wavelength one can extract the bandgap of the absorber as the intercept with the $h\upsilon$-axis, see Fig. 3.6

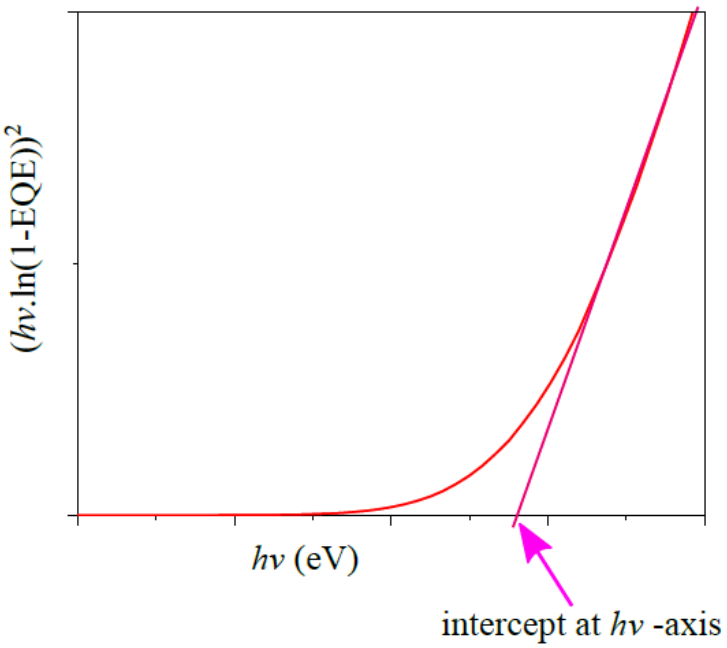

Figure 3.6: Bandgap extraction from a plot of $[\ h\upsilon.\ln(1-EQE)\ ]^2$ vs $h\upsilon$

In this thesis, EQE measurement was carried out using a system (Bentham PVE300) equipped with both quartz halogen and xenon lamps, measured at room temperature. Prior to the measurement, the system was calibrated using a certified Si and Ge reference detector.

3.2.8 Electroreflectance spectroscopy

Modulation spectroscopy techniques such as electromodulated reflectance — or commonly called electroreflectance (ER) — was further used to study the bandgap of CZTSe solar cells. This technique is simple and non-destructive and can be used to measure complete solar cells. In this technique, an AC external electric field is applied to a full solar cell to tilt the band structure of the material, resulting in a change in the dielectric function and consequently the reflectance [112]. The change in reflectance can be collected as specular reflectance or diffuse reflectance. The detailed information about this technique can be found in the Ph.D. thesis of Christoph Krämmer [9].

The custom-built system was used for electroreflectance measurement at room temperature. The light from a 250 W quartz-tungsten-halogen lamp was dispersed in a 0.32 m focal-length monochrometer with a 600 1/mm. The diffuse reflected light was collected via the lens system and detected by thermoelectrically cooled InGaAs photodiode. Using a function generator, a square wave modulation in reverse bias (f~223 Hz, U ~ -1.5 V) was applied and the relative change of the reflected intensity (ΔR/R) under an angle of incidence (AOI) and an angle of detection (AOD) was measured utilizing a lock-in technique.

Further details may be found in the Ph.D. thesis of Christoph Krämmer [9]. All the measurements regarding the electroreflectance spectroscopy were performed on the complete solar cell by Ms. Jasmin Seeger

.

4. CZTSe solar cells fabricated from low-temperature co-evaporated Cu-Zn-Sn-Se precursors followed by selenization

The results of this chapter are not yet published or submitted for publication.
Several people contributed to this chapter. Lwitiko Mwakyusa and Luis Kussi were involved in Samples preparation and characterization (XRD, Raman spectroscopy, J-V, and J-V-T measurements). Markus Neuwirth, Simon Woska, Volker Zibalt helped with SEM analysis. Erich Müller and Xiaowei Jin helped with TEM/EDX measurements. Raman spectroscopy using an excitation wavelength of 514.5 nm was performed with the help of Monika Rinke. Will Kogler, Erik Ahlswede, and Teoman Teskesen were involved in the deposition of the window layer. It should be noticed that all Mo substrates used in this chapter were supplied by Erik Ahlswede from ZSW.

4.1 Introduction

One of the key challenges in kesterite research is to establish a robust fabrication protocol to create the best absorber and thus attaining high efficient devices. Due to the chemistry of the kesterite, a two-step process i) where a precursor is deposited using either a wet-chemical or a vacuum-based process, followed by ii) recrystallization in chalcogen ambient at a temperature above 500 °C is preferred. The latter requires meticulous control over the annealing conditions such as temperature, annealing time, ramping rate, and chalcogen partial pressure. However, a high annealing temperature is the prerequisite to achieve high-quality kesterite with large grains. Nevertheless, that kesterite decomposes at high annealing temperature (above 500 °C) severely impedes the quality of the absorber and device performance. It is well known that a high-pressure chalcogen atmosphere suppresses surface decomposition of kesterite[12]. As described previously and reported in ref. [12], [84] that a minimum partial pressure of 7×10^{-4} mbar for S(e) and a minimum pressure of 1.4×10^{-3} mbar for SnS(e) is sufficient to substantially obstruct the surface decomposition of CZTS(e). To achieve that pressure, the selenization step is carried out under relatively high N_2 pressure in a semi-isolated graphite box as proposed in ref [12]. However, the main issue is the homogeneity of the kesterite layer—during the incorporation of chalcogens, the absorber could be obtained with a composition gradient as demonstrated in refs [24], [113]. It is expected that the homogenous chalcogen containing precursor could substantially suppress the composition gradient in the absorbers. In this section, following the critical points aforementioned to establish a baseline fabrication

process for the absorber, CZTSe layers were prepared by annealing the low-temperature co-evaporated Cu-Zn-Sn-Se precursors. Moreover, as it is documented in [33], [80], [114] that the kesterite reaction pathways could proceed via the formation of binaries or ternaries depending on the precursor configuration and Se partial pressure. This suggests that there is no common route for the CZTS(e) formation. Thus, in this line of argument, CZTSe formation pathways are investigated and reported.

First, the CZTSe solar cells under test were fabricated and analyzed. Table 4.1 summarize the precursor growth conditions used to fabricate the device under test. The corresponding deposition rates were used with a view of achieving an average precursor bulk composition of [Cu]/[Zn] + [Sn] = 0.71 and [Zn]/[Sn] = 1.01 which was expected to give high-efficient devices as reported in [10], [12], [18].

4.2 Study of the co-evaporated Cu-Zn-Sn-Se precursors

To confirm the material phases presenting in the co-evaporated Cu-Zn-Sn-Se precursor, XRD measurement was performed and analyzed. As illustrated by the XRD pattern in Fig. 4.1 (a), the as-deposited film exhibited a mixture of the selenide compounds CZTZSe (PDF No. 00-052-0868), ZnSe (PDF No. 01-080-0021), Cu_2SnSe_3 (PDF-number 01-070-8930), $SnSe_2$ (PDF No. 01-089-2939), and CuSe (PDF No. 00-027-0184)) and the alloys of the Cu_6Sn_5 (PDF No. 00-047-1575) and the Cu_5Zn_8 (PDF No. 00-025-1228). Therefore, it revealed that Se started to be incorporated during the precursor growth.

To gain more conclusive information about the selenide compound, micro-Raman spectroscopy measurement was performed using an excitation laser source of 514. 5 nm. As it appears in fig. 4.1 (a) (the black line), broad Raman vibrational bands at 192 cm^{-1}, 233 cm^{-1}, and 245 cm^{-1} were observed. It is well known that the A1 vibrational modes of CZTSe are located at 172 cm^{-1}, 195 cm^{-1} [61], [67], [113], [115]–[117]. The presence of the broadband at 192 cm^{-1} indicated that the CZTSe phase possessed a poor crystallization [61], [114]. In this sense, it can be postulated that the formation of the CZTSe phase starts during precursor growth. Further investigation on the surface and cross-section images of the film reveals the fact that the quality of the Cu-Zn-Sn-Se layer seemed to be not ideal for solar cell application (see figs 4.2 (a) and (b)). Therefore, to improve the morphology and crystal quality the sample was annealed at high temperature.

Table 4.1: Precursor growth parameters: the precursor was deposited at a substrate temperature of around 100 °C.

Sample number	Deposition rate (nm/min)				Elemental ratio			Precursor thickness (nm)
	Cu	Zn	Sn	Se	[Cu]/[Zn]+[Sn]	[Zn]/[Sn]	[Se]/[M]	
AA0157	1.65	1.6	2.7	4.3	0.71	1.01	0.46	650

[M] Sum of [Cu] + [Zn] + [Sn]

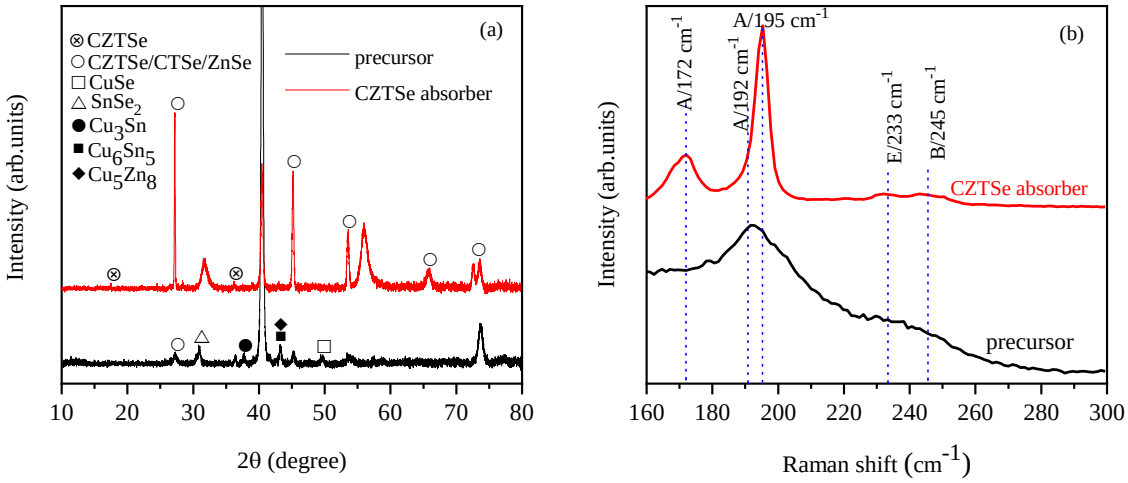

Figure 4.1:(a)The XRD pattern and (b) Raman spectra of Cu-Zn-Sn-Se precursor and CZTSe absorber, respectively.

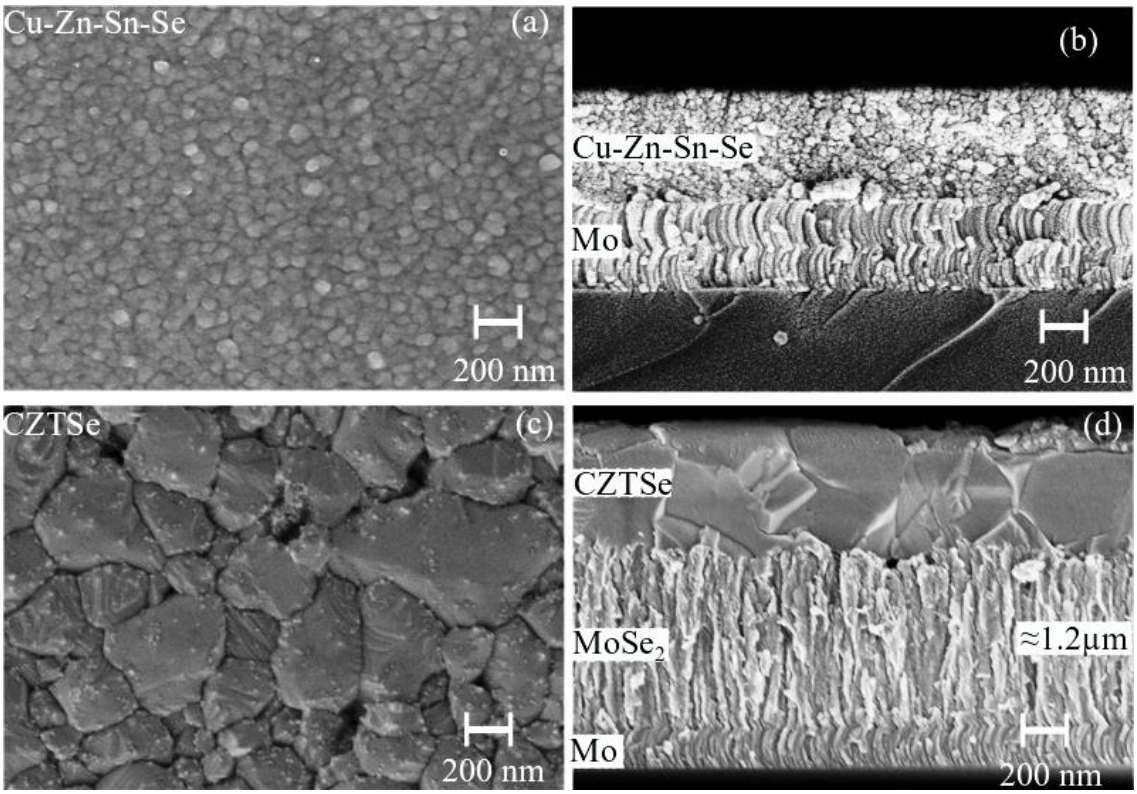

Figure 4.2:Top view and cross-sectional images for (a) and (b) as-deposited Cu-Zn-Sn-Se layer, (c) and (d) CZTSe layer.

4.3 Study of the CZTSe absorbers

The annealing of precursors to obtain a better quality CZTSe layer was implemented in the custom-built tubular furnace under the N_2 + Se atmosphere as described in section 3.1.2 and in ref. [12]. Detailed selenization parameters are summarized in table 4.2. Note that, the relatively low heating rate during selenization was used to suppress CZTSe films peeling off.

The XRD pattern of the CZTSe layer agreed with that of the tetragonal CZTSe phase (PDF No. 00-052-0868). It shows four main peaks around 27.1°, 45.2°, 53.7°, and 66.0°, corresponding to the (112), (204/220), (312/116), and (400/008), along with two minor peaks (17.5° and 36.4°). However, as documented in other reports [17], [33], [114], tetragonal secondary phases such as Cu_2SnSe_3 and ZnSe cannot be distinguished in XRD pattern as their lattice constant is almost identical to that of CZTSe.

Table 4.2: Selenization parameters

Selenization conditions				Composition ratios			CZTSe thickness (nm)
Heating rate (°C/min)	Temperature(°C)	Time (min)	Pressure (mbar)	[Cu]/[Zn]+[Sn]	[Zn]/[Sn]	[Se]/[M]	
40	540	10	200	0.82	1.3	1.1	1000

[M] represent sum of [Cu] + [Zn] + [Sn]

In order to determine the material phases in this case, micro-Raman spectroscopy measurement with an excitation wavelength of 514.5 nm was our method of choice. The excitation wavelength of 514.5 nm was chosen purposely because such a probing beam cannot penetrate so deeply into the sample (maximum 100nm beneath the surface) and therefore the collection Raman signal conveys only the information of the sample surface. As it can be observed in Fig 4.1 (b) (the red color curve), the A1 vibrational modes of CZTSe are located at 172 cm^{-1}, 195 cm^{-1}, alongside with E and B at 233 cm^{-1}, and 245 cm^{-1} were found. There is no evidence from the Raman measurement for the secondary phases.

As has been predicted that the annealing process will help to ameliorate the morphological property of the CZTSe absorber. It can be seen in Figs 4.2, indeed, the morphology significantly enhanced after selenization. The layer was more compact associated with larger grains that extend from the surface to the back (see figs 4.2 (d)). Because a thicker layer of $MoSe_2$ (1200 nm) was found after selenization, it suggests that Se reacted with Mo to form $MoSe_2$. However, an interesting question about the final composition and elemental distribution in the CZTSe absorber still piques our curiosity. To further explore this aspect, combined BF-TEM and STEM-EDXS measurements were performed on a complete solar cell as a device under test. Figs 4.3 shows a scanning TEM (STEM) mode using a High Angle Annular Dark Field

(HAADF) detector, BT-TEM image, and EDXS elemental distribution of Cu, Zn, Sn, and Se across the layer. As appears in Fig. 4.3 (a-i), the absorber was characterized by a more uniform morphology. This observation was in good agreement with the cross-sectional SEM image in Fig. 4.2 (d). As illustrated in Fig. 4.3 (b), the CZTSe appeared to have few micro-twins indicated by the red arrow. Moreover, few voids at the CZTSe/$MoSe_2$ interface were visible. The elemental distribution was uniformly distributed (see figs 4.3 (a-(ii)-(iv))). A possible explanation of this observation is that for co-evaporated Cu-Zn-Sn-Se precursor all the four elements are uniformly distributed. Consequently, Cu_2SnSe_3 and ZnSe are uniformly distributed across the precursor and reaction to form the CZTSe absorber. The average bulk composition measured by EDXS was around [Cu]/[Zn] + [Sn] = 0.82 and [Zn]/[Sn] = 1.3. The ratio of [Zn]/[Sn] slightly increased relative to the precursor composition, indicating Sn loss during selenization. Similar observations were acknowledged in previous reports [53], [63], [113].

4.4 Study on the CZTSe bandgap

As has been described previously, the main issue limiting the performance of kesterite solar cell is the larger V_{OC}-deficit, as expressed in [17]:

$$V_{OC}\text{-deficit} = \frac{E_g}{q} - V_{OC} \qquad 4.1$$

where, E_g and q are the bandgap energy of the absorber and electronic charge, respectively. Based on equation 4.1, it is clear that E_g of the absorber material plays a critical role in the maximum achievable V_{OC} as well as overall device performance. To extract this value, diffuse electroreflectance (D-ER) spectroscopy measurement was performed on a complete solar cell. The measurement technique was fully presented in chapter 3 and in ref. [112]. Fig. 4.4 shows the D-ER spectra of CZTSe solar cells measured at an angle of incidence (AOI) -60° and angle of detection (AOD) at -20°. As it appears in Fig. 4.4, the bandgap of CZTSe is around 0.99 eV. The extracted value of the bandgap by D-ER shows good agreement with previous studies [19], [112], despite a slight difference with the one reported in [20], [64]. A plausible reason for this discrepancy is that the analyzed CZTSe solar cell exhibited a larger degree of Cu-Zn disorder due to the rapid cooling downstage in our selenization process [112].

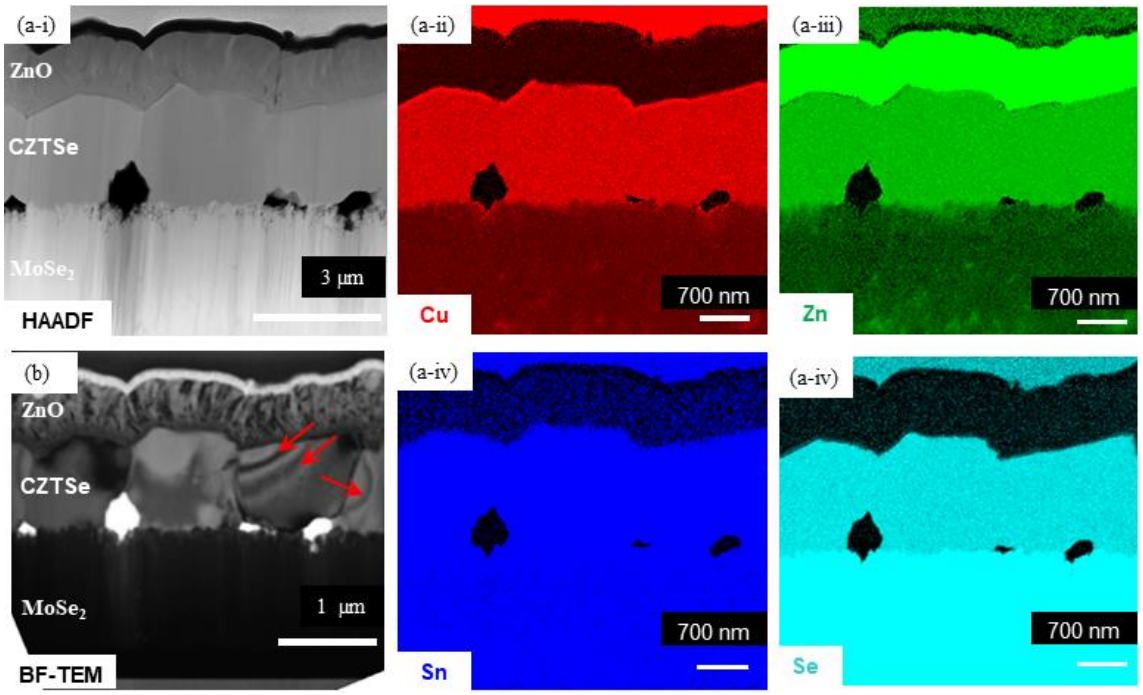

Figure 4.3: (a-i) Cross-sectional STEM-HAADF image of (a-(ii-iv)) corresponding elemental distributions obtained from EDXS maps of Cu, Zn, Sn, and Se, respectively. Different elements are denoted in a different color (Cu in red, Zn in green, Sn in blue, and Se in turquoise) (b) BT-TEM image of a solar cell. The micro-twins are marked with red arrows.

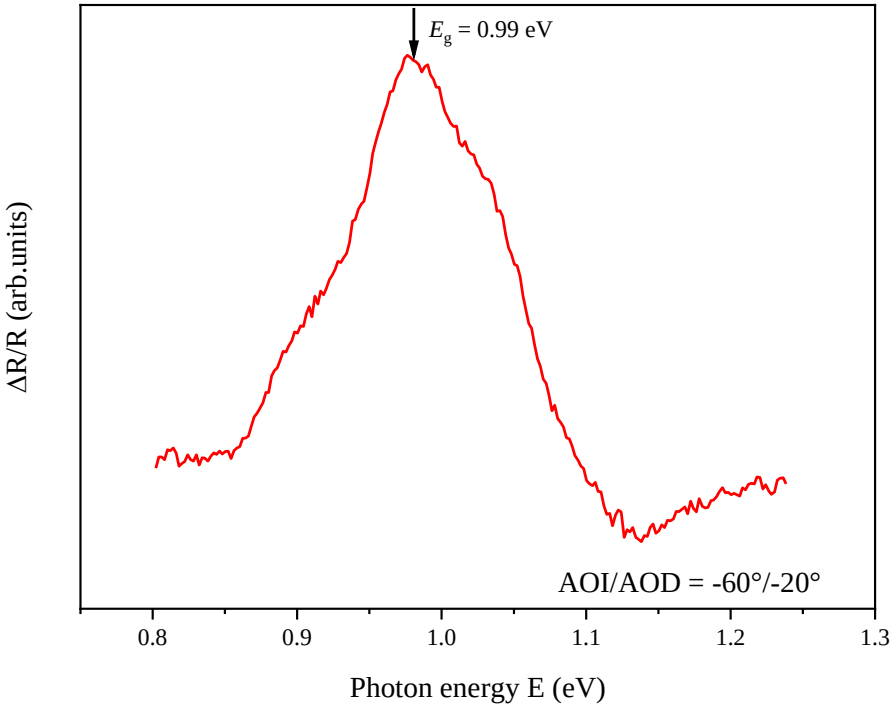

Figure 4.4: D-ER spectra of the CZTSe solar cell measured at AOI/AOD of -60°/-20°.

4.5 Study on solar cell performance

To explore the CZTSe quality, after annealing in the Se atmosphere for 10 min, CZTSe solar cell was fabricated and analyzed. The dark and illuminated current density-voltage (*J-V*) curves for the champion solar cell is shown in Fig. 4.5. The illuminated curve was not very flat and exhibited an efficiency of up to 6.4 % which corresponded to the V_{OC} of 351 mV, J_{SC} of 39 mA/cm^2 and *FF* of 50 %. The device showed the V_{OC} deficit of 640 mV with respect to the bandgap. Values of R_S and R_p were also extracted as described in section 3.2.6 and in refs [95], [106], they were around 2.7 Ωcm^2 and 314 Ωcm^2 for the minimum R_S and the maximum R_P, respectively. The R_S obtained in this study is somewhat higher than high efficient CZTSe devices reported in the literature [7], [17], [27]. There was a strong cross-over (at 6.0 mA/cm^2) between the dark and illuminated curves and whether or not it embodies for a higher electrical barrier either at the Cd/CZTSe interface, in the bulk of the CZTSe layer, or at the Mo/$MoSe_2$/CZTSe interface it will be addressed later on in this section. Concerning the ideality factor (*n*), it stayed above 2. This situation implies the unusual recombination mechanisms in the device which are possibly the tunneling-enhanced recombination (in the space charge region), recombination via coupled defects, and donor-acceptor pair recombination [27].

To elucidate the nature of the dominant recombination mechanism in our devices, *J-V-T* measurement was performed on the champion solar cell. Firstly, the relationship between the V_{OC} and temperature were taken into account. As can be seen in Fig. 4.6 (a), from 220 K the V_{OC} significantly deviated from the ideally expected linear behavior. This effect is commonly reported in the literature [27], [64], [118], [119] and mainly related to the carrier freeze-out effect at low temperature. Using equation 4.2, we plot V_{OC} versus temperature in order to extract the value of the activation energy E_A of the main recombination mechanism.

$$V_{OC} = \frac{E_A}{q} - \frac{nk_BT}{q}\ln\left(\frac{J_{00}}{J_L}\right) \qquad 4.2$$

where k_B, J_{00}, and J_L are the Boltzmann constant, reverse saturated current density prefactor, and photocurrent density, respectively.

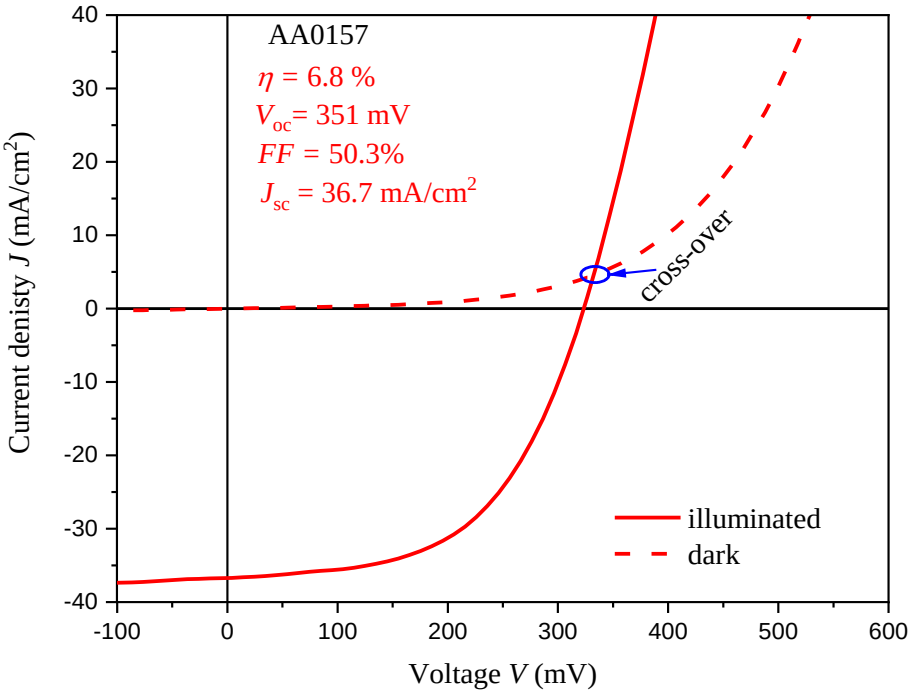

Figure 4.5: The dark and illuminated J–V curves for the champion solar cells fabricated from a co-evaporated precursor.

The linear extrapolation to 0 K yields E_A = 0.80 eV, see fig. 4.6 (a). The device exhibited a lower E_A as compared to the bandgap (0.99 eV) extracted from the electroreflectance measurement. From these findings, it is concluded that the CdS/CZTSe interface recombination strongly influences the device performance, thus deteriorating their V_{OC} at room temperature. The dependence of the dark R_S on the temperature is shown in Fig 4.6 (b). The dark R_S increased roughly exponentially with decreasing temperature in the range between from 300 K to 170 K and saturated beyond 170 K. A possible explanation for this behavior is the presence of a back contact blocking (Schottky) barrier or the carrier freeze-out effect due to the lack of shallow acceptors in CZTSe layer [20], [64]. The blocking Schottky barrier height Φ_B can be obtained using equation as [64]:

$$R_S = \frac{k_B}{qA^*T}\exp\left(\frac{\Phi_B}{k_BT}\right) \qquad 4.3$$

where A^* and Φ_B are the Richardson constant and blocking Schottky barrier height, respectively. A fit from a plot of ln(R_ST) versus 1/T (see Fig. 4.6 (c)) yields Φ_B = 227 meV. The Φ_B obtained from this study is slightly higher as compared to those reported in the literature (see table 4.3). Based on the ref. [64] and our own findings we concluded that the strong cross-over in our devices is due to CdS/CZTSe interface recombination and blocking the Schottky barrier at the Mo/$MoSe_2$/CZTSe interface. The R_S of our devices is still relatively high and remains to be one of the limiting factors for the performance of the devices.

Table 4.3: Device characteristics of the selected CZTSe and CZTSSe solar cells in the literature.

Absorber	η (%)	FF (%)	V_{oc} (mV)	j_{sc} (mA/cm^2)	R_s (Ωcm^2)	n	Φ_B (meV)	Reference
CZTSSe	12.6	69.8	513.4	35.2	0.72	1.42	N/A	[10]
CZTSe	11.7	66.6	423	41.7	0.38	1.57	N/A	[18]
CZTSe	11.6	67.3	423	40.6	0.32	1.57	N/A	[19]
CZTSe	8.7	56.7	418	36.2	0.62	1.78	24	[64]
CZTSe	9.7	61.4	408	38.9	1.05	3.5	135	[27]
CZTSe	6.8	50.0	351	39	2.7	2.2	227	This work

N/A no data available

It should be noticed that adequate statistics on device efficiency have to be carried out in order to provide a reasonable measure to evaluate the quality of CZTSe absorber and device performance. Table 4.4 displays the solar cell parameters obtained from 8 solar cells of the sample set AA0157 (sample under test) in one. The devices showed to have a large fluctuation in solar cell parameters, indicating a very inhomogeneous growth across the CZTSe absorbers. Cross-sectional SEM images in three different spots of the device were acquired in order to assure this argument. It was observed that the morphology differs significantly for different spots on the same samples (see Figs.4.7). Based on these findings, it might be assumed that the baseline process is not reliable and reproducible. To make this assumption more convincing, 4-samples were fabricated and analyzed. Judging in Fig 4.8, it is evident that the baseline process of the experiment is not reliable and reproducible—thus the need for improvement is necessary. A feasible measure to improve the quality of the CZTSe layer, as well as the reproducibility of the fabrication process, can be devised by recapitulated several valuable conclusions published previously in refs [12] [121 and [127]. Firstly, it was confirmed that Se partial pressure during holding time plays a critical role in the quality of the absorber and device performance [24], [118]. Secondly, from our own findings and results reported in the literature [12], [24], it could be hypothesized that a high Se partial pressure during holding time could improve CZTSe quality and reproducibility.

Table 4.4: Solar cell parameters for the CZTSe solar cell

η (%)	FF (%)	V_{OC} (mV)	J_{SC} (mA/cm^2)	R_S (Ωcm^2)	n
5.4	45	325	37	3.2	1.9
6.2	48	348	39	3.0	2.0
5.9	48	326	38	2.9	2.1
5.5	45	325	38	3.2	2.1
6.8	50	351	39	2.7	2.2
6.2	47	337	39	3.0	2.0
6.2	48	342	39	3.0	2.4
5.1	43	321	38	3.7	2.4

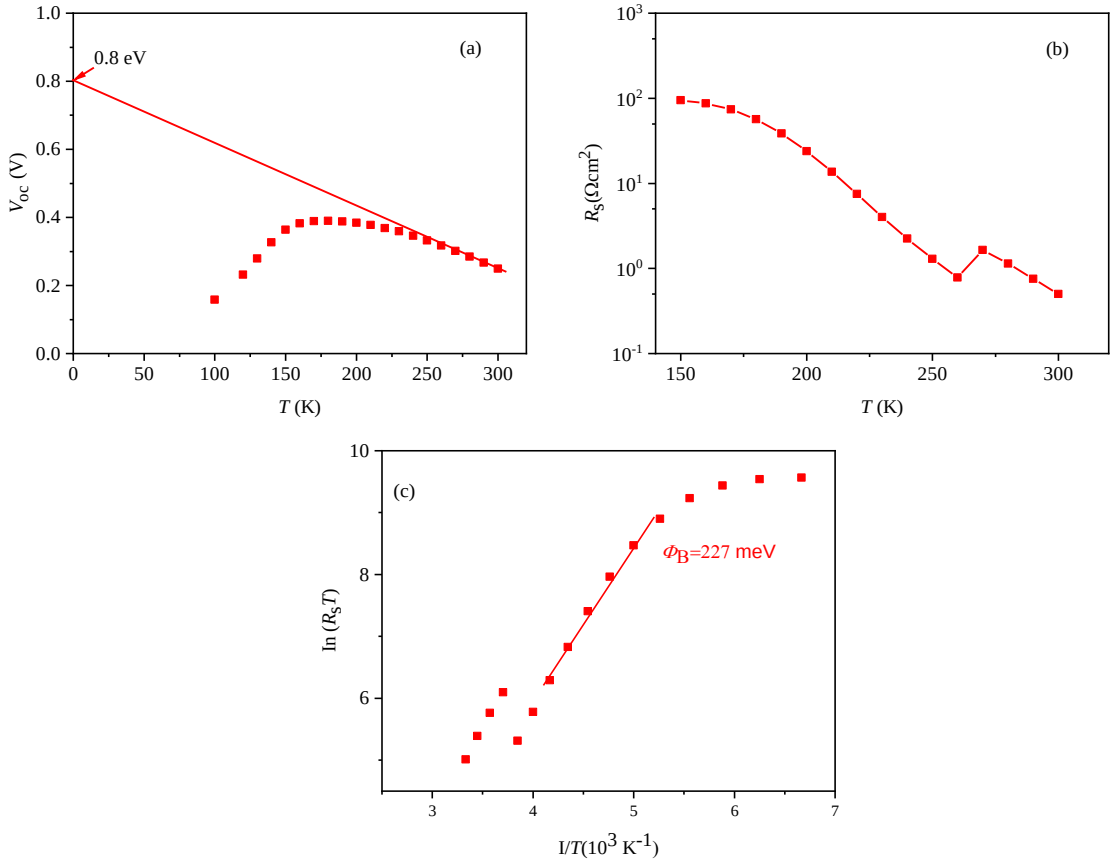

Figure 4.6: (a) Temperature dependence of Voc for the devices from stacked and pre-annealed precursors (b) Temperature-dependent dark series resistance and (c) ln(RsT) versus 1/T with corresponding for a stacked, and pre-annealed devices, respectively.

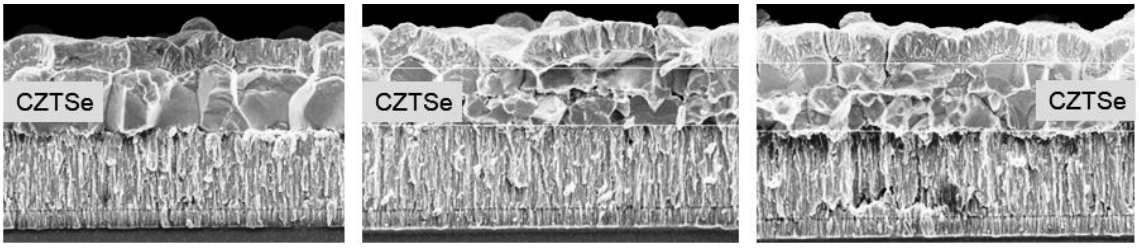

Figure 4.7: SEM cross-sectional images for the CZTSe device prepared from co-evaporated precursors scanned at different spots.

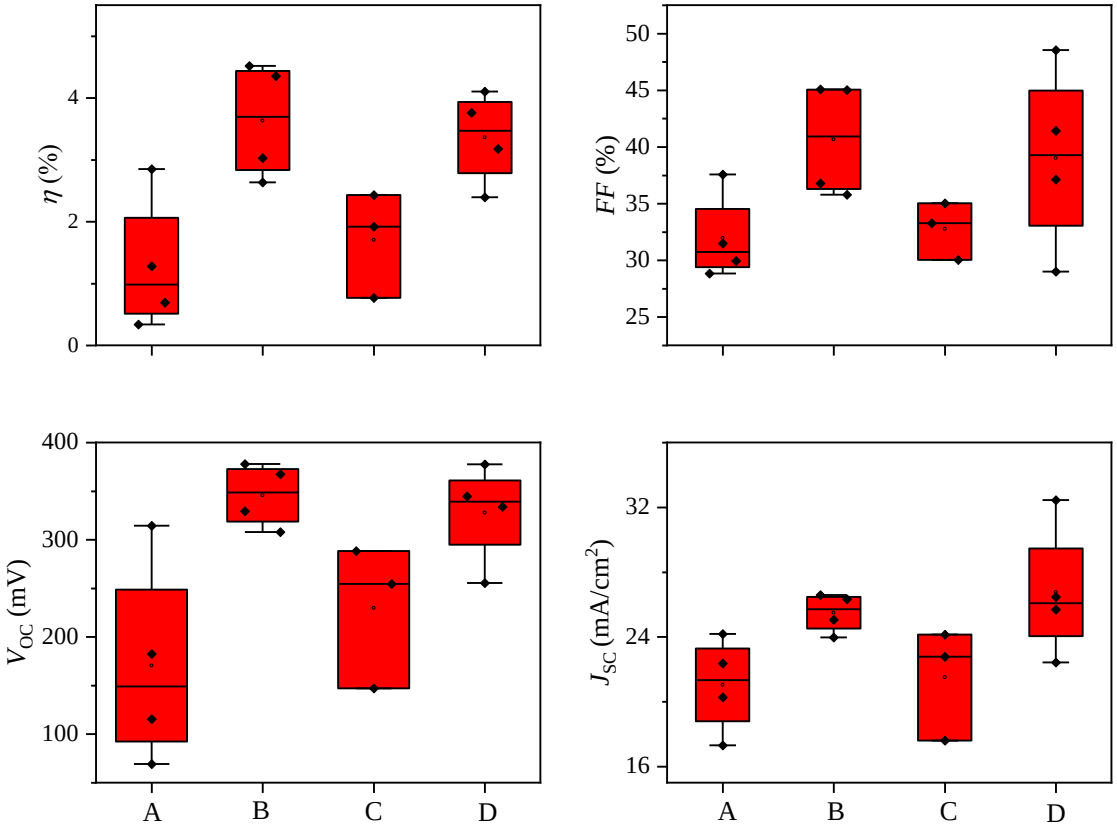

Figure 4.8: Comparison of device performance for the solar cells prepared from different experiments. A, B, C, and D represent experimental no: 1, experimental no: 2, experimental no: 3, and experimental no: 4, respectively.

4.6 Summary

CZTSe solar cells were prepared from low-temperature co-evaporation of Cu-Zn-Sn-Se precursors following selenization in Se + N_2 ambient. The results showed that the CZTSe absorber with larger grain sizes in the order of the film thickness could be demonstrated. However, the performance of this device was limited by the CdS/CZTSe interface recombination, high barrier height, and reproducibility problem. The later prevents further baseline fabrication process optimization.

4.7 Influence of Sn-incorporation during selenization on the CZTSe growth and device performance

4.7.1 Motivation

The CdS/CZTSe interface recombination largely contributes to the high V_{OC}-deficit [5], [36]. This could be attributed to the surface decomposition of the CZTSe absorber. The CZTSe phase decomposition is driven by an instability of the Sn-Se phase [80]. The formation of the Sn-Se (SnSe and $SnSe_2$) phases is very sensitive to the selenium partial pressure (P_{Se}), because of the ability of Sn to change its oxidation states [24], [80]. Low P_{Se} favors the formation of Sn (II), resulting in the decomposition of the $SnSe_2$ phase to the SnSe phase [80]. Following this line of argument, it could be postulated that instability of Se partial pressure during the selenization process may play a critical role in the surface decomposition, consequently limiting the quality of the absorber and device performance. Moreover, we further observed instability in our baseline fabrication process, see Fig. 4.8. Teoman *et al*. [22] demonstrate that it is possible to stabilize the CZTSe baseline process by providing Sn in the graphite box during selenization. Moreover, the higher Se partial pressure could facilitate the formation of the Sn-Se liquid phase at a high processing temperature, resulting in the larger grain growth. Moreover, at high-temperature the $SnSe_2$ liquid phase could act as a chalcogen source (see reaction 4.2), thus stabilizing the Se partial pressure.

$$SnSe_{2(l)} \leftrightharpoons SnSe_{(s)} + Se_{(g)} \qquad 4.2$$

In this section, the effect of Sn incorporation during the selenization of Cu-Zn-Sn-Se precursors on the absorber growth and device performance is investigated in order to find a good measure to stabilize the baseline process. To have better control over the selenization process, Sn wire (diameter 0.25 mm, purity 99.998%) was utilized. This approach was adapted from our project partners, the University of Oldenburg and ref. [22]. In order to explore the impact of Sn incorporation during selenization, the amount of Sn was varied by changing the length of Sn wire in the graphite box (see Table 4.5). The final devices are compared to establish optimal growth conditions.

4.7.2 A study on the CZTSe absorber morphology and minor phases

To evaluate the influence of Sn incorporation on the absorber growth, the SEM image of the complete devices was acquired and compared. As can be seen in Fig. 4.9, the Sn incorporation slightly influenced the size of the grains and the quality of the CZTSe/$MoSo_2$ interface. The latter increases with the increase in the Sn amount during selenization. Our results are in good agreement with those reported in ref. [24] and from which we suggest that the formation of the $SnSe_2$ liquid phase facilitates the formation of larger grains. The thickness of the CZTSe layer fluctuated in the range of 0.9 to 1 µm, while the $MoSe_2$ thickness remained constant

Table 4.5: Sample preparation parameters

	Precursor growth rate (nm/min)				Selenization conditions				
Sample number	Cu	Zn	Sn	Se	Length of Sn (cm)	Mass of Se (mg)	Heating rate (°C/min)	Selenization temperature (°C)	Selenization time (min)
AA0200-4	1.4	1.3	2.2	3.7	0	200.5	40	540	10
AA0200-1	1.4	1.3	2.2	3.7	4	200.9	40	540	10
AA0200-2	1.4	1.3	2.2	3.7	6	198.9	40	540	10
AA0200-3	1.4	1.3	2.2	3.7	8	198.4	40	540	10
AA0199-1	1.4	1.3	2.2	3.7	10	200.3	40	540	10

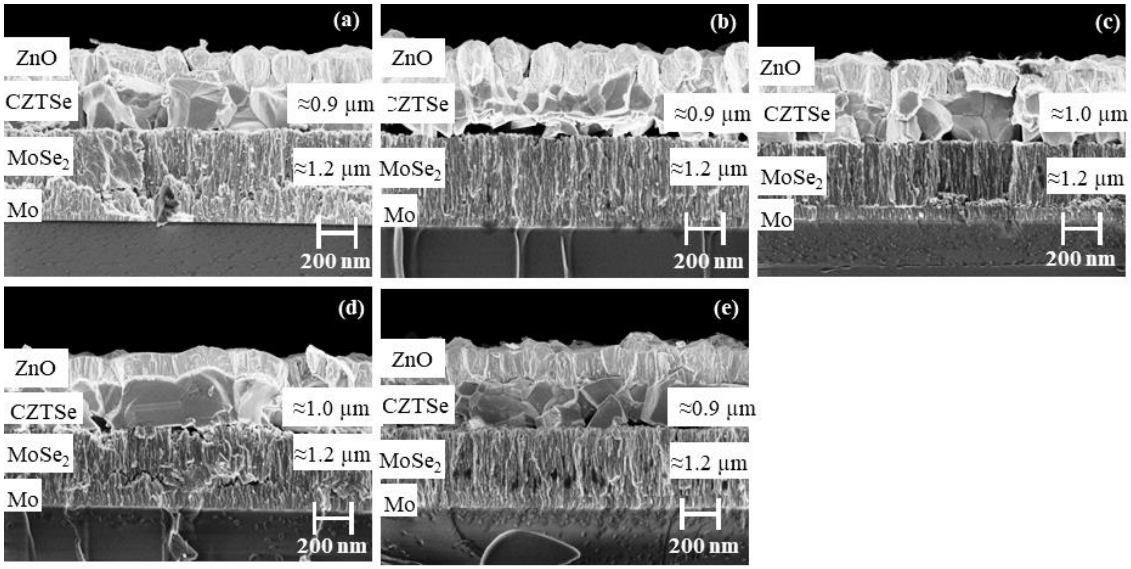

Figure 4.9:Cross-sectional SEM images of CZTSe absorbers prepared from (a) 0 cm, (b) 4 cm, (c) 6 cm, (d) 8 cm, and (e) 10 cm of Sn wire added during selenization of co-evaporated precursor, respectively.

Concerning to dependencies of the minor phase on the amount of Sn wire added during selenization, the micro-Raman measurement was taken using 785 nm red laser excitation, see fig 4.10. The Raman spectra of all samples exhibit the A1 vibrational mode at 173 cm^{-1}, 195 cm^{-1} and that of E1 and B1 at 233 cm^{-1} and 245 cm^{-1}, respectively, corresponding to CZTSe phase. Interestingly, the fingerprints of Sn-Se or Cu_2SnSe_3 phases were not found in our Raman results. It should be noted that due to the sensitivity of the Raman system using a red laser excitation (785 nm), the signature of the ZnSe phase cannot be detected. Thus, the shorter excitation wavelength would be needed to detect this phase.

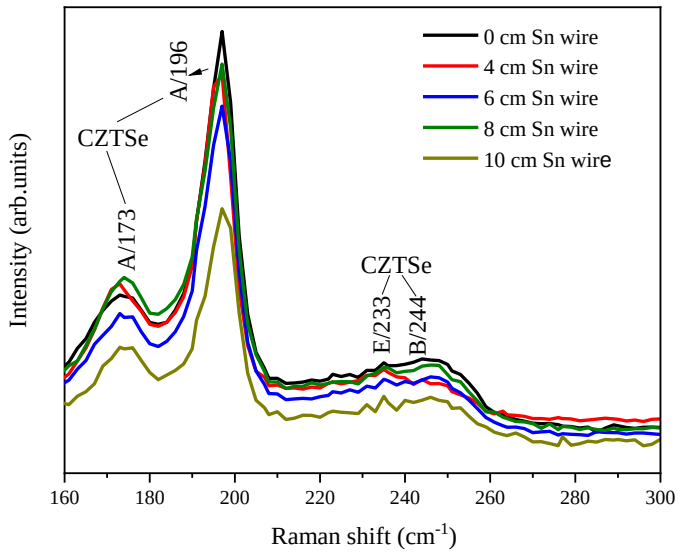

Figure 4.10: Raman scattering spectra of the CZTSe absorber selenized with different amount of Sn

4.7.3 A study on solar cell performance

After investigating the impact of Sn incorporation on the structural properties of the CZTSe absorber, we now assess its influences on device performance. For this purpose, the dark and illuminated *J–V* characteristics of the various devices prepared from different amounts of Sn were measured and analyzed. In Fig. 4.11, the *J–V* curves of the champion solar cells on the five samples prepared with different amounts of Sn during selenization are shown. The corresponding parameters of the solar cells are presented in Table 4.6 and the box plot in Fig. 4.12. As can be observed in Fig 4.11 and Table 4.6, the *J–V* curves and solar cell parameters were strongly influenced by the amount of Sn added during selenization. The reference sample (without Sn in the graphite box) yielded a maximum η of 5.8 % with a V_{OC} and *FF* of 342 mV and 55 %, respectively. For the case of 6 cm of Sn wire in the graphite box, η increased up to 6.9 %. This improvement mainly results from a significant increase in V_{oc} (from 342 mV to 374 mV). Increasing the amount of Sn beyond 6 cm leads to a poorer device performance with η dropping from 6.9 % (6 cm of Sn) to 5.8 % (10 cm of Sn), see Table 4.6. A similar trend can be seen in V_{OC}, *FF*, and J_{SC}. Considering the R_P of the devices (increased from around 840 Ωcm^2 (reference sample) to 2733 Ωcm^2 (4 cm of Sn) and 968 Ωcm^2 (6 cm of Sn), then decreased to 106 Ωcm^2 (10 cm of Sn)). As it can be seen in Table 4.6, Sn incorporation seems not to significantly impact the J_{SC} of the devices.

Concerning the *n*, both devices exhibited the value higher than 2 indicates the fact that the solar cell somewhat deviates from the ideal case and unusual recombination is unfortunately present. This aspect will be addressed later on in this section.

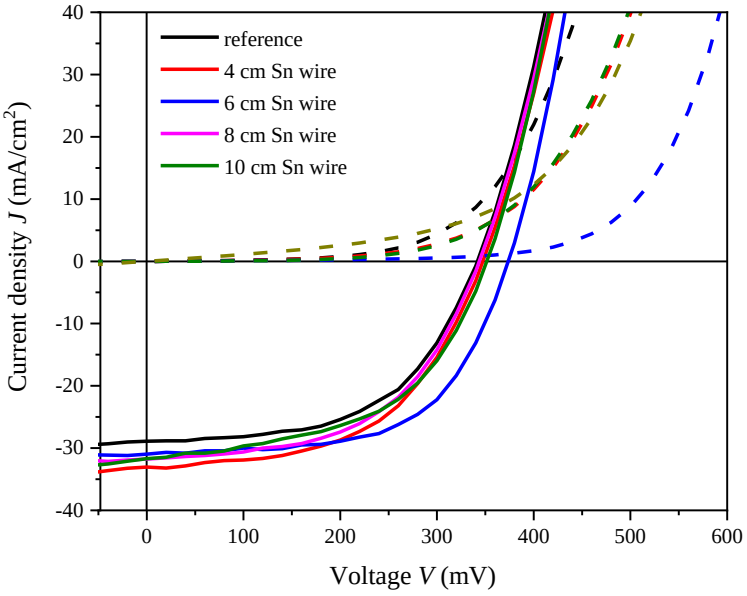

Figure 4.11: Comparison of the dark and illuminated J–V curves for the champion solar cells fabricated from different amounts of Sn added during selenization.

Table 4.6: Solar cell parameters of CZTSe solar cell prepared from absorber selenized with different amount of Sn in the graphite box

Length of Sn wire (cm)	η (%)	*FF* (%)	V_{OC} (mV)	J_{SC} (mA/cm^2)	R_S (Ωcm^2)	$R_{P\text{-}dark}$ (Ωcm^2)	*n*
Reference (0 cm Sn)	5.4	55	342	29	2.5	840	3.1
4	5.8	53	344	31	2.3	2733	2.0
6	6.9	60	374	31	2.0	968	2.3
8	6.2	53	348	32	2.2	764	3.4
10	5.8	52	351	30	2.4	106	3.6

After assessing the influence of the Sn amount added during selenization on the solar cell performance for the champion solar cells, we now compare the solar cell parameters η, V_{OC}, J_{SC}, FF, R_S, and R_P for all devices as shown in Fig 4.12. It is evident that solar cells prepared from 6 cm of Sn were generally superior in performance relative to the other samples. It demonstrated that η fluctuates from 6.6 to 6.9 % corresponding with V_{OC}, J_{SC}, and FF of 365 to 374 mV, 32 to 31 mA/cm^2, and 5 to 60 %, respectively. While for devices prepared from 8 cm and 10 cm of Sn demonstrated the η from 5.9 to 6.2 % and 4.9 to 5.8 %, respectively. The V_{OC} and FF of these devices fluctuated from 343 to 348 mV, 52 to 53 % and 304 to 351 mV, 43 to 52 % for 8 cm and 10 cm of Sn, respectively. Regarding the solar cells prepared from 4 cm of Sn, η fluctuated from 4.9 to 5.8 % while the V_{OC} and FF stayed above 320 mV and 48 %. The J_{SC} of all devices in this series stayed above 29 mA/cm^2, confirming that this parameter is not strongly influenced by the amount of Sn added during selenization. Considering the R_P of the solar cells, devices from the reference sample exhibited a R_P in the range from 502 to 840 Ωcm^2 while that from 4 and 6 cm of Sn wire demonstrated R_P in the range from 1201 to 2733 Ωcm^2 and 461 to 968 Ωcm^2, respectively. On the other hand, R_P of the devices from 8 and 10 cm of Sn fluctuated from 663 to 764 Ωcm^2 and 64 to 106 Ωcm^2, respectively. Judging on the statistics of R_P, it is evident that the quality of absorber decreases with the further addition of Sn during annealing. Based on these findings, we concluded that 6 cm of Sn in the graphite box is enough to substantially stabilize the annealing steps. However, the device fabricated under this condition is characterized by a strong cross-over (occurs at 1.0 mA/cm^2) between illuminated and dark curves. Thus, this sample will be selected to study the nature of the recombination mechanism.

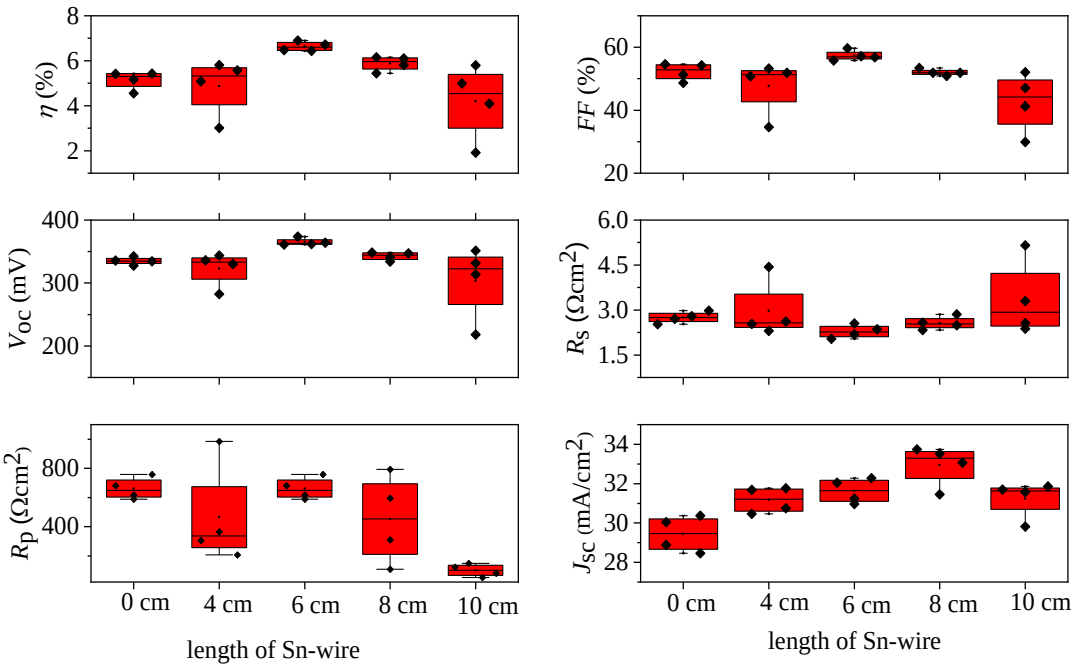

Figure 4.12: Comparison of the device performance for the solar cells fabricated from different amounts of Sn during selenization.

To understand the nature of the recombination mechanism in the devices, *J-V-T* characteristics of the champion CZTSe solar cell prepared from the CZTSe absorber selenized with 6 cm of Sn wire with that from the reference sample. Fig 4.13 (a) illustrated the dependence of V_{OC} and temperature, as can be seen, its linearity behavior strongly influenced by the amount of Sn added. The reference sample shows a similar trend as reported in section 4.1.2. On the contrary, the sample prepared from 6 cm of Sn, from 180 K the V_{OC} deviated from the ideally expected linear behavior. The linear extrapolation to 0 K provides E_A = 0.78 and 1.01 eV for reference sample and sample prepared from 6 cm of Sn wire, respectively (see Fig. 4.13(a)). The reference sample demonstrates a lower E_A compared to the bandgap extracted from electroreflectance measurement (Fig. 4.6 (a)), revealing that the CdS/CZTSe interface recombination strongly influences the device performance as reported in section 4.1.2. On the other hand, the device prepared from 6 cm of Sn wire demonstrated an E_A equal to the bandgap, revealing that bulk Schottky Read-Hall (SRH) recombination is the dominant recombination mechanism and CdS/CZTSe interface recombination is significantly suppressed. It suggests that incorporation of 6 cm of Sn wire during selenization strongly circumvent surface decomposition of CZTSe, thus suppress the formation of unwanted defects that are expected to enhance the CdS/CZTSe interface recombination.

As demonstrated in Fig 4.13 (b), the dark R_S of the devices increased exponentially with decreasing temperature in the range between from 300 K to 170 K. A similar trend can be seen in section 4.1.4 and in ref. [116]. As proposed in section 4.1.4, this behavior is attributed to the presence of a back contact blocking (Schottky) barrier or carrier freeze-out effect due to the lack of shallow acceptors in the CZTSe layer [64], [116]. Using equation 4.3, a fit from a plot of ln($R_S T$) versus 1/T (see Fig. 4.11 (c)) yielded Φ_B = 214 and 142 meV, suggesting that Sn incorporation somewhat reduces the Φ_B. However, Φ_B obtained from this study is still higher compared to those reported in the literature (see table 4.3).

4.7.4 A study on the process reliability and reproducibility

Following the demonstration on the influence of Sn incorporation during selenization on the absorber morphology and device performance, now reliability and reproducibility of the baseline process were seriously examined. For this task, solar cell performance four samples from different runs were fabricated and compared. Fig. 4.14 displays a comparison of four devices prepared from different runs. Comparing these devices, the performance was nearly the same on each run. The devices from run no. 1 demonstrated an average η of 6.6 %, corresponding to the average $V_{OC,}$ $j_{SC,}$ and *FF* of 390 mV, 32 mA/cm^2, and 53 %, respectively.

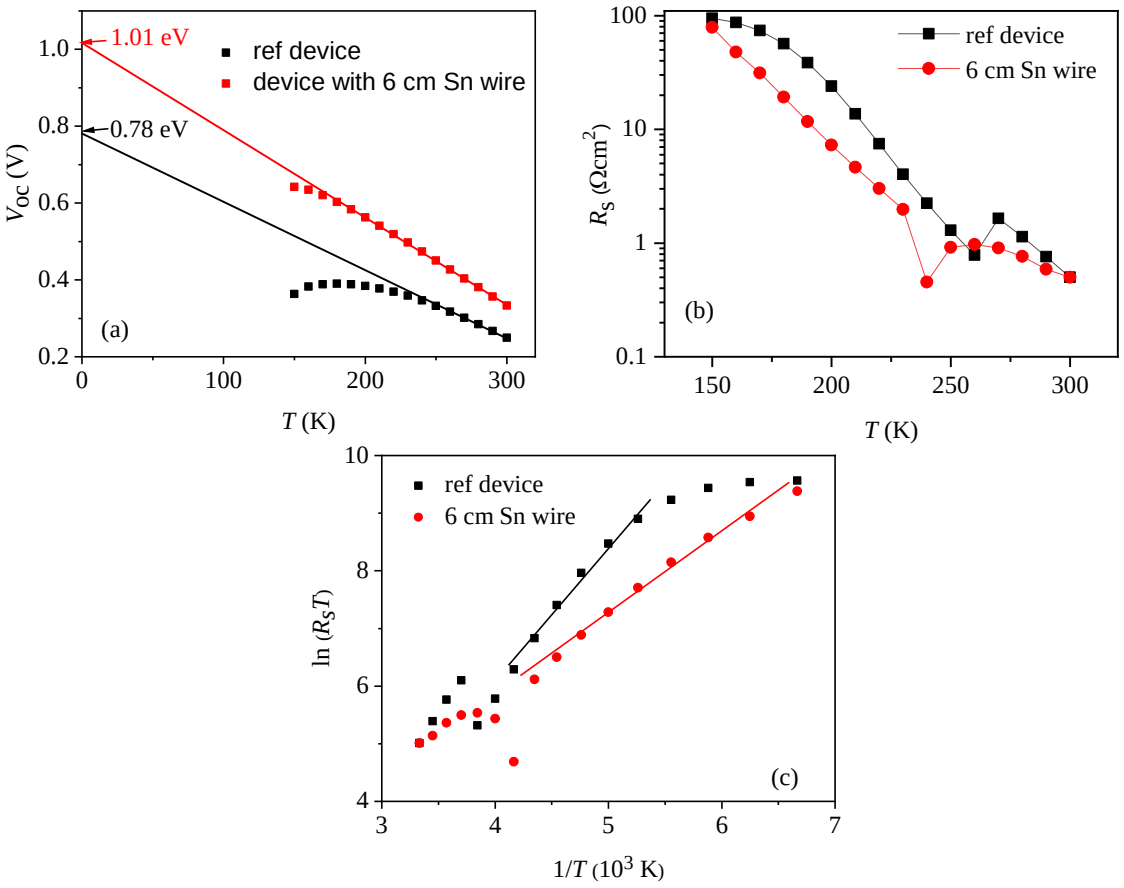

Figure 4.13: (a) Temperature dependence of Voc for the devices from stacked and pre-annealed precursors (b) Temperature-dependent dark series resistance and (c) ln(RsT) versus 1/T with corresponding for a stacked, and pre-annealed devices, respectively.

The R_P of this device fluctuated from 2855 Ωcm^2 to 5269 Ωcm^2 (with an average value around 4197 Ωcm^2) while the R_S is around 3.5 Ωcm^2 on average. A similar trend was obtained on the sample prepared from run no. 2 and 3. The sample prepared from run no. 4 demonstrated a lower average η (6.7 % best cell (5.4 % on average) corresponding to V_{OC} and FF of 55 % (51 % on average) and 384 mV (336 mV, on average), respectively) relative to the sample from run no. 1-3. It should be noted that a similar glass tube and graphite box was used to prepare samples in sections 4.1. and 4.2, thus contamination could be expected and in some way reduces the quality of the absorber, resulting in more fluctuation in the device performance. Although many aspects of the fabrication process have been improved when adopting our proposed measure, extra effort is required to reduce the relatively high value of R_S, which is a main negative factor impacting the performance of the devices. Thus, a continuing optimization of background pressure can be expected to further improve device performance.

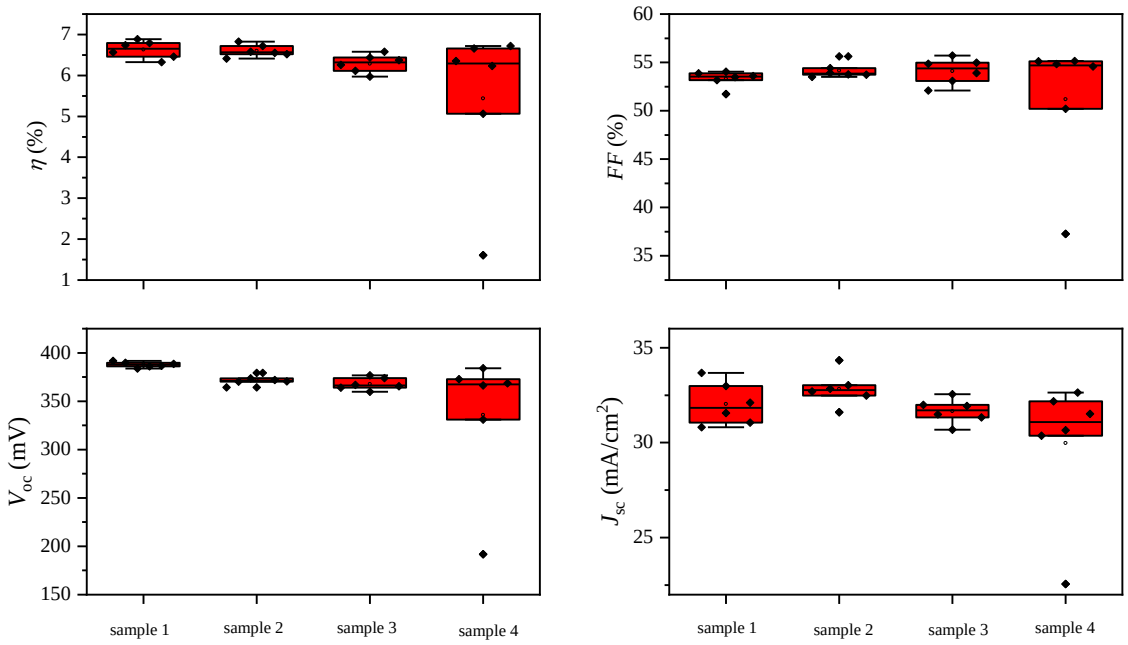

Figure 4.14: Comparison of the device performance for the solar cells prepared from different experiments.

4.7.5 Summary

In this section, we demonstrated that the incorporation of Sn during selenization can substantially suppress the CdS/CZTSe interface recombination and partially reduce the barrier height at Mo back contact. The highest solar cells efficiencies could be demonstrated when 6 cm of Sn wire is incorporated in the graphite box. This length was adapted for further baseline optimization. Moreover, this approach showed to be advantageous as it stabilizes our baseline fabrication process. However, a thicker $MoSe_2$ was detected.

4.8 Influence of initial N_2 background pressure during selenization on the CZTSe growth and device performance

4.8.1 Motivation

It is often postulated that V_{OC}-deficit in kesterite solar cells originates from its interfaces (front and back interfaces) or from the bulk material. The latter could be significantly suppressed by Sn incorporation as demonstrated in section 4.2. Many studies further associated this with the band tail (due to electrostatic potential fluctuations) which was directly linked to structural defects in the absorber (existing of secondary phases in the bulk of the material and Cu/Zn disorder [17], [24], [92]. However, it has been demonstrated that Cu–Zn disorder does not significantly alter the room temperature V_{OC} of the solar cell [54], although it can significantly deteriorate the device performance [54]. Gang *et al* demonstrated experimentally the impact of the initial background pressure on the band tail at room temperature. An increase in the initial background pressure from 400 mbar to 500 mbar leads to a drop of the band tail from 110 meV to 10 meV. As a result, a device with η up to 11.7 % can be obtained. Gao *et al*. discussed the impact of N_2 background pressure on the quality of the CZTSe absorber [12]. The size of the grain and thickness of $MoSe_2$ increases with the increase in the N_2 background pressure. In this consideration, in this section, the relationship between the initial N_2 background pressure during the selenization of the Cu-Zn-Sn-Se precursor on the absorber growth and device performance was examined with the motivation to optimizing the baseline process. The initial N_2 background pressure was systematically varied by controlling the N_2 refill level in the tube furnace as shown in Table 4.7.

Table 4.7: Selenization parameters

	Selenization conditions					
Sample number	Length of Sn (cm)	Mass of Se (mg)	Heating rate (°C/min)	Selenization temperature (°C)	Selenization time (min)	N_2 background pressure (mbar)
AA0221-7	6	200.5	40	540	10	10
AA0221-6	6	200.9	40	540	10	50
AA0205-7	6	198.9	40	540	10	100
AA0205-6	6	198.4	40	540	10	150
AA0205-8	6	200.3	40	540	10	200

4.8.2 A study on the CZTSe absorber

Firstly, the impact of N_2 background pressure on the formation of the CZTSe absorber by characterizing the structural and morphological properties of the absorber selenized under different pressures was explored. As it can be observed in Fig 4.15(a), there was no correlation between N_2 background pressure and structural properties because CZTSe absorbers demonstrated similar XRD patterns. No secondary phases related to either Cu-Se or Sn-Se phase were found. These observations suggest that N_2 background pressures do not deteriorate the quality of CZTSe absorbers.

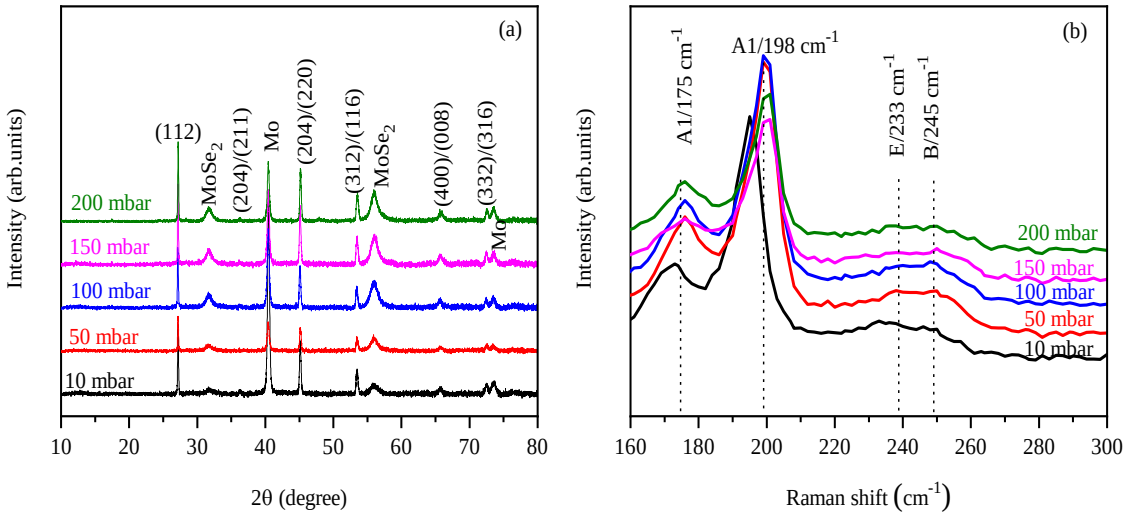

Figure 4.15: (a)The XRD pattern and (b) Raman spectra of the CZTSe absorber prepared at different N2 background pressure, respectively.

Further, the strong correlation between the intensity of the XRD peak related to $MoSe_2$ and N_2 background pressure was obtained. As the N_2 background pressure increases, the XRD peak related to $MoSe_2$ becomes more and more obvious. It is strongly indicated that Se partial pressure is always in direct proportion to the N_2 background pressure—thus, Se reacts with Mo to form $MoSe_2$. Based on this finding, we postulated that the formation of $MoSe_2$ strongly depends on the N_2 background pressure. Further conclusive information on the CZTSe phases was retrieved from Micro-Raman spectroscopy measurements with the excitation laser source 785 nm implemented on the all CZTSe absorber types. As depicted in Fig 4.15 (b), all CZTSe absorbers exhibit A1 vibrational mode at 171 cm^{-1}, 195 cm^{-1} and E mode at 233 cm^{-1} and B mode 245 cm^{-1}, but no evidence for the pure CZTSe phase exists.

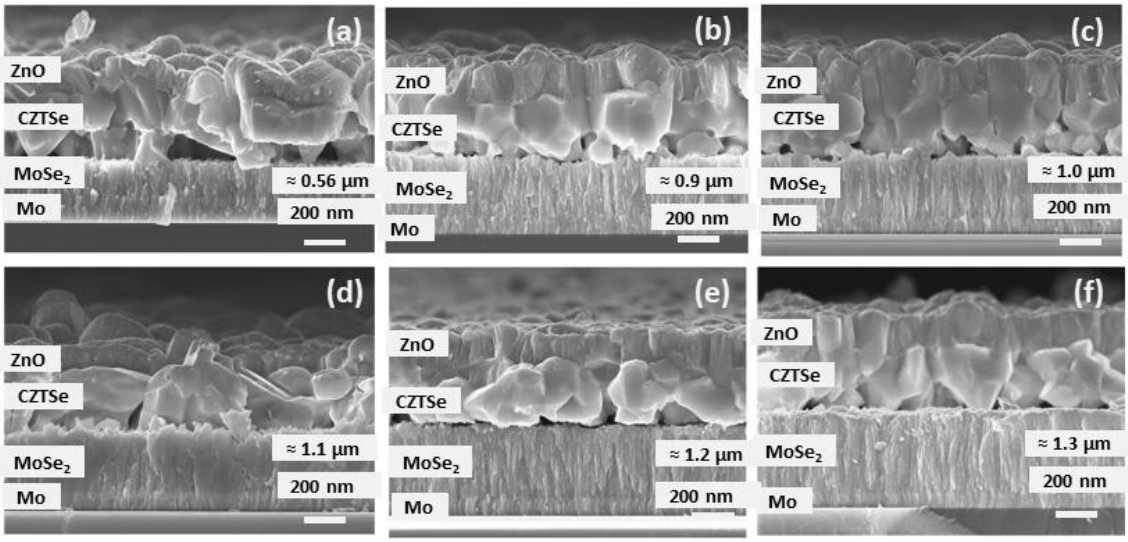

Figure 4.16: Cross-sectional SEM images of CZTSe absorbers prepared from (a) 10 mbar, (b) 50 mbar, (c) 100 mbar, (d) 150 mbar, and (e) 200 mbar of N2 background pressure.

Fig. 4.16 shows cross-sectional SEM images for the CZTSe absorber prepared from different N_2 background pressure levels. The N_2 background pressure significantly influenced the absorber quality and the CZTSe/$MoSe_2$ interface quality. The CZTSe absorber, prepared at 10 mbar demonstrated bilayered morphology, consists of larger grain sized and void at the back $MoSe_2$/CZTSe interface. Obviously, the increment in the N_2 background pressure resulted in the single-layered structure with larger grain compared to the samples prepared at the pressure of 10 mbar. Our results are consistent with that reported by Gao *et al* [12]. Together with the information found in ref [12], [17], our findings assure that the N_2 background pressure strongly impacts the Se partial pressure. As illustrated in Fig. 4.16, the thickness of $MoSe_2$ increased from around 0.6 µm to 1.3 µm when the N_2 background pressure increased from 10 mbar to 200 mbar. This observation was in good agreement with XRD results (see Fig 4.15).

4.8.3 A study on solar cell performance

Our previous argument emphasized the fact that tailoring the N_2 background pressure can enhance the device's performance. To confirm this, solar cells with the absorber selenized at different N_2 background pressure was examined. Fig. 4.17 shows a box plot of the device parameters including η, FF, V_{OC}, J_{SC}, R_S, and illuminated R_P. The devices with the absorber selenized at an N_2 background pressure of 10 mbar demonstrated the η up to 3.9 % on average. Increasing the N_2 background pressure to 50, 100, and 150 mbar resulted in η of 5.4 %, 6.9 %, and 7.1 % on average, respectively. The N_2 background pressure beyond 150 mbar resulted in the η of 6.1 %. The sample prepared at 50 mbar exhibits more fluctuation as compared with other devices. When the N_2 background pressure varied in the scale from 10 mbar to 150 mbar, the higher the N_2 background pressure, the larger the average V_{OC}, FF, and R_P. However, further,

increase the N_2 background pressure beyond 150 mbar breaks down this relationship and in fact ensuing the falling down of the average V_{OC}, *FF*, and R_P. Judging from the SEM image (see fig. 4.16) it is not surprising to observe such a trend as the morphology quality significantly improves with the increase in the N_2 background pressure. It could be expected that high N_2 pressure leads to the high Se partial pressure, resulting in the formation of the Sn-Se and Cu-Se liquid phases which enhances elemental diffusion during selenization [12].

Surprisingly, a higher N_2 background pressure depressed down the value of the J_{SC}. A possible explanation is that the increase in the N_2 background pressure ameliorates the surface roughness and eventually improves the absorption [24]. There was no evidence that N_2 background pressure altered the R_S of the devices. However, $MoSe_2$ thickness significantly increased in the direct proportion to the N_2 background pressure (see fig. 4.16). Therefore, the origin of the high R_S in our devices is still obscure.

Considering the dark and illuminated *J-V* curves of the champion solar cell obtained in this series, we observed a strong cross-over (3.1 mA/cm^2) between the dark and illuminated curve. This strongly suggests that there is a block layer either at the front interface or at the back interface as proposed in section 4.1.3. This aspect will be addressed later on in this section. The champion solar cell demonstrated a V_{OC}-deficit of 663 mV which is somewhat higher than the word recorded value on the pure-Se-kesterite solar cell [16]. The high V_{OC}-deficit in this study can be linked to the recombination loss at either in the CdS/CZTSe or CZTSe/$MoSe_2$ as it is supported by the strong cross-over between dark and illuminated curve (see Fig. 4.18 (a)).

Moreover, the value of *n* for the champion solar cell stayed above 2, strongly indicating an unusual recombination mechanism as proposed in section 4.1.3. To address this aspect we perform the EQE measurement on the champion solar cell (see fig 4.18 (b)). The EQE of this cell reached a maximum of 89 % at a wavelength of 535 nm. However, it is a bit lower than that reported in the literature [20], [27]. In a shorter wavelength range, an absorption loss was observed. It could be related to the CdS layer. It is reported that the decrease in the buffer layer thickness, equivalent to utilizing a higher bandgap buffer layer, can enable the further improvement in the EQE at lower wavelength region [20].

Further, the EQE showed a rapid decreased in a longer wavelength, indicating the decrease in the probability of charge collection which could be related to the recombination in the absorber bulk or at the CZTSe/$MoSe_2$ interface. One should be aware that the peak obtained in room temperature PL measurement is not the true value of the energy bandgap. In fact, the room temperature PL measurement was carried out on the champion solar cells. As presented in Fig. 4.18 (d), the device demonstrates the PL peak at 1.0 eV which is 70 meV below the bandgap (1.06 eV) extracted from the EQE measurement. This shift could be associated with the band tailing in the CZTSe absorber [17], [20].

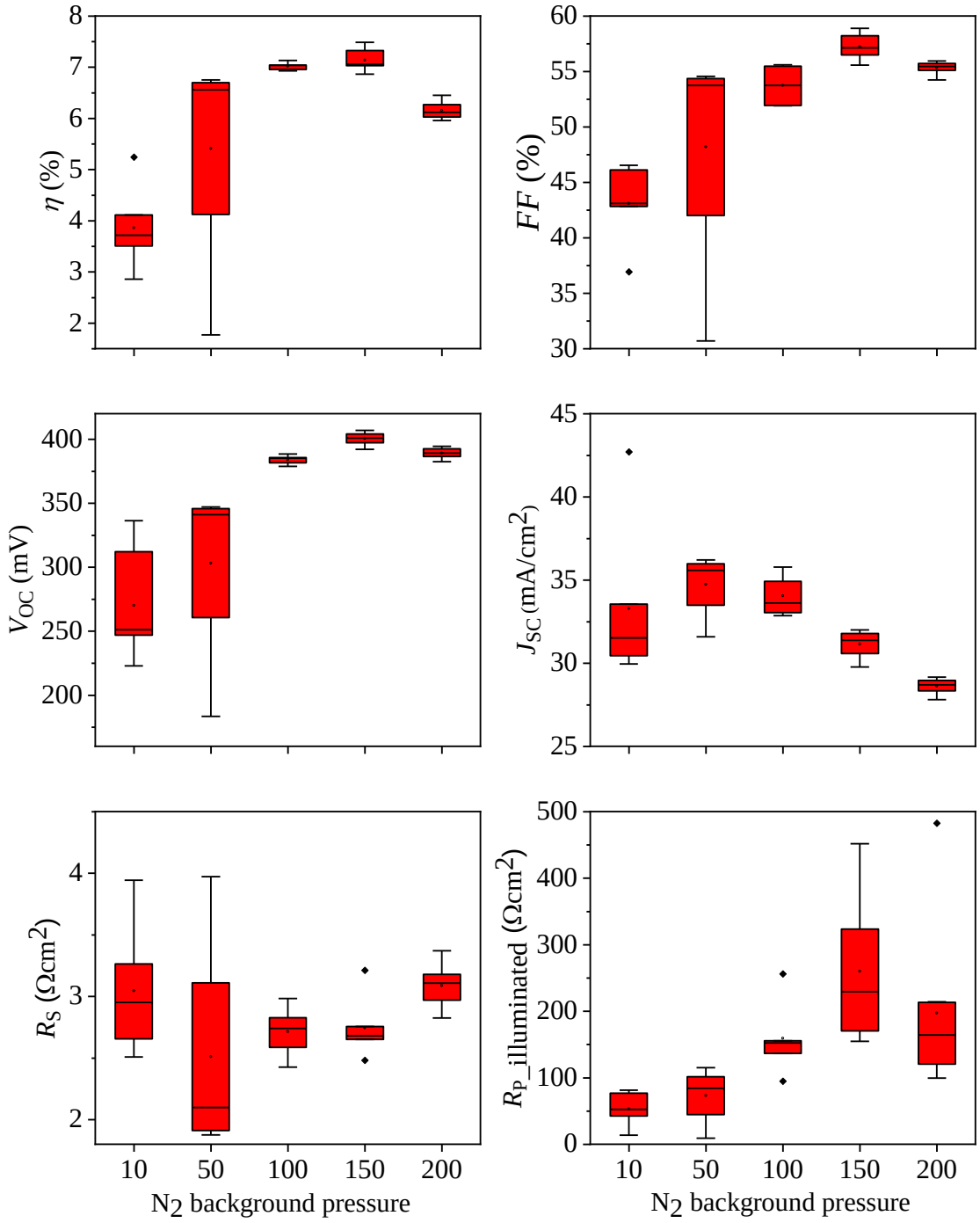

Figure 4.17: Comparison of the device performance for the solar cells prepared from the N_2 background pressure.

The *J-V-T* measurement has been also performed on this sample to discover the nature of the recombination mechanism. Looking at the dependence of V_{OC} on temperature, as it is expected, the device demonstrated a similar behavior like that in section 4.2.3, the V_{OC} slightly deviated from its linearity behavior at a lower temperature.

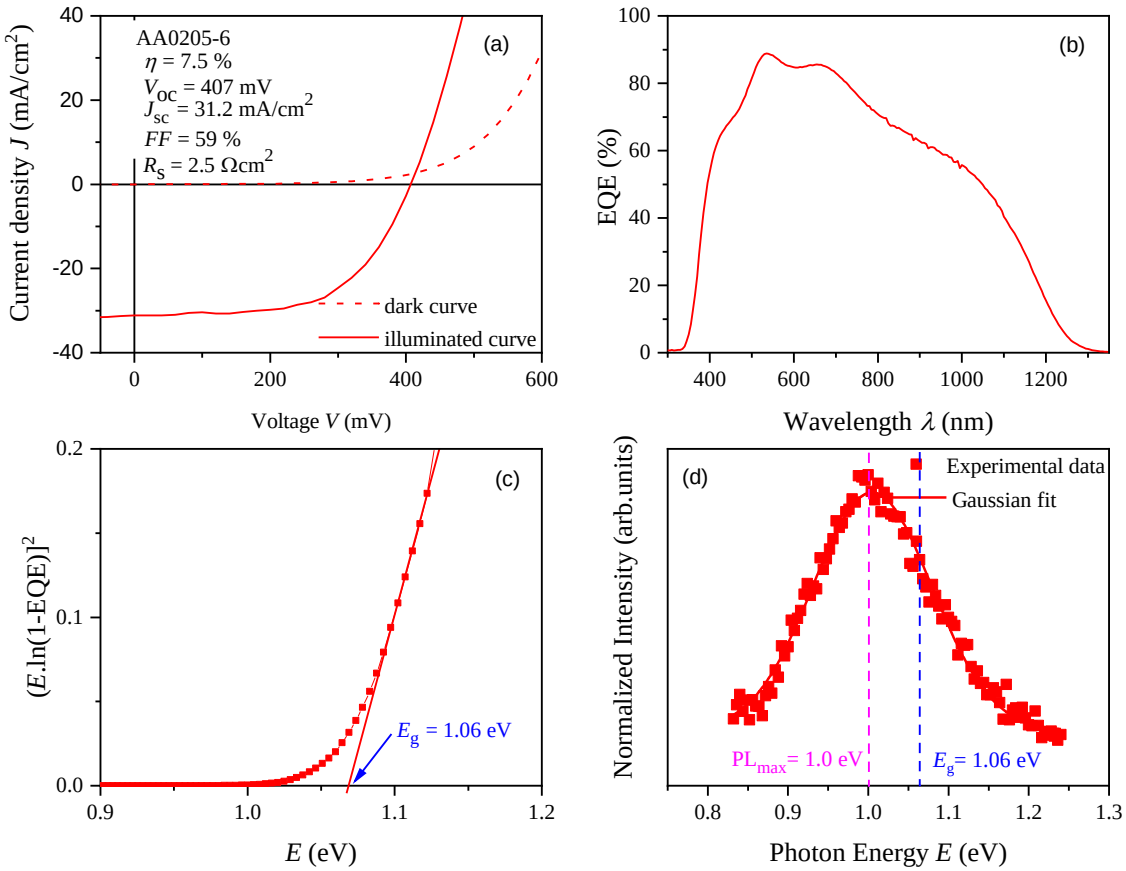

Figure 4.18: (a) J–V curve, (b) the external quantum efficiency (EQE) of a similar device (c) bandgap estimated by $[E \cdot \ln(1\text{-EQE})]^2$ vs E,, and (d) PL spectrum measured at room temperature corresponding to the best solar cell obtained at an initial background pressure of 150 mbar, respectively.

As can be demonstrated in fig 4.19 (a), the extrapolation to 0 K provides E_A = 1.01 eV which nearly equals the E_g (1.04 eV) extracted from the EQE measurement see Fig 4.18 (c).

Based on these results, it can be concluded that the bulk Schottky Read-Hall (SRH) recombination is the dominant recombination mechanism and the CdS/CZTSe interface recombination is significantly suppressed. The R_s of the devices crudely increased as the temperature decreases. This observation is in good agreement with previous studies in sections 4.1.3 and 4.2.3. The fit from the plot of ln ($R_S T$) versus 1/T yields Φ_B = 169 meV (see Fig. 4.19 (c)), which is still high as compared to the previous studies (see Table 4.8). Based on our own findings and those reported in [16], [18], [20], [64], it is clear that low current, FF, high R_S and Φ_B could be the main causes limiting the efficiency of our devices.

Table 4.8: Selected best CZTSe solar cell reported in the literature

Absorber	η (%)	FF (%)	V_{oc} (mV)	J_{sc} (mA/cm^2)	R_s (Ωcm^2)	n	V_{OC}-deficit (meV)	Reference
CZTSe[I]	11.95	76.21	432.22	36.28	0.76	N/A	638	[16]
CZTSe	11.7	66.6	423	41.7	0.32	1.56	577	[18]
CZTSe	11.6	67.3	423	40.6	0.32	1.57	577	[19]
CZTSe	11.4	68	443	38.1	0.05	1.2	587	[20]
CZTSe	7.4	59	407	31.2	2.5	2.2	663	This work

N/A no data available
[I]Current world record CZTSe solar cell

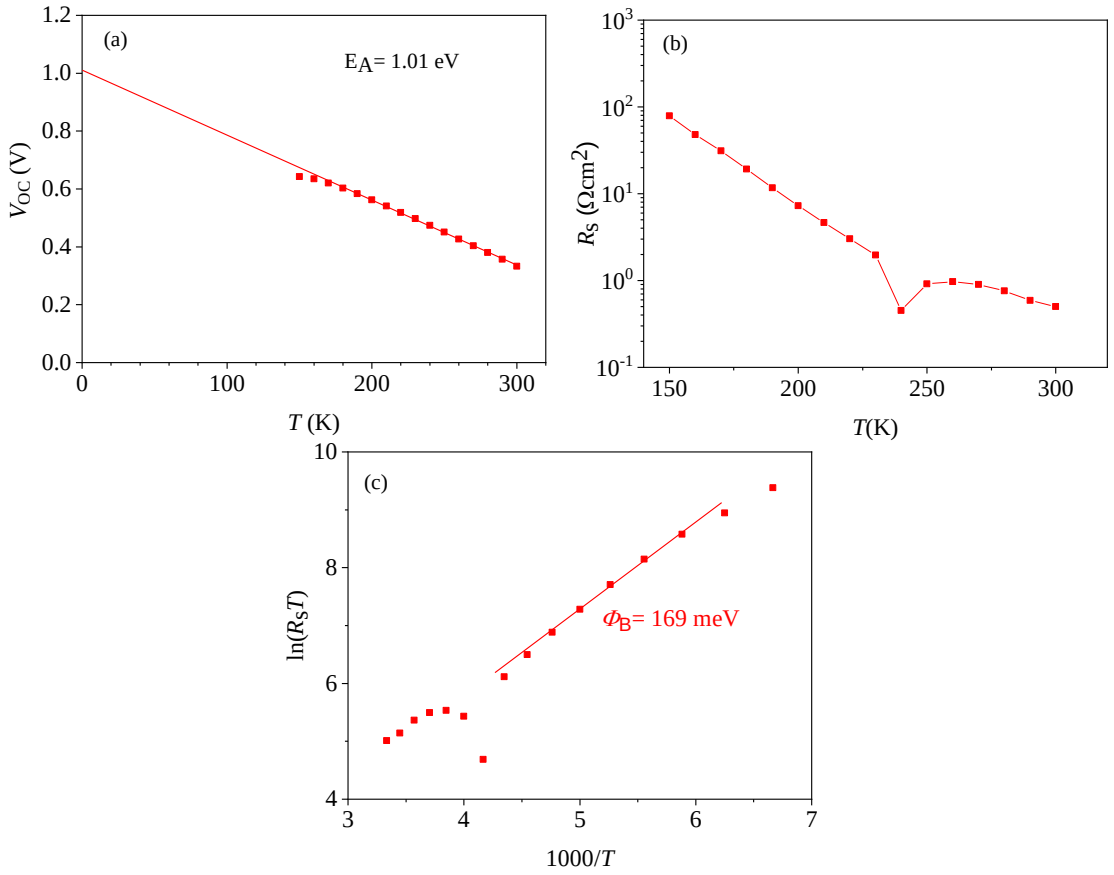

Figure 4.19: (a) Temperature dependence of *V*oc for the devices from stacked and pre-annealed precursors (b) Temperature-dependent dark series resistance and (c) ln(*Rs*T) versus 1/*T* with corresponding for a stacked, and pre-annealed devices, respectively.

4.9 An investigation on the phases transition during selenization of low-temperature co-evaporated Cu-Zn-Sn-Se precursors

As it has been discussed in section 2.1.4.1 that initial precursor composition and configuration strongly impact the CZTSe formation mechanism. Nevertheless, our approach involved low-temperature co-evaporation of Cu, Zn, Sn, and Se, resulting in the Se-poor precursor. This configuration leads to the formation of the precursor layer with a mixture of selenide compounds and metal alloys—thus, it is expected that the CZTSe formation pathway could be somewhat different from the previous reports [59], [65], [72], [80], [82]. To explore this aspect, both phase and morphology evaluations realized during the selenization of co-evaporated Cu-Zn-Sn-Se precursor are systematically investigated. The standard selenization process was interrupted at different temperatures (see Fig. 4.20) and the obtained samples were *ex-situ* analyzed using, the XRD, micro-Raman spectroscopy, SEM, and TEM.

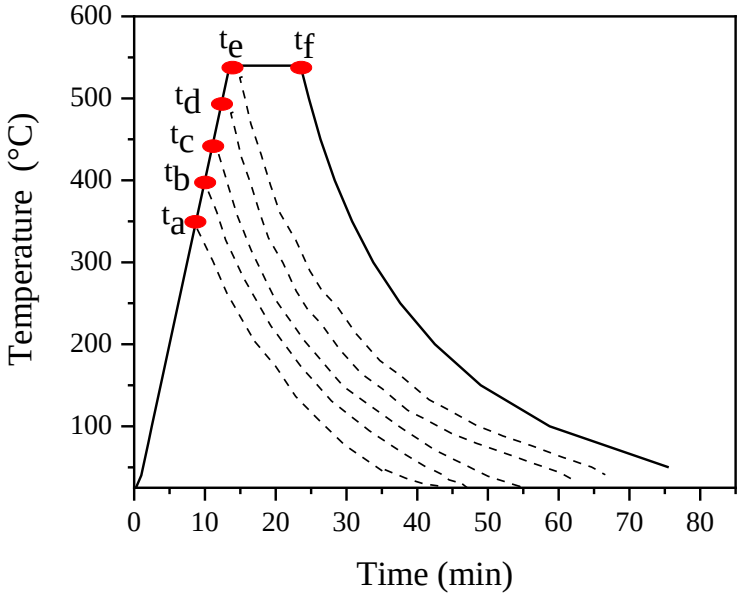

Figure 4.20: Temperature profile during selenization of precursor layers with different interruption temperatures: t_a = 350 °C, t_b = 400 °C, t_c = 450 °C, t_d = 500 °C, t_e = 540 °C, and t_f = 540 °C (10 min) [94].

The material phase composition of the as-deposited Cu-Zn-Sn-Se layer was analyzed by XRD and micro-Raman spectroscopy is presented in Fig. 4.21 (a) and (b) black line. The results demonstrated here are in good agreement with the Cu-Zn-Sn-Se analyzed in section 4.1.1. The film showed to have a mixture of the selenide compounds (CZTSe, $SnSe_2$, and CuSe) and the alloys of the Cu_6Sn_{10} and the Cu_5Zn_8 (see Fig.

4.21 (a)). The micro-Raman spectroscopy measurement on the surface of the film further revealed the existence of a poor crystallinity CZTSe phase as observed in section 4.1.1.

As the precursor annealed to 350 °C (t_a), the XRD pattern displayed peaks of $CuSe_2$, CuSe, $SnSe_2$ as well as those of ZnSe, Cu_2SnSe_2, and CZTSe. Surprisingly, a trace of an elemental Sn at the XRD peak located $2\theta \approx 30.7°$ was found. The detection of selenide compounds and elemental Sn revealed the decomposition of the Cu_6Sn_5 and the Cu_5Zn_8 alloys as proposed in ref. [63].

$$Cu_5Zn_{8(s)} + 18Se_{(g)} \rightarrow 8ZnSe + 5CuSe_{2(s)} \quad 4.2$$

$$Cu_6Sn_{5(s)} + 12Se_{(g)} \rightarrow 6CuSe_{2(s)} + 5Sn_{(l)} \quad 4.3$$

To elicit further information about phase formation at this temperature, the micro-Raman measurement was performed. Amongst detected phases with this technique were the CZTSe phase (at Raman peaks of 192 $cm^{-1}$and 233 cm^{-1}), Cu_2SnSe_3 (at Raman peak of 178 cm^{-1}), $SnSe_2$ (at Raman peak of 183 cm^{-1}), and Cu-Se (at Raman peak of 262 cm^{-1}). The existence of the CZTSe Raman mode at 192 cm^{-1} is an indication of no improvement in the crystal quality of the CZTSe phase at this temperature, while the evolution of Raman peak of 178 cm^{-1} indicates the formation of Cu_2SnSe_3. Raman mode related to ZnSe was not found. The presence of the Cu-Se phase at the surface strongly suggests that Cu out-diffuses to the surface and at the same time Zn atoms move in the bulk of the film. To provide more convincing evidence, cross-sectional and top-view SEM images were acquired, see figs. 4.21 (b1) and (b2). In the case of the top view SEM image, the clusters of fine grains on the surface of the analyzed sample were observed. The cross-sectional SEM image showed a two-layered structure with a 560 nm compact layer on the surface and 580 nm fine porous grains extended to the Mo interface.

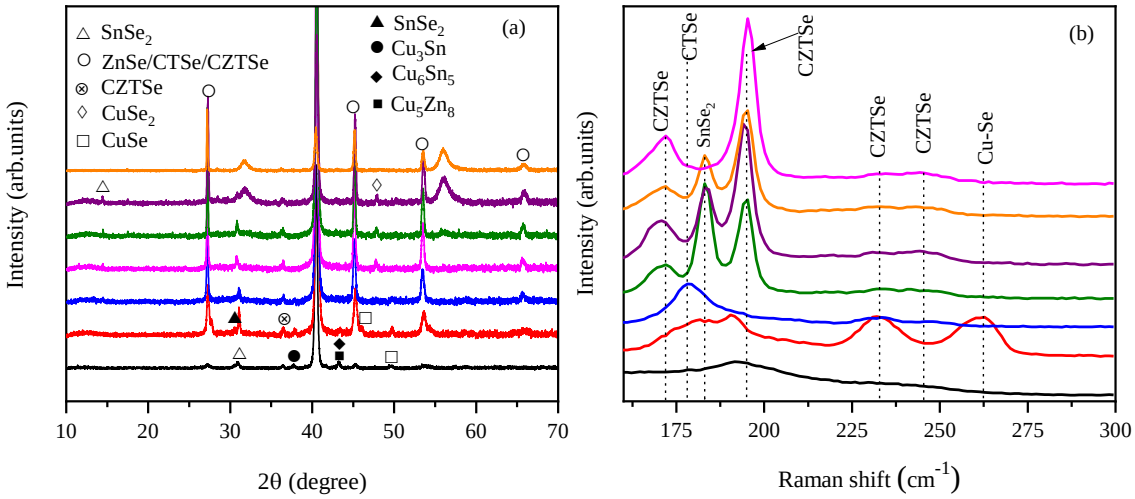

Figure 4.21: (a) XRD patterns of the films when the selenization process was interrupted at different temperatures and (b) corresponding Raman spectra

The STEM-HAADF image and EDXS elemental mapping were taken to further confirm this matter. Fig. 4.22 (a-i) and (an ii-v) presents the cross-sectional STEM-HAADF image and EDXS elemental mapping of Cu, Zn, Sn, and Se, respectively. The cross-sectional STEM-HAADF image showed a good agreement with the cross-section SEM image (see Fig. 4.21 (a-ii)). The upper layer was more compact, while the bottom was more porous. The interface between the two layers is marked by a yellow arrow (see fig. 4.22 (a)). Looking at the EDXS mapping, a clear distinction in the composition was found. The upper layer appeared to be Cu-rich (see Fig. 4.22 (a-ii)), while the bottom layer was Zn- and Sn-rich (see Fig. 4.22 (an iii-iv)), while Se was uniformly distributed across the film.

Interestingly, as the temperature reaches point t_b, the intensity of the XRD peak related to CuSe significantly reduced (see Fig. 4.20 (a) blue line). Raman spectra showed a broad Raman mode at 178 cm^{-1}, which confirms the formation of the Cu_2SnSe_3 phase on the surface as shown in Fig. 4.20 (b) blue line. Moreover, the signature of the Cu-Se phase was not detected in the Raman spectra. Additionally, Raman peaks at 233 cm^{-1} and 242 cm^{-1} were visible, indicating the co-existence of Cu_2SnSe_3 and CZTSe phases. Concerning to morphology, the two layered-structures was still visible (see fig 4.21 (b2)). The upper layer was more compact with a large grain while the bottom part contains numerous pores.

Increasing temperature to the point t_c (450 °C) resulted in the evolution of the XRD peak at $2\theta \approx 47.8°$ which could be assigned to $CuSe_2$. The Raman spectra showed the dominance of vibrational modes at 172 cm^{-1}, 195 cm^{-1}, 233/243 cm^{-1}, and 184 cm^{-1} which corresponded to the CZTSe and the $SnSe_2$ phases, respectively. Concerning to morphology, the two layered-structures was visible (see fig 4.21 (c2)). The top surface SEM image exhibited a mixture of the plate-like crystal (marked by the red arrow) and a larger grain (see fig. 4.21(d1)). Based on the previous studies in [24], [114], the plate-like crystal belongs to the $SnSe_2$ phase. The two-layered structure was observed with large grains and fewer pores at the bottom layer (see fig. 4.22 (d2)). The cross-sectional STEM-HAADF image and EDXS mapping were acquired to provide more knowledge about the material properties of this film. As it appears in Fig 4.22 (b-i), a clear distinction of the two-layered structure was found. The upper layer was more compact while the bottom layer contains numerous pores and fine grains. The interface of the two layers was more porous (denoted with yellow arrow), see Fig 4.22 (b-i)

Concerning the elemental distribution across the film, EDXS mapping revealed that the distribution was fairly homogeneous in the upper layer. We further observed that large spots extended from the layer to the surface of the film (denoted by a white arrow). EDXS composition measurement of that spot revealed it was Cu-rich (34 at %), Sn-rich (20 at %), Se-rich (43 at %), with respect to Zn (1 at %). In contrast, the bottom layer consisted of a numerous number of spots which seemed to have a similar composition as that of the big spot in the upper layer. Interestingly, the interface of the two layers appeared to be Cu-rich with slightly Se-depleted.

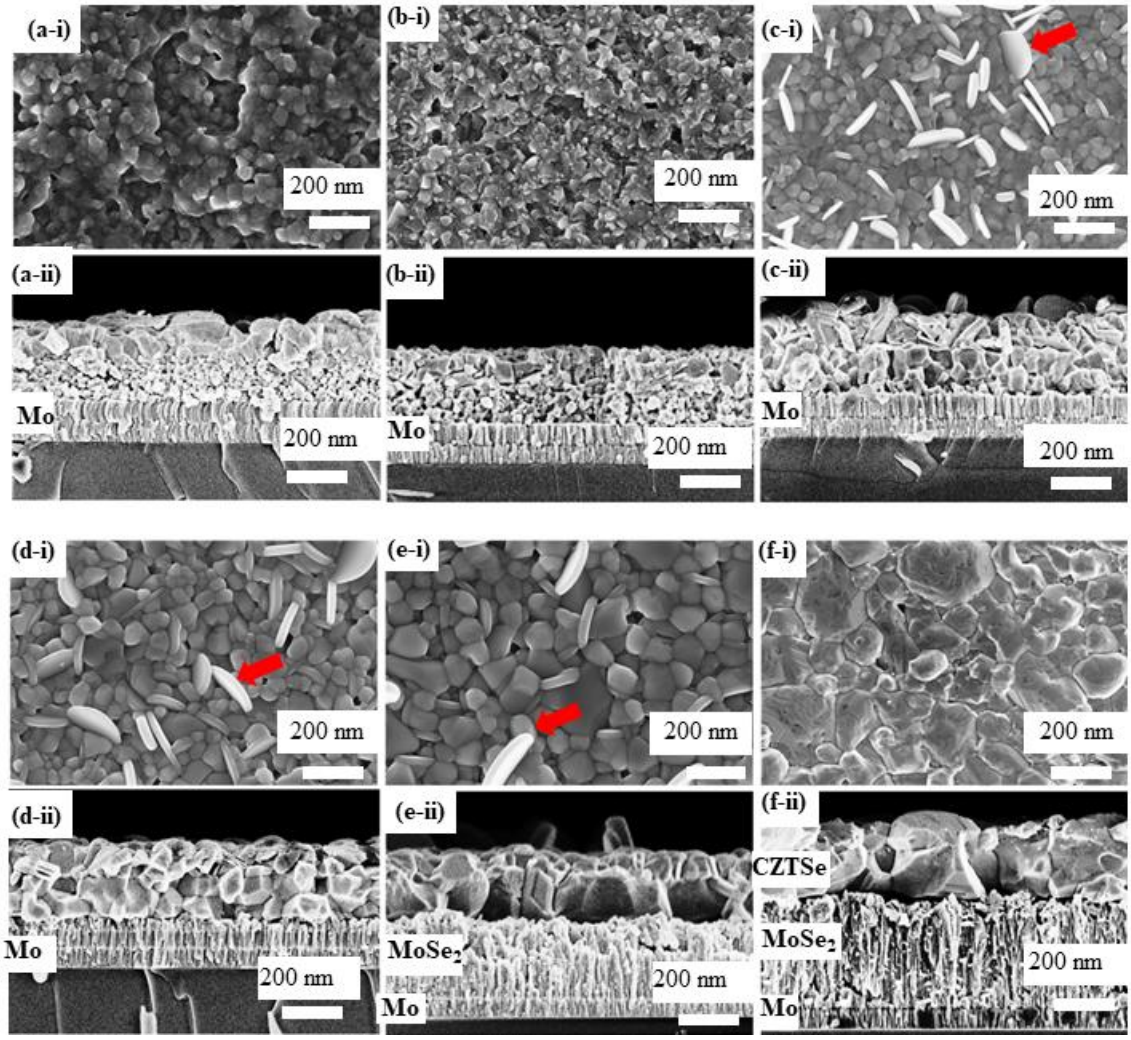

Figure 4.22: ((a-i)-(f-i)) Top-view and ((a-ii)-(f-ii)) cross-sectional SEM images of films prepared when the selenization process was interrupted at different temperatures.

Considering the SEM images, the micro-Raman spectroscopy, XRD measurement together with STEM-HAADF and EDXS mapping at t_a and t_b, it is evident that the binaries phases (Cu-Se and $SnSe_2$) co-existed in the bulk of the film, suggesting that two reaction pathways were competing and resulted into formation of CZTSe phase. Moreover, the confirmation of the two-layered structure and numerous spots Cu_2SnSe_3 phase at the bottom layer confirmed that Cu out-diffusion significantly altered the phase distribution across the film.

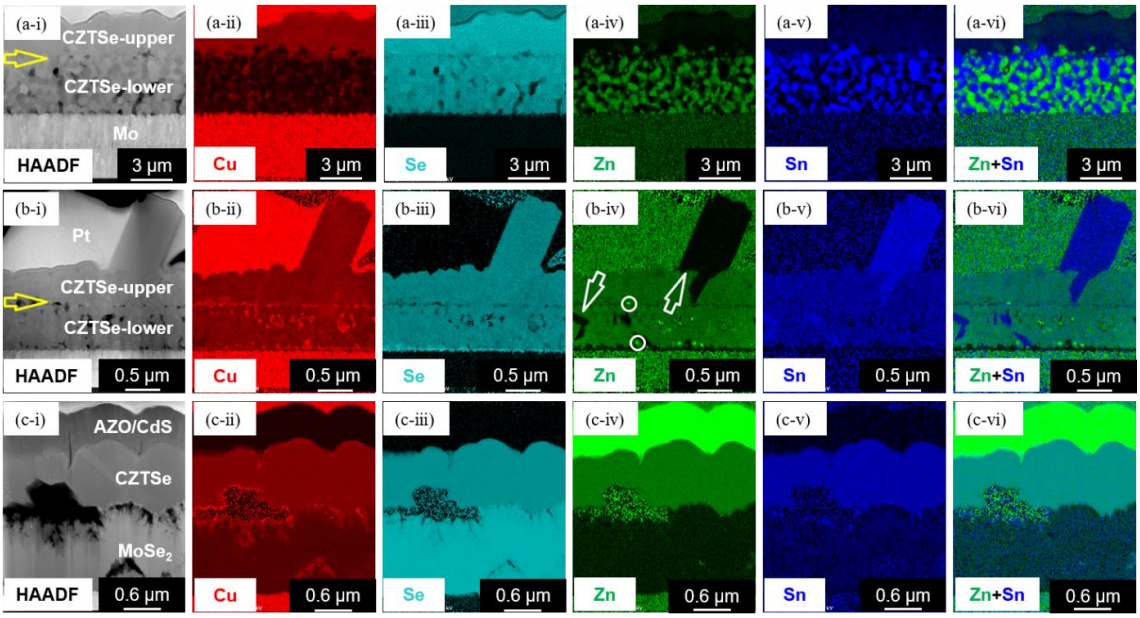

Figure 4.23: Cross-sectional STEM-HAADF images and corresponding element distributions obtained from EDXS maps of Cu, Se, Zn and Sn of the film produced when the selenization process was interrupted (a) 350 °C and (b) 450 °C, while (c) solar cell, respectively. Different elements are denoted in a different color (Cu in red, Se in turquoise, Zn in green and Sn in blue). The interface between the CZTSe upper layer and the CZTSe lower layer is marked by a horizontal yellow arrow in (a-i) and (b-i).

When the temperature reached point t_d and t_e, the XRD pattern showed the dominance of the $SnSe_2$, $CuSe_2$, and CZTSe (see fig 4.20 (a)) phase. Raman spectra indicated the dominance of the CZTSe and $SnSe_2$ phases. Concerning the morphology, the two-layered structure at point t_d was observed which then disappeared as the temperature reached point t_e (540 °C). Regarding morphology, the surface of the film characterized by the large grains together with plate-like crystal marked with the red arrow (see Fig. 4.21 (d)). It further reveals that the $SnSe_2$ phase co-exists with CZTSe.

As the sample annealed for 10 min (at point t_f), the surface of the sample showed the dominance of the CZTSe phase, indicating both $SnSe_2$ phases are eliminated (see fig 4.20 (b) orange line). The dominance of the CZTSe phase in this temperature regime discloses the fact that the reaction is completed. Concerning the morphology, we observed larger grain in the surface, extended to the bulk of the sample. Fig. 4.22 (c -i) presents the STEM-HAADF image corresponding with EDXS elemental mapping in Fig. 4.22 (c-ii-iv). STEM-HAADF shows a good agreement with the SEM image (Fig.4.21 f2). Additionally, from fig 4.22 (c), it is recognized that all four elements are uniformly distributed, suggesting the fact that no secondary phases co-exist with the CZTSe phase.

4.10 Summary

Gathering critical information, gained from all characterization techniques, about the composition, morphological and phases present in the film annealed in different temperatures, different reaction pathways are proposed. The schematic diagrams in Fig. 4.24 interpret the reaction pathways of low-temperature Cu-Zn-Sn-Se precursor following selenization. The co-existing of Cu-Se, $SnSe_2$, and Cu_2SnSe_3 phases indicates that two reaction pathways were competing and contribute to the formation of the CZTSe phase.

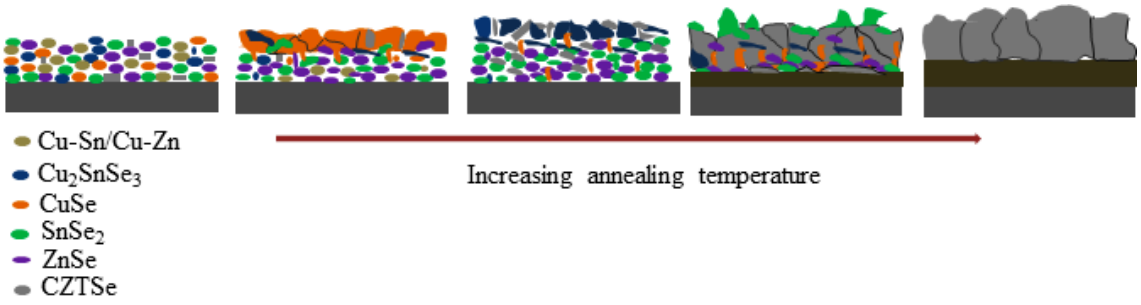

Figure 4.24: Schematic sketch of the formation pathway during annealing of a co-evaporated precursor at a different temperature.

5. CZTSe solar cells fabricated from co-evaporated multilayer stacks

Part of the results in this chapter has already been published.

Section 5.1 and partially section 5.3 were published in Phys. Scr. 2019, 94 105007. The author was mainly involved in sample preparation and characterization. Co-author Markus Neuwirth helped with SEM analysis. Will Kogler, Thomas Schnabel, Erik Ahlswede helped with supplying Mo substrated, EDXS and GDOES measurements. Ulrich W. Paetzold, Bryce S. Richards, and Michael Hetterich helped with the organization of the work and proofreading the manuscript. Moreover, following people were involved in this chapter Teoman Teskesen was involved in deposition of window layer. Erich Müller and Xiaowei Jin helped with TEM/EDX measurement. Jasmin Seeger and Simon Woska were involved in Electroreflectance spectroscopy measurement and introduction to the J-V-T system, respectively.

5.1 Introduction

As demonstrated in the previous chapter that the high-pressure Se atmosphere can lead to the formation of thicker $MoSe_2$ layer between the CZTSe absorber and Mo back contact and large grain. The latter has a beneficial impact on the device performance —as it is known that $MoSe_2$ layer assists the formation of Ohmic contact when its thickness is around a few 100 nm, while excessive thickness is expected to harm the device performance —this holds particularly to R_S of the device [120]. Further, it has been shown previously that CZTSe is unstable to Mo. It is well-known that CZTS(e) is unstable at normal processing temperature (500— 600 °C) in the presence of Mo [121], [122]. The reaction 5.1 shown the reaction between CZTS(e) absorber and Mo [45], [121], [122].

$$2CZTS(e) + Mo \rightarrow 2Cu_2S(e) + 2ZnS(e) + 2SnS(e) + MoS(e)_2 \quad 5.1$$

As a result of this reaction, the formation of i) thicker layer of $MoS(e)_2$ as well as ii) unwanted phases and defects, which could harm device performance are expected [121], [122]. Therefore, in order to suppress the reaction between CZTS(e) and Mo, it is crucial to limit the interaction between CZTS(e) absorber and Mo back contact. For instance, an intermediate layer of TiN [122], [123], TiB [124], Ag [125], ZnO [126], [127], and MoO_3 [128], [129] has been used to suppress the interaction of CZTS(e) and Mo back contact at the same time act as a chalcogen diffusion barrier. It has been demonstrated that the utilization of TiN and TiB intermediate layer could lead to high R_S and poor crystal quality [64], [123]. Moreover,

the utilization of ZnO can lead to high R_S and poor CZTS(e)/Mo interface [64]. To avoid a comprise between the absorber quality, CZTS(e)/Mo interface quality, and the interaction of CZTS(e) and Mo, alloying of the Mo/Zn/Cu/Sn/Cu metal precursor before selenization has been proposed by Li et al. [64]. As a result of alloying, in-depth composition gradient such as Zn, Cu_5Zn_8/Cu_6Sn_5 could be achieved. The formation of the $MoSe_2$ layer was significantly suppressed to less than 10 nm and a device with a η up to 8.7 % could be demonstrated [64]. It was experimentally demonstrated that in-depth composition gradient in the precursor could substantially improve CZTSe growth and device performance [56]. For instance, the device with η up to 9.7 % could be demonstrated when $Cu_{10}Sn_{90}$/Zn/Cu precursor configuration is utilized [27] [95]. Further, depth composition gradient such as $Zn_xSn_{1-x}/Cu_2SnSe_3/Cu_xSe$ could result in a double-gradient bandgap CZTSe absorber [56].

In this line of argument, in this chapter different precursor stacks are introduced with the motivation of i) trigger a different reaction path ii) a delayed the earlier interaction between CZTSe and Mo back contact, consequently suppress a reaction between Mo and CZTSe absorber. To shed light on this aspect, a precursor with a configuration of Mo/Cu-Sn/Cu-Zn-Sn-Se/ZnSe/Cu-Zn-Sn-Se is investigated.

5.2 Fabrication of CZTSe solar cells by co-evaporation of multilayer Cu-Sn/Cu-Zn-Sn-Se/ZnSe/Cu-Zn-Sn-Se stacks

In this study, CZTSe thin-film absorbers are prepared using a novel precursor configuration of Mo/Cu-Sn/Cu-Zn-Sn-Se/ZnSe/Cu-Zn-Sn-Se as illustrated in Fig. 5.1 (a). A novel precursor configuration was employed with the motivation of i) to force the formation of CZTSe at the back contact to proceed via a ternary path as shown in equation 5.2 and ii) to delayed an earlier interaction between CZTSe and Mo back contact, consequently suppress decomposition of CZTSe at the rear interface. Thus, a Cu-Sn layer was intentionally *in-situ* pre-annealed at a temperature of around 250 °C for 15 min. The details of the precursor growth and selenization conditions are presented in Table 5.1.

Table 5.1: Precursor growth conditions

	Deposition rate (nm/min)				Cu-Sn alloying conditions	
Sample Number	Cu	Zn	Sn	Se	Temperature (°C)	Time (min)
AA0174-2	1.4	1.3	2.15	3.7	250	15

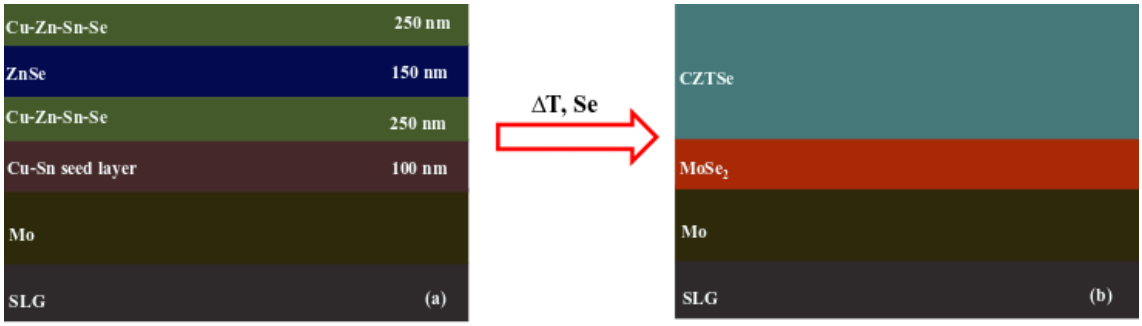

Figure 5.1: Schematic diagrams of (a) stacked precursor and (b) selenized CZTSe absorber.

5.2.1 Study of the precursors' material phases

To confirm the main material phases of the stacked precursor, the XRD measurement of the stacked precursor was performed. As displays in Fig. 5.2 (red line), the precursor mainly composed of the selenide compounds of ZnSe (PDF-number 01-080-0021), Cu_2SnSe_3 (PDF-number 01-070-8930), CuSe (PDF-number 00-034-0171), and $SnSe_2$ (PDF-number 01-089-3197), together with the alloys of Cu_6Sn_5 (PDF-number 00-047-1575), Cu_5Zn_8 (PDF-number 00-025-1228), $Cu_{10}Sn_3$ (PDF-number 03-065-2064), Cu_3Sn (PDF-number 00-001-1240), $Cu_{41}Sn_{11}$ (PDF-number 00-030-01510). The alloyed phase of Cu_6Sn_5, Cu_5Zn_8, and Cu_3Sn could be originated from Cu-Zn-Sn-Se as supported by the XRD pattern in Fig. 4.1 (a) (black line).

In order to understand the origin of other alloys in the stacked precursor, the XRD measurement of the *in-situ* alloyed Cu-Sn seed layer was acquired. As it appears in Fig 5.2 (black line), the Cu-Sn seed layer was composed of the alloy of CuSn, $Cu_{10}Sn_3$, and Cu_6Sn_5. Comparing the material phases of the Cu-Sn seed layer with that from stacked precursor it is evident that some of the alloys in the seed layer decomposed during the deposition of all stacks. For instance, it was noticed that the CuSn alloy extincted and $Cu_{41}Sn_{11}$ evolved together with the $SnSe_2$ phase. The presence of the $SnSe_2$ phase strongly suggests that Se diffuses during the deposition of other stack and reacts with the Cu-Sn seed layer, causing an evolution of the $Cu_{41}Sn_{11}$ and $SnSe_2$ phase. From these findings, it could be concluded that the *in-situ* alloyed Cu-Sn seed layer of the stacked precursors contains the alloys of $Cu_{41}Sn_{11}$, Cu_6Sn_5, and selenide compound of $SnSe_2$.

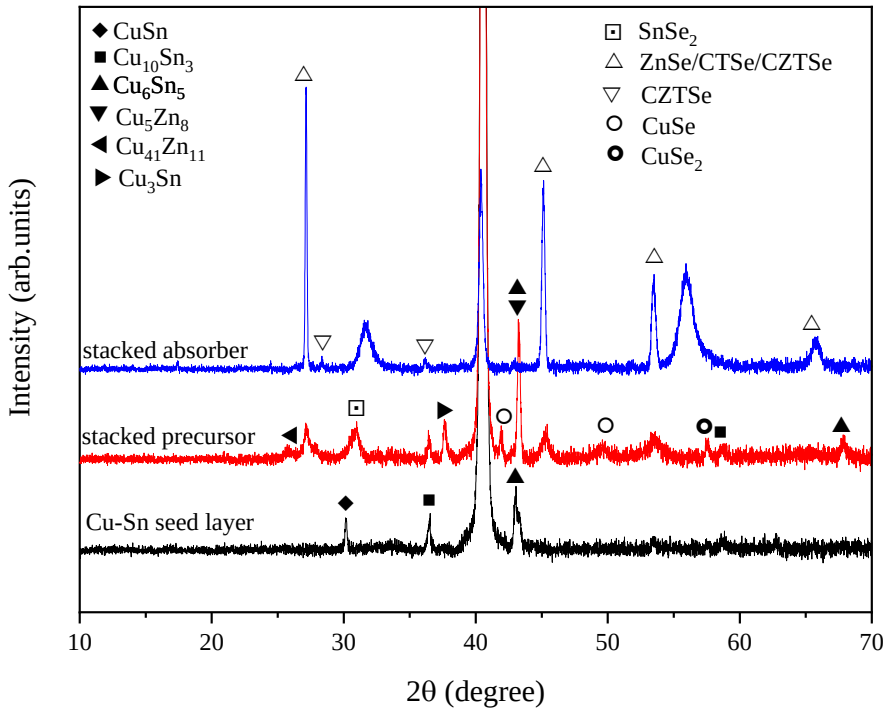

Figure 5.2: XRD pattern of a Cu-Sn seed layer, a stacked precursor, and a stacked absorber [37].

5.2.2 Study of the CZTSe absorber

To learn more about the influence of Mo/Cu-Sn/Cu-Zn-Sn-Se/ZnSe/Cu-Zn-Sn-Se precursor configuration on the material growth, the precursors were selenized to prepared CZTSe layer as described in section 4.1.2. To explore the quality of CZTSe absorber, XRD measurement was acquired and analyzed. As illustrated in fig 5.2 (blue line) no evidence of secondary phases related to $SnSe_2$, CuSe, and Cu_2Se was found. The XRD pattern demonstrated a similar pattern as that reported in section 4.1.2.

Fig. 5.3 shows the cross-sectional SEM image of the complete solar cell was taken. It was observed that the CZTSe absorber was very compact and associated with a 1200 nm—thick layer of $MoSe_2$ at the Mo interface. This indicates that utilizing a 100 nm—thick Cu-Sn alloyed seed layer does not fully prevent Se diffusion to Mo back contact. Comparing this observation with that reported in section 4.1.2, it is clear that the formation of $MoSe_2$ layer was not associated with the interaction of CZTSe and Mo back contact rather than Se diffusion during selenization. The thickness of the CZTSe absorber was found to be 1 µm. The crack at the CZTSe/$MoSe_2$ interface was visible. Concerning to the grain size of the absorber, the absorber showed a mixture of larger grains on the surface and fine grains at the interface to the $MoSe_2$ layer. A similar observation has been reported by Zhang *et al.* [119].

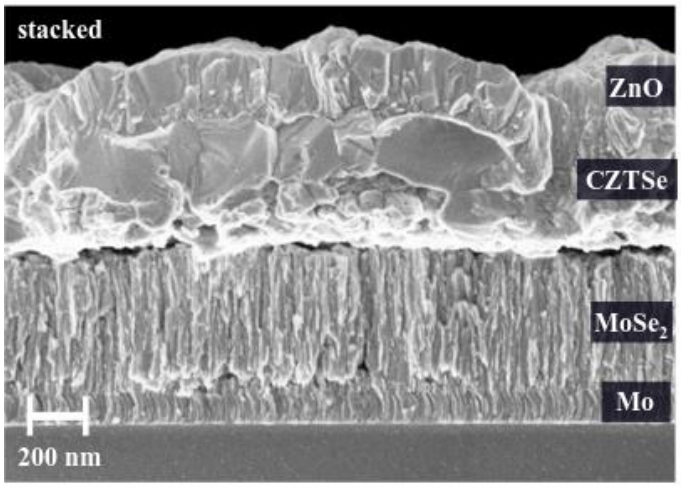

Figure 5.3: Cross-sectional SEM image of a complete solar cell prepared from stacked precursors [37].

However, this observation is slightly different from those reported in homogenous co-evaporated precursors in section 4.1.2 and by Gao *et al*. [12]. A possible explanation for this discrepancy is, for the case of homogenous co-evaporated precursors, the four elements are uniformly distributed across the precursor, resulting in the homogenous distribution of binaries and ternaries phases during selenization and reacting to form CZTSe phase [119]. In contrast to that, for the stacked precursor, all the four elements are not uniformly distributed across the precursor layer, consequently, binaries and ternaries are not homogeneously, causing only a partial reaction between them. Thus, based on these observations, it can be assumed that the stacked precursor grain growth starts at the surface and a non-uniform distribution of the ZnSe and Cu_2SnSe_3 phase might delay the formation of the CZTSe phase at Mo back contact.

Having described the structural and morphological properties of the CZTSe absorber, special attention was paid on the elemental distribution. To address this aspect, the HAADF-STEM image and STEM-EDXS elemental mapping were taken. Fig 5.4 shows the HAADF-STEM image and STEM-EDXS elemental maps. To make a better visualize of the elemental distribution-relationship between Cu, Zn, Sn, and Se, the elemental map of these elements are displayed in Fig 5.4 (f). As expected, the void at the $MoSe_2$ interface was visible as shown by the white arrow in fig 5.4 (a). Moreover, the crack at the Mo/$MoSe_2$ interface can be seen. STEM-EDXS maps showed the presence of nano—Sn-riched and Se-deficiency particles at the absorber/voids interface shown by a red arrow in fig. 5.4 (d) and (f). This strongly suggests that the voids are might be promoted by Cu out-diffusion during absorber growth.

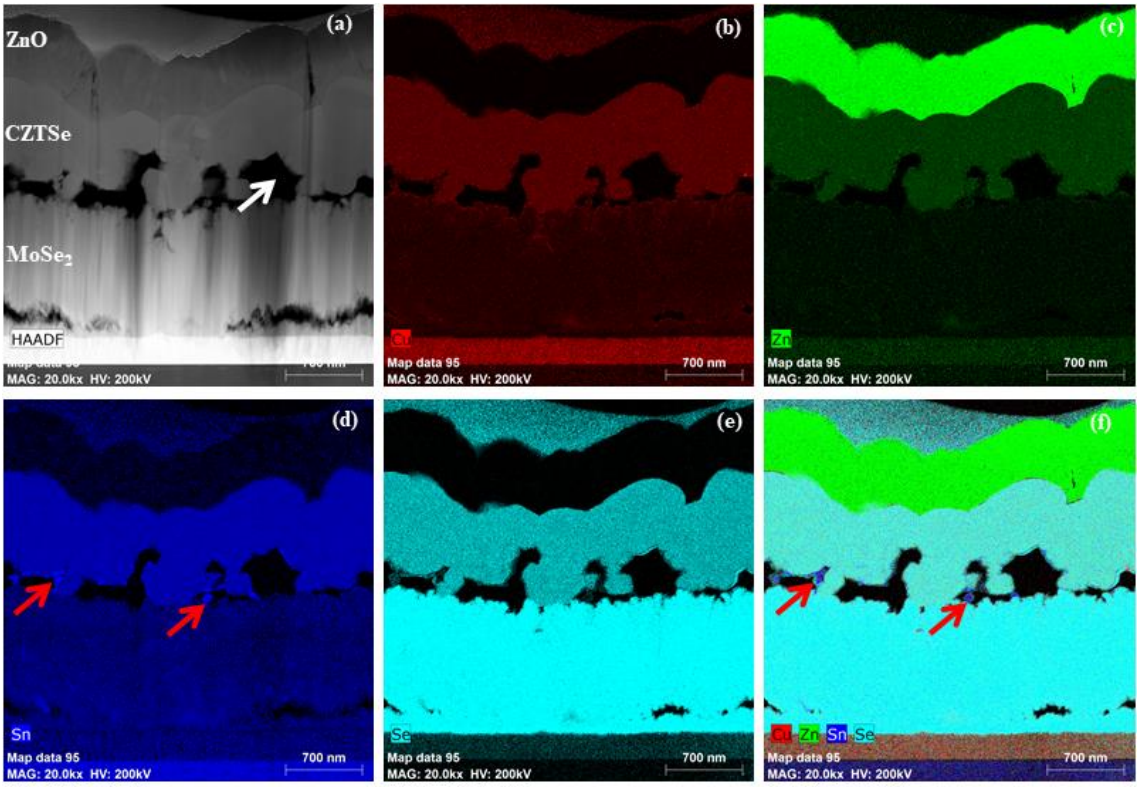

Figure 5.4:(a) Cross-sectional STEM-HAADF image of (b-e) corresponding elemental distribution obtained from TEM-EDXS maps of Cu (red color), Zn (green color), Sn (blue color), and Se (turquoise color) (f) the elemental map of Cu, Zn, Sn, and Se.

5.2.3 Study on solar cell performance

To further investigate the quality of absorber, CZTSe solar cells with an active area of around 0.16 cm^2 were fabricated and analyzed. The dark and illuminated *J-V* curves for champion solar cells with corresponding full data are shown in Fig 5.5 and Table 5.2, respectively. The champion solar cell exhibited a η up to 7.9 %, corresponding to the V_{OC} and the *FF* of 429 mV and 62 %, respectively. Both V_{OC} and *FF* are close to the high efficient devices reported in the literature (see Table 4.3). The device demonstrated a maximum J_{SC} of 29.7 mA/cm^2 which is somewhat lower than that reported in section 4.1.2 and in the literature (see Table 4.3). Based on the SEM image in Fig. 5.3, fine grains at the Mo interface of the device provide more grain boundaries that can acts as a leakage pathway for the generated photocurrent, consequently deteriorating the current of the device [119], [130]. Further, the device exhibited the minimum saturated current density (J_0) of 1.1×10^{-6} mA/cm^2, suggesting less recombination at the interfaces. This could further be supported by less cross-over between dark and illuminated curves (occurs at 27

mA/cm^2), revealing a proposed precursor configuration hampers the formation of the blocking layer relative to the homogeneous co-evaporated precursor presented in section 4.1.3.

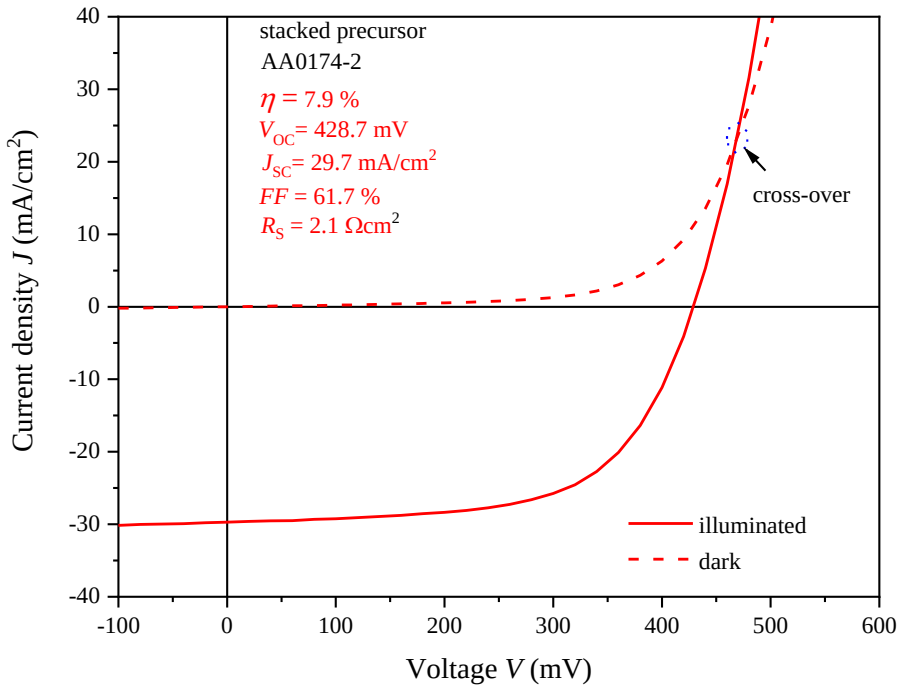

Figure 5.5: The J-V curves for the champion solar cell prepared from the stacked precursor [37].

Table 5.2: Solar cell parameters for the solar cells prepared from the stacked precursor [37].

Sample	η (%)	V_{OC} (mV)	J_{SC} (mA/cm^2)	FF (%)	R_S (Ωcm^2)	n	J_O (mA/cm^2)
Stacked (AA0174-2)	7.0	392	30	59	2.4	1.8	1.7×10^{-6}
	7.6	417	29	62	2.4	1.5	2.4×10^{-7}
	7.9	429	30	62	2.1	1.8	1.1×10^{-6}
	7.1	390	31	58	2.4	1.8	9.1×10^{-7}
	7.4	408	30	60	2.2	1.5	3.3×10^{-7}
	7.8	426	30	61	2.0	1.6	3.1×10^{-7}

Concerning the n, the device exhibited a minimum value of 1.8 which is lower than that reported in section 4.1.2. It indicates that stacked configuration significantly suppresses unusual recombination in the devices. To further elucidate the nature of the recombination mechanism, *J-V-T* measurement on the champion solar cell was performed and evaluated. Looking at the dependence of the V_{OC} and temperature, it significantly deviated from expected linearity behavior as shown in Fig. 5.5 (a). The findings are in

good agreement with those reported in section 4.1.3, 4.2.3, 4.2.4, and in refs [27], [64], [118], [119]. Employing equation 4.1, the linear extrapolation of the temperature dependence of V_{OC} to T = 0 K gives E_A = 1.04 eV which is equal to the bandgap estimated from electroreflectance measurement (see Fig. 5.6 (d)). It is concluded that the bulk Schottky Read-Hall (SRH) recombination is the dominant recombination mechanism in the devices.

Fig. 5.6 (b) illustrates the dependence of R_S of the champion devices with temperature. The R_S increases exponentially with decreasing temperature in the range between from 300 K to 170 K. A similar trend can be seen in section 4.1.2, 4.2.3, 4.2.4 and in refs [64], [118], [119]. Using equation 4.2, a fit from a plot of $\ln(R_S T)$ versus $1/T$ provided Φ_B = 103 meV which is lower than that obtained in section previous sections, however, it is a bit higher than those reported in pure-Se-kesterite reported in the literature [64], [119]. We account for this with a thicker layer of the $MoSe_2$ formed in between CZTSe and Mo back contact.

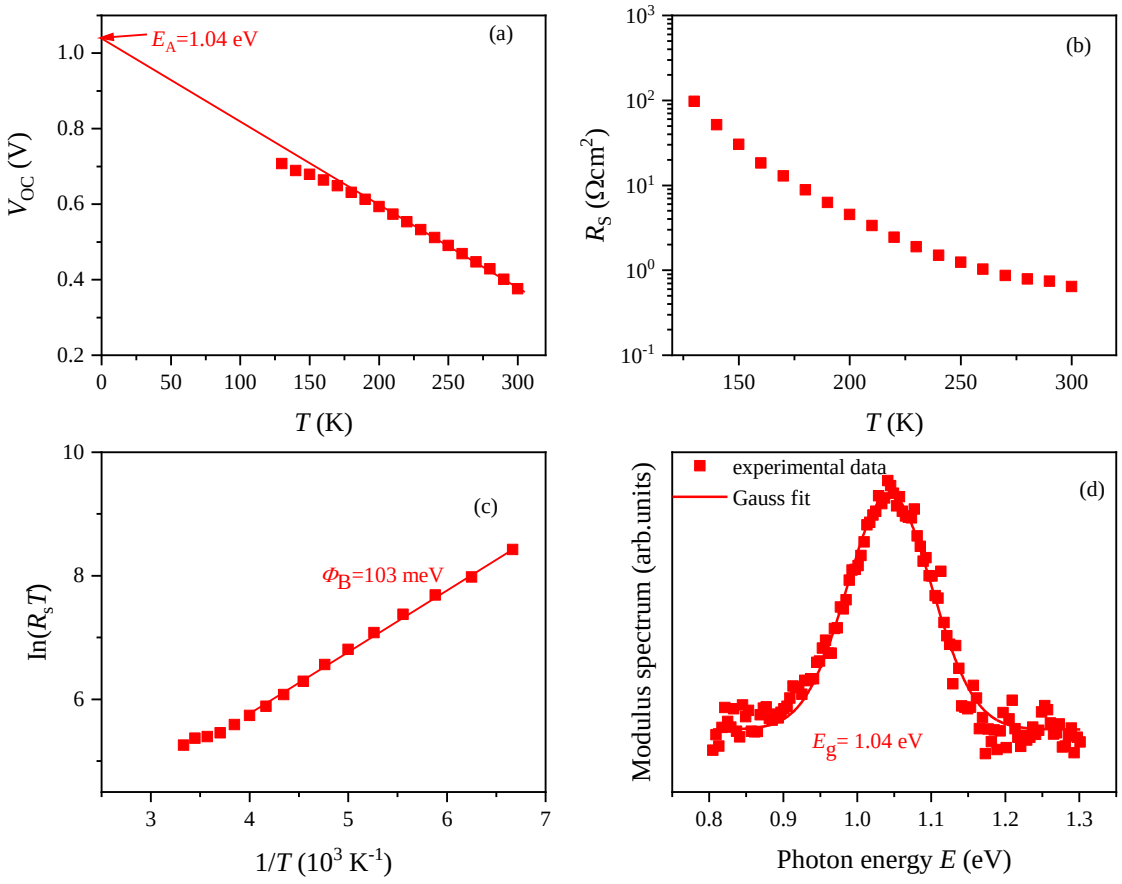

Figure 5.6: (a) Temperature dependence of V_{OC}, (b) Temperature-dependent dark R_S, and (c) In ($R_S T$) versus 1/T for a champion solar cell prepared from the stacked precursor.

5.3 Elimination of fine grains at Mo back contact

Fine grains exit in CZTSe absorber prepared by selenization of Cu-Sn/Cu-Zn-Sn-Se/ZnSe/Cu-Zn-Sn-Se significantly degrade the back interface, consequently impact the J_{SC} of the device. Thus, the influence of seed layer alloying temperature and pre-annealed of each individual layer on the absorber growth were investigated with a motivation of eliminating the fine grains at the CZTSe/$MoSe_2$ interface and improves the device performance, especially J_{SC}.

5.3.1 A study on the influence of alloying temperature on the CZTSe growth and device performance

In order to learn the impact of alloying temperature on CZTSe absorber growth and device performance, two sets of the devices were fabricated i) Cu-Sn seed layer was not alloyed (named as-deposited stacked precursor) and ii) Cu-Sn seed layer was alloyed at 150 °C (named 150 °C stacked precursor). The details of the precursor growth conditions are presented in Table 5.3. It should be noticed that selenization conditions are the same as those presented in Table 5.2.

To explore more about the influence of seed layer alloying temperature on the absorber growth, XRD measurement was performed on the selenized samples. Fig. 5.7 shows the XRD pattern for as-deposited stacked, stacked precursor (reference sample), and 150 °C stacked precursors. It should be pointed out that the alloying temperature had a significant impact on the film adhesion. A peeling off was observed to all as-deposited samples. Thus, only an XRD measurement will be discussed for this sample. All CZTSe absorbers showed to have a similar XRD pattern as that presented in previous sections which agree with that of the tetragonal CZTSe phase with a major peak at 27.16° (PDF Number 00-052-0868).

Table 5.3: Precursors growth parameters

Sample Number	Deposition rate (nm/min)				Cu-Sn alloying conditions	
	Cu	Zn	Sn	Se	Temperature (°C)	Time (min)
AA0178-1	1.4	1.3	2.15	3.7	N/A	N/A
AA0178-2	1.4	1.3	2.15	3.7	150	15
AA0174-2	1.4	1.3	2.15	3.7	250	15

N/A not applicable

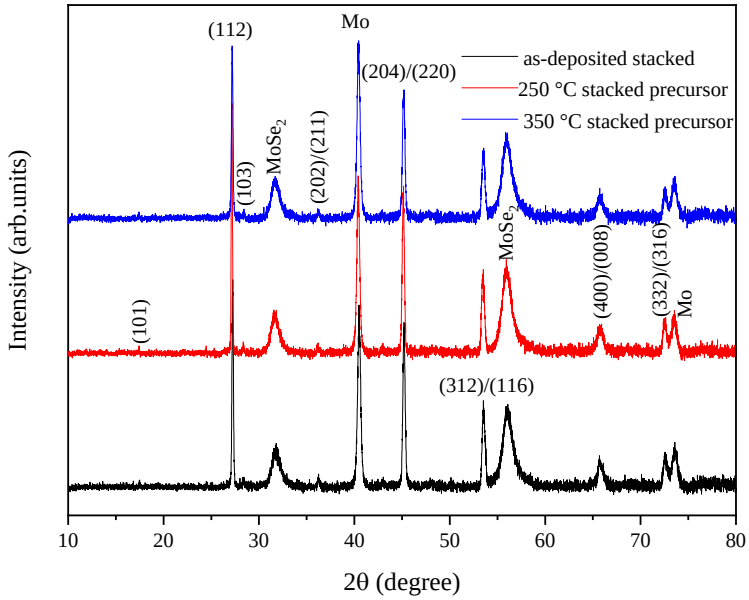

Figure 5.7: The XRD pattern for the CZTSe absorber prepared from the as-deposited stacked precursor, 150 °C stacked precursor, and 250 °C stacked precursor, respectively.

To have conclusive information about the CZTSe crystal quality as a function of alloying temperature, a cross-sectional SEM image of the CZTSe absorber prepared from 150 °C was taken and compared with that from 250 °C stacked precursor (a reference sample) shown in section 5.2.2. The CZTSe absorber prepared from a 150 °C stacked precursor composed of a less compact layer associated with a thicker layer of $MoSe_2$ (1.3 µm), see Fig. 5.8 (a). The CZTSe/$MoSe_2$ interface was not as clear as that observed in the stacked precursor (see section 5.2.2). Based on these observations, it can be hypothesized that the alloying temperature of Cu-Sn seed layer could have a significant impact on the device performance.

As a proof of concept, solar cells based on 150 °C stacked absorber were fabricated and analyzed. Fig. 5.8 (b) and Table 5.4 show the *J-V* curves and corresponding solar cell parameters of the best solar cell of the device prepared from 150 °C stacked precursor, respectively. The cell showed poorer performance compared to the best device of champion solar cell presented in section 5.2.2. The cell demonstrated a maximum η up to 3.7 % (2.9 % on average), associated with the V_{OC} and *FF* of 297 mV (260 mV on average) and 45 % (41 % on average), respectively. The J_{SC} was much worse than that in the stacked precursor. Looking at the R_S and R_P of the device is not surprising to observe that trend (see Table 5.5). The device demonstrated the R_S and R_P of 3.3 Ωcm^2 (3.9 Ωcm^2 on the average) and 88 Ωcm^2 (67 Ωcm^2 on average), respectively.

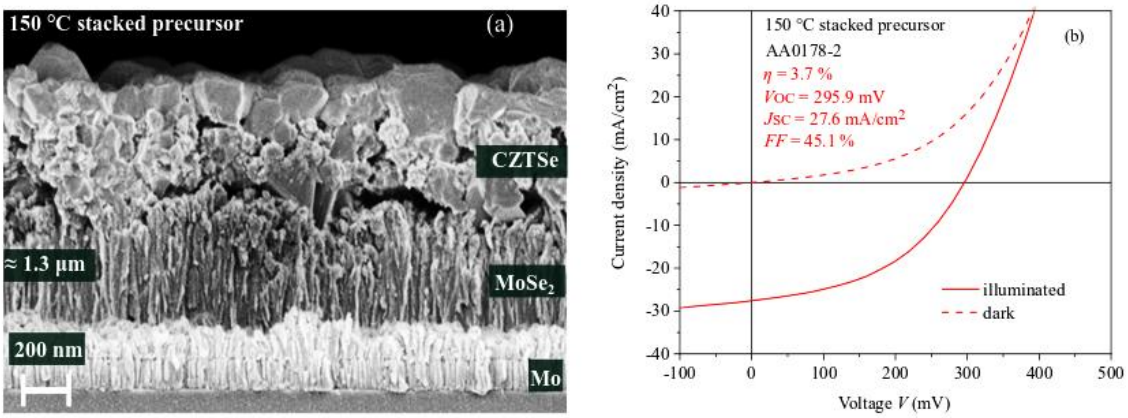

Figure 5.8: a) Cross-sectional SEM image of CZTSe absorber prepared from 150 °C stacked precursor, (b) the dark and illuminated *J-V* curves for the champion solar cell prepared from the 150 °C stacked precursor

Judging from the SEM image (see Fig. 5.7 (a)), it is not surprising to observe this behavior as the absorber composed of the less compact layer with fine grains and numerous porous. As documented in ref. [130] that fine grains and voids could lead to the higher photocarrier recombination rate thus harm the device performance.

Table 5.4: Solar cell parameters for the solar cells prepared from the 150 °C stacked precursor.

Sample	η (%)	V_{OC} (mV)	J_{SC} (mA/cm^2)	FF (%)	R_S (Ωcm^2)	R_P (Ωcm^2)	n
Stacked (AA0178-2)	2.0	231	26	33	4.8	36.1	3.2
	3.3	290	26	44	3.8	86.3	2.6
	2.3	218	27	42	3.4	88.0	2.1
	2.3	232	28	35	4.2	41.5	3.4
	3.4	297	28	42	4.1	66.4	2.9
	3.2	276	28	41	3.9	68.6	2.8
	2.6	227	28	40	3.3	58.2	2.4
	3.1	270	27	42	3.6	67.9	2.5
	3.7	297	28	45	3.6	87.9	2.5

5.3.2 A study on the influence of pre-annealing of individual stacks on the CZTSe growth and device performance

As demonstrated in section 5.2.1 that alloying solar cells somewhat eliminate the fine grains at Mo back contact but compromises the quality of the CZTSe absorber and back interface. One could hypothesize that a partially intermixing of stacks could trigger a different reaction path toward the formation of the CZTSe absorber. To elucidate this hypothesis, three sets of devices were fabricated and examined, i) each individual layer (4 stacks) of the stacked precursor was *in-situ* pre-annealed (named as 4 stacks pre-annealed precursors), ii) three stacks (Cu-Sn/Cu-Zn-Sn-Se/ZnSe) of the stacked precursor was *in-situ* pre-annealed (named as 3 stacks pre-annealed precursors), and iii) the whole precursor was *in-situ* pre-annealed (named as precursor pre-annealed). It should be noticed that the pre-annealing conditions are the same as for the Cu-Sn seed layer (see Table 5.1). The obtained precursors were selenized the same as those reported in section 4.1.2.

To confirm the main material phases in the CZTSe absorbers, XRD measurement was performed. As displayed in Fig. 5.5, the composition of the absorber is the same, matches with that of the tetragonal CZTSe phase (PDF Number 00-052-0868). No secondary phases related to Sn-Se and Cu-Se phases were found. Cross-sectional SEM images of the complete devices prepared from the 4 stacks pre-annealed precursors, 3 stacks pre-annealed precursors, and precursor pre-annealed were taken with a motivation of further exploring the quality of the CZTSe absorber, grains size, and back interface. As it appears in Fig. 5.6, the morphology of CZTSe absorbers is different. The absorbers prepared from 4 stacks pre-annealed and 3 stacks pre-annealed precursors composed of a compact single-layered CZTSe absorber with a morphology that appeared to be in between that of the absorber prepared from homogenous co-evaporated precursor and stacked precursor discussed previously. They showed smaller grains and a more uniform and homogenous morphology than the stacked absorber. The fine grains at the back interface were completely disappeared. It illustrates that a partial intermix of the stacks could somewhat subject the ZnSe phase close or at the Cu-Sn seed layer. This could provoke a partially homogenous distribution of the Cu_2SnSe_3 and ZnSe phase during selenization.

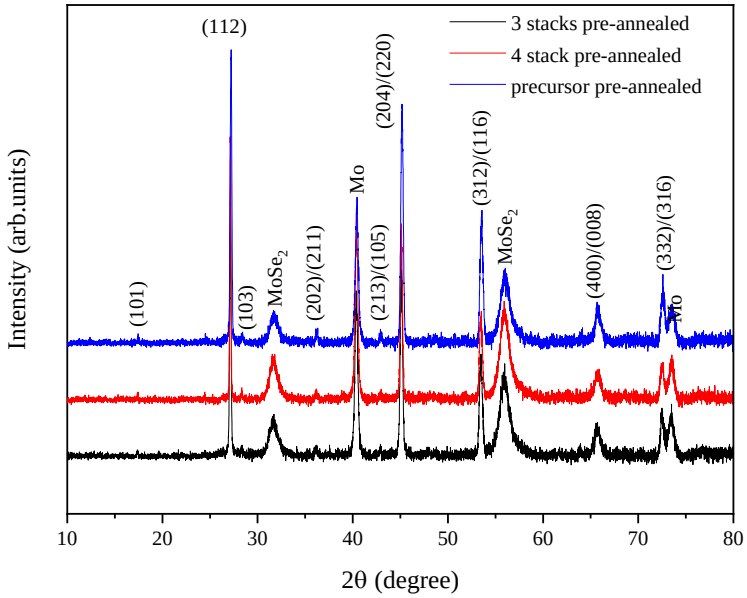

Figure 5.9: XRD pattern for CZTSe absorber prepared from 3 stacked pre-annealed precursor, 4 stacked pre-annealed precursor, and pre-annealed precursor, respectively.

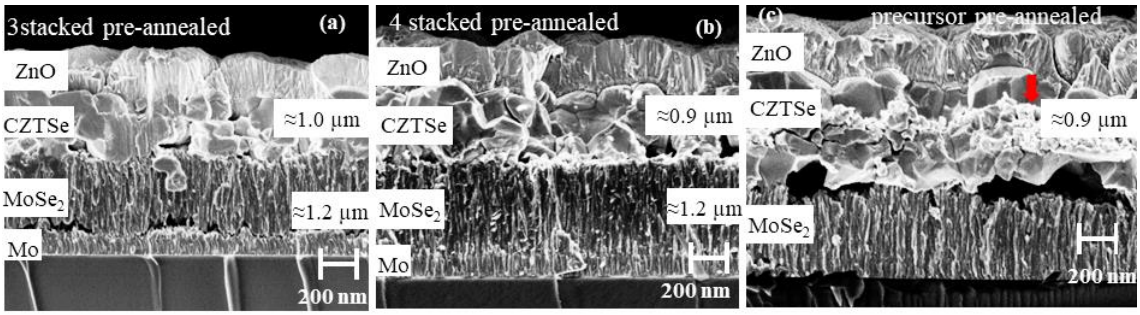

Figure 5.10: Cross-sectional SEM images for solar cells prepared from (a) 3 stacked pre-annealed precursor, (b) 4 stacked pre-annealed precursor, and (c) pre-annealed precursor, respectively.

In contrast, the absorber prepared from a pre-annealed stacked precursor exhibited a two layered-structured which associated with fine grains in between a compact layer of large grains. The presence of the fine grains is expected to cause an electrical problem reading an increased in series resistance, thus significantly impact the *FF* and J_{SC} of the device. A crack at the CZTSe/$MoSe_2$ interface was still visible for all absorber types, however, it much pronounced in the pre-annealed absorber.

Based on these findings, it could be concluded that a crack at the CZTSe/$MoSe_2$ is related to the presence of the Cu-Sn alloyed layer at the Mo interface. It was reported in ref. [77] that the volume expansion of the metals during selenization could lead to cracking or peeling off of the CZTSe absorber if thermal stress is not effectively released.

After making clear that a fine grain at the Mo back interface could be eliminated by pre-annealing techniques, special attention was paid to the device performance. Three sets of CZTSe device was fabricated using a 3 stacked pre-annealed precursor, 4 stacked pre-annealed stacked, and pre-annealed precursor. The dark and illuminated *J-V* curves for the champion solar cell with corresponding cell parameters are shown in Fig 5.7 and Table 5.5. The *J-V* curves for the cell from the pre-annealed precursor showed to have a stronger cross-over between the dark and illuminated curves (occurred at 10 mA/cm^2) compared to the cells from the 4 stacked pre-annealed precursor (occurred at 20 mA/cm^2) and 3 stacked pre-annealed precursors (occurred at 31 mA/cm^2). It strongly suggests the existence of an electrical barrier in the CZTSe absorber or back interface. On the basis of these findings, it can be concluded that 4 stacked and 3 stacked pre-annealed precursors hampers the formation of such a blocking layer. Based on SEM images in Fig. 5.10 (c), the presence of fine grains between two compact layers strongly impacts the electrical properties of the device.

As it can be seen in Table 5.5, the cell from 3 stacked pre-annealed precursors showed poorer performance than cells prepared from 4 stacked pre-annealed and pre-annealed precursors. The cell from 3 stacked pre-annealed precursors demonstrated a maximum η up 5.7 % while that from 4 stacked pre-annealed precursors and pre-annealed stacked precursors exhibited the maximum η up to 6.8 % and 6.7 %, respectively. The reason behind this could be a higher V_{OC} of 381 mV and 432 mV for the 4 stacked pre-annealed precursor and pre-annealed precursor, respectively. It should be noticed that the V_{OC} of 432 mV obtained using the pre-annealed precursors is among the highest in pure-Se-kesterite reported in the literature (see Table 5.6). On the contrary, the cell prepared from the 4 stacked pre-annealed precursors demonstrated higher *FF* (56 %) relative to 51 % and 51 % for the cell prepared from pre-annealed and 3 stacked pre-annealed precursors, respectively. Concerning the J_{SC}, the cells from 3 stacked pre-annealed 4 stacked pre-annealed precursors showed a slightly higher J_{SC} (33 mA/cm^2) than cell from pre-annealed stacked.

The cells prepared from the 4 stacked pre-annealed and 3 stacked pre-annealed showed nearly constant R_S values of around 2.7 Ωcm^2 and 2.8 Ωcm^2, respectively. On the contrary, cells prepared from the pre-annealed stacked exhibited a higher value of R_S (3.9 Ωcm^2) relative to the cells from 4 stacked pre-annealed and 3 stacked pre-annealed. The reason is, on the one hand, the presence of fine grains in between compact layers of the CZTSe absorber and a big crack between $MoSe_2$ and CZTSe at the back interface is expected to significantly impact the electrical properties of the devices, especially the R_S and *FF*. The device from pre-annealed stacked precursor showed relatively high J_0 (3.0×10^{-5} mA/cm^2) and *n* (3.0) with respect to the 3 stacked pre-annealed ($J_0 = 9.9 \times 10^{-6}$ mA/cm^2 and *n* of 1.9) and 4 stacked pre-annealed ($J_0 = 2.9 \times 10^{-6}$ mA/cm^2 and *n* of only 1.7).

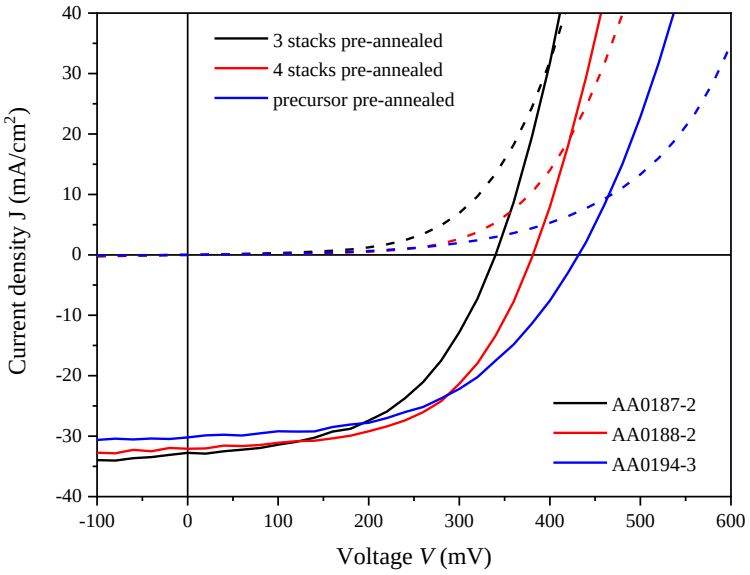

Figure 5.11: The dark and illuminated *J-V* curves for the champion solar cell prepared from the 3 stacked pre-annealed precursor, 4 stacked pre-annealed precursor, and pre-annealed precursor, respectively.

Table 5.5: Solar cell parameters for the solar cells prepared from the 3 stacked pre-annealed precursor, 4 stacked pre-annealed precursor, and pre-annealed precursor, respectively.

Sample	η (%)	V_{OC} (mV)	J_{SC} (mA/cm^2)	FF (%)	R_S (Ωcm^2)	n	J_0 (mA/cm^2)
3 stacked pre-annealed	5.8	340	33	51	2.8	1.8	9.9×10^{-6}
4 stacked pre-annealed	6.8	381	32	56	2.8	1.8	2.9×10^{-6}
Pre-annealed precursor	6.7	432	30	51	3.9	3.0	3.0×10^{-5}

The lower n indicates that a solar cell behavior closely to the ideal case, bulk recombination could be dominating the recombination mechanism. Based on these findings, it can be concluded that the pre-annealing techniques could completely eliminate the fine grains at Mo back contact, thus improves in J_{SC} to above 30 mA/cm^2 is possible. However, the approach leads to deterioration in FF and partially lower in V_{OC}—this holds particularly to the 3 stacked pre-annealed and 4 stacked pre-annealed precursors. Comparing our results and those reported in [16], [18]–[20], one can conclude that our device's performance is limited by low J_{SC}, high R_S and partially of FF.

Table 5.6: Selected publication with the highest V_{OC} for pure-Se-kesterite reported in the literature.

	η (%)	V_{OC} (mV)	J_{SC} (mA/cm^2)	FF (%)	R_S (Ωcm^2)	n	Reference
CZTSe	11.95[1]	433.22	36.28	76.21	0.76	N/A	[16]
CZTSe	11.7	423	41.7	66.6	0.38	1.56	[18]
CZTSe	11.6	423	40.6	67.3	0.32	1.57	[19]
CZTSe	11.4	443	38.1	68	0.05	1.2	[20]
CZTSe	7.9	429	30.0	62	2.1	1.7	This study
CZTSe	6.7	432	30.0	51	3.9	3.0	This study

[1]Current world record device for a pure-Se-kesterite reported.

Having demonstrated the influence of the pre-annealing techniques on the solar cell performance for the champion devices, now examination of the fluctuation of the solar cell parameters was implemented and the results were displayed in the box plot in Fig. 5.8. It can be seen that the η of 3 stacked pre-annealed fluctuates from 4.0 to 5.7 % with V_{OC} and FF in the range of 301 to 340 mV and 41 to 51 %, respectively. The devices from 4 stacked pre-annealed showed less fluctuations in solar cell parameters. The η varied from 6.6 to 6.8 % and the V_{OC} from 379 to 385 mV. The J_{SC} for these devices stayed above 31 mA/cm^2. On the other hand, the devices from the pre-annealed precursor demonstrated less fluctuation in the V_{OC}, it varied from 432 to 439 mV. The η of these devices ranged from 5.9 to 6.7 %, while the FF and J_{SC} fluctuated between 46 to 51 % and 29 to 31 mA/cm^2. Moreover, the devices prepared from the pre-annealed precursor exhibited the R_S in the range of 3.9 to 5.8 Ωcm^2 while that from 4 pre-annealed stacked and 3 pre-annealed stacked precursors demonstrated R_S in the range of 2.6 to 3.0 Ωcm^2 and 2.8 to 3.5 Ωcm^2. Regarding the n, the devices from 4 pre-annealed stacked and 3 pre-annealed stacked precursors showed the lowest value relative to the devices from the pre-annealed precursor. They showed the value in the range of 1.8 to 2.1 while that from the pre-annealed precursor demonstrated the value in the range of 2.9 to 3.0. Thus, judging from this observation, it could be assumed that the device from 4 pre-annealed precursors is stable with respect to the devices from 3 stacked pre-annealed precursors and pre-annealed precursor.

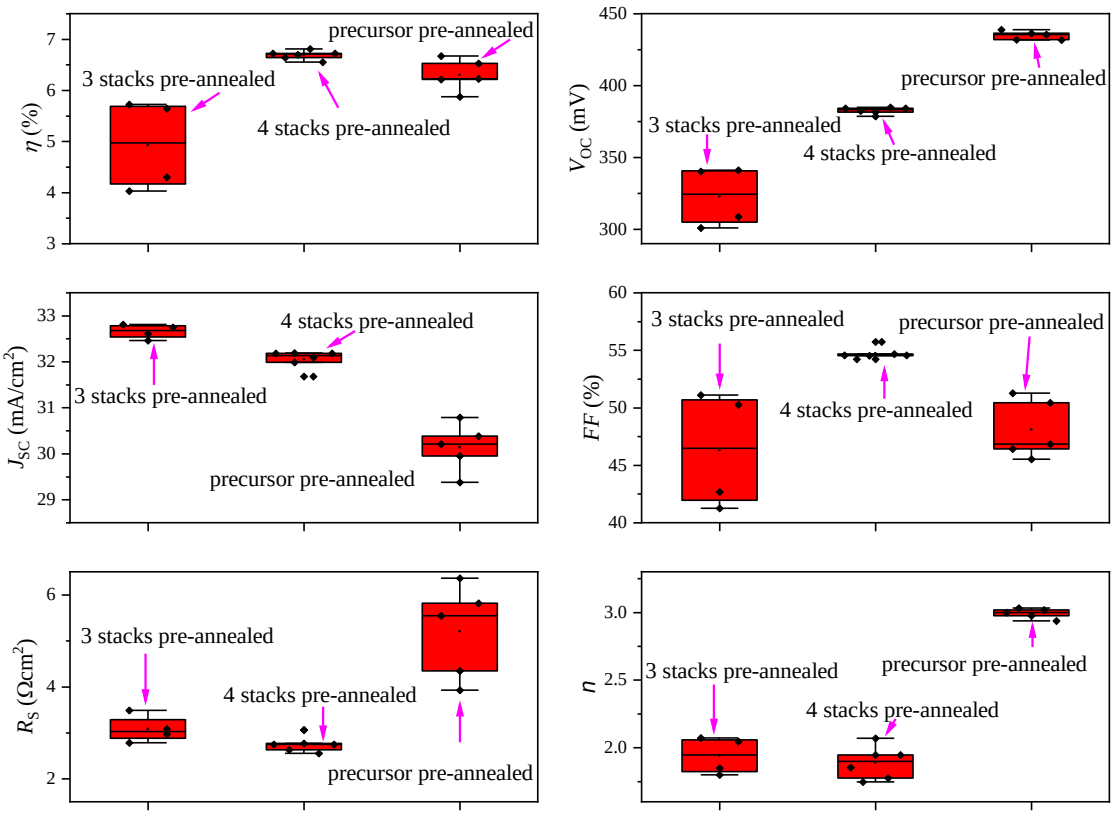

Figure 5.12: Comparison of the cell parameters η, V_{OC}, J_{SC}, FF, R_S, and n for the sample prepared from a 3 stacked pre-annealed, a 4 stacked pre-annealed, and pre-annealed precursors, respectively.

5.3.3 Summary

In this section, the impact of Cu-Sn seed layer alloying temperature on the absorber growth and device performance were conducted. It was shown that the effect of alloying temperature has a negative impact on the absorber adhesion as well as the quality. Thus, it is not a promising approach to eliminate fine grains and sometimes improving device performance. However, pre-annealing of each stack demonstrates to be an effective approach to suppress the formation of fine-grains at Mo back contact. The *J-V* result demonstrated that an *in-situ* pre-annealing of the whole stack (precursor pre-annealed) in more promising as it results in the solar cell with the lowest V_{OC}-deficit.

6. Impact of Silver Incorporation at the Back Contact of Kesterite Solar Cells on Structural and Device Properties

Part of results in this chapter has been submitted for publication ***"Lwitiko P. Mwakyusa, Lennart Leist Monika Rinke, Alexander Welle, Ulrich W. Paetzold, Bryce S. Richards, and Michael Hetterich, Impact of Silver Incorporation at the Back Contact of Kesterite Solar Cells on Structural and Device Properties"*** *Author and co-author Lennart Leist was involved in sample preparation and characterization. Alexander Welle helped with ToF-SIMS analysis and discussion. Monika Rinke helped with Raman Measurement. Will Kogler, Thomas Schnabel, Erik Ahlswede helped with supplying Mo substrated and deposition of the window layer. Ulrich W. Paetzold, Bryce S. Richards, and Michael Hetterich helped with the organization of the work and proofreading the manuscript.*

Moreover, the following people were involved in this chapter. Jasmin Seeger and Simon Woska were involved in Electroreflectance spectroscopy and SEM measurements, respectively. Volker Zibalt helped with SEM and EDXS analysis. Sabine Schlabach and Vanessa Wollersen helped with introduction to the dimple grinder setup.

6.1 Introduction

As documented in several reports and discussed in chapters 2, 4, and 5, CZTSe solar cell's performance is limited with high V_{OC}-deficit. To our case (see chapters 4 and 5), CdS/CZTSe interface recombination is not a limiting factor as commonly proposed in the literature. Moreover, as reported in [5], [36], [53], [131], [132], the presence of secondary phases, high level of compensated defects, small grains, and poor grain boundary passivation are considered as a cause of low minority carrier lifetime. Thus, control the formation and distribution of secondary phases and defects in the interfaces and absorber bulk has been paramount importance recently. It was suggested that partial substitution of Cu^{+} and Zn^{2+} with an atom with different atomic radius could suppress the formation of Cu_{Zn} antisites [86], [89], [133] and a high level of compensated defects. Further, it was also demonstrated that Ag incorporation enhances grain growth as well as tuning the bandgap [89], [134]. As shown in Fig 2.6, there are several reports on Ag

incorporation into the kesterite lattice via a chemical route, but only very few using vacuum deposition. It has been reported that the enhancement in grain growth for Ag-containing kesterite is due to the formation of the liquid grain growth mechanism owing to a lower melting point (217 °C) of the eutectic Cu–Ag–Sn alloy [89], [134]. However, in practice, it remains challenging to form a Cu–Ag–Sn alloy in a chalcogen-containing precursor prepared from the wet-chemical route. Moreover, Ag-containing kesterite formation pathways during annealing of Ag-containing precursors have not yet investigated. Thus, in this chapter, the material growth and device performance of the CZTSe and $(Cu,Ag)_2ZnSnSe_4$ (CAZTSe) solar cells are presented, interpreted, and discussed. The main purposes of this investigation have been to study the

(i) impact of alloying temperature on the CZTSe growth and device performance.
(ii) impact of Ag incorporation at the back contact of CZTSe solar cells on growth and device properties.

The samples were investigated utilizing the measurement techniques described in chapter 3.

6.2 CZTSe solar cells prepared from co-evaporated Cu-Zn-Sn precursors: A study on the impact of alloying temperature on the absorber and device properties

6.2.1 Study on the Cu-Zn-Sn precursors and CZTSe absorber

In order to learn the effect of alloying temperature on the alloys formation and CZTSe growth, Cu, Zn, and Sn were deposited onto Mo-coated SLG at relatively low temperatures (100 °C). Prior to selenization, the Cu-Zn-Sn layers were alloyed at a different temperature with a motivation for enhancing film adhesion and alter the CZTSe reaction pathways. A detailed on the alloying and selenization conditions are presented in Table 6.1. It should be noticed that Cu-Zn-Sn layers were deposited in the same conditions as those presented in the previous chapters.

To have a clear picture of the precursor material phases, the XRD measurement of the as-deposited and alloyed Cu-Zn-Sn layer was performed. As presented in Fig. 6.1 (a), the material phase of the layers is different. As-deposited Cu-Zn-Sn layer composed of the alloys of Cu_6Sn_5 (PDF No. 00-045-1488) and Cu_5Zn_8 (PDF No. 00-025-1228) together with elemental Sn (PDF No. 03-065-0296). The presence of the alloys in the as-deposited Cu-Zn-Sn film is an indication that the alloying process already starts during precursor growth even without annealing. Our observation is somehow different from that reported by Gang *et al*. during the investigation of the sputtered Cu/Sn/Zn stacked-layer—where both elementals of Cu and Sn co-exist with the alloys of Cu_6Sn_5 and Cu_5Zn_8 [29].

Table 6.1: Sample preparation parameters

Sample number	Alloying conditions				Selenization conditions			
	Temp (°C)	Pressure (mbar)	Heating Rate (°C/min)	Time (min)	Temp (°C)	Pressure (mbar)	Mass of Se (mg)	Length of Sn wire (cm)
AA0209-3	250	1000	10	15	540	250	200	6
AA0215-8	280	1000	10	15	540	250	207	6
AA0209-7	300	1000	10	15	540	250	199	6
AA0211-4	320	1000	10	15	540	250	203	6
AA0211-5	350	1000	10	15	540	250	209	6

However, as the precursor was annealed at 250 °C for 15 min, the XRD pattern showed additional XRD peaks at 2θ ≈ 30.2°, 36.4°, and 45.1° which would be assigned to the $Cu_{10}Sn_3$ (PDF No. 03-065-3632) together with 2θ ≈ 45.1° related to the alloy of $Cu_{40.5}Sn_{11}$ (PDF No. 01-071-0121) (see Fig. 6.1 (a) the red line). Furthermore, the sample alloyed at 280 °C demonstrated unique features since it showed more additional XRD peaks related to the cubic CuZn (PDF No. 00-002-1231) alloyed (2θ ≈ 53.7°) and mono-clinic CuZn (PDF No. 00-008-0349) alloy (2θ ≈ 55.2°). For the high alloying temperature i.e. 300 to 350 °C, the signature of CuZn alloys was not clearly observed.

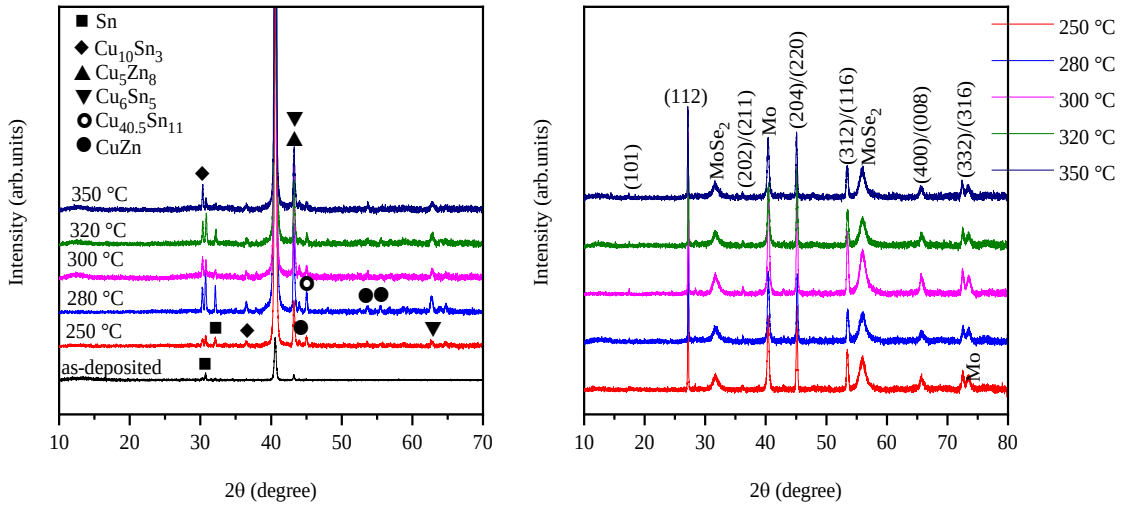

Figure 6.1: (a) XRD pattern for Cu-Zn-Sn layer alloyed at (b) XRD pattern for CZTSe absorber prepared from Cu-Zn-Sn layer alloyed at a temperature of 250 °C, 280 °C, 300 °C, 320 °C, and 350 °C, respectively.

After the serious study on the influence of alloying temperature on the precursors' material phase, special attention was paid on its impact on the CZTSe growth. To explore the influence of the alloying temperature on the structural properties of the CZTSe layer, Cu-Zn-Sn alloyed layers were selenization under the same condition as shown in Table 6.1. The XRD pattern of the CZTSe absorber was measured to investigate the material phases after selenization. As can be seen in Fig. 6.1 (b), all absorbers showed the similar XRD pattern which characterized by the three main XRD peaks at $2\theta \approx 27.12°$, 45.07°, 53.4° and the minor peaks at $2\theta \approx 17.45°$ and 36.30° assigned to the tetragonal CZTSe phase (PDF Number 00-052-0868). Moreover, no cogent evidence of Cu-Se and Sn-Se secondary phases was found.

Fig 6.2 visualizes the SEM cross-section images of the complete CZTSe solar cells prepared from co-evaporated metallic precursors alloyed at different temperatures. As presented in Figs. 6.2 (a-e), all CZTSe absorber exhibited a compact single layer associated with the thick layer $MoSe_2$ layer at the Mo interface. The discrepancy of the grain size among CZTSe absorber samples fabricated at different temperatures is tangible. The CZTSe absorber prepared from the precursors alloyed at a temperature of 250 °C showed a mixture of larger and fine grains (see Fig. 6.2 (a)). On the contrary, all CZTSe absorbers prepared from the precursors alloyed at a temperature > 250 °C appeared to have a larger grain and a more uniform and homogenous morphology. It was noticed that there was an obvious crack at the CZTSe/$MoSe_2$ interface which is, in my opinion, associated with the volume expansion of metals during the selenization process.

6.2.2 Study on the Cu-Zn-Sn precursors and CZTSe absorber

In this section, we presented how the quality of the CZTSe absorber, as well as the device performance, altered according to the change of the temperature in the alloying. For this purpose, CZTSe solar cells with an active total area of 0.16 cm^2 were fabricated and characterized. The dark and illuminated *J-V* curves for the best solar cells in this series corresponding to the box plot are presented in Figs 6.3 and 6.4. The devices prepared from Cu-Zn-Sn precursor alloyed at 250 °C exhibited a strong cross-over between the dark and illuminated curves as compared to the devices prepared from precursors alloyed at a higher temperature (280 to 350 °C). The η of the solar cells improved from 4.8 % (4.4 % on average) to 7.0 % (on average) when the alloying temperature of Cu-Zn-Sn precursors increased from 250 to 300 °C, then dropped to 6.2 % (5.7 % on average) and 4.3 % (4.2 % on average) when further increasing the alloying temperature to 320 °C and 350 °C, respectively. The V_{OC} and *FF* exhibited a similar trend on the alloying temperature for the Cu-Zn-Sn precursors. However, for the solar cells from Cu-Zn-Sn alloyed precursors at 250 °C show somewhat a lower *FF* relative to other devices.

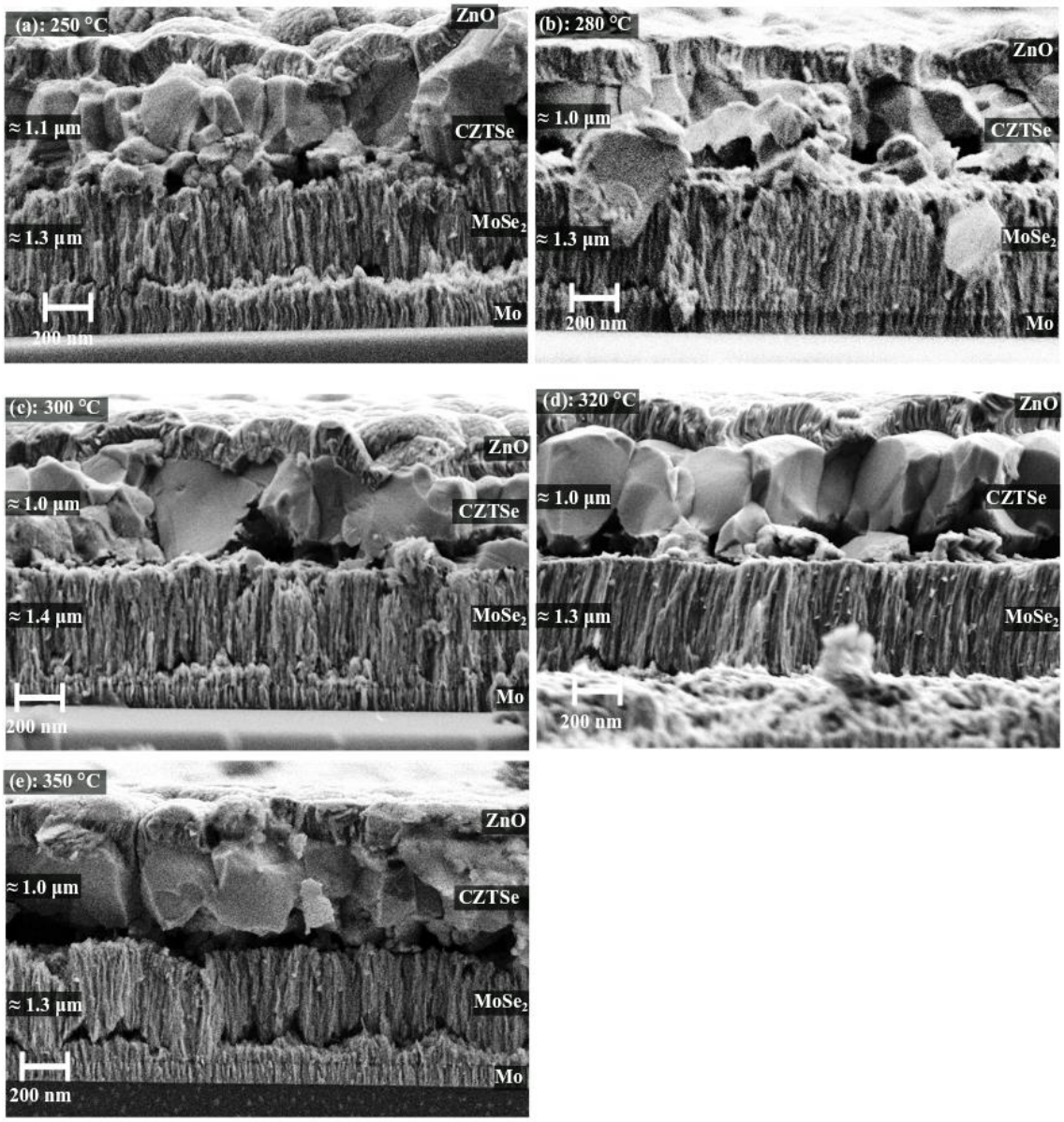

Figure 6.2: Cross-sectional SEM images for CZTSe solar cell prepared from the Cu-Zn-Sn precursors alloyed at (a) 250 °C, (b) 280 °C, (c) 300 °C, (d) 320 °C, and (e) 350 °C, respectively

Judging from the XRD measurement (see Fig. 6.1 (a)), the precursor material phases for this sample exhibited additional alloys of monoclinic and cubic CuZn. It is well known that the presence of Cu-Sn alloys accelerates the formation of Cu_2SnSe_3, then CZTSe [2]. Thus, in our case, the presence of the CuZn alloy might slightly impede the formation of CZTSe as it must be decomposed during selenization as shown in reactions 6.1(a-c). This situation might provoke the local inhomogeneities and voids in the CZTSe absorber causing a significant influence on the device performance. Additionally, according to the box plot, there was no clear correlation between R_S and R_P of the device on the alloying temperature.

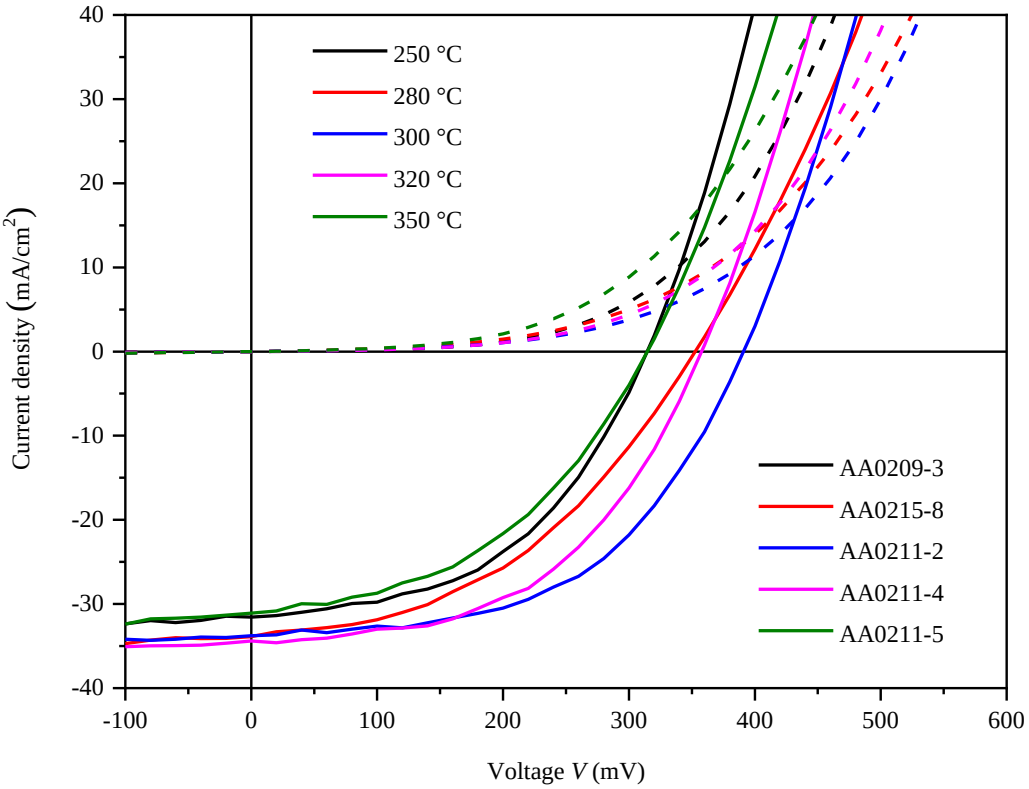

Figure 6.3: Comparison of dark and illuminated J-V curves of the best solar cell fabricated from Cu-Zn-Sn precursors alloyed at a temperature of 250 °C, 280 °C, 300 °C, 320 °C, and 350 °C, respectively.

$$CuZn + 3Se \rightarrow CuSe_2 + ZnSe \quad 6.1(a)$$

$$CuSe_2 + SnSe_2 \rightarrow Cu_2SnSe_3 \quad 6.1(b)$$

$$Cu_2SnSe_3 + ZnSe \rightarrow Cu_2ZnSnSe_4 \quad 6.1(c)$$

To further assess the impact of alloying temperature on the device performance, EQE measurement under AM 1.5 G (1000 Wm^{-2}) was performed on the best solar cells attained so far. The measurement results show that the EQE of the devices strongly depends on the alloying temperature. As shown in Fig. 6.5 (a), the EQE increased from 80 % (630 nm) to 86 % as the alloying temperature increased from 250 °C to 320 °C. However, the EQE decreased to 70 % if the alloying temperature increased further to 350 °C. Interestingly, as shown in Figure 6.3, the devices prepared from a precursor alloyed at a temperature of 280 °C, 300 °C, and 320 °C appeared to have a better current collection in the region of a longer wavelength relative to the samples prepared from precursors alloyed at a temperature of 250 °C and 350 °C. Using equation 6.1, it could be hypothesized that alloying temperature of 280, 300, and 320 °C lead to a sufficient long diffusion length (L_n) and a wide space-charge with (W).

$$EQE(\lambda) = 1 - \frac{\exp(-\alpha(\lambda)W)}{1+\alpha(\lambda)L_n} \quad 6.1$$

where α is the absorption coefficient and λ is the wavelength. This observation is in good agreement with the J_{SC} observed using a solar simulator (see Fig. 6.3). To account for the V_{OC} trend observed in the devices, the bandgap of the CZTSe absorbers was estimated using EQE data. As illustrated in Fig. 6.5 (b), the bandgap maintained almost constant at around 1.06 eV for the sample prepared using 250 °C alloyed Cu-Zn-Sn precursor and 1.08 eV for a sample from 350 °C alloyed precursors. It implies the alloying temperature does not significantly alter the absorber composition.

Based on these findings, it is evident that the alloying temperature of 300 °C is an optimal alloying temperature. Thus, this temperature will be used for further describing the CZTSe formation pathways during selenization. Moreover, the temperature will be kept in the fabricating process of samples used to study the impact of Ag incorporation in the back contact of CZTSe on the structural, morphological, and device properties (see section 6.2).

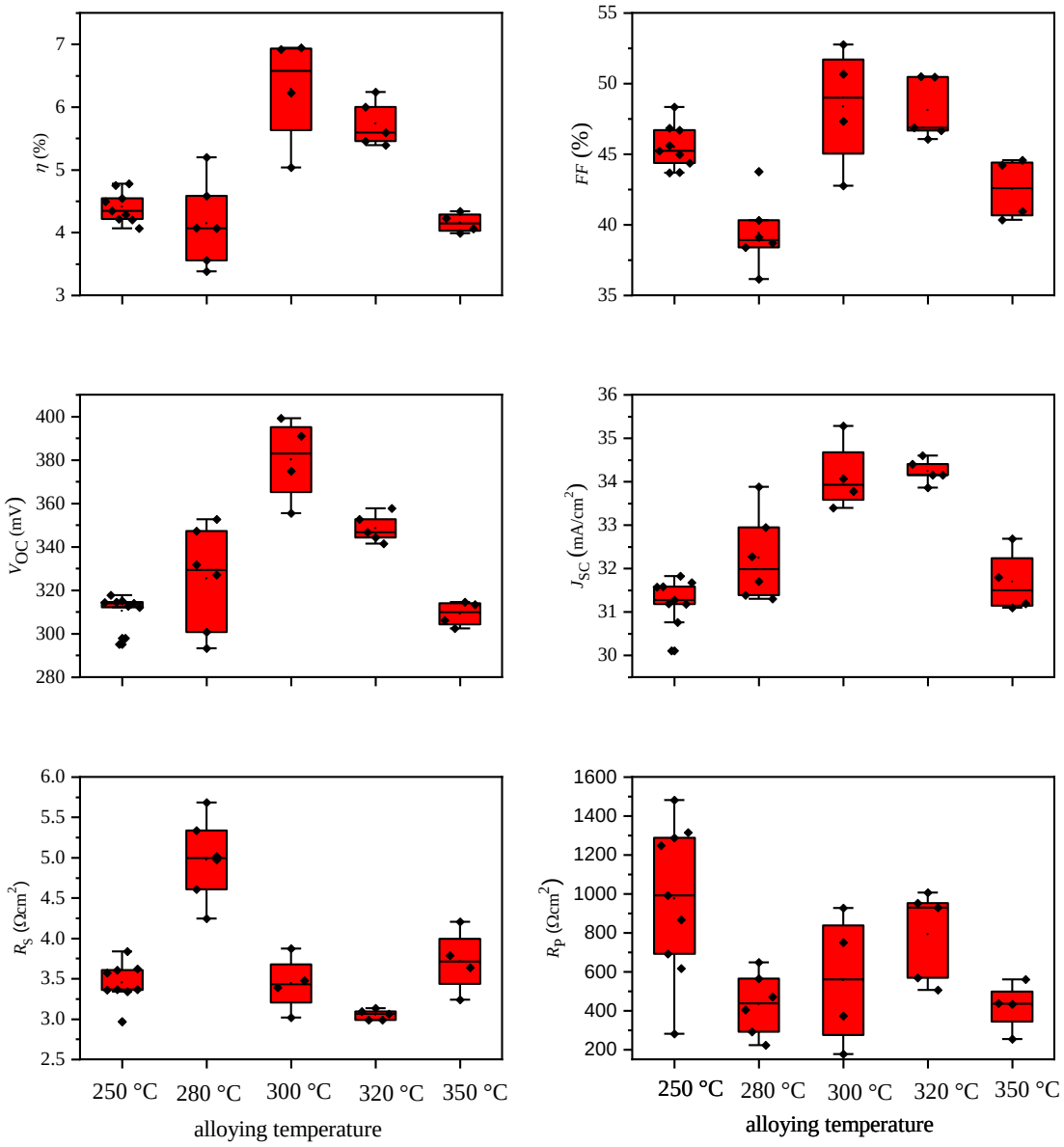

Figure 6.4: Comparison of the device performance for the devices from the Cu-Zn-Sn alloyed precursors at a temperature of 250 °C, 280 °C, 300 °C, 320 °C, and 350 °C.

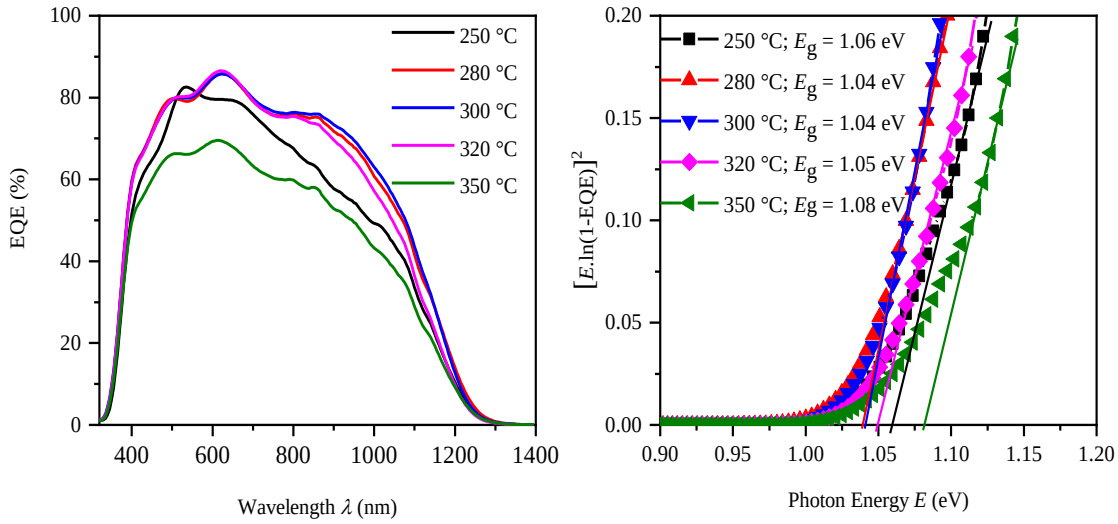

Figure 6.5: (a) The EQE of the devices and (b) the bandgap of CZTSe absorber estimated from EQE data for the devices prepared from Cu-Zn-Sn precursors alloyed at a temperature of 250 °C, 280 °C, 300 °C, 320 °C and 350 °C.

6.2.3 An investigation on the morphology and phase evolution during selenization of the Cu-Zn-Sn precursors

To shed light on the phases and morphology transition during annealing of Cu-Zn-Sn alloyed precursor, a standard selenization protocol was interrupted at the different temperatures as illustrated in Fig. 4.19 and the obtained films were analyzed using XRD, micro-Raman spectroscopy, and SEM. The XRD of the alloyed precursor was first analyzed and compared with selenized films. It can be seen in the XRD pattern (Fig. 6.6 (a) the black line), the alloyed precursor contained the alloys of $Cu_{10}Sn_3$, Cu_6Sn_5, Cu_5Zn_8, CuZn (PDF No. 00-002-1231), and $Cu_{40.5}Sn_{11}$, together with elemental Sn.

As the alloyed precursor annealed to 350 °C (the point ta), the XRD pattern showed a mixture of the selenide compounds (ZnSe, Cu2SnSe3, and CZTSe) together with elemental Sn at $2\theta \approx 30.60°$. The presence of the element Sn strongly suggested that all Sn atoms did not completely reacted with the Se to form $SnSe_2$ as Se partial pressure was not high enough in the graphite box.

To have a clear understanding of the composition of the selenide compounds in the films, micro-Raman spectroscopy with an excitation wavelength at 514.5 nm was performed. It should be noticed that the depth of focus was around 100 nm, thus the measurement was surface sensitive. As illustrated by the red line in Fig. 6.6 (b), the Raman spectra showed the broad Raman band at around 178 cm^{-1} which could be assigned to the Cu_2SnSe_3 phase together with minor Raman band at 233 cm^{-1} and 245 cm^{-1} related to CZTSe phase. These Raman bands indicated the early formation of the CZTSe phase. However, the purity of the CZTSe film was not promising for solar cell applications. The cross-sectional SEM image

also showed a rough surface and fine grains across the absorber (see Fig. 6.7 (a)). Interestingly, there was no evidence of the Cu-out diffusion as observed in chapter 4 and in ref. [3].

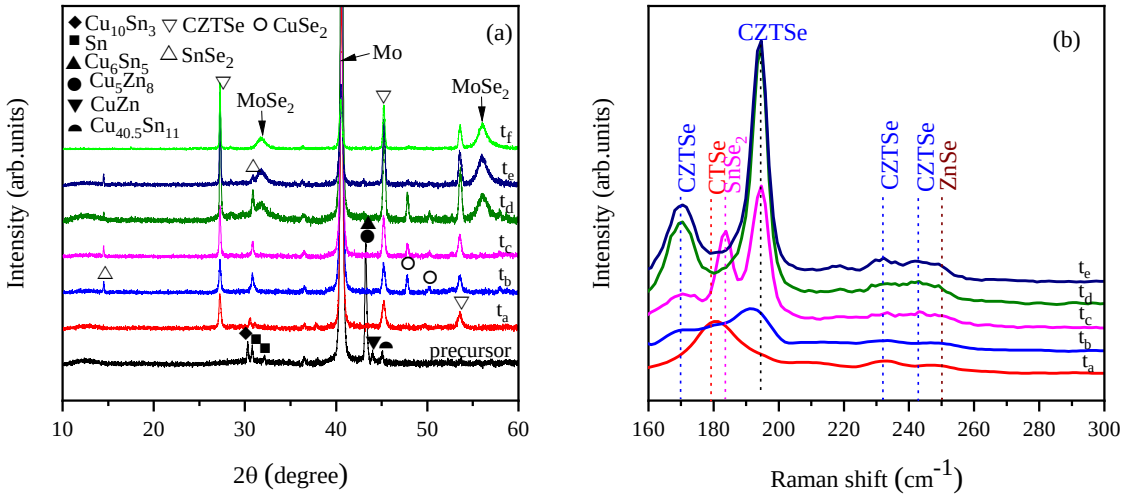

Figure 6.6: (a) XRD patterns of the films prepared from Cu-Zn-Sn precursors produced when the annealing process was interrupted at different temperatures. (b): Corresponding Raman spectra.

As a temperature reached to point t_b (400 °C), the XRD peaks related to $SnSe_2$ and $CuSe_2$ was evolved. No XRD peak related to elemental Sn was detected, implying that Sn reacted with Se vapor to form the $SnSe_2$ phase. Indeed, the micro-Raman measurement demonstrated the existence of CZTSe phases (Raman bands at 170 cm^{-1} and 192 cm^{-1}). The presence of the Raman band around 192 cm^{-1} was cogent evidence of the poor crystallization of the CZTSe thin film as described by the cross-sectional SEM image (see Fig 6.7 (b)).

As observed in the XRD pattern, there was no significant change as the temperature reached point tc (450 °C). The pattern displayed selenide compounds of $SnSe_2$, $CuSe_2$, and CZTSe phases indicating that the process was under Se overpressure [3]. Additionally, the micro-Raman measurement indicated the dominance of the CZTSe and the $SnSe_2$ phases due to the existence of the Raman band around 183 cm^{-1}. A less rough surface with larger grains was visible at this temperature. Moreover, when the selenization temperature reached point td (500 °C), the dominance of the $SnSe_2$, $CuSe_2$, and CZTSe phases was still obtainable as shown in the XRD pattern. Contrariwise, the Raman pattern, in this case, displayed only the existence of the CZTSe phase. It strongly suggests that the CZTSe single phase only exists on the surface of the film. As the morphology was taken into account, the sample seemed to have a larger grain size associated with the $MoSe_2$ layer at the back interface. This observation coincided with the XRD measurement as it also indicated $2\theta \approx 31.80°$ and 56.20° assigned to the $MoSe_2$ phase.

A weak XRD pattern related to $SnSe_2$ was visible as the temperature reaches point te (540 °C) while that of the $CuSe_2$ almost vanished (see Fig. 6.6 (a) - the navy color). It implies that at a lot of $CuSe_2$ phases reacted with $SnSe_2$ to form Cu_2SnSe_3, and then the reaction with ZnSe to form CZTSe took place consecutively. The surface of the sample showed the dominance of the CZTSe phase (see Fig. 6.6 (b) – the navy color**).** The morphology of the sample was characterized by a large grain associated with a 1200 nm—thick layer of $MoSe_2$ at the Mo interface. As selenization time prolonged up to 10 min, more compact morphology with the well-defined grain boundaries was observed. This observation explained why the XRD pattern of this sample demonstrated only a single phase of the CZTSe.

On the basis of these results, it can be assumed that the rate of morphology transition is relatively low. Nevertheless, the formation of CZTSe may initiate even at a lower temperature (400 °C). It is well established that in order to achieve high-quality CIGSe absorbers, the formation of the Cu-Se liquid phase has been considered as a critical phenomenon because it assists the elemental diffusion. Thus, providing that the formation of the Cu-Se liquid phase has been taking place, large grains and good crystallinity of the CIGSe absorbers can be achieved [12]. In the case of the CZTSe, the phenomena are completely analogy. Moreover, the presence of $CuSe_2$ and $SnSe_2$ phases in the bulk of the film strongly suggests that the CZTSe phase is formed due to the competitive reaction pathways, i.e. ternaries phases (Cu_2SnSe_3 + ZnSe), competes with the binaries phases ($CuSe_2$ + $SnSe_2$ + ZnSe) to form CZTSe.

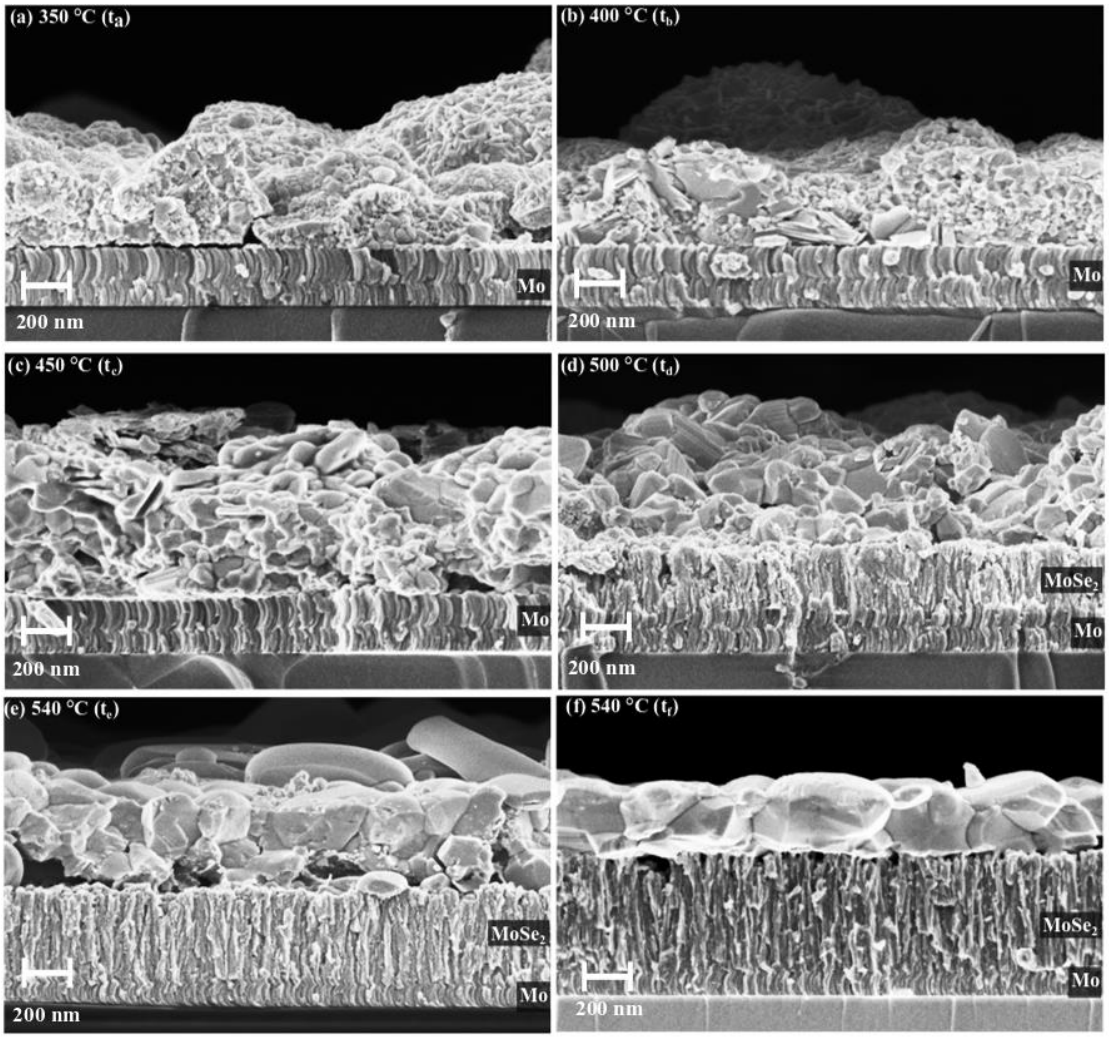

Figure 6.7: (a-f) The cross-sectional images for the sample prepared from Cu-Zn-Sn alloyed precursors produced when the standard selenization process was interrupted at different temperatures.

6.2.4 Summary

CZTSe absorber layers and device performance fabricated utilizing co-evaporated Cu-Zn-Sn alloyed precursors were examined. The impact of alloying temperature on the precursors, absorber, and solar cell properties was systematically investigated. It was found that alloying temperature resulted in the formation of both metal alloys of Cu-Zn and Cu-Sn together with elemental Sn. An investigation on the solar cell properties showed an improved in solar cell performance with an increase in alloying temperature form 250 °C to 300 °C, while higher alloying temperature deteriorated the solar cell parameters. Moreover, a temperature-dependent investigation of the formation mechanism of CZTSe layers during the selenization of co-evaporated alloyed Cu-Zn-Sn precursors demonstrated that the CZTSe formation mechanism proceeds via competitive reactions of binary and ternary phases. It was further found that the rate of the morphology changes was relatively low compared to the Se-containing precursors.

.

6.3 Impact of silver incorporation at the bak contact of CZTSe solar cell on structural and device properties

6.3.1 Motivation

The evolution of the material phases in CZTSe layers has been regarded as the vital process for attaining a good device performance. In fact, lower performance is due to a device comprising of a CZTSe layer with small grains, the presence of secondary phase, local inhomogeneities, voids, and CuZn antisite. As it has been described previously that Ag incorporation in the CZTSe absorber is expected to enhance the grain growth as well as to suppress the formation of the CuZn antisite defects. There has been some investigation on the impact of Ag incorporation into the kesterite lattice via the wet-chemical route. However, only a few research using vacuum deposition—as it holds for the in pure—Se—kesterite system. Moreover, the impact of Ag incorporation on the material phases and the morphology transition during annealing has not been studied so far.

With this motivation, the effect of Ag incorporation at the back contact of kesterite solar cells on the structural and device properties is presented and systematically interpreted in this section. In addition, the impact of Ag incorporation on the phases and morphology transition is also systematically interpreted and discussed. In order to address those aspects, Ag layers were thermally evaporated onto Mo-coated SLG using a belljar thermal evaporation unit described in chapter 3. The concentration of the element Ag in the CZTSe absorber was varied by varying the Ag film thickness (see the inset in Fig. 6.8).

6.3.2 A study on the influence of Ag incorporation at the back of Cu-Zn-Sn precursors on the morphology and phase evolution during selenization

A 20 nm Ag film was deposited at the back of Cu-Sn-Sn precursor and the temperature-dependent analysis of the selenization process was performed to study phases and morphology transition during annealing. Our standard selenization protocol was interrupted at different points in the temperature profile (see Fig. 6.8) in order to capture the diffusion of Ag into the Cu-Zn-Sn precursor. All the obtained films were examined using XRD, micro-Raman spectroscopy, and SEM.

To have a systematic investigation on this matter, the XRD of the alloyed Ag-Cu-Zn-Sn was first analyzed and compared with the annealed films. The black line in Fig 6.9 (a) shows the XRD pattern of the alloyed Ag-Cu-Zn-Sn precursor. As shown, The Ag-Cu-Zn-Sn precursor contains alloys of the $Cu_{10}Sn_3$, Ag_4Sn (PDF No. 00-029-1151), Cu_5Zn_8, Cu_6Sn_5, CuZn, and $Cu_{40.5}Sn_{11}$, together with the elemental Sn. Interestingly, no XRD peak related to the elemental Ag and alloy of Cu–Ag–Sn was detected. Annealing

the alloyed precursor at 350 °C and in Se + Sn-Se atmosphere lead to the extinction of all alloys. It implies that all alloys decomposed to selenide compounds. As it appears in Fig 6.9 (a) - the red line, major CZTSe XRD peaks at 2θ ≈ 27.16° and 44.9 ° characterized with a shoulder at 2θ ≈ 27.30° (it could be assigned to the $AgSnSe_2$ phase (PDF No. 00-033-1194)) and 45.35° (could be assigned to the Ag_2Se phase (PDF No. 00-024-1041)), respectively. Those XRD peaks indicate that more than one phase present in the film. Micro-Raman measurement demonstrated bands around 178 cm^{-1} and 245 cm^{-1}. It strongly suggests that the surface of this sample composed a mixture of the ternaries phases (Cu_2SnSe_3) and the CAZTSe phase. As has been described previously, for a CZTSe phase the major Raman vibrational modes are located at 172 cm^{-1} and 195cm^{-1}. Hence, the absence of those modes is evidence of the poor crystal quality of the CZTSe film [5], [7] and the dominance of Cu_2SnSe_3 at the surface. It is not surprising to observe the dominance of Cu2SnSe3 phase at the surface since, in a presence of Se vapor, all Cu-Sn alloys may react or decompose to form Cu_2SnSe_3 phase while the alloys of Cu-Zn decomposed to $CuSe_2$ and ZnSe. This conjecture is supported by the presence of $CuSe_2$ indicated by the peak at 2θ ≈ 47.70° in the XRD pattern. In this sense, it could also be postulated that the temperature is too low for Zn to be incorporated into the Cu_2SnSe_3 lattice, and thus impeding the formation of the CAZTSe phase. To further understand this aspect, the cross-sectional SEM image was taken. As presented in Fig. 6.10 (a), the film composed a mixture of larger and fine grains with a rough surface.

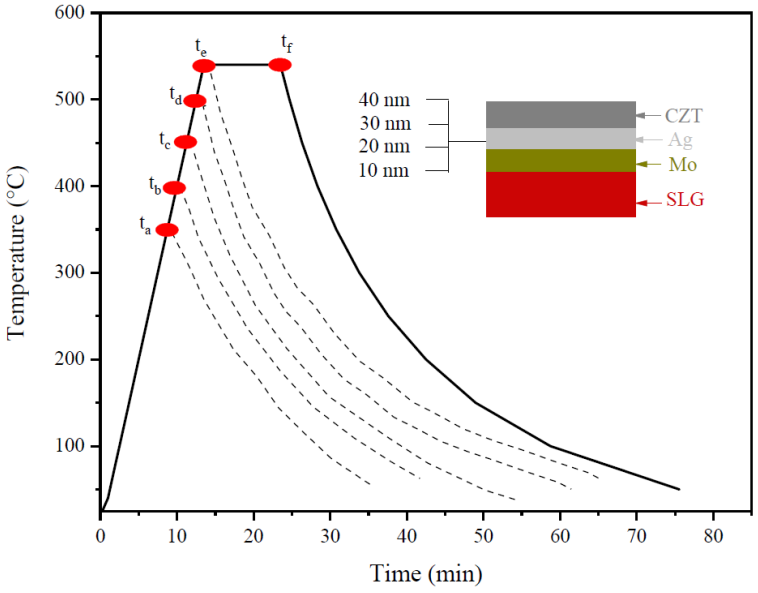

Figure 6.8: Temperature profile during selenization of precursor layers with different interruption temperatures: t_a = 350 °C, t_b = 400 °C, t_c = 450 °C, t_d = 500 °C, te = 540 °C, and t_f = 540 °C (10 min) [94].

Increasing the selenization temperature to the point t_b leads to the shift of the major XRD peak at 2θ ≈ 27.16° to the lower 2θ value (2θ ≈ 26.60°) and a clear splitting of the XRD peak at 2θ ≈ 27.30° and

45.35° is tangible as shown in Fig 6.10 (a), (the blue line). Interestingly, the extinction of the Ag_2Se phase ($2\theta \approx 44.90°$) and the evolution of $2\theta \approx 44.50°$ which can be assigned to the Cu_2Se phase (PDF No.

03-065-2982) was found. The appearance of the XRD peak at $2\theta \approx 26.60°$ together with the extinction of the Ag_2Se phase strongly indicate the formation of the Ag-rich CAZTSe phase as shown in reaction 6.2:

$$Ag_2Se + SnSe_2 \rightarrow AgSnSe_2 \quad 6.2\ (a)$$

$$AgSnSe_2 + ZnSe \rightarrow Ag_2ZnSnSe_4 \quad 6.2\ (b)$$

To provide more evidence to support our hypothesis, a pure Ag–kesterite ($Ag_2ZnSnSe_4$ (AZTSe)) film was prepared at 400 °C and its structure was analyzed by means of the XRD method. As it can be seen in Fig 6.9 (d), the XRD pattern characterized by one major XRD peak (112) at $2\theta \approx 26.60°$ which agrees with that of the tetragonal [135], [136]. Hence, it can be concluded that the XRD peak at $2\theta \approx 26.60°$ belongs to the Ag-rich CAZTSe phase. It is also worth noting that this film comprising of a bit larger grains distributed uniformly across the whole layer (see Fig. 6.10 (c)).

As the selenization temperature reached the point t_c, (450 °C), the XRD peak corresponding to the $AgSnSe_2$ phase almost vanished and the re-evolution of the Ag_2Se phase at $2\theta \approx 44.90°$ was found. The main CAZTSe XRD peak shifted back to $2\theta \approx 27.08°$ as shown in Fig 6.9 (a), the magenta color line. This observation strongly suggests that the Ag-rich CAZTSe phase decomposed and converted to the CAZTSe phase. Furthermore, the micro-Raman measurement indicated the dominance of the CAZTSe phase (Raman modes at 168 cm^{-1}, 195 cm^{-1}, and 233/245 cm^{-1}) and the $SnSe_2$ (184 cm^{-1}) phases Fig. 6.9 (b). Regarding the morphology, the films have a larger grain across the whole layer as displayed in Fig. 6.10 (c).

Increasing the selenization temperature to the point t_d, (500 °C), the XRD measurement demonstrated the dominance of CAZTSe, $SnSe_2$, Ag_2Se, and $CuSe_2$ as the main material phases (see Fig 6.9 (d)). On the contrary, the micro-Raman measurement indicated the dominance of the CAZTSe and the $SnSe_2$ phase (see Fig 6.9 (d)). These observations pointed out the fact that the Ag_2Se and $CuSe_2$ phases co-existed with the CAZTSe phase in the bulk of the film. This sample also contained a larger grain across the layer. No formation of $MoSe_2$ layer was observed. Interestingly, these observations are somewhat different from those reported in the previous section, during annealing of Ag-free Cu-Zn-Sn precursors. Despite the promising morphology of the back interface, the material purity of the film is not good for solar cell application because it contains a lot of $SnSe_2$ phases at the surface as well as the Ag_2Se and $CuSe_2$ phases in the bulk which are expected to adversely impact the device performance.

As further annealing, the precursor to 540 °C (t_e), the Ag_2Se and $CuSe_2$ phases vanished in the bulk while the $SnSe_2$ phase still co-existed with the CAZTSe phase as shown in (see Fig. 6.9 (a)). The surface of this film showed the dominance of the CAZTSe phase (see Fig. 6.9 (b)). Concerning the morphology of this sample, the film exhibited large grains across the layer associated with a thicker $MoSe_2$ layer. Interesting-

ly, as the sample was annealed for 10 mins (see Fig. 6.9 (a)), the XRD pattern showed the dominance of CAZTSe.

Increasing selenization temperature to point te, the surface of the film contained only the CAZTSe phase. However, the XRD pattern in Fig. 6.9 (a) still indicated the dominance of the $SnSe_2$ phase over the CAZTSe phase. Only when the sample was annealed for 10 min, the XRD pattern finally showed the dominance of CAZTSe**.** At this point, the selenization process was complete.

In order to provide a more convincing statement, the findings from section 6.3.5 and 6.1.3 are compared. Concerning the phase transition, in both cases, the formation of Cu_2SnSe_3, CZTSe, and CAZTSe phases starts at comparable low temperatures. It was further observed that the reaction pathway processes via a competitive reaction of binaries and ternary phases. The presence of the Ag_2Se phase-in the path of the CAZTSe formation strongly suggests that the Ag–Se phase alters the rate of Ag–Sn–Se, Cu–Ag–Sn–Se, and CAZTSe phase formation, and consequently absorber recrystallization [94].

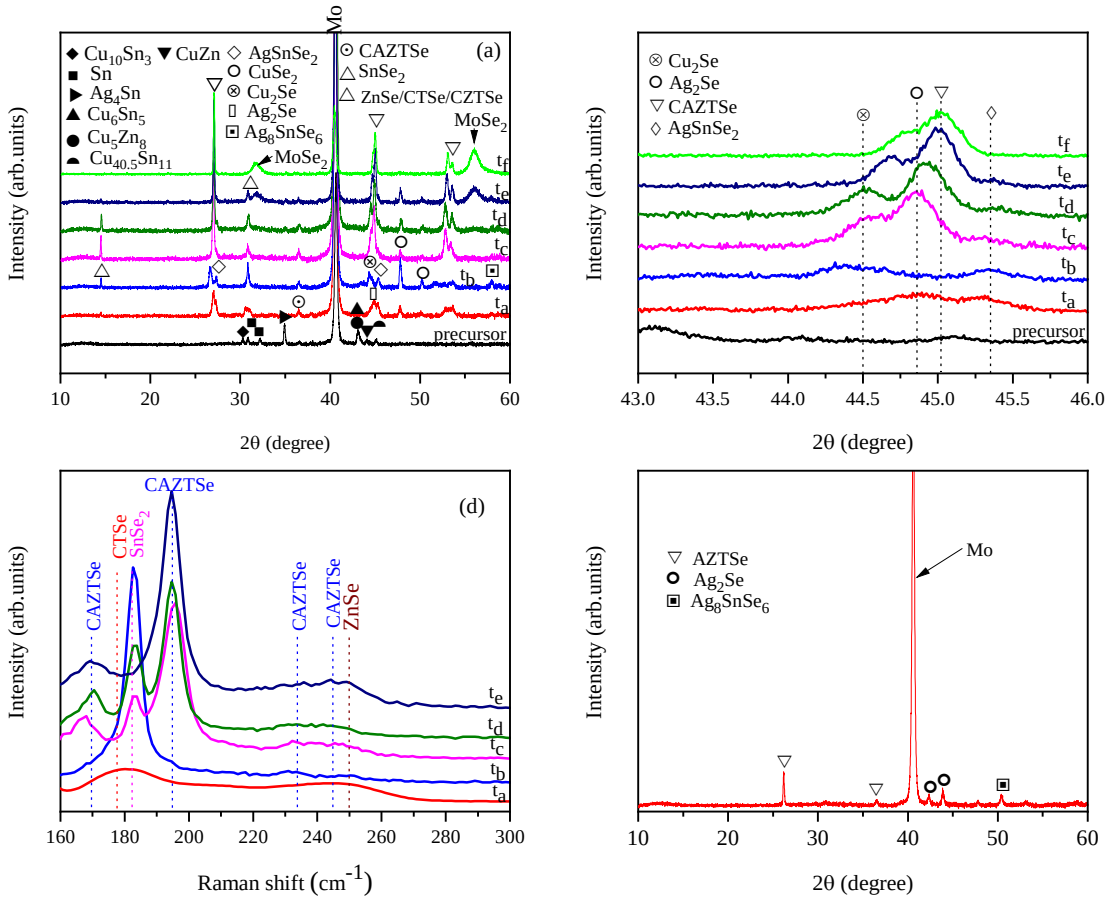

Figure 6.9: (a) The XRD pattern (b) a detailed XRD pattern for Ag-Cu-Zn-Sn precursors produced when the annealing process was interrupted at different temperatures (c) Corresponding Raman spectra (d) the XRD pattern for AZTSe film [94].

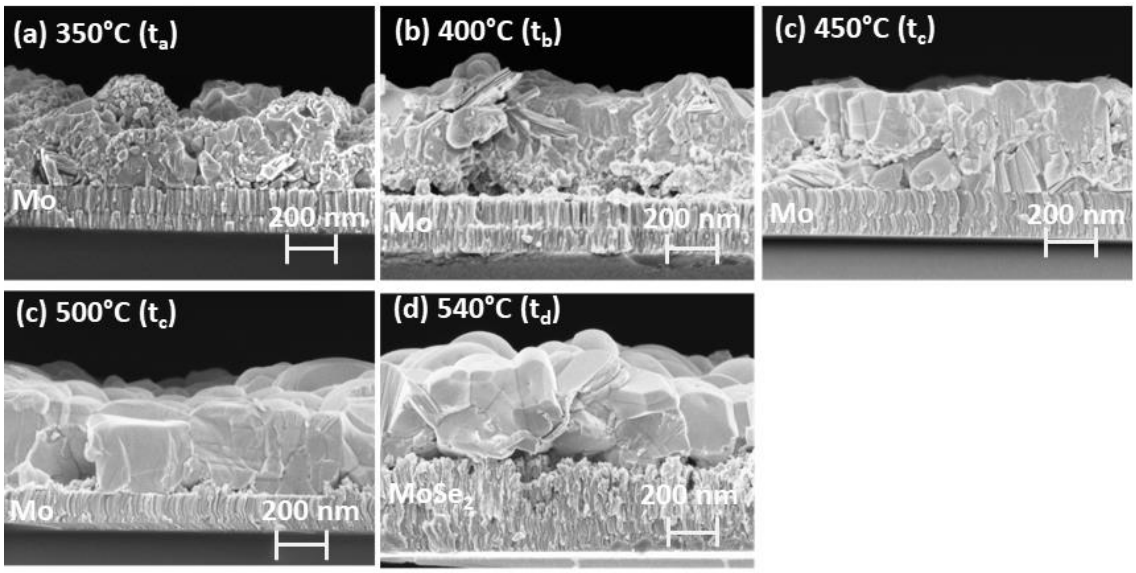

Figure 6.10: (a-f) The cross-sectional images for the sample prepared from Ag-Cu-Zn-Sn precursors produced when the standard selenization process was interrupted at different temperatures [94].

6.3.3 Impact of Ag thickness at the back of Cu-Zn-Sn precursor on the absorber growth and solar cells properties

After demonstrating the impacts of the Ag incorporation at the back on Cu-Zn-Sn precursors and on the phases and morphology transition during selenization, the impacts of the Ag concentration on the absorber growth and device properties are carefully studied. To evaluate this aspect, the concentration of Ag was varied by changing the thickness of the thermally evaporated Ag layer at the back of the Cu-Zn-Sn precursor as shown in Fig. 6.10. As it has been described previously, Ag incorporation into the CZTSe lattice is expected to change the volume of the unit cell. Thus, XRD measurement was first performed on the absorbers. Fig 6.11 (a) shows the XRD pattern of the CZTSe absorber prepared by selenization of Cu-Zn-Sn precursor with Ag thickness ranging from 0 to 40 nm.

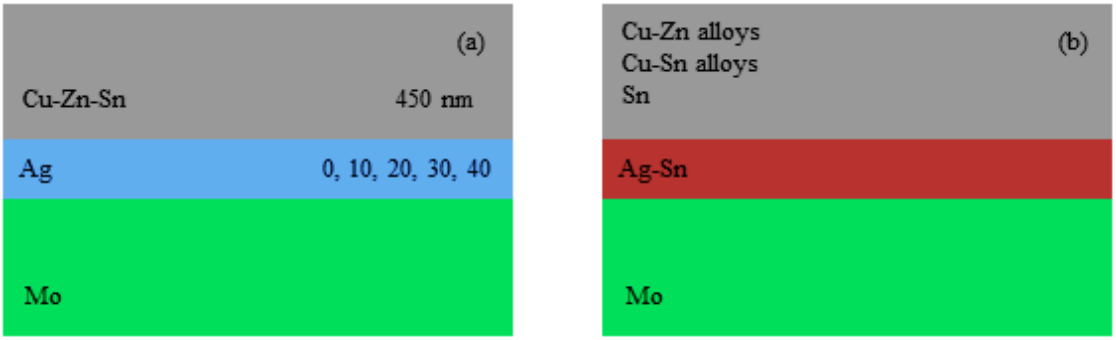

Figure 6.11: Schematic diagram (a) precursors configuration before alloying and (b) precursor after alloying in 300 °C

Table 6.2: (112) XRD peak positions and resulting [Ag] / ([Ag] + [Cu]) ratios estimated using Vegard's law for CZTSe and CAZTSe absorber prepared from Cu-Zn-Sn precursors with different Ag thickness at the back [94].

Ag thickness (nm)	0	10	20	30	40
(112) XRD peak position (°)	27.26	27.12	27.09	27.04	26.99
[Ag] / ([Ag]+[Cu])	0	0.03	0.05	0.10	0.15

The XRD patterns of both absorber types exhibited the diffraction peaks which could be indexed according to the tetragonal pure-Se-kesterite phase (PDF No. 00-052-0868). However, the shift of the XRD peak related to (112) to the lower 2θ value was found (see Fig 6.11 (b)). This observation illustrates an increase in the CZTSe unit volume upon Ag incorporation. This observation is in a good agreement with the literature [86], [90], [91]. As obviously shown in Fig. 6.11 (c), the thicker the Ag film at the back of the Cu-Zn-Sn precursor, the higher the XRD peak splitting at $2\theta \approx 53.30°$. To estimate the concentration of Ag, Vegard's law was used. To evaluate this aspect, the XRD peak related to (112) was corrected with respect to the Mo XRD peak at $2\theta \approx 40.40°$, then its maximum peak position was extracted using a Gaussian fit. Table 6.2, shows the ratio of [Ag]/[Ag]+[Cu] as a function of Ag thickness at the back of Cu-Zn-Sn precursors. As presented in Table 6.2, a nearly linearly increase in [Ag]/[Ag]+[Cu] with Ag thickness at the back of the Cu-Zn-Sn precursors was found. Based on these findings, it can be concluded that Ag atoms are successfully incorporated in the CZTSe to form CAZTSe. However, the concentration is not high enough to significantly impact the shape of XRD.

To have conclusive information about crystal quality, micro-Raman spectroscopy measurement was performed on both absorber types. As can be seen in Fig. 6.11 (d), both absorber types show Raman modes at 171 cm^{-1}, 195 cm^{-1}, and 233/245 cm^{-1} which corresponding to the CZTSe phase. It reveals that no significant impact of Ag incorporation on the shape of the spectra and deterioration of the absorber crystal quality. Having described the impact of Ag concentration of the phase formation, its influence on

the absorber morphology is now taken into account. In order to address this issue, the top view and cross-section SEM images were taken. As it appeared in Fig. 6.12, indeed, Ag concentration significantly impacted the absorber morphology. As the Ag film at the bottom of the Cu-Zn-Sn layer became thicker, the absorber grain size became larger. As it has been experimentally demonstrated in section 6.3.1, it is evident that improved in the absorber morphology is related to the concentration of the Ag-Se phase which is expected to promotes elemental diffusion during growth, thus leading to the better crystallinity and larger grains of the CZTSe absorber. It could be assumed that the concentration of Ag-Se during selenization depends on the Ag film thickness at the bottom of the Cu-Zn-Sn layer.

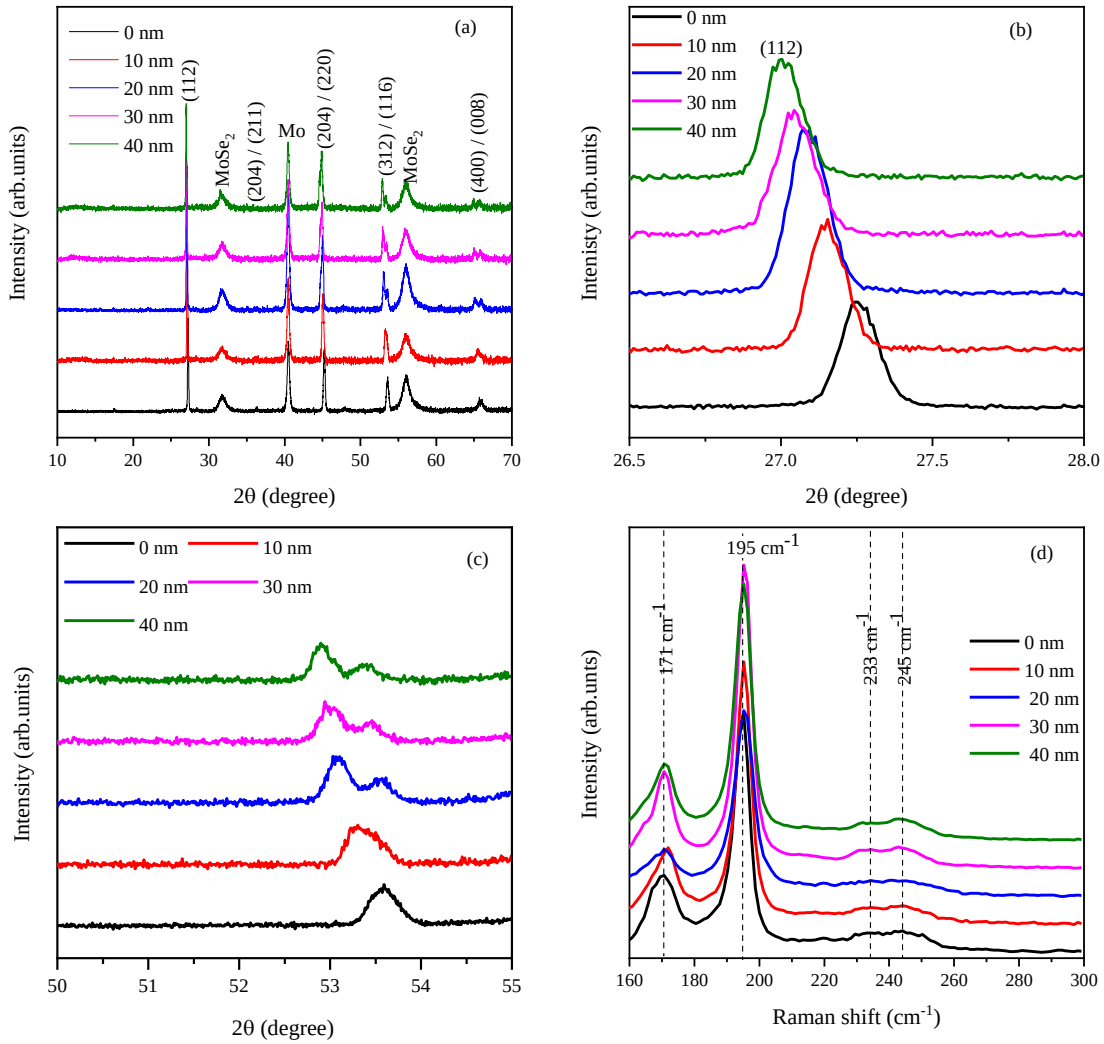

Figure 6.12: (a) XRD pattern, (b) a detailed view of the (112) XRD peak, (c) a detailed view of the (312)/(116) XRD peak, (d) the corresponding Raman spectra of the CZTSe absorbers prepared from Cu-Zn-Sn precursors with different Ag thickness at the back [94].

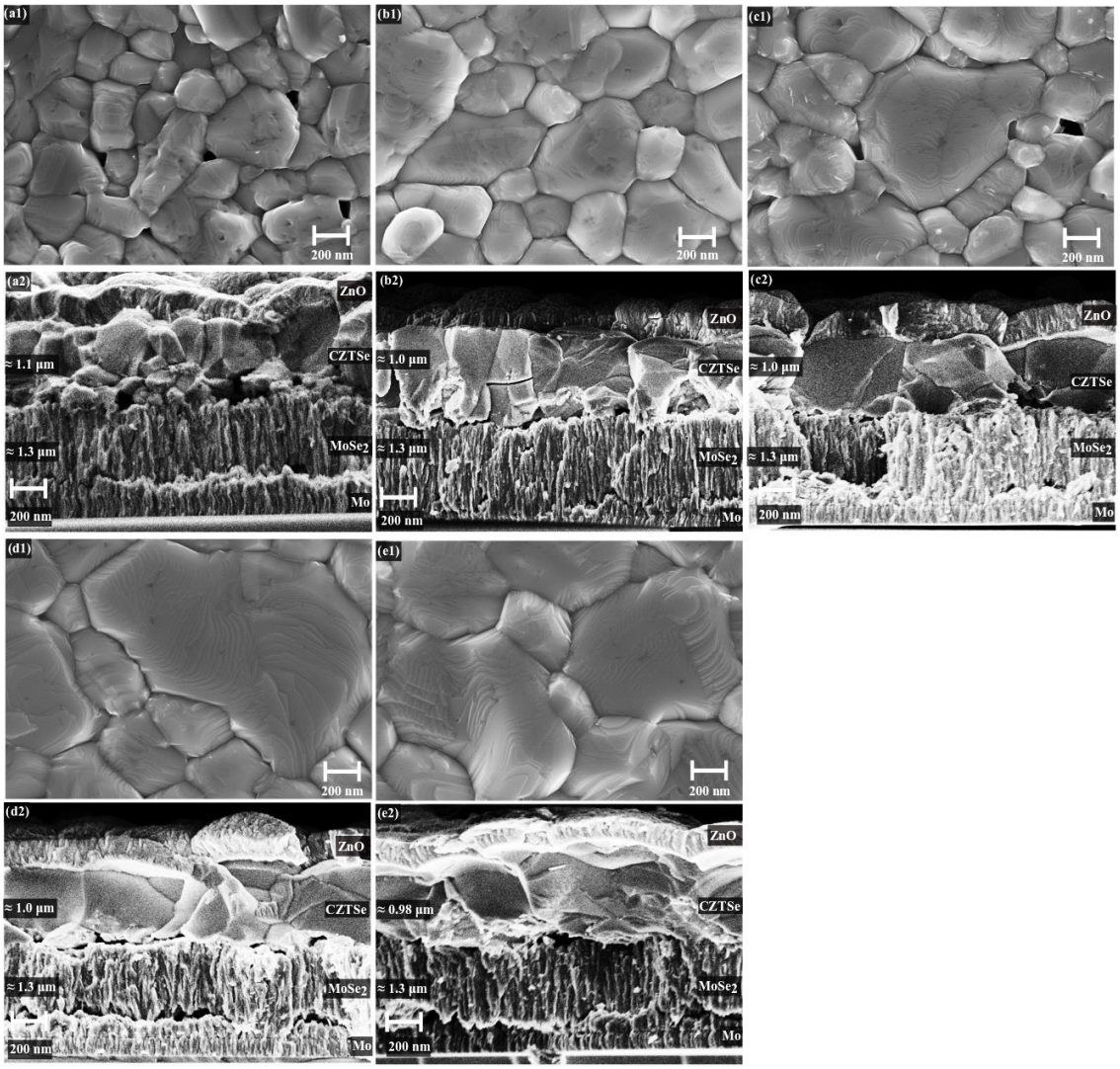

Figure 6.13: Top-view and cross-sectional SEM images of C(A)ZTSe absorbers prepared from (a) 0 nm, (b) 10 nm, (c) 20 nm, (d) 30 nm, and (e) 40 nm of Ag thickness at the bottom of the CZT precursors, respectively [94].

Moreover, from the [Ag] / ([Ag] + [Cu]) ratios estimated from XRD data (see Table 6.2), it is clear that a small concentration of Ag leads to a significant change in the absorber morphology. To the best of our knowledge, no comparable grains sized and morphologies have been reported in previous work. This indicates that Ag incorporation in vacuum-processed kesterite is more promising.

The Ag distributed uniformly in the CZTSe absorber has been so far the remaining question needed to be addressed. Thus, in order to address this aspect, the ToF-SIMS measurement depth profile measurement on complete solar cells prepared from both absorber types was performed. Special attention was paid to the elemental distribution of Cu, Zn, Sn, Se, and Ag across the absorbers. Since the measurement was performed on the complete devices, the signal of Se and Mo was used to identify the position of the window layer (ZnO and ZnO: Al layers), the absorber, the $MoSe_2$, Mo, and SLG. It should be noticed that

Depth profiles in Fig. 6 (a)–(f) are plotted as secondary ion intensities (Σ ^{64}Zn, ^{66}Zn, ^{68}Zn; Σ ^{118}Sn, ^{120}Sn; Σ ^{63}Cu, ^{65}Cu; Σ ^{76}Se, ^{77}Se, ^{78}Se; Σ ^{92}Mo, ^{95}Mo, ^{96}Mo, ^{98}Mo; and Σ ^{107}Ag, ^{109}Ag) normalized to their maximum plotted over sputter ion fluence to obtain an arbitrary depth scale. Moreover, the density of the layers is not the same, it is expected to have a strong impact on the sputtering yield during ToF-SIMS measurement—thus, and the scale is usually not linearly.

Considering the signal of Cu, Zn, Sn, Se, Ag, and Mo, as we sputtered the film from the surface during the Tof-SIMS measurement, the Zn signal was only detected until the fluence of around 1.0×10^{18} ions/cm^2 was reached. It indicates that to this depth, we sputtered through the window layer and reached the absorber layer. After reaching the absorber layer, special attention was paid on the elemental distribution of Cu, Zn, Sn, Se, and Ag. The homogenous distribution of all elements can be observed in both absorber types as shown in Fig. 6.12. This strongly indicates that elemental Ag uniformly diffuses from the back to the surface and incorporated in the CZTSe lattice during selenization as it had been observed in the XRD measurement (see Fig 6.11).

Interestingly at the fluence of around 2.7×10^{18} ions/cm^2, the signal from Zn vanished while that from Cu, Sn, and Ag significant decreased. A significant increase of the signal of Se and Mo can be observed, indicating we eroded through the absorber to the $MoSe_2$ layer. Note, a significant increase in the Mo and Se signals revealed that the density of CZTSe absorber and that of the $MoSe_2$ layer were different, thus, sputtering yield varied. Surprisingly, the signal of Cu, Sn, and Ag was present in the $MoSe_2$ layer. Since the signal of Zn completely vanished at the fluence of around 3.40×10^{18} ions/cm^2, it strongly suggests that Cu, Sn, and Ag out-diffused to the $MoSe_2$ from the absorber as proposed by Dalapati *et al*. [137]or measurement artifacts.

To learn more about this aspect, the dimpling micro-Raman measurement was performed on the dimpled devices. For this measurement, Ag-free device and device prepared from the precursors with 10 nm and 40 nm of Ag at the bottom of Cu-Zn-Sn precursors were used. The dimpling-Raman measurement using a laser excitation wavelength of 514.5 nm was performed on the $MoSe_2$/Mo interface (position P1), $MoSe_2$ layer (position P2), and CZTSe back and surface (positions P3 and P4) as illustrating Fig. 6.13 (a) and (b). At this point, the reader is reminded that, since the absorption coefficient at each interface is different, the probing depth is not the same. However, it is expected that the probing depth to below and in the order of a few 100 nm. As we probe at position L1, both absorber types display Raman vibrational modes at 167 cm^{-1}, 240 cm^{-1}, 285 cm^{-1}, and 350 cm^{-1}, respectively.

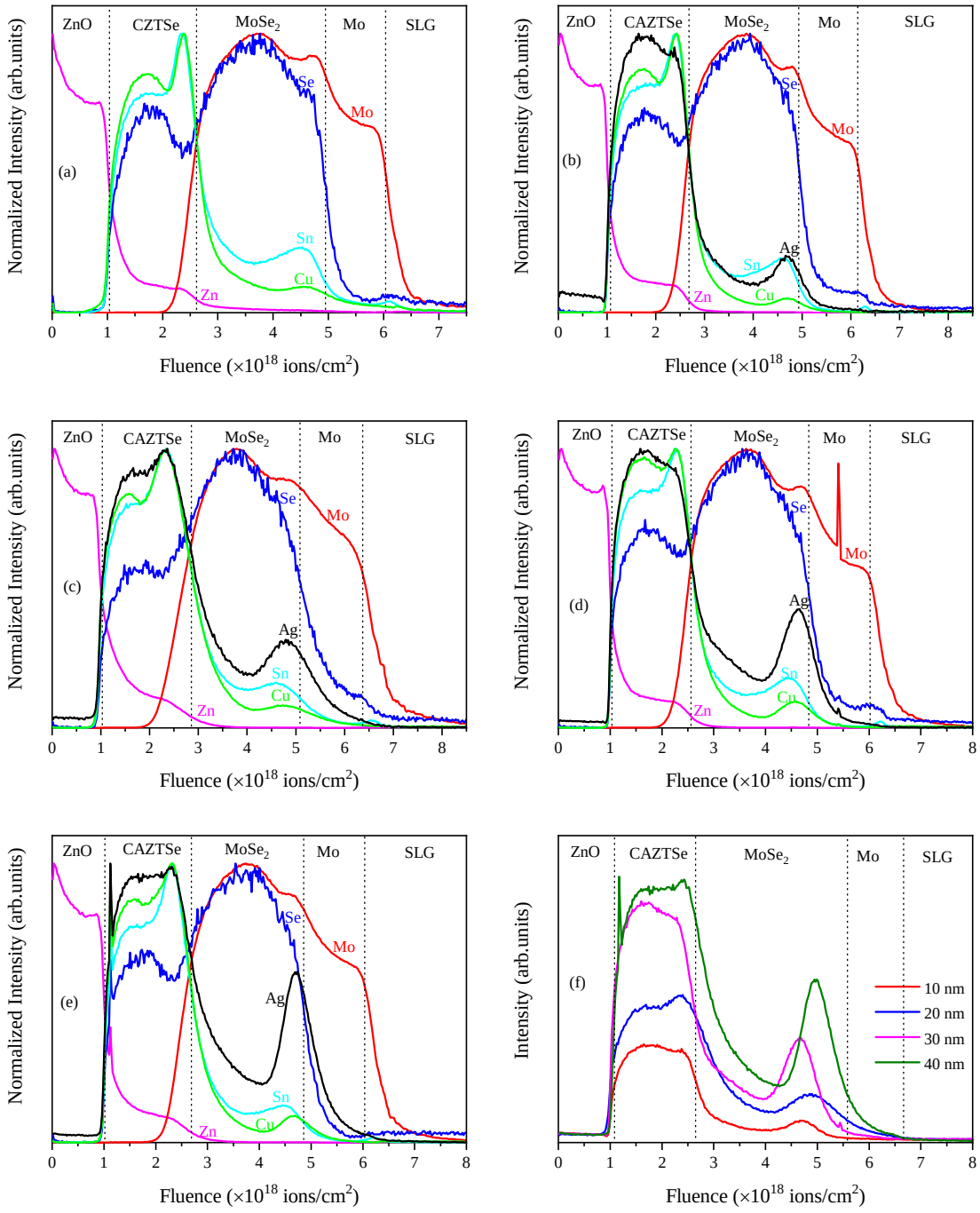

Figure 6.14: ToF-SIMS profiles of solar cells prepared from both absorber types (a) CZTSe absorber prepared from a Cu-Zn-Sn precursor. (b–e) CAZTSe absorbers prepared from Cu-Zn-Sn precursors with Ag thickness of 10 nm, 20 nm, 30 nm, and 40 nm at the bottom, respectively. (f) Ag distribution in the absorber and at the $MoSe_2$/Mo interface for precursors with different Ag layer thicknesses [94].

Based on the previous studies [137] that mode could be assigned to the $MoSe_2$ phase. When probing at the $MoSe_2$, as anticipated more intense vibrational Raman mode related to $MoSe_2$ layers are visible in both absorber types. No signal related to the Cu-Se, Sn-Se, Ag-Se, Cu_2SnSe_3, and Ag-Sn-Se phases is detected on both analyzed absorber types. Based on these findings, it could be concluded that the presence of Cu, Sn, and Ag id measuring artifacts. However, Raman spectra at a point P3 and P3 demonstrated the vibrational Raman modes at 170 cm^{-1}, 195 cm^{-1}, and 233/245 cm^{-1} corresponding to the CZTSe phase and that at 300 cm^{-1} which related to CdS. The absence of Raman mode related to any secondary phase at the position P3 indicates no decomposition of CZTSe phases at the Mo back interface as it has been reported in the prior studies [121], [122].

To further explore the Ag distribution in the absorbers, the intensity of the Ag signals are plotted vs. fluences. As expected the depth-integrated Ag signals (layer (530, 960, 1370, and 1800 kcts) are linear with the Ag thickness (10, 20, 30, and 40 nm) layer deposited at the bottom of Cu-Zn-Sn precursors.

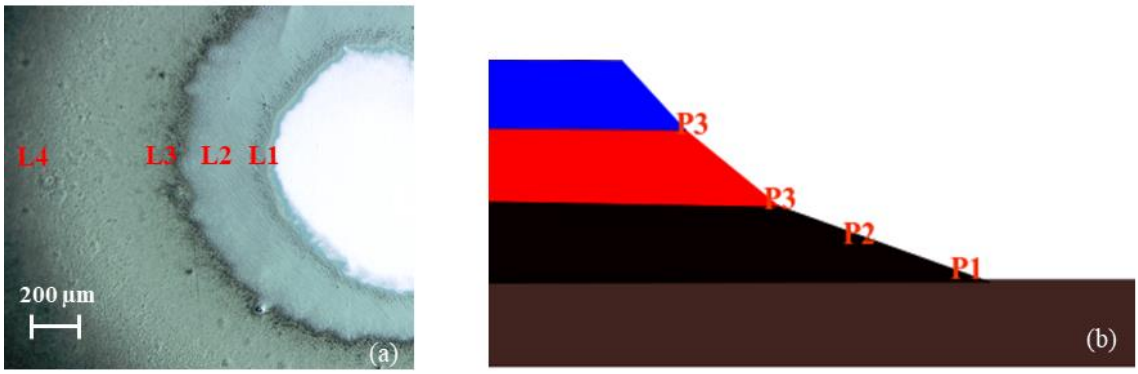

Figure 6.15: (a) Optical microscope image of a dimpled CAZTSe solar cell and (b) Schematic of dimpling Raman measurement points [94].

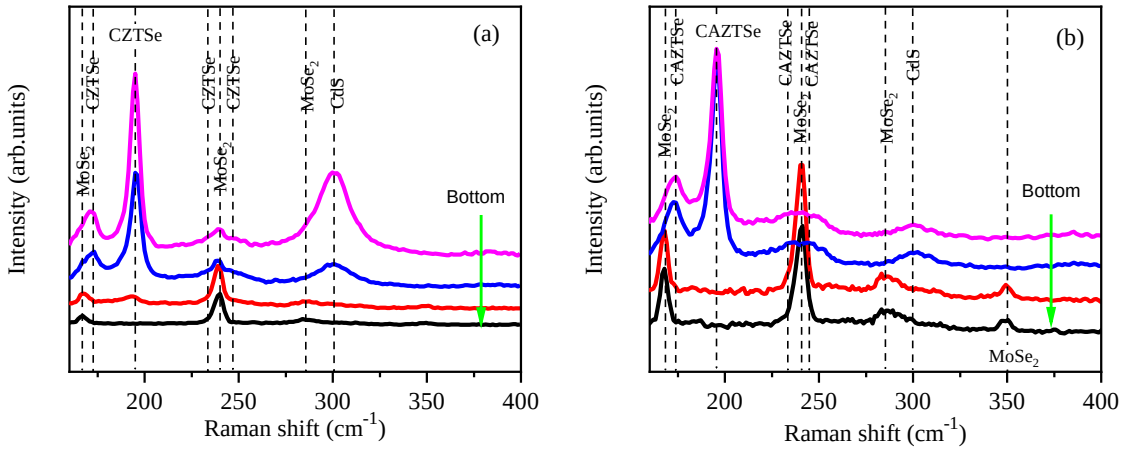

Figure 6.16: (a) dimpling-Raman spectra of the CZTSe and CAZTSe absorbers prepared from (a) Cu-Zn-Sn and (b) 40 nm Ag at the bottom of Cu-Zn-Sn precursors, respectively [94].

6.3.4 Influence of Ag thickness at the bak of CZTSe solar cell on the absorber bandgap

The previous experimental studies in ref. [89], [90] demonstrated that by incorporation Ag in the kesterite lattice the bandgap of the material can be tailored and improvement of the grain size of the CAZTSe absorber can be achieved. However, the motivation of this study is to enhance grain growth without altering the CAZTSe bandgap. Thus, the question of what happened to the bandgap of the CZTSe absorber with a thickness of the Ag layer at the bottom of the Cu-Zn-Sn precursor is yet to be addressed. To address this matter, the bandgap of the CZTSe and the CAZTSe was estimated from EQE data and ER measurement. ER measurement only measures the bandgap at the vicinity of the *p-n* junction was used to further support the bandgap obtained from EQE data. Table 6.3 presents the bandgap extracted from ER measurement and that from EQE data.

As can be seen in Table 6.3, there is no significant difference between bandgap extracted from ER measurement and that from EQE data. Based on the [Ag]/[Ag]+[Cu] estimated using XRD data (see Table 6.2), it is clear that the concentration of Ag incorporated in the CZTSe lattice is not high enough to significantly alter the material bandgap, however, it shows a substantial impact on the grain growth.

Table 6.3: Extracted CZTSe and CAZTSe absorber bandgap from the electroreflectance spectroscopy measurement and EQE data for the devices prepared from absorbers with different Ag thickness at the bottom of Cu-Zn-Sn precursor.

Silver thickness (nm)	The bandgap of CZTSe absorber (eV)	
	Extracted from ER measurement	Extracted from EQE data
0	N/A	1.04
10	1.03	1.06
20	1.05	1.07
30	1.05	1.08
40	1.04	1.09

N/A not measured sample available.

6.3.5 Impact of Ag thickness at the back of CZTSe solar cells on device performance

To further explore the impact of Ag thickness at the back of Cu-Zn-Sn on the absorber qualities after selenization, solar cells on both absorber types were fabricated and analyzed. Fig. 6.16 (a) plots the *J-V* curves of the best solar cells prepared from both absorber types, corresponding to the solar cell parameters in Table 6.4.

As it appears from Fig. 6.16 (a), the shape of the *J–V* curve is strongly influenced by the thickness of Ag at the bottom of Cu-Zn-Sn precursors. The devices prepared from the reference sample (Ag-free absorber) and that from 10 and 20 nm of Ag at the bottom of Cu-Zn-Sn seem to have a flatter slope, suggesting a better performance relative to the sample from 30 and 40 nm of Ag at the bottom of precursors. Looking at the R_S of the devices, it not surprising to observe that trend. The R_S of the devices increases (11.0 Ωcm^2 on average) (40 nm of Ag at bottom of Cu-Zn-Sn precursors). This increase in the R_S could be expected to strongly influence the maximum power point voltage, resulting in the significant drop in the FF, the V_{OC}, the J_{SC}, and the η of the devices.

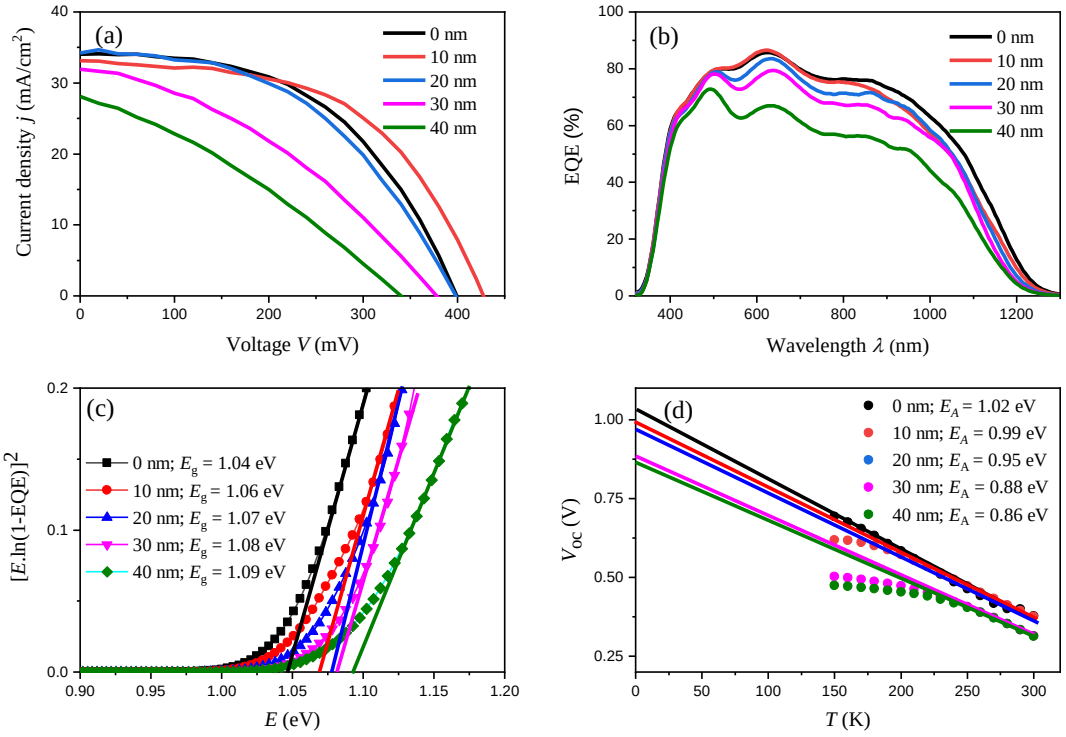

Figure 6.17: (a) Current density-voltage characteristics, (b) EQE spectra, (c) bandgap estimated by $[E{\cdot}\ln(1\text{-EQE})]^2$ vs E, and (d) variation of V_{OC} vs. temperature for solar cells prepared from Cu-Zn-Sn precursors with 0 nm, 10 nm, 20 nm, 30 nm, and 40 nm of Ag at the bottom of the precursor, respectively [94].

Table 6.4: Device parameters of cells prepared from absorbers using the CZT precursors with 0 nm, 10 nm, 20 nm, 30 nm, and 40 nm of Ag at the bottom of the precursor, respectively [94].

Sample	η (%)	FF (%)	V_{OC} (mV)	J_{SC} (mA/cm^2)	R_S (Ωcm^2)	n	j_o (×10^{-5} mA/cm^2)
0 nm	6.9 (6.2[1])	50 (48[1])	390 (380[1])	34 (34[1])	3.4 (3.4[1])	2.7 (2.7[1])	3.6 (4.9[1])
10 nm	7.6 (6.9[1])	54 (51[1])	428 (408[1])	33 (34[1])	3.1 (3.5[1])	2.7 (2.4[1])	0.6 (0.4[1])
20 nm	6.5 (6.2[1])	48 (46[1])	398 (390[1])	34 (34[1])	4.0 (4.1[1])	2.5 (2.8[1])	0.5 (2.6[1])
30 nm	4.4 (4.0[1])	36 (36[1])	378 (353[1])	32 (31[1])	6.6 (6.4[1])	2.5 (2.3[1])	0.3 (6.3[1])
40 nm	3.0 (2.6[1])	32 (31[1])	340 (323[1])	28 (27[1])	10.2 (9[1])	2.5 (2.5[1])	0.2 (1.7[1])

[1]Average device parameters

To address this, FF, the V_{OC}, the J_{SC}, and the η of the five devices prepared from both absorber types will be discussed. The best solar device prepared from Ag-free absorber (reference absorber) results to a maximum η of 6.9 % which corresponding with the V_{oc} and the FF of 390 mV (380 mV on average) and 50 % (48 % on average), respectively. It can be seen that the η increases to 7.6 % (7.0 % on average) when 10 nm of the Ag layer is deposited on the bottom of the Cu-Zn-Sn layer. The reason for this im-

provement is a significant increase in the V_{oc} (from 390 mV to 427 mV) and partially *FF* (from 50 % (48 % on average) to 54 % (51 % on average)). No effect of the J_{SC} of the device has been found. However, increasing the Ag thickness beyond 10 nm leads to the drop in the devices η due to the significant decrease in the V_{OC}, *FF*, and partially J_{SC} as shown in Table 6.4. The observed poorer device performance with an increase beyond 10 nm could be related to the significant increase in the R_S of the devices. It has been reported that the resistance of the kesterite absorber increases with an increase in the Ag concentration [89], [90].

It should be noticed that the bandgap of the absorber stays almost constant around 1.04 eV for the Ag-free reference and 1.09 eV for the devices containing 40 nm Ag, suggesting the change in the V_{OC} and partially in the J_{SC} do not relate with the bandgap. However, an interesting question remains—why huge grains observed (see Fig 6.12) results in poorer device performance? To further address this aspect, the *n* of all five devices were extracted from the dark *J-V* curves and compared as shown in Table 6.4. Interestingly, the *n* for all devices stays almost constant, above 2.5. This strongly indicates an unusual recombination mechanism in all the devices. To further understand the nature of the recombination mechanism on our devices, EQE measurement from 320 nm to 1395 nm was performed on the best solar cell of each sample. As illustrated in Fig. 16. 16 (b), the maximum EQE response (wavelength) decreases with increases in the Ag thickness at the bottom of the Cu-Zn-Sn layer. This suggests Ag incorporation induced defects in the CZTSe lattice which promotes the recombination in the devices. Moreover, the EQE response of all best solar cells prepared from the CAZTSe decreases in the longer wavelength region relative to the Ag-free absorber (CZTSe). Longer wavelength photons are expected to penetrate deeper into the kesterite absorber, thus, the photocarrier generated has a long way to the buffer and thus the probability of recombination is higher. In this line of argument, it could be hypothesized that Ag incorporation could induce Ag-related defects in the bulk of the absorber which strongly enhances recombination loss.

To further elucidate the nature of the recombination mechanism in all five devices in this series, *J-V-T* measurement was performed on the best solar cell as described in previous chapters. First, the dependence of V_{OC} and Temperature from 300 to 150 K was evaluated. The V_{OC} deviated from its linearity as shown in Fig. 6.16 (c). However, the effect is more pronounced from the sample prepared from the CAZTSe absorber. A linear extrapolation to 0 K of the plot of V_{OC} and temperature provided an E_A = 1.02, 0.99, 0.95, 0.88, and 0.86 eV for the Ag-free sample, 10 nm, 20 nm, 30 nm, and 40 nm of Ag at the bottom of Cu-Zn-Sn precursors, respectively. Based on these findings it can be concluded that while bulk recombination is dominant in devices prepared from CZTSe absorbers, while CdS/CAZTSe interface contributes more significantly to recombination losses in Ag-containing devices as well as bulk recombination.

7. Conclusions and future work

The main objective of this thesis was to examine the properties of the CZTSe absorbers and the solar cells prepared from the co-evaporated homogenous and stacked precursors. Moreover, the impacts of Ag incorporation on the CZTSe structure and solar cells properties have been examined. The fundamental aspects of the CZTSe properties, as well as formation pathways together with solar cell performance comprising both types of absorbers, have been systematically explored. In this chapter, the main results are summarized.

7.1 Conclusion

CZTSe solar cells were fabricated utilizing three precursor configurations, namely, i) homogenous Se-containing co-evaporated precursors (Cu-Zn-Sn-Se), ii) homogenous metallic co-evaporated (Cu-Zn-Sn) precursors and iii) co-evaporated multilayer stacks (Cu-Sn/Cu-Zn-Sn-Se/ZnSe/Cu-Zn-Sn-Se and Cu-Zn/Sn). The influence of selenization parameters such as initial N_2 background pressure and Sn incorporation during the selenization of Cu-Zn-Sn-Se precursors were explored. The complete solar cells fabricated from homogenous Se-containing precursors were compared in order to optimize the amount of Sn to be added during the selenization of Cu-Zn-Sn-Se precursors. Moreover, the impact of Ag incorporation at the back of Cu-Zn-Sn precursors on the structural properties of CZTSe and the characteristics of respective solar cells were investigated and discussed.

CZTSe absorbers and respective solar cells prepared by selenization of low-temperature co-evaporated Cu-Zn-Sn-Se precursors were investigated. The experimental details gained from Raman spectroscopy, X-ray diffractometry (XRD), TEM/EDXS mapping, and *J-V* measurements have yielded a clear picture of the CZTSe absorber and solar cells properties and have revealed that the selenization parameters (Sn incorporation and N_2 background pressure) strongly impact the absorber growth and device performance. The results demonstrated that Sn incorporation during the selenization suppressed the Cd/CZTSe interface recombination. A second and parallel experimental activity presented in this section was focused on the optimization of the N_2 background pressure during the selenization of Cu-Zn-Sn-Se precursors with the view of improving the CZTSe absorber quality and device performance. There is a clear correlation between the CZTSe absorber quality and the formation of the $MoSe_2$ layer with N_2 background pressure. Upon choosing an optimal background pressure, 150 mbar, we demonstrated a solar cell with η up to 7.6 % corresponding to the V_{OC} of 409 mV and the energy difference of 70 meV between bandgap extracted from EQE data and PL measurement. The electrical-temperature measurement revealed that Bulk Schott-

ky Read-Hall (SRH) recombination is the dominant recombination mechanism in the devices. Comparing the solar cell performance with those reported in the literature, it was shown that our solar cell is limited by R_S which partially impacts the *FF*.

Moreover, the phases transition during the selenization of Cu-Zn-Sn-Se precursors were investigated with a view of establishing the CZTSe formation pathways. It was observed that Cu out-diffuses during the selenization process. Further, it was found that both the morphology and phase transition depends on the annealing temperature. The co-existing of Cu_2Se, $SnSe_2$, and Cu_2SnSe_3 indicated that both binaries and ternaries phases were competing and contribute to the formation of the CZTSe phase.

CZTSe absorber and solar cells prepared from a co-evaporated multilayer Cu-Zn/Cu-Zn-Sn-Se/ZnSe/Cu-Zn-Sn-Se precursor stacks was investigated. *In-situ* pre-alloying of 100 nm Cu-Sn seed layer is an attempt to investigate if the alloys can temporary prevent Se diffusion and consequently suppress the formation of $MoSe_2$. To prove this concept, SEM and STEM images together with EDXS elemental mapping were acquired. The analysis revealed that the pre-alloyed 100 nm Cu-Sn seed layer did not fully prevent Se diffusion. It was further shown that the large grains were formed on the surface and fine grains at the Mo interface. Moreover, the emphasis in this study has been put on the device performance. Solar cells fabricated with this precursor configuration demonstrated high power conversion efficiency relative to the cells from co-evaporated precursors—mainly, due to the improvement of V_{OC} and *FF*. Two attempts have been made to suppress the formation of fine grains at the Mo interface.

The first attempt shade light on the impact of *in-situ* pre-alloying temperature on the Cu-Sn seed layer on the absorber growth and device performance. The proposed approach had a negative impact on the CZTSe adhesion, morphology quality as well as solar cell performance. Pre-annealing individual stacks or the whole precursor layer was another attempt to suppress the formation of fine grains at the Mo interface. Three different batches of samples were prepared and evaluated: one batch comprised of the sample prepared when three-stacks were *in-situ* pre-annealed, one being sample prepared when all four-stacks were in *in-situ* pre-annealed, and the last batch containing sample prepared when the whole stacked precursor was *in-situ* pre-annealed. Utilizing this technique, the formation of fine grains at the Mo interface was completely eliminated with a partial negative impact on the performance of the solar cells. However, the solar cell from CZTSe absorber prepared when the whole stacked were *in-situ* pre-annealed showed to had the highest V_{OC} (431.8) comparable to the certified record (433.2 mV) of the device from pure-Se-kesterite [16].

Furthermore, two parallel studies were conducted—one was mainly involved optimization of pre-alloying temperature on the CZTSe absorber growth and solar cells performance, while the second was focused on the impact of Ag at the back of kesterite solar cell on the structural and device properties. The investigation of reaction pathways during annealing of Ag free and Ag containing Cu-Zn-Sn precursors has been part of this work.

CZTSe absorbers and solar cells have been prepared to utilize co-evaporated Cu-Zn-Sn precursors. The investigations of the effect of pre-alloying temperature on the CZTSe absorber growth and device performance revealed that the morphology and solar cell parameters are very sensitive to the alloying temperature. Further, the study demonstrated that high efficient solar cells could be obtained by utilizing pre-alloying temperature of 300 °C. The phase transitions during annealing of co-evaporated Cu-Zn-Sn precursors were studied. The investigations showed that the phase and morphology transitions were very sensitive to the alloying temperature as observed in Se-containing precursors. It was further observed an intimate co-existing of binaries and ternaries phases in the course of CZTSe formation—suggesting that the two reaction pathways are competing in the formation of CZTSe. However, under the investigated conditions, the rate morphology transition for Cu-Zn-Sn is relatively slow with respect to Se-containing precursors.

The possible benefits due to the incorporation of Ag at the back of Cu-Zn-Sn precursors were examined. The standard annealing protocol was firstly interrupted with the motivation of investigating the sequence of the reactions during annealing of Ag-containing co-evaporated precursors. It was observed that the formation of the Ag_2Se phase during selenization speeds up the rate of morphology transition as well as the formation of the CZTSe absorber. Moreover, an intimate co-existing of binaries and ternaries phases in the course of CZTSe formation was found.

An extended study on the impact of Ag concentration in the CZTSe absorber was performed. The concentration of Ag in the absorber was varied by changing the thickness of the Ag layer at the bottom of the copper-zinc-tin (CZT) precursor. An overall observation is that the Ag incorporation considerably enhances the CZTSe grain growth. ToF-SIMS measurements demonstrated a uniform distribution of Ag across the absorber. It was further observed that a conversion efficiency improvement compared to Ag-free reference solar cells can be achieved for very thin Ag layers (10 nm) at the back contact, while thicker layers lead to device deterioration related to both enhanced bulk and interface recombination.

7.2 Future work

CZTSe materials and their derivatives (CZTS and CZTSSe) based technology needs further improvement that could shift the current record η of 12.6 %, for CZTSSe, 11.95 % for pure-Se-kesterite, and 8.4 % pure-S-kesterite close to that of CIGS (22.3 %) and CdTe (21.1 %). The main limitation being the high V_{OC}-deficit—and the cause is still an open question to the kesterite community. To narrow this gap, optimization of the formation path through the phase diagram during kesterite formation could be the key to further improvement. Thus, both precursor growth and selenization conditions should be investigated to understand their effect on the precursors and absorber properties as well as solar cell performance.

As discussed in ref. [19] that pure-Se-kesterite possesses shallower defect levels and a lower V_{OC} deficit relative to pure-S-kesterite. Moreover, the formation of pure-Se-kesterite seems to proceed at a relative

lower temperature (300 °C) than the formation of the pure-S-kesterite (350 °C) [33], [138]. However, based on our own findings in chapter 4 and refs [16], [53], this strongly depends on the concentration of Se in the precursor. It could be assumed that the Se-poor precursor allows an intimate mixing of selenide compounds (it could be ZnSe, $SnSe_2$ Cu-Se, Cu_2SnSe_3, and CZTSe) and metal alloys (Cu-Zn and Cu-Sn) in the bulk. Based on the precursor's material phases, it is most probably CZTSe formation pathways proceed via competition of binaries and ternaries phases. To elucidate this aspect, it can be proposed that a systematical investigation on the morphology and phases transition of CZTSe during annealing of Se-rich and Se-poor containing precursors should be carried out.

As illustrated previously within this work, the main limiting factor for our devices is high series resistance, barrier height, and V_{OC}. The cause of high R_S is not yet known. To understand this matter, it could be proposed that a systematic study on the relationship between selenization parameters and CZTSe absorber sheet resistance, carrier mobility, and lifetime as well as solar cell performance should be performed.

Another possible approach to reduce the V_{OC}-deficit could be by following the strategies that boosted CIGS and CdTe technologies beyond 20 %. For instance, there are two main research topics that boosted the development of CIGS technology that has not fully investigated for kesterite materials. The first one is the preparation of kesterite with bandgap grading. Commonly the bandgap of kesterite can be tuned from 1 eV to 1.5 eV by changing the ratio of Se and S ([Se]/[Se]+[S]). Several attempts have been reported in the literature so far in which a solar cell with η up 12.3 % could be achieved [15]—however, the absorber was somehow Se-rich with a front bandgap around 1.1 eV. Selenization following sulfurization is another attempt reported in the literature [106]—deterioration of the absorber morphology was observed, significantly reduce the solar cell performance. The formation energy of CZTS and CZTSe is -4.596 and -3.648 eV per formula unit, respectively—revealing that the replacement of S by Se in CZTS lattice is an endothermic reaction, thus occur at relatively high temperature [139]. However, at high processing temperature, the decomposition of CZTSSe becomes a serious problem—thus, the formation of secondary phases and unfavorable defects are expected.

On the contrary, Se replacement by S is an exothermic reaction, consequently, S replaces Se at relatively low temperature and in a short time [139]. This approach is more promising for the preparation of CZTSSe with bandgap graded at low temperatures; however, it has not been explored yet in-depth.

Partial substitution of Sn with Ge [85], [87], [140] and Cu with Ag [91], [93], [111], [134] have been successfully proved a method to tune the bandgap of kesterite absorbers. This implies that the strategies could possible induced bandgap graded in the kesterite absorber. For instance, Qi *et al*. [93] demonstrate the importance of Ag-composition-graded in CZTSe solar cells. Utilizing this approach a V-shaped band structure that depresses recombination at the interfaces could be achieved. Despite promising properties, this approach has not been intensively investigated—this holds particularly to the vacuum processed kesterite absorbers.

A bandgap gradient in CIGS is directly generated during material processing by utilizing a non-uniformity of Ga/In composition in CIGS absorber [141], [142]. A similar analogy could be employed in kesterite material. By utilizing the nature of each element which causes interdiffusion during precursors growth and selenization process the non-uniform of [Cu]/[Zn]+[Sn] composition versus absorber depth was achieved [56]. The self-formation of the non-uniform of the [Cu]/[Zn]+[Sn] composition is expected to invoke a double gradient bandgap in kesterite devices. However, the proposed strategy has not yet fully investigated. Moreover, different precursor configurations that are expected to induced in-depth non-uniform of the [Cu]/[Zn]+[Sn] composition should be investigated to prove the feasibility of the proposed approach.

8. References

[1] IAE report, World Energy Outlook: Executive summary, IAE Publishing, 2018. Available at https://webstore.iea.org/download/summary/190?fileName=English-WEO-2018-ES.pdf (accessed 03.09.2019)

[2] Giraldo. S., Jehl, Z., Placidi, M., Izquierdo-roca, V., Pérez-rodríguez. A., Saucedo. E. (2019 Progress and Perspectives of Thin Film Kesterite Photovoltaic Technology : A Critical Review. *Adv. Mater*. **31** 1806692

[3] MED-CSP final report. 2005 Concentrating Solar Power for the Mediterranean Region. Executive summary,

[4] The United Republic of Tanzania, National electrification program propectus, 2013. Available at http://www.tzdpg.or.tz/fileadmin/documents/dpg_internal/dpg_working_groups_clusters/cluster_1/Energy_and_Minerals/Key_Documents/Strategy/PROSPECTUS_-_Report_v4.pdf. (accessed 03.09.2019)

[5] Rey. G, Larramona. G, Bourdais. S, Choné. C, Delatouche. B, Jacob. A, Dennler. G and Siebentritt. S, On the origin of band-tails in kesterite. *Sol. Energy Mater. Sol. Cells*, **179** 151 (2018).

[6] Schäfer I. A and Richards. S. B, Renewable Energy Powered Water Treatment Systems, *npj Clean Water* **1(1),** 24 (2018).

[7] Todorov, T. K., Tang, J., Bag, S., Gunawan, O., Gokmen, T., Zhu, Y.,Mitzi, D. B. 2013. Beyond 11 % Efficiency : Characteristics of State-of-the-Art $Cu_2ZnSn(S,Se)_4$ Solar Cells. *Adv.Energy Mater*. **3** 34–38

[8] Ullal, H. S. and Von Roedern, B. Thin Film CIGS and CdTe Photovoltaic Technologies : Commercialization , Critical Issues , and Applications *22nd European Photovoltaic Solar Energy Conf. (PVSEC) and Exhibition* (Milan, Italy) pp 1926–9 (2007).

[9] Krämmer, C. D., (2015) Optoelectronic Characterization of Thin-Film Solar Cells by Electroreflectance and Luminescence Spectroscopy, Ph.D. thesis Karlsruhe Institute of Technology (KIT), Karlsruhe

[10] Wang, W., Winkler, M. T., Gunawan, O., Gokmen, T., Todorov, T. K., Zhu, Y., Mitzi, D. B. 2014 Device Characteristics of CZTSSe Thin-Film Solar Cells with 12.6 % efficiency. *Adv.Energy Mater*. **4** 1301465

[11] Pal K., Singh P., Bhaduri A., Thapa K. B. 2019 Current challenges and future prospects for a highly efficient (> 20 %) kesterite CZTS solar cell : A review. *Sol. Energy Mater. Sol. Cells* **196** 138-156

[12] Gao C., Schnabel T., Abzieher T., Ahlswede E., Powalla M., Hetterich M. 2016 Preparation of $Cu_2ZnSnSe_4$ solar cells by low-temperature co-evaporation and following selenization. *Appl. Phys. Lett.* **108 (1)** 013901

[13] Repins, I., Beall, C., Vora, N., Dehart, C., Kuciauskas, D., Dippo, P., To, B., Mann, J., Hsu, W., Goodrich, A., Noufi, R. 2012 Co-evaporated $Cu_2ZnSnSe_4$ films and devices. *Sol. Energy Mater. Sol. Cells* **101** 154–159

[14] Repins, I. L., Li, J. V., Kanevce, A., Perkins, C. L., Steirer, K. X., Pankow, J., Teeter, G., Kuciauskas, D., Beall, C., Dehart, C., Carapella, J., Bob, B., Park, J., Wei, S. 2015 Effects of deposition termination on $Cu_2ZnSnSe_4$ device characteristics. **582** 184–187

[15] Son D., Sung S., Park S., Jeon D. 2016 A band-gap-graded CZTSSe solar cell with 12.3% efficiency *J. Mater. Chem. A* **4** 10150

[16] Li, X., Zhuang, D. Zhang, N., Zhao, M., Yu, X., Liu, P., Wei, Y., Ren G. 2019 Achieving 11.95% efficient $Cu_2ZnSnSe_4$ solar cells fabricated by sputtering a Cu–Zn–Sn–Se quaternary compound target with a selenization process. *J. Mater. Chem. A.* **7** 994

[17] Song Z., Jang J. S., Yun J. H., Cheong H., Yan Y. 2018 Band Tail Engineering in Kesterite $Cu_2ZnSn(S,Se)_4$ Thin-Film Solar Cells with 11.8 % Efficiency. *J. Phys. Chem. Lett.* **9** 4555–4561

[18] Tampo H., Kim S., Nagai T., Shibata H., Niki S. 2019 Improving the Open Circuit Voltage through Surface Oxygen Plasma Treatment and 11.7% Efficient $Cu_2ZnSnSe_4$ Solar Cell. *ACS Appl. Mater. Interfaces*, **11** 13319–13325

[19] Lee Y. S., Gershon T., Gunawan O., Todorov T. K., Gokmen T. 2015 $Cu_2ZnSnSe_4$ Thin-Film Solar Cells by Thermal Co-evaporation with 11.6 % Efficiency and Improved Minority Carrier Diffusion Length. *Adv. Energy Mater.* **5** 1401372

[20] Taskesen, T., Neerken, J., Schoneberg, J., Pareek, D., Steininger, V., Parisi, J., Gütay, L. 2018 Device Characteristics of an 11.4% CZTSe Solar Cell Fabricated from Sputtered Precursors. *Adv. Energy Mater.* **8 (16)** 1703295

[21] Kato, T., Sakai, N., Sugimoto, H. 2014 Efficiency Improvement of $Cu_2ZnSn(S,Se)_4$ Submodule with Graded Bandgap and Reduced Backside ZnS Segregation *IEEE 40th Photovoltaic Specialist Conference (PVSC)* 0844-0846

[22] Taskesen, T., Steininger, V., Chen, W., Ohland, J. Mikolajczak, U. Pareek, D., Parisi, J., Gütay, L 2018 Resilient and reproducible processing for CZTSe solar cells in the range of 10 %. *Prog Photovolt Res Appl.* **26 (12)** 1003–1006

[23] Oueslati, S., Brammertz, G., Buf, M., Elanzeery, H., Touayar, O., Köble, C., Bekaert, J. 2015 Physical and electrical characterization of high-performance $Cu_2ZnSnSe_4$ based thin film solar cells. *Thin solid film* **582** 224–228

[24] Li, J.,Wang, H., Wu, L., Chen, C., Zhou, Z., Liu, F., Sun, Y., Han, J., Zhang, Yi. 2016 Growth of Cu_2 $ZnSnSe_4$ Film under Controllable Se Vapor Composition and Impact of Low Cu Content on Solar Cell E fficiency *ACS Appl. Mater. Interfaces* **8(6)** 10283-10292

[25] Lu, Y., Wang, S., Ma, X., Xu, X., Yang, S., Li, Y., Tang, Z. 2018. The characteristic of

Cu_2ZnSnS_4 thin film solar cells prepared by sputtering CuSn and CuZn alloy targets. *Curr. Appl. Phys.*18 (12) 1571-1576

[26] Li, J., Kim, S., Nam, D., Liu, X., Kim, J., Cheong, H., Liu, W., Li, H., Sun, Y., Zhang, Y. 2016 Tailoring the defects and carrier density for beyond 10 % efficient CZTSe thin-film solar cells *Sol. Energy Mater. Sol. Cells* **159** 447–455.

[27] Brammertz, G., Buffière, M., Oueslati, S., ElAnzeery, H., Ben Messaoud, K., Sahayaraj, S., Köble, C., Meuris, M., Poortmans, J. 2013 Characterization of defects in 9.7 % efficient $Cu_2ZnSnSe_4$-CdS-ZnO solar cells *Appl. Phys. Lett.* 103, 163904

[28] Andres, C., Haass, S. G., Romanyuk, Y. E., Tiwari, A. N. 2017 9.4% efficient $Cu_2ZnSnSe_4$ solar cells from co-sputtered elemental metal precursor and rapid thermal annealing, *Thin Solid Films*. **633** 141–145

[29] Gang, M. G., Seung Wook Shin, W. S., Hong, W. C., Gurav, V., Gwak, J., Yun, H. J., Jeong Yong Lee, Y. J., Kim, H. J. 2016 Sputtering processed highly efficient $Cu_2ZnSn(S,Se)_4$ solar cells by a low-cost, simple, environmentally friendly, and up-scalable strategy *Green Chem*. 2016 **18 (3)** 700

[30] Kim, G. Y., Son, D., Thi, T., Nguyen, T., Yoon, S., Kwon, M., Jeon, C., Kim, D., Kang, J., Jo, W. 2015 Enhancement of photo-conversion ef ficiency in $Cu_2ZnSn(S,Se)_4$ thin- fi lm solar cells by control of ZnS precursor-layer thickness. *Prog Photovolt Res Appl.* **24 (3)** 292-306

[31] Neuschitzer, M., Sanchez, Y., López-marino, S., Xie, H., Fairbrother, A., Placidi, M., Haass, S., Izquierdo-roca, V., Perez-rodriguez, A., Saucedo, E. 2015 Optimization of CdS buffer layer for high-performance $Cu_2ZnSnSe_4$ solar cells and the effects of light soaking : elimination of crossover and red kink. *Prog Photovolt Res Appl.* **23 (1)** 1660–1667

[32] Fairbrother, A., Fourdrinier, L., Fontane, X., Izquierdo-roca, V., Dimitrievska, M., Perez-rodriguez, A., Saucedo, E. 2014 Precursor Stack Ordering Effects in $Cu_2ZnSnSe_4$ Thin Films Prepared by Rapid Thermal Processing. *J. Phys. Chem.* **118 (31)** 17291-17298

[33] Hernandez Martinez, A., Placidi, M., Arques, L., Giraldo, S., Sánchez, Y., Izquierdo-Roca, V., Pistor, P., Valentini, M., Malerba, C., Saucedo, E. 2018 Insights into the formation pathways of $Cu_2ZnSnSe_4$ using rapid thermal processes *ACS Appl. Energy Mater.* **1** 1981−1989

[34] Kussi, L. 2018 Co-evaporated CZTSe solar cells: influence of Sn-incorporation during selenization on the growth and device performance Bachelor's thesis Karlsruhe Institute of Technology (KIT), Karlsruhe

[35] Powalla, M., Paetel, S., Hariskos, D., Wuerz, R., Kessler, F., Lechner, P., Wischmann, W., Friedlmeier, T. M. 2017 Advances in Cost-Efficient Thin-Film Photovoltaics Based on $Cu(In,Ga)Se_2$ *Engineering*, **3 (4)** 445–451.

[36] Grenet, L., Suzon, A. A., Emieux, F. 2018 Analysis of Failure Modes in Kesterite Solar Cells *ACS Appl. Energy Mater*. **1** 2103−2113

[37] Schorr S. 2011 The crystal structure of kesterite type compounds : A neutron and X-ray diffraction study *Sol. Energy Mater. Sol. Cells* **95 (6)** 1482–1488

[38] Schorr, S. Berlin, H., Hoebler, H. 2007 A neutron diffraction study of the stannite-kesterite solid solution series. *Eur. J. Mineral.* **19** 65–73.

[39] S Khalate, S. A., Kate, R. S., Deokate, R. J., 2018 A review on energy economics and the recent research and development in energy and the Cu_2ZnSnS_4 (CZTS) solar cells: A focus towards efficiency. *Sol. Energy* **169** , 616–633

[40] Klein, A., Baranowski, L. L., Zawadzki, P., Lany, S., Toberer, S. E., Zakutayev, A. 2016 A review of defects and disorder in multinary tetrahedrally bonded semiconductors *Semicond. Sci. Technol.* **31 (2)** 123004

[41] Kim, S., Park, J., Walsh, A. 2018 Identification of Killer Defects in Kesterite Thin-Film solar cells. *ACS Energy Lett.* **3 (2)** 496-500

[42] Chen, S., Walsh, A., Gong, X., Wei, S. 2013 Classification of Lattice Defects in the Kesterite Cu_2ZnSnS_4 and $Cu_2ZnSnSe_4$ Earth-Abundant Solar Cell Absorbers *Adv. Mater.* **25 (11)** 1522–1539

[43] Lafond, A., Choubrac, L., Guillot-deudon, C., Deniard, P., Jobic, S. 2012 Crystal Structures of Photovoltaic Chalcogenides , an Intricate Puzzle to Solve : the Cases of CIGSe and CZTS Materials. *Z. Anorg. Allg. Chem.* **638** 2571–2577

[44] Yin, X., Tang, C., Sun, L., Shen, Z., Gong, H. 2014 Study on Phase Formation Mechanism of Non-and Near-Stoichiometric $Cu_2ZnSn(S,Se)_4$ Film Prepared by Selenization of Cu−Sn−Zn−S Precursors. *Chem. Mater.* **26 (6)** 2005-2014

[45] Liu X., Feng Y., Cui H., Liu F., Hao X., Conibeer, G., Mitzi, B. D. , Green, M. 2016 The current status and future prospects of kesterite solar cells : a brief review. *Prog. Photovolt., Res. Appl.* 24 (6) 879-898

[46] Scragg, J. J., Dale, P. J., Colombara, D., Peter, L. M. 2012 Thermodynamic Aspects of the Synthesis of Thin-Film Materials for Solar Cells. *ChemPhysChem* **13 (12)** 3035-3046

[47] Katagiri, H., Sasaguchi, N., Hando, S., Hoshino, S., Ohashi, J., Yokota, T. 1997 Preparation and evaluation of Cu_2ZnSnS_4 thin films by sulfurization of E-B evaporated precursors. *Sol. Energy Mater. Sol. Cells* **49** 407–414

[48] Green, M. A., Hishikawa, Y., Dunlop, E. D., Levi, D. H., Hohl, J., Masahiro, Y., Anita W.Y. H-B. 2019 Solar cell efficiency tables (Version 53) *Prog. Photovolt., Res. Appl.* **2** 3–12

[49] Kamada, R., Yagioka, T., Adachi, S. Handa, A., Tai. K. F., Kato, T. Sugimoto, H. 2016 New world record Cu $(In,Ga)(Se,S)_2$ thin film solar cell efficiency beyond 22% *IEEE 43rd Photovoltaic Specialists Conference (PVSC)* 1287–1291.

[50] Haight, R. Barkhouse, A., Gunawan, O., Shin,B, Copel, M., Hopstaken, M., Mitzi B. D. 2017 Band alignment at the interface Cu2ZnSn(S,Se)4/CdS interface. *Appl. Phys. Lett.* **98**, 253502

[51] Suzanne, K. W., Mitzi, B. D., Walsh, A. 2017 The Steady Rise of Kesterite Solar Cells *ACS Energy Lett.* **2 (4)** 776-779

[52] Gokmen, T. Gunawan, O.,Todorov, K. T., Mitzi, B. D. 2014 Band tailing and efficiency limitation in kesterite solar cells Band tailing and efficiency limitation in kesterite solar cells.

Appl. Phys. Lett. **103**, 103506

[53] Wei, Y., Zhuang, D., Zhao, M., Gong, Q., Sun, R., Ren, G., Wu, Y., Zhang, L., Lyu, X., Peng, X. 2018 An investigation on phase transition for as-sputtered $Cu_2ZnSnSe_4$ absorbers during selenization. *Sol. Energy*, **164** 58–64

[54] Lang, M., Renz, T., Opolka, A., Zimmermann, C., Krämmer, C., Neuwirth, M., Kalt, H., Hetterich, M. 2018 Impact of the degree of Cu–Zn order in $Cu_2ZnSn(S,Se)_4$ solar cell absorbers on defect states and band tails *Appl. Phys. Lett.* **113** 033901

[55] Lai, F., Yang, J., Wei, Y., Kuo, S. 2017 High quality sustainable $Cu_2ZnSnSe_4$ (CZTSe) absorber layers in highly efficient CZTSe solar cells. *Green Chem.* 19 795–802

[56] Lai F., Yang, J., Chen, W., Kuo, S. 2017 $Cu_2ZnSnSe_4$ Thin Film Solar Cell with Depth Gradient Composition Prepared by Selenization of Sputtered Novel Precursors. *ACS Appl. Mater. Interfaces* 9 (46) 40224-40234

[57] Liu, F.,Sun, K., Li, W., Yan, C., Cui, H., Jiang, L.,Hao, X.,Green, M. 2014 Enhancing the Cu_2ZnSnS_4 solar cell efficiency by back contact modification : Inserting a thin TiB_2 intermediate layer at Cu_2ZnSnS_4/Mo interface. *Appl. Phys. Lett.* **104 (5)** 51105

[58] Karade, V., Lokhande, A., Patil, P., Hyeok, J., Babar, P., Gang, M. G., Suryawanshi, M. 2019 Insights into kesterite's back contact interface : A status review *Sol. Energy Mater. Sol. Cells* **200** 109911, 2019

[59] Son, D. H., Kim, D. H., Park, S. N., Yang, K. J., Nam, D., Cheong, H., Kang, J. K. 2015 Growth and Device Characteristics of CZTSSe Thin-Film Solar Cells with 8.03% E fficiency. *Chem. Mater.* **27 (15)** 5180-5188

[60] Duren, S. V., Sylla, D., Fairbrother, A., Sánchez, Y., López-marino, S., Márquez, J. A., Izquierdo-roca, V., Saucedo, E., Unold, T. 2018 Pre-annealing of metal stack precursors and its beneficial effect on kesterite absorber properties and device performance *Sol. Energy Mater. Sol. Cells* **185** 226–232

[61] Juškenas, R., Niaura, G., Mockus, Z., Kanapeckaite, S., Giraitis, R., Kondrotas, R., Naujokaitis, A., Stalnionis, G., Pakštas, V., Karpavičiene, V. 2016 XRD studies of an electrochemically co-deposited Cu-Zn-Sn precursor and formation of a $Cu_2ZnSnSe_4$ absorber for thin-film solar cells. *J. Alloys Compd.* 655 281–289

[62] Yoo, H., Kim, J., Zhang, L. 2012 Sulfurization temperature effects on the growth of Cu_2ZnSnS_4 thin-film. *Curr. Appl. Phys.***12 (4)** 1052–1057

[63] Giraldo, S., Saucedo, E., Neuschitzer, M., Oliva, F., Placidi, M., Alcobe´, X., Izquierdo-Roca, V., Kim, S., Tampo, H., Shibata, H. Perez-Rodrıguez A., Pisto, P. 2018 How small amounts of Ge modify the formation pathways and crystallization of kesterites. *Energy Environ. Sci.* **11** 582

[64] J. Li, Y. Zhang, W. Zhao, D. Nam, H. Cheong, and L. Wu, "A Temporary Barrier Effect of the Alloy Layer During Selenization : Tailoring the Thickness of MoSe 2 for Effi cient Cu 2 ZnSnSe 4 Solar Cells," 2015.

[65] Rim, H., Wook, S., Suryawanshi, P. M., Jung, S., Ho, J., Ha, J., Hyeok, J. 2017 Phase evolution

pathways of kesterite Cu_2ZnSnS_4 and $Cu_2ZnSnSe_4$ thin films during the annealing of sputtered Cu-Sn-Zn metallic precursors," *Sol. Energy* **145** 2–12

[66] Wibowo, R. A., Yoo, H., Hölzing, A., Lechner, R., Jost, S., Palm, J., Gowtham, M., Louis, B., Hock, R, 2013 A study of kesterite $Cu_2ZnSn(Se,S)_4$ formation from sputtered Cu – Zn – Sn metal precursors by rapid thermal processing sulfo-selenization of the metal thin films. *Thin Solid Films* **535** 57–61

[67] Izquierdo-roca, V., Espindola-Rodriguez, M., Fairbrother, A., Fontane, X., Placidi, M., Calvo-barrio, L., Perez-Rodriguez, A., Lopez-Marino, S., Saucedo, E. 2013 On the formation mechanisms of Zn-rich Cu_2ZnSnS_4 films prepared by sulfurization of metallic stacks *Sol. Energy Mater. Sol. Cells* **112** 97–105

[68] Ericson, T., Kubart, T., Scragg, J. J. Platzer-björkman, C. 2012 Reactive sputtering of precursors for Cu_2ZnSnS_4 thin film solar cells *Thin Solid Films* **520 (24)** 7093–7099

[69] Ericson, T., Scragg, J. J., Kubart, T., Törndahl, T., Platzer-björkman, C. 2012 Annealing behavior of reactively sputtered precursor fi lms for Cu_2ZnSnS_4 solar cells. *Thin Solid Films*, 535 22-26

[70] Scragg, J., Flammersberger, H., Kubart, T., Edoff, M., 2012 Influence of precursor sulfur content on film formation and compositional changes in Cu_2ZnSnS_4 films and solar cells. *Sol. Energy Mater. Sol. Cell* **98** 110–117

[71] Kuo, D., and Hsu, J. 2013 Property characterizations of $Cu_2ZnSnSe_4$ and $Cu_2ZnSn(S,Se)_4$ films prepared by sputtering with single Cu–Zn–Sn target and a subsequent selenization or sulfo-selenization procedure *Surf. Coat. Tech.* **236** 166–171

[72] Kim K., and Amal I. 2011 Growth of $Cu_2ZnSnSe_4$ Thin Films by Selenization of Sputtered Single-Layered Cu-Zn-Sn Metallic Precursors from a Cu-Zn-Sn Alloy Target. Electron. Mater. Lett. 7 (3) 225–230

[73] Neuschitzer, M., Sylla, D., Fairbrother, A., Izquierdo-roca, V., Perez-Rodriguez, A., Saucedo, E. 2014 Impact of Sn(S,Se) Secondary Phases in $Cu_2ZnSn(S,Se)_4$ Solar Cells: a Chemical Route for Their Selective Removal and Absorber Surface Passivation. *ACS Appl. Mater. Interfaces* **6 (15)** 12744-12751

[74] Colombara, D., Robert, E. V. C., Crossay, A., Taylor, A., Guennou, M., Arasimowicz, M., Malaquias, J. C. B., Djemour, R., Dale, P. J. Quantification of surface ZnSe in $Cu_2ZnSnSe_4$-based solar cells by analysis of the spectral response. *Sol. Energy Mater. Sol. Cells* **123** 220–227

[75] Redinger, A., Hönes, K., Fontané, X., Izquierdo-roca, V., Saucedo, E., Valle, N., Pérez-rodríguez, A., Siebentritt, S. 2011 Detection of a ZnSe secondary phase in coevaporated $Cu_2ZnSnSe_4$ thin films *Appl. Phys. Lett.* **98** 101907

[76] Kaur, K., Kumar, N., Kumar, M. 2017 Strategic review of interface carrier recombination in earth abundant Cu–Zn–Sn–S–Se solar cells: current challenges and future prospects. *J. Mater. Chem. A* **5**, 3069–3090

[77] Kaur, K., Kumar, N., Kumar, M. 2017 Strategic review of interface carrier recombination in earth abundant Cu–Zn–Sn–S–Se solar cells: current challenges and future prospects. *J. Mater. Chem. A*

5, 3069–3090

[78] Li, J., Zhang, Y., Wang, H., Wu, L., Wang, J., Liu, W., Zhou, Z. 2015 On the growth process of $Cu_2ZnSn(S,Se)_4$ absorber layer formed by selenizing Cu – ZnS – SnS precursors and its photovoltaic performance. *Sol. Energy Mater. Sol. Cells* **132** 363–371

[79] Han, J., Shin, W. S., Gang, G. M. Jin Hyeok Kim, H. J, Jeong Yong Lee, Y. J. 2013 Crystallization behaviour of co-sputtered Cu_2ZnSnS_4 precursor prepared by sequential sulfurization processes. Nanotechnology 24 (9) 095706

[80] Ren, Y., Ross, N., Larsen, J. K., Rudisch, K. Scragg, J. J. S. Platzer-Björkman, C., 2017 Evolution of Cu_2ZnSnS_4 during Non-Equilibrium Annealing with Quasi-*in-Situ* Monitoring of Sulfur Partial Pressure. *Chem. Mater.* **29 (8)** 3713–3722

[81] Temgoua, S., Bodeux, R., Naghavi, N. 2017 A better understanding of the reaction pathways in the formation of $Cu_2ZnSn\ (S_x,Se_{1-x})_4$ thin-films. *Sol. Energy Mater. Sol. Cells* **172** 160–167

[82] Sun, R., Zhuang, D., Zhao, M., Gong, Q., Wei, Y., Rena, G., Wua, Y. $Cu_2ZnSnSSe_4$ solar cells with 9.6 % efficiency via selenizing Cu-Zn-Sn-S precursor sputtered from a quaternary target. *Sol. Energy Mater. Sol. Cells* **174** 42–49

[83] Yao, L., Ao, J., Jeng, M., Bi, J., Gao, S., He, Q., Zhou, Z., Sun, G., Sun, Y., Chang, L. B., Chen, J. W. 2014 CZTSe solar cells prepared by electrodeposition of Cu/Sn/Zn stack layer followed by selenization at low Se pressure. *Nanoscale Res. Lett.* 9 (1) 1–11

[84] Redinger, A.,. Berg, D. M., Dale, P. J., Siebentritt, S. 2011 The consequences of kesterite equilibria for efficient solar cells, *J. Am. Chem. Soc.* **133 (10)** 3320–3323

[85] Khadka, D. B., and Kim, J. 2015 Band Gap Engineering of Alloyed $Cu_2ZnGe_xSn_1- xQ_4$(Q =S,Se) Films for Solar Cell. *J. Phys. Chem. C* **119 (4)** 1706-1713

[86] Hages, C. J., Koeper, M. J., Agrawal, R. 2016 Optoelectronic and material properties of nano-crystal-based CZTSe absorbers with Ag-alloying *Sol. Energy Mater. Sol. Cells* **145** 342–348

[87] Hages, C. J., Levcenco, S., Miskin, C. K., Alsmeier, J. H., Abou-ras, D. Wilks, R. G., Bär, M., Unold, T., Agrawal, R. 2015 Improved performance of Ge-alloyed CZTGeSSe thin-film solar cells through control of elemental losses," no. December *Prog. Photovolt., Res. Appl.* **23** 376–384

[88] Scragg, J. J. S., Larsen, J. K., Kumar, M., Persson, C., Sendler, J., Siebentritt, S. 2015 Cu–Zn disorder and band gap fluctuations in $Cu_2ZnSn(S,Se)_4$: Theoretical and experimental investigations. *Phys. Status Solidi B* **253** (2) 247–254

[89] Kumar, J., and Ingole, S., 2017 Structural and optical properties of $(Ag_xCu_{1-x})_2ZnSnS_4$ thin-films synthesised via solution route. *J. Alloys Compd.* **727** 1089–1094

[90] Gershon, T., Lee, Y. S. Antunez, P., Mankad, R., Singh, S., Bishop, D., Gunawan, O., Hopstaken, M., Haight, R. Photovoltaic Materials and Devices Based on the Alloyed Kesterite Absorber $(Ag_xCu_{1-x})_2ZnSnSe_4$. *Adv. Energy Mater.* **6** 1502468

[91] Huang, W. C., Wei, S. Y., Cai, C. H., Ho, W. H., Lai, C. H. 2018 The role of Ag in aqueous

solution processed $(Ag,Cu)_2ZnSn(S,Se)_4$ kesterite solar cells: Antisite defect elimination and importance of Na passivation. *J. Mater. Chem. A* **6 (31)** 15170–1518

[92] Gershon, T., Bishop, D., Antunez, P., Singh, S., Brew, K. W., Lee, Y. S., Gunawan, O., Gokmen, T., Todorov, T., Haight, R. 2017 Unconventional kesterites: The quest to reduce band tailing in CZTSSe *Curr. Opin. Green Sustain. Chem.* **(4)** 29–36

[93] Qi, Y. F., Kou, D. X., Zhou, W. H., Zhou, Z. J., Tian, Q. W., Meng, Y. N., Liu, X. S., Du, Z. L., Wu, S. X. 2017 Engineering of interface band bending and defects elimination via a Ag-graded active layer for efficient $(Cu,Ag)_2ZnSn(S,Se)_4$ solar cells. *Energy Environ. Sci.* **10 (11)** 2401–2410

[94] Mwakyusa, L., Leist, L., Rinke, M., Welle, A., Paetzold, U., Richards B., Hetterich, M. Impact of Silver Incorporation at the Back Contact of Kesterite Solar Cells on Structural and Device Properties **Submitted**

[95] Mwakyusa, P. L., Neuwirth, M., Kogler, W., Schnabel, T., Ahlswede, E., Paetzold, W. U., Richards, S. B., Hetterich, M. CZTSe solar cells prepared by co-evaporation of multilayer Cu–Sn/Cu,Zn,Sn,Se/ZnSe/Cu,Zn,Sn,Se stacks *Phys. Scr.* **94** 105007

[96] Hetterich, M. 1998 *Molekularstrahlepitaxie, strukturelle und optische Eigenschaften ultradünner CdS/ZnS-Quantenstrogstrukturen.* Shaker Verlag, Aachen Germany

[97] Musiol, T. 2014 Investigation into the selenization process of precursors for CZTSSe thin-film solar cells. Master's thesis, Karlsruhe Institute for Technology, Karlsruhe

[98] Fraser D. B. and Melchior H. 1972 Sputter-Deposited CdS Films with High Photoconductivity through Film Thickness. *J. Appl. Phys.* 43, 31203

[99] Tsai, C. T., Chuu, D. S., Chen, G. L., Yang S. L. 1996 Studies of grain size effects in rf sputtered CdS thin films. *J. Appl. Phys.* 79, 9105

[100] Khallaf, H., Oladeji, I. O., Chai, G., Chow, L. 2008 Characterization of CdS thin films grown by chemical bath deposition using four different cadmium sources. *Thin solid films* 516 **(3)** 7306–7312

[101] Dudchak, I. V., and Piskach, L. V 2013 P hase equilibria in the Cu_2SnSe_3–SnSe –ZnSe system. *J. Alloys Compd* vol. **351**145–150, 2003.

[102] Dofia J. M. and Herrero J. Chemical Bath Deposition of CdS Thin Films : An Approach to the Chemical Mechanism through Study of the Film Microstructure. *J. Electrochem. Soc.* **144 (11)** 4081-4091

[103] Neuwirth, M. 2015 Nasschemishe Hesttellung von CZTSSe-absorber-und-CdS-Pufferschnichetn für Dünnschichtsolarzellen. Masters's thesis Karlsruhe Institute of Technology (KIT), Karlsruhe

[104] Cliff, G. and Lorimer, G. W. 1975 The quantitative analysis of thin specimens *J. Microsc.* **103 (2)** 203–207

[105] Pode, R. and Diouf, B. 2011 *Solar lighting.* Springer-Verlag London Limited

[106] Neuwirth, M., Seydel, E., Seeger, J., Welle, A., Kalt, H., Hetterich, M. 2017 Band-gap tuning of $Cu_2ZnSn(S,Se)_4$ solar cell absorbers via defined incorporation of sulphur based on a post-

sulphurization process," *Sol. Energy Mater. Sol. Cells* **182** 158–165

[107] Woska, S. 2017 Analysis of loss mechanism in CZTSSe thin-film solar cells via current-voltage characteristcs. Master's thesis karlsruhe Institute of Technology

[108] Ginley, D. S. and Cahen, D. 2012 *Fundamentals of Materials for Energy and Environmental Sustainability*. Cambridge University Press, New york, US

[109] Honsberg, C. B. and Bowden S. G. 2012 Photovoltaics Education 2019. Available at https://www.pveducation.org. (accessed on 03.09.2019)

[110] Neuschitzer, M., Rodriguez, E., Guc, M., Marquez, J. A. Giraldo, S., Forbes, I., Perez-rodriguez, A., Saucedo, E. 2018 Revealing the beneficial effects of Ge doping on Cu2ZnSnSe4 thin film solar cells. *J. Mater. Chem. A* **6** 11759

[111] Nguyen, T. H., Kawaguchi, T., Chantana, J., Minemoto, T., Harada, T., Nakanishi, S., Ikeda, S. 2018 Structural and Solar Cell Properties of a Ag-Containing Cu_2ZnSnS_4Thin Film Derived from Spray Pyrolysis. *ACS Appl. Mater. Interfaces* **10 (6)** 5455–5463

[112] Krämmer, C., Huber, C., Redinger, A., Sperber, D., Rey, G., Siebentritt, S. 2015 Diffuse electroreflectance of thin-film solar cells : Suppression of interference-related lineshape distortions *Appl. Phys. Lett.* 107 222104

[113] Fernandes, P. A., Salome P. M. P., da Cunha, A. F. 2009 Precursors ' order effect on the properties of sulfurized Cu_2ZnSnS_4 thin films. *Semicond. Sci. Technol.* **24** 105013

[114] Fella, C. M., Uhl, A. R., Hammond, C., Hermans, I., Romanyuk, Y. E., Tiwari, A. N. 2013 Formation mechanism of $Cu_2ZnSnSe_4$ absorber layers during selenization of solution deposited metal precursors *J. Alloys Compd.* **567** 102–106

[115] Dimitrievska, M., Fairbrother, A., Fontané, X., Jawhari, T., Izquierdo-Roca, V., Saucedo, E. 2014 Multiwavelength excitation Raman scattering study of poly-crystalline kesterite Cu_2ZnSnS_4 thin films, *Appl. Phys. Lett.* **104 (2)** 021901

[116] Wang, K., Gunawan, O., Todorov, T., Shin, B., Chey, S. J., Bojarczuk, N. A., Mitzi, D., Guha, S. 2010 Thermally evaporated Cu_2ZnSnS_4 solar cells. *Appl. Phys. Lett.* **97 (14)** 2-5

[117] Redinger, A., Hönes, K., Fontané, X., Izquierdo-roca, V., Siebentritt, S. 2011 Detection of a ZnSe secondary phase in coevaporated $Cu_2ZnSnSe_4$ thin films Detection of a ZnSe secondary phase in coevaporated $Cu_2ZnSnSe_4$ thin films. *Appl. Phys. Lett.* **98** 101907

[118] Haass, S. G., Diethelm, M., Werner, M., Bissig, B., Romanyuk, Y. E., Tiwari, A. N., 11.2 % Efficient Solution Processed Kesterite Solar Cell with a Low Voltage Deficit. *Adv. Energy Mater.* **5 (18)** 1–7

[119] Zhang, Z., Yao, L., Zhang, Y., Ao, J., Bi, J., Gao, S., Gao, Q., Jeng, M., Sun, G., Zhou, Z., He, Q., Sun, Y. 2018 Modified Back Contact Interface of CZTSe Thin Film Solar Cells: Elimination of Double Layer Distribution in Absorber Layer. *Adv. Sci.* **5** 1700645

[120] Shin, B., Nestor A. B., Guha S. 2013 On the kinetics of $MoSe_2$ interfacial layer formation in chalcogen-based thin film solar cells with a molybdenum back contact. *Appl. Phys. Lett.* 102, 091907

[121] Scragg, J.J., Wa, J. T., Edo, M., Ericson, T., Kubart, T., Platzer-björkman, C. 2012 A Detrimental Reaction at the Molybdenum Back Contact in $Cu_2ZnSn(S,Se)_4$ Thin-Film Solar Cells. *J. Am. Chem. Soc.* **134** 19330−19333

[122] Scragg, J. J., Kubart, T., Wätjen, J. T., Ericson, T., Linnarsson, M. K., Platzer-björkman, C. 2013 Eff ects of Back Contact Instability on Cu_2ZnSnS_4 Devices and Processes. *Chem. Mater.* **25** 3162−3171

[123] Schnabel, T. and Ahlswede, E. 2016 On the interface between kesterite absorber and Mo back contact and its impact on solution-processed thin-film solar cells. *Sol. Energy Mater. Sol. Cells* **159** 290–5

[124] Liu, F., Sun, K., Li, W., Yan, C., Cui, H., Jiang, L., Hao, X., Green, M. 2014 Enhancing the Cu_2ZnSnS_4 solar cell efficiency by back contact modification: Inserting a thin TiB_2 intermediate layer at Cu_2ZnSnS_4/Mo interface. *Appl. Phys. Lett.* **104 (5)** 51105

[125] Cui, H., Liu, X., Liu, F., Hao, X., Song, N., Yan, C. 2014 Boosting Cu_2ZnSnS_4 Solar Cells Efficiency by a Thin Ag Intermediate Layer Between Absorber and Back Contact. *Appl. Phys. Lett.* **104** 041115

[126] Li, W., Chen, J., Cui, H., Liu, F., Hao, X. 2014 Inhibiting MoS_2 formation by introducing a ZnO intermediate layer for Cu_2ZnSnS_4 solar cells. *Mater. Lett.* **130** 87–90

[127] Lopez-Marino, S., Placidi, M., Perez-Tomas, A., Llobet, J., Izquierdo-Roca, V., Fontane, X., Fairbrother, A., Espindola-Rodriguez, M., Sylla, D., Perez-Rodriguez, A., Saucedo, E. 2013 Inhibiting the absorber/Mo-back contact decomposition reaction in $Cu_2ZnSnSe_4$ solar cells: the role of a ZnO intermediate nanolayer," *J. Mater. Chem. A* **29** 8338–8343

[128] Sardashti, K., Chagarov, E., Antunez, P., Gershon, T., Ueda, S., Gokmen, T., Bishop, D., Haight, R., Kummel, A. 2017 Nanoscale Characterization of Back Surfaces and Interfaces in Thin- Film Kesterite Solar Cells. *ACS Appl. Mater. Interfaces* 9 (20) 17024-17033

[129] Ranjbar, S. , Brammertz, G. , Vermang, B. , Hadipour, A. , Cong, S. , Suganuma, K. , Schnabel, T. , Meuris, M. , da Cunha, A. F. and Poortmans, J. (2017), Improvement of kesterite solar cell performance by solution synthesized MoO_3 interfacial layer. *Phys. Status Solidi A*, 214: 1600534.

[130] Major J. D. 2016 Grain boundaries in CdTe thin film solar cells: a review. *Semicond. Sci. Technol.* **31 (9)** 93001

[131] Repins, I. L., Moutinho, H., Choi, S. G., Kanevce, A., Kuciauskas, D., Dippo, P., Beall, C. L., Carapella, J., DeHart, C., Huang, B., We S. H. 2013 Indications of short minority-carrier lifetime in kesterite solar cells. *J. Appl. Phys.* **114** 084507

[132] Hages, C. J., Redinger, A., Levcenko, S., Hempel, H., Koeper, M.ark J., Agrawal, R.akesh Greiner, D. Kaufmann, C. A., Unold, T. 2017 Identifying the Real Minority Carrier Lifetime in Nonideal Semiconductors : A Case Study of Kesterite Materials. 1–10

[133] Li, W., Liu, X., Cui, H., Huang, S., Hao, X. 2015 The role of Ag in $(Ag,Cu)_2ZnSnS_4$thin film for solar cell application *J. Alloys Compd.* **625** 277–283

[134] Qi, Y., Tian, Q., Meng, Y., Kou, D., Zhou, Z., Zhou, W., Wu, S. 2017 Elemental precursor solution processed $(Cu_{1-x}Ag_x)2ZnSn(S,Se)_4$ photovoltaic devices with over 10 % efficiency. *ACS Appl. Mater. Interfaces* **9** (25) 21243-21250

135] Gershon, T., Sardashti, K., Seog, Y., Gunawan, O., Singh, S., Bishop, D., Kummel, A. C., Haight, R. 2017 Compositional effects in $Ag_2ZnSnSe_4$ thin films and photovoltaic devices. *Acta Mater.* **126** 383–388

[136] Jiang, Y. Y., Yao, B., Jia, J., Ding, Z., Deng, R., Liu, D., Sui, Y., Wang, H., Li, Y., 2019 Structural, electrical, and optical properties of $Ag_2ZnSnSe_4$ for photodetection application, *J. Appl. Phys* **125** 025703

[137] Dalapati, G. K., Zhuk, S., Masudy-panah, S., Kushwaha, A., Seng, L., Chellappan, V., Suresh, V., Su, Z., Batabyal, S. K. 2017 Impact of molybdenum out diffusion and interface quality on the performance of sputter grown CZTS based solar cells. *Nature Scientific Report* **7** 1350

[138] Feng, Y., Lau, T., Cheng, G., Yin, L., Li, Z., Luo, H., Liu, Z., Lu, X., Yang, C., Xiao, X. 2016 A low-temperature formation path toward highly efficient Se-free Cu_2ZnSnS_4 solar cells fabricated through sputtering and sulfurization. *CrystEngComm* **18** 1070

[139] Singh, A. K., Aggarwal, G., Singh, R. K., Klein, T. R., Das, C., Neergat, M., Kavaipatti, B., van Hest, M. 2018 Synthesis of CZTS/Se and Their Solid Solution from Electrodeposited Cu–Sn–Zn Metal Precursor: A Study of S and Se Replacement Reaction *ACS Appl. Energy Mater.* **1** 3351−3358

[140] Collord A. D. and Hillhouse H. W. 2016 Germanium Alloyed Kesterite Solar Cells with Low Voltage De ficits. *Chem. Mater.* 28 (7) 2067-2073

[141] Gloeckler, M. Sites, J. R. 2005 Band-gap grading in $Cu(In,Ga)Se_2$ solar cells. *J. Phys. Chem. Solids* **66** 1891–1894

[142] Wang, Y., Shieh, H. D., Wang, Y., Shieh, H. D. 2014 Double-graded bandgap in $Cu(In,Ga)Se_2$ thin film solar cells by low toxicity selenization process. *Appl. Phys. Lett.* **105** 073901